Stimulus and post-stimulus olfactory representations in health and disease

A thesis

Submitted in partial fulfillment of the requirements

Of the degree of

Doctor of Philosophy

By

Anindya S. Bhattacharjee

20153391

IISER PUNE

INDIAN INSTITUTE OF SCIENCE EDUCATION

AND RESEARCH PUNE

2021

Dedication

'*To my dida and dadu*'

Declaration

      I declare that this written submission accurately reflects my ideas in my own words, as well as the ideas of others, and that I have properly quoted and referenced the original sources. I also declare that I have followed all principles of academic honesty and integrity and have not misrepresented, fabricated, or falsified any thought, data, fact, or source in my submission. I understand that failure to comply with the above will result in disciplinary action by the Institute, and can also evoke penal action from the sources that have not been properly cited or from whom proper permission has not been taken when needed.

Date: 01/05/2021

Anindya S. Bhattacharjee

20153391

Certificate

This is to certify that the work incorporated in the thesis entitled '**Stimulus and post-stimulus olfactory representations in health and disease**', submitted by **Anindya S. Bhattacharjee** was carried out by the candidate, under my supervision. The work presented here or any part of it has not been included in any other thesis submitted previously for the award of any degree or diploma from any other University or Institution.

Date: 01/05/2021

Dr. Nixon M. Abraham

Acknowledgments

First and foremost, I would like to express my sincere gratitude to my supervisor, Dr. Nixon M. Abraham, for providing me with the opportunity to work in his lab. His unrivaled passion for science, enormous knowledge, and determination to take on challenging projects are qualities I admire and hope to emulate as I progress through my professional career. He gave me direction, encouragement, and, most importantly, lessons on how to do good science, and over time, he became more of a mentor and friend than a boss. I've learned a lot from him, both professionally and personally, and I owe him my undying gratitude. I'm also grateful to Nixon for giving me the opportunity to assist in the lab's setup. Being one of the first students in the lab, helping to set it up, and seeing it evolve was an exciting experience.

I would also take this opportunity to thank all my Research Advisory Committee members – Dr. Aurnab Ghose, Dr. Collins Assisi, and Dr. Raghav Rajan. They have constantly guided me and provided critical feedback on my project. In September 2019, I was awarded the 'Swiss Government Excellence Scholarship' by the Federal Commission for Scholarships for Foreign Students, Government of Switzerland. The scholarship supported my visit to The University of Geneva to work with Prof. Alan Carleton. My time at the Carleton lab has been productive and working with Prof. Carleton was a great experience. Much of the calcium imaging analysis presented in chapter 4 is owed to my time in the Carleton lab.

I would like to express my gratitude to Prof. L. S. Shashidhara for his support, as well as Prof. N. K. Subedar for his guidance and blessings.

My doctoral studies needed more than just academic support, and I owe my lab mates a debt of gratitude for putting up with me for the past six years. I consider myself fortunate to have these wacky nerds as friends. Every single person in the lab has always gone out of their way to assist me whenever I've had a problem with my work. Sarang, Meenakshi, Shruti, Rajdeep, Priya, Atharva, Sanyukta, Susobhan, Suhel, Kaushik, Arpan, Lisni, Meher, Felix, Deepshikha, Eleanor, Siddharth, Shohini, Prasad, Rishabh, and Ananthi made the lab a fun environment to work. I've found Sarang and Meenakshi to be excellent companions for not only science but also philosophical discussions and frustration venting after a hard day in the lab. Shruti and Rajdeep, along with Atharva, made sure there was never a dull moment in the lab. A special thanks to Atharva for assisting me with some important analyses. I have been fortunate to mentor Priya, Atharva, Prasad, and Shohini during their Master's dissertation. They've all been highly motivated and fast learners, and I wish them all the best in their future endeavors. I miss Sasank as I recall

the happy memories we shared in the lab. It was difficult to say goodbye, but you will live on in our memories forever.

The life outside the lab was just as interesting and exciting as the life inside. Special thanks to Soumen, Nelchi, Sanket, Siddhi, Akanksha, Devika, Simran, and Debayan for the many memorable times we all spent together. I share a special bond with Soumen, who was my flatmate for a great many years. We both have shared our many failures and very few achievements and supported each other during our Ph.D. journey.

Above all, none of this would have been possible without my family – Maa, Baba, Papai, and Isha. They had always been a pillar of strength for me and have always helped me in all of my life's decisions. I can't thank Isha enough for being my better half, believing in me, and bringing a smile to my face even in the worst of times. This thesis stands as a testament to your unconditional love and encouragement.

-Anindya

Table of Content

List of figures

List of tables

Synopsis

Animals use sensory systems to detect and integrate stimuli features from their immediate environment to generate optimal behavioral responses. Understanding how sensory systems process stimulus-evoked neural activity to form decisions and commit to appropriate actions is a significant challenge in neuroscience. The olfactory system represents an excellent model to study the relationship between stimuli, neural activity dynamics, and decision-making behaviors. Almost all animals use their sense of smell to detect and differentiate between conspecifics and predators, locate potential mates and food sources. Moreover, impaired olfaction negatively impacts life as appetite is reduced, maintenance of personal hygiene becomes difficult, ability to detect warning odor is impaired, and fostering social relationships becomes challenging (*1*, *2*). Over recent years, meticulous investigations have recognized the link between olfactory dysfunctions and neurodegenerative diseases (*3–5*). The high prevalence, early manifestation, and persistence throughout the disease progression have incited keen interest amongst the researchers to probe olfactory dysfunctions as a prognostic marker for different neurodegenerative diseases, like Parkinson's (*6*, *7*) and Alzheimer's disease (*8*, *9*). Recent data suggest that attention to maladaptive changes in smell may improve chances for early diagnosis of these neurodegenerative diseases (*1*). To achieve this, understanding the mechanisms underlying olfactory functions is of utmost importance.

In nature, odor molecules vary in their physical and chemical properties and can exist either as monomolecular entities or combine to form complex molecule mixtures. The first step in odor perception initiates by inhaling odor molecules through the nose. Inside the nasal epithelium, odorants travel through a mucus layer to bind to odorant receptors (OR) present on olfactory sensory neurons (OSN). Most OSNs express one type of OR, and all OSNs expressing the same receptor converge together to neuropil-like structures in the olfactory bulb (OB), called glomeruli. Depending on odor chemical class, different odors activate distinct and complex spatiotemporal patterns of glomeruli (*10–14*). The similarity of glomerular activity patterns is higher for odors with high structural similarity like enantiomer pairs or when odorants are mixed in certain ratios (*15–17*). Within the glomerulus, OB's major relay neurons, mitral and tufted cells (MTCs), make excitatory synaptic connections with axonal terminals of OSNs (*18*). MTCs also receive inhibitory inputs from periglomerular interneurons in the glomerular layer (GL) as well as interneurons in the external plexiform layer (EPL) and granule cell layer (GCL). Recent research has discovered that these inhibitory interneurons mediate progressive decorrelation in MTC odor representations during discrimination learning of similar odors (*19–21*).

We set out to ask how olfactory representations change with differences in stimuli factors ultimately influencing odor-driven behavior in mice. By using sensitive behavioral readouts, this study's first aim was to determine if odor similarity determines the speed with which animals discriminate between two odors. In the past, researchers have investigated how stimulus similarity influences odor reaction times in rodents. Since the early 2000s, a series of studies have debated this topic, with one school of thought claiming that animals improve their accuracy in discriminating complex odors when allowed to sample for longer durations (*22–28*). On the contrary, some believe that odor reaction times are invariant of task accuracies (*29–31*), challenging the theory of speed-accuracy trade-off in olfactory decision-making. Many of these studies concluded their findings using a restricted set of odors, making a generalized conclusion correlating speed-accuracy trade-off with stimulus complexity, a highly debated topic in the olfaction field. Using odors belonging to various chemical classes, we attempted to overcome this limitation. We trained animals to discriminate simple (monomolecular) and complex (binary mixture) odors and measured odor discrimination times across various stimuli pairs. We observed that odor discrimination times change with odor complexities, and binary mixture discriminations require more time than monomolecular odor discriminations while performing with high accuracy. We further recorded animal's sniffing behavior while they were performing odor discriminations and found that their sampling strategies did not change for different odors. However, animals learned to synchronize their breath initiations at a fixed latency from odor onset independent of the odor identity. The peak of breath initiation count coincided with the decision-making time window of simple odors. For complex discriminations, the breath initiation peak preceded the decision-making time window. The temporal difference between breath peak latency and the decision-making time window for complex discrimination reflected the additional time taken by OB neural circuits to process binary odor mixtures compared to monomolecular odor discriminations.

Training mice with different odors gave us odor discrimination times ranging from ~200 ms to ~350 ms. Our discrimination time measurements and other studies indicate that olfaction is a fast sense, with animals taking complex decisions within 350-400 ms (*17*, *22*, *25*, *32*). However, olfactory representations dynamically change during and after the decision-making period. These representations carry odor-specific information and persist even after odor cessation (*33*, *34*). Such post-stimulus activities are extensively studied in vision, observed in audition, touch, taste, and insect olfaction (*35–40*). Post-stimulus activities across different sensory systems indicate a functional relevance; however, in olfaction, the significance of post-stimulus representations in modulating olfactory functions remains unexplored. *In vivo* recordings from MTCs in awake, head-restrained mice show that post-odor representations are stimulus duration-dependent. It is more

robust and prolonged for longer stimulus durations (*33*). We investigated the influence of stimulus and post-stimulus representations on different facets of olfactory behavior by training mice to different odor stimuli durations. Reducing the stimulus duration from 2 s to 0.5 s for complex odor discriminations impacted animals' learning speed and long-term memory formation. Microendoscopic calcium (Ca^{2+}) imaging from GCL interneurons revealed that population activity in GCs was stimulus duration-dependent. With an increase in stimulus duration, Ca^{2+} transients were more robust and persisted even after cessation of the stimulus compared to shorter stimuli.

Previously, it has been shown that sustained activity of GCs brings about refinement in MTC ensemble activities (*41*). Additionally, stimulating or inhibiting local OB interneurons by optogenetic or chemogenetic approaches can alter pattern refinement in MTC ensembles, thereby influencing odor discrimination accuracies in a bidirectional way (*14*). As the interneurons are transiently active with shorter stimuli, it may lead to incomplete refinement in MTC ensembles, thereby impacting learning and long-term memory formation. To test this hypothesis, we aimed to modulate the inhibitory activity within OB during discrimination of olfactory stimuli with varying durations. To achieve this, we expressed light-activated excitatory cation channels (Channelrhodopsin) or inhibitory proton pumps (Archeorhodopsin) in glutamic acid decarboxylase (65-kDa isoform, GAD65) +ve interneurons, the major population of inhibitory interneurons in OB (*42*). By photostimulating GAD65 +ve interneurons during odor presentation, we observed an acceleration in the learning speed with short stimuli duration. Conversely, photoinhibition of GAD65 +ve interneurons during long odor presentation hindered learning efficacy. The bidirectional modification of OB interneurons during stimulus duration altered firing activities in MTC ensembles, thereby determining behavioral discrimination performance during the learning phase. Overall, pattern refinement in MTC ensembles appears to be an effective mechanism for disambiguating olfactory stimuli with overlapping representations, which aids in odor discrimination learning. We further investigated whether neural representations during the stimulus period influence long-term memory formation. We found that mice showed a long-term memory deficit when they were trained with short odor stimuli. Furthermore, even with optogenetic stimulations during the stimulus period, memory deficit persisted.

Despite rescuing learning deficits by modulating odor representations during stimulus delivery, we observed impairment in long-term memory formation. This suggests a differential circuitry mechanism regulating long-term memory formation in the olfactory system. The prolonged post-odor responses may provide a mechanism to stabilize odor representations as a function of time, thereby controlling memory formation. To check this possibility, we modulated post-odor MTC activities by optogenetically controlling GAD65 +ve interneuron responses. When

we inhibited post-stimulus firing of MTCs, we observed impairment in long-term memory. Further, disinhibiting post-stimulus firing activities in MTCs rescued the deficits in long-term memory formation. In summary, post-odor representations help to strengthen odor information, which aids in forming long-term memories. The study of odor representations during the stimulus and post-stimulus period improved our understanding of olfactory learning and long-term memory formation. Our results now pose a mechanistic question; how are post-odor activities maintained in OB? The potential sources contributing to post-odor activities may include lingering input from OSNs, recurrent activity within OB, or feedback from olfactory cortical areas. Recordings from OSNs have ruled out its involvement in maintaining these activities (*33, 34*). Our microendoscopic Ca^{2+} imaging data from anesthetized and awake animals show stimulus duration-dependent post-odor activities in GCL interneurons. Such activities may be due to recurrent OB activities and feedback from higher cortical areas. More studies targeting specific subpopulations of neurons in OB and cortical regions will be required to dissect the circuit regulating post-odor activities.

Finally, this study's broad aim was to extend the knowledge of odor representations to study human olfactory dysfunctions. Anosmia, the loss of sense of smell, is a common symptom in many neurodegenerative disorders and a few upper respiratory tract diseases (*43–48*). Amidst the coronavirus disease 2019 (COVID-19) outbreak triggered by severe acute respiratory syndrome coronavirus 2 (SARS-CoV-2) virus, researchers across the globe identified that patients manifest anosmia as a prevalent symptom (*49–54*). Subsequently, single-cell sequencing studies revealed supporting (sustentacular) cells residing in the human olfactory epithelium as an entry point for SARS-CoV-2 virus, but not OSNs (*55, 56*). It is unclear how virus-induced damage to supporting cells affects the functioning of OSNs. The damage may be induced by the possible ionic imbalances in supporting cells or increased levels of inflammatory cytokines in the epithelium (*57–59*). Moreover, as OSNs are continuously replaced in the epithelium, virus-induced damage on the functioning of OSNs may have a gradual onset depending on the severity of infection (*60*). Thus, the magnitude of olfactory dysfunctions may vary in COVID-19 patients, and assessing minor reduction in the sense of smell may not be possible with traditionally used methods (*53, 61, 62*). One of the crucial observations from my work over the last few years has been the importance of maintaining stimulus precision while addressing the neural basis of different olfactory behaviors. Therefore, establishing a strategy for precise stimulus delivery and sensitive behavioral measurements becomes critical to assess olfactory dysfunctions in humans. To quantitatively evaluate olfactory abilities in asymptomatic COVID-19 patients, we developed an innovative olfactory-action meter that accurately measures olfactory acumen in human subjects. To suit the requirements for usage in COVID-19 clinics, we fitted the instrument with multiple membrane

filters guarding it against any form of cross-contamination. After standardizing the test parameters with healthy subjects, we designed an olfactory function test, combining an odor detection test to measure the detectability towards different odors and an olfactory matching test that examines the patients' cognitive skills.

Measurement of detectability indices at threshold odor concentrations revealed a 38-55% deficit in asymptomatic COVID-19 patients compared to normal healthy subjects for different odors tested. On averaging responses for all odors, asymptomatic COVID-19 patients had a 50% reduction in their detectability index. The use of detectability index as a sensitive measure of olfactory loss in patients was ratified after conducting a series of sensitivity analyses that included receiver operating characteristic (ROC) analysis, detection of outliers, and estimating the effects of confounding variables. Recent reports have indicated mild to severe neurological complications in certain COVID-19 patients (*63–67*). While long-term neurological effects from SARS-CoV-2 infection are yet to be determined, temporary changes in the central nervous system (CNS) are extremely concerning. We devised an olfactory matching test that involves detection, discrimination, and memorizing the perceived odor information along with olfactory detection. The asymptomatic COVID-19 patients exhibited severe impairments in olfactory matching performance relative to normal healthy subjects. The quantification of matching accuracy in asymptomatic patients alludes to cognitive impairments caused by possible neurological changes in CNS followed by COVID-19 infection. By combining the readouts from odor detection abilities and matching skills, we observed olfactory deficits in 82% of asymptomatic COVID-19 patients (*68*). To summarize, quantitative estimation of olfactory function using our olfactory-action meter indicates severe olfactory dysfunctions among asymptomatic COVID-19 patients. As countries are slowly emerging from lockdown policies, our work lays the groundwork for developing a sensitive, quick, and cost-effective strategy for screening large populations to halt COVID-19's further spread.

CHAPTER 1

Introduction

Olfaction, the sense of smell, is one of the earliest senses to emerge during development (*69, 70*). Animals use their sense of smell to detect and distinguish between conspecifics and predators, as well as find prospective mates and food sources. As a result, olfaction is regarded as a crucial sense for survival and reproductive success. In mammals, the sense of smell starts as odor molecules are drawn inside the nasal cavity. Here, odorants traveling through nasal epithelium bind to ORs on OSNs, triggering a biochemical cascade to give a perception of a smell. Like other mammals, humans can distinguish amongst an incredible number of odors, and the sense of smell plays a vital role in attraction, mood, dietary preferences, and detection of danger. Intriguingly, a person's ability to smell declines with age, but it can be exacerbated at an early age via inadvertent exposure to viruses and xenobiotics (*4*), as well as due to various neurological conditions (*71–74*). It is estimated that 3-20% of the world population suffers from a diminished sense of smell (hyposmia) or a total loss of sense of smell (anosmia) (*75, 76*). More recently, during the COVID-19 pandemic, reports revealed that smell dysfunction is a major symptom and a significant predictor of COVID-19 infection worldwide (*53, 77–79*). These reports provide strong evidence that olfactory dysfunction is an early predictor of many disease conditions. Thus, a good understanding of circuitry mechanisms involved in forming odor representations will help develop olfactory tests for an early diagnosis of olfactory dysfunctions.

1.1 Olfactory circuit

Natural olfactory stimuli are almost always a mixture of diverse components varying in their physicochemical properties. How the brain perceives such complex multidimensional stimuli has been a topic of great interest. The odor processing circuit in mammals consists of nasal epithelium, OB, and olfactory cortical areas. Three types of cells line the nasal epithelium: OSNs, supporting cells, and basal cells (*80*). The ORs are expressed on the ciliary end of OSNs. The binding of odor molecules on ORs initiates a biochemical cascade, and electrical impulse is transmitted to OB. Within the OB, projection neurons receive the impulse and transmit odor information to upstream olfactory cortical areas of the brain. The activity of projection neurons is extensively modulated by diverse interneurons present within OB across different layers. The OB also receives inputs from the olfactory cortex (*81–83*) and neuro-modulatory inputs from different noradrenergic, cholinergic, and serotonergic systems of the brain (*84–88*). In the following sections, how odor stimulus is processed in each subsystem of the olfactory circuit is elaborated.

1.1.1 Odor processing in olfactory epithelium

1.1.1.1 Sensory neurons comprise of multiple receptor types

The Nobel laureates Linda Buck and Richard Axel, through their studies, provided a great impetus to the advancement in the field of olfaction research when they were successful in cloning ORs located on OSN's cilia (*89*). The ORs expressed on OSNs are part of a superfamily of G-protein coupled receptor (GPCR) proteins. The total number of receptor types deviates with species, ranging from ~50 in *Drosophila melanogaster* (*90*), ~140 in *Danio rerio* (*91*), ~400 in humans (*92*), and ~1000 in rodents (*92, 93*). The binding of ligands to OR evokes a series of biochemical reactions by activating specific G-proteins, which then activates adenylyl cyclase type III (*89, 94*) and facilitates the conversion of Adenosine triphosphate (ATP) to 3',5'-cyclic adenosine monophosphate (cAMP). An increase in the intracellular concentration of cAMP opens cyclic nucleotide-gated (CNG) channels, causing an influx of Na^+ and Ca^{2+} and activates a Cl^- channel (*95, 96*). The net influx of Na^+ as well as Ca^{2+} and efflux of Cl^- causes OSN depolarization. The depolarization propagates by passive electrotonic spread to the soma and axon hillock of OSN and triggers action potentials. A single OR can bind to a wide range of odorants that share a common epitope, while a single odorant that contains multiple epitopes can activate different ORs (*97, 98*). The simultaneous activation of different types of OSNs by odorants has been termed combinatorial coding, which broadens the molecular receptive range of animals with a restricted number of ORs.

In mammals, most OSNs follow a singular expression of ORs from a pool of different receptor types (*89*). The only exception is neurons expressing Membrane-spanning, four-pass A (MS4A) receptors. These four-pass transmembrane non-GPCRs are specifically expressed within necklace sensory neurons (*99*), and more than one receptor type can be expressed in a single sensory neuron (*100*). Although we lack a clear understanding of different molecular mechanisms controlling the singular expression of GPCRs in OSNs, some evidence points towards stringent expression profiling (*101*). The choice of OR to be expressed depends on the transcriptional availability of OR genes. The transcribed OR gene exhibits an H3K4me3 epigenetic mark, typical for transcriptionally active genes (*102*). Along with epigenetic marks, several cis-acting elements and OR-mediated feedback mechanisms prevent the co-transcription of other OR genes and help maintain monogenic expression (*103–105*). Although these models convincingly outline mechanisms that prevent co-expression of multiple ORs within a single chromosome, these models fail in explaining the suppression of ORs across different chromosomes. Apart from conventional GPCRs and MS4A type receptor, there are a few other broad classes of receptors expressed in the epithelium; trace amine-associated receptors (TAAR) (*106*) and Transient receptor potential

channel M5 (TRPM5) (*107*). Amines at low concentration selectively activate TAARs mapped to a discrete subset of glomeruli in OB's dorsal surface, while TRPM5, a member of the melastatin-related TRP channel family, is implicated in pheromone transduction.

1.1.1.2 Functional organization of OSNs in olfactory epithelium

OSNs expressing different ORs are not ambiguously scattered but are expressed in distinct zones across different areas of the epithelium (*108*, *109*), and even within a zone, there is a mosaic expression of different receptor types. The expression profiling of several molecular markers demarcates dorsal and ventral zones across the epithelium. A tight connection between OR identity and the zonal organization of OSNs prompted the hypothesis that ORs help in spatially segregating sensory neurons. The expression pattern of ORs along the epithelium classified them into two broad classes – Class I and Class II ORs (*110*). The class I ORs are specifically expressed on the dorsal surface of OE, while class II ORs are expressed throughout the surface of OE (*108*, *110*). Recently, transplantation studies have shown that progenitor neurons derived from the dorsal surface, when grafted onto a ventral surface, express ventral OR after progenitor cell engraftment (*111*). This study demonstrates that along with OR, exogenous spatial cues can direct the differentiation of OSNs. Furthermore, ORs belonging to a particular class also guides the projection of OSN axons to stereotypic positions in OB (*112*) (Figure 1-1). The OR genes regulate the expression of different axon guidance molecules, for e.g., Slit-1, Robo-2, Neuropilin-2, and Sema-3F (*113*, *114*), which influences OSN axon projection in the dorsal and ventral areas of OB (*104*, *115*, *116*).

1.1.2 Odor coding in olfactory bulb

1.1.2.1 Connectivity from olfactory epithelium to olfactory bulb

The axons of OSNs expressing the same OR pass through basal lamina and cribriform plate to accurately project to two glomeruli, one each on the lateral and medial surface of OB (*117*). The specificity of axonal guidance is essential during OSN development and critical in recovering OSNs after injury (*118*, *119*). The specific convergence of all OSNs expressing the same receptor is dependent on the spontaneous activity generated in OSNs. The temporal pattern of these activities controls the expression of certain axon-sorting molecules, which guide axons to specific glomeruli through their adhesive or repulsive interactions (*120–122*). Eliminating spontaneous activities by overexpressing the K^+ channel Kir2.1 in OSNs leads to unrefined glomerular maps (*123*, *124*). Further, optogenetically modulating spontaneous activity in OSNs can modulate levels of axon-guiding molecules, thereby modulating glomerular map formation (*121*). Along with ORs, olfactory marker protein (OMP) plays a role in OSN axonal convergence in OB. In OMP$^{-/-}$ null

mice, glomerular mistargeting occurs, leading to heterogenous glomeruli formation due to convergence of OSNs expressing different ORs (*125*).
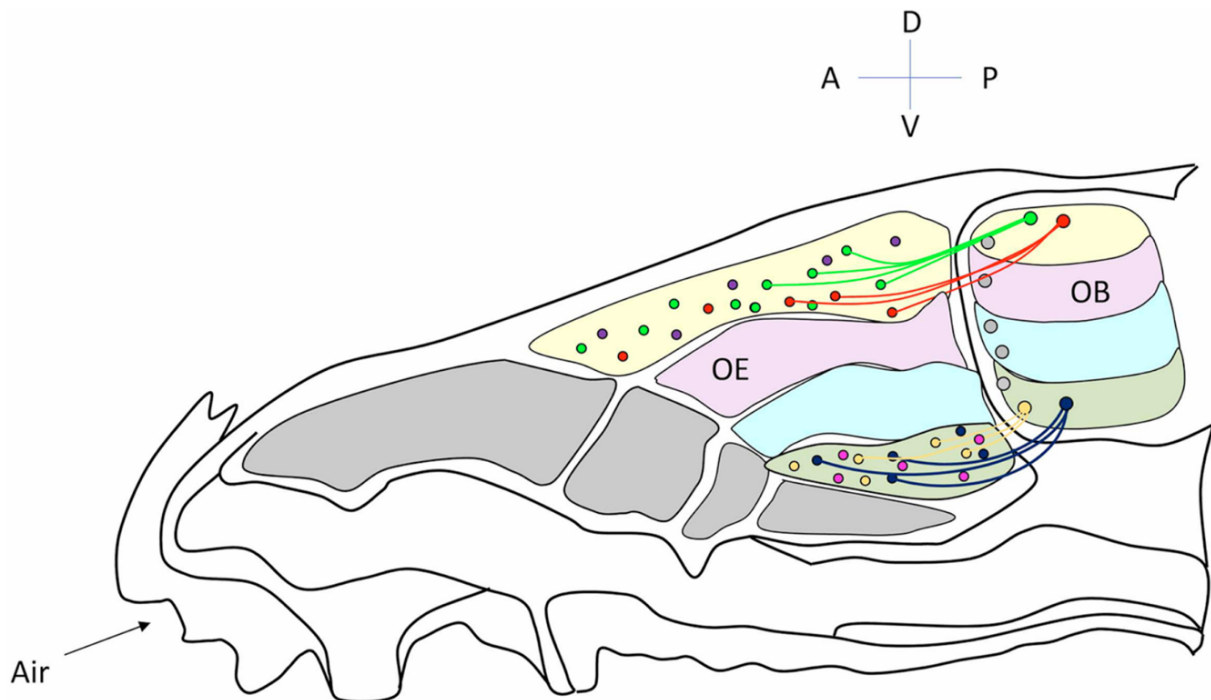
Figure 1-1: Axonal targeting of OSNs from OE to OB.

The schematic diagram illustrates the distribution of OSNs expressing different ORs along the dorsal and ventral zones of the epithelium. These OSNs expressing different ORs specifically converge to glomeruli on corresponding areas in OB. The different subdivisions are colored, and corresponding zones in OB are represented with the same color. Within a zone, OSNs expressing different ORs are represented as circles with different colors. The mosaic representation of ORs within a zone can be appreciated. *Adapted from Lodovichi C. 2021. Cell and Tissue Research* (*126*).

1.1.2.2 Activity-dependent glomerular map formation

Sensory experiences can modulate the connectivity between olfactory epithelium and OB. During early development, glomerular circuit refinement is highly sensitive to sensory experience (*127*). Accordingly, suppression of spontaneous neural activities in subsets of OSNs alters glomerular targeting and perturbs sensory map formation (*124*). In contrast, exposure to odors during the prenatal and early postnatal stages leads to enlarged glomerular size (*128*). In one study, mice expressing GFP-tagged ORs were exposed to odors cognate for the receptors during gestation and nursing. A significantly larger volume of tagged glomeruli was observed in these animals. In yet another study, postnatal chronic exposure to odors led to permanent supernumerary glomeruli formation in a time-dose-dependent manner. Compared to naive mice, in passively exposed animals, glomeruli were formed in the same region, but the number of glomeruli increased, which occupied small volumes (*129*).

1.1.2.3 Odor representation in OB

Each OB contains ~1,800 glomerular modules arranged in stereotypical positions (*130, 131*). The axonal convergence of OSNs into specific glomeruli generates a meaningful topographic organization in OB. It has been discovered that odorant representations are preserved among animals of the same species, have bilateral symmetry across the two lobes of OB, and rely on odor identity and concentration. These investigations also revealed evidences for chemotopic maps based on the chemical characteristics of odorants. For example, glomeruli activated by odor molecules with same functional group but different carbon chain length tend to cluster together (*15, 131–133*). However, higher-resolution imaging studies have revealed that odorants belonging to a particular chemical class activate only a subset of the glomeruli present within a domain (*134–136*). The other inactive glomeruli in such domains, however, readily respond to other odorant chemical classes (*134*). Such glomerular representations can be reflected by MTC activity within a local region showing diverse odor tuning properties (*137*). The following sections will go through various mechanisms by which odor activity patterns are transformed within the glomerulus and at the projection neuron level.

1.1.2.4 Transformation of odor information in OB

In OB, about 20-30 MTCs send their primary dendrites to a single glomerulus, where they receive odor information from ~5000 OSNs (*138, 139*). This creates a high convergence ratio, which could represent a powerful means of signal amplification. Different interneurons in GL and EPL form lateral interactions with MTCs to transform odor information. Periglomerular (PG) cells, short-axon (SA) cells, as well as External Tufted (ET) cells are interneurons found in GL and are collectively known as Juxtaglomerular cells. The granule cells (GC) located in GCL and parvalbumin (PV) expressing interneurons located in EPL form lateral synaptic connections with MTCs in the EPL (*140*) (Figure 1-2). The vast dendritic arborization within a single glomerulus by Juxtaglomerular cells provides compelling evidence that substantial odor information is transformed even within GL. Interactions within a glomerulus are inhibitory as well as excitatory. The PG cells are inhibitory interneurons that release gamma-aminobutyric acid (GABA), dopamine, or both within a single glomerulus (*139, 141*). Molecular identification has revealed two subclasses of PG cells: one expressing GAD65 isoform while the other subclass expresses GAD67 (*142*). PG cells expressing GAD67 are also Tyrosine hydroxylase positive and are thus dopaminergic-GABAergic neurons. GAD65 +ve PG cells are exclusively GABAergic in nature. OSNs and MTCs form a direct excitatory synapse with PG cells, and neurotransmitters released from PG cells mediate inhibition of MTCs, retrograde inhibition of OSNs, and lateral signaling

onto neighboring PG cells (*141, 143–145*). Along with the direct activation, OSNs can activate PG cells disynaptically via the OSN→ET→PG circuit. In fact, 67% of PG cells receive an excitatory drive from the OSN→ET→PG circuit, while the remaining 33% of cells receive direct excitation from OSNs (*146*). PG cells by presynaptically inhibiting OSNs or by postsynaptically inhibiting MTCs control odor-evoked sensory inputs to MTCs. Further, weak inputs to MTCs may be shunted by PG cells (*147*), sharpening its odor responses (*148*). Intraglomerular excitatory interneurons include ET cells. Within a glomerulus, ET cells receive glutamatergic inputs from OSNs, which can then provide monosynaptic glutamatergic inputs to SA and PG cells (*143, 149*). The glutamate spillover at ET synapses can evoke population bursts in MTCs (*150–152*). Moreover, the electrical coupling through gap junctions can also mediate ET→mitral cell signaling (*153*). Thus, ET cells can balance the excitation and inhibition of MTCs and allow a slow rhythmic activity to persist in the OB network. A subpopulation of ET cells is also responsible for forming an 'intrabulbar associational system' (IAS). The axonal projections of these ET cells are found in IPL on two sides of the same bulb, where they synapse with GC's dendrites (*154*). These ET cells involved in the formation of IAS use cholecystokinin (CCK) as a neurotransmitter. As CCK is an excitatory neurotransmitter, it is considered to excite a discrete population of GCs, thereby exerting inhibition on a discrete population of MTCs.

More global modulation of glomerular activity is accomplished through interglomerular interactions mediated by SA cells. These cells are inhibitory interneurons due to their GABAergic and dopaminergic identity (*142, 155*). SA cells' interesting feature is the long interglomerular axonal projections over long distances that form excitatory synapses with PG neurons as far as 20–30 glomeruli away (*156*). Like PG cells, approximately 33% of SA cells are activated mono-synaptically by OSNs, while the remaining 67% are activated di-synaptically by OSNs through the OSN→ET→SA circuit (*142, 146*). The interglomerular network mediated by SA cells allows an activated glomerulus to suppress activities of surrounding glomeruli through center-surround inhibition. This inhibition of surrounding glomerular units could be a key mechanism for increasing the spatial contrast between odor-evoked glomerular activity patterns.

EPL lies below the GL where MTCs extend several secondary lateral dendrites, which form dendrodendritic synapses with GC and PV cells (*139*). GABAergic GCs, which outnumber MTCs by a factor of 50 to 100, primarily contribute to the dendrodendritic inhibition in EPL (*139*). The inhibitory GCs have a small cell body (6-8 µm) (*157*), with their soma primarily located in GCL. Early morphological characterizations revealed three subpopulations of GCs depending on their dendritic arborization patterns in EPL (*138*). Type-I GC branch out its spiny dendrites across the EPL. The type-II GC extends its dendrites only in deep EPL, while type-III GC extends spiny

dendrites primarily in the superficial EPL. Later, the fourth type of GC, type-S cell, was discovered, which forms reciprocal synapses with the peri-somatic region of MTCs (*158*). Recently, Merkle et al., 2014 characterized two more GCs differing from the earlier types, termed type-IV GC and type-V GC (*159*). The type-IV GC shows frequent dendritic branching in GCL, rarely extending beyond the internal plexiform layer (IPL). Type-V has soma restricted to MCL and spread out its spiny shrub-like apical dendrites, specifically in the deep EPL. The GCs can also be classified as deep and superficial GCs depending on where the soma is localized in GCL (*138*, *160*).
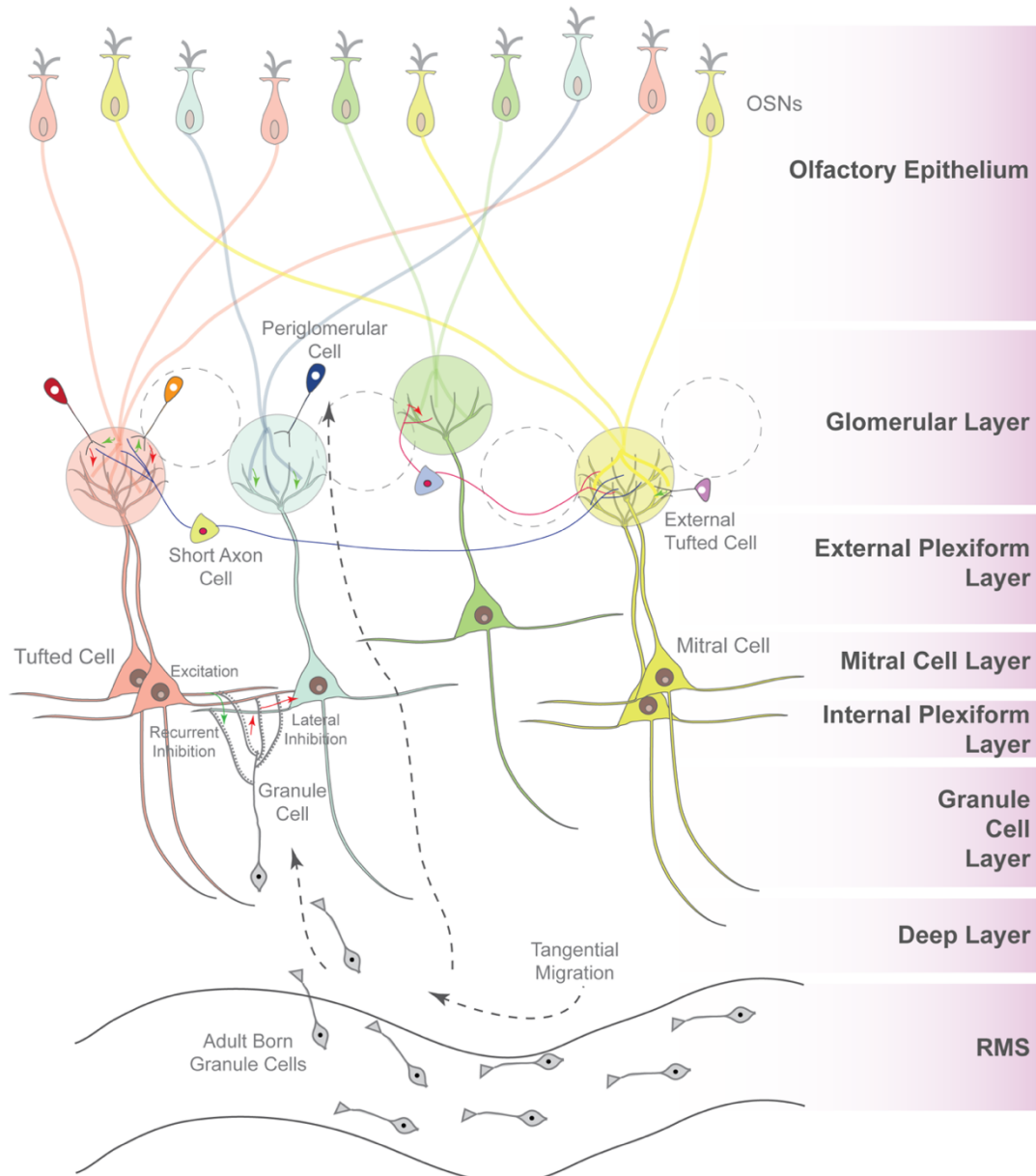
Figure 1-2: Schematic diagram illustrating OB circuitry.

Within a glomerulus, odor information is transmitted to MTCs. The activity of MTCs is heavily modulated by interneurons in GL, viz. periglomerular cells (PG), external tufted (ET) cells, and short-axon (SA) cells. The MTCs also receive inhibitory inputs from granule cells (GC) in the GCL. The excitatory and inhibitory contacts are represented as green and red arrows, respectively.

When MTCs receive excitatory input from OSNs, action potentials are generated, which travel to the lateral dendrites and open voltage-gated Ca^{2+} channels. The Ca^{2+} influx triggers the dendritic release of glutamate, which activates ionotropic glutamate receptors on GCs. This produces stochastic Ca^{2+} transients in GC spines that cause GABA release from GCs (*161–163*). If GABA released inhibits the same MTC, it is known as recurrent inhibition, while GABA inhibiting neighboring MTCs is known as lateral inhibition (*164, 165*). The reciprocal dendrodendritic interactions between MTCs and GCs function to control the gain-output of OB. The GCs form inhibitory connections with MTCs in a spatially limited area and are usually odor specific, so the gain-output is likely to be spatially heterogeneous (*166, 167*). The GCs can decorrelate firing activities of MTCs by different network mechanisms. Firstly, due to the lateral inhibition between mitral and granule cells, a strongly-activated mitral cell can selectively reduce nearby weak MTC responses to certain odors. The selective inhibition of surrounding mitral cells can enhance the subtle differences between firing patterns evoked by similar odors (*165, 168*). Secondly, on odor stimulation, GCs are activated with different latencies (*169*). The GCs' temporally distributed activity aids in increasing the temporal variability of MTC ensemble firing activities (*41*). Finally, by differentially acting on mitral and tufted cells, GC-mediated inhibition may orchestrate temporal synchrony amongst MTCs (*170, 171*).

In addition to dendrodendritic connections mediated by GCs, anatomical studies have indicated that EPL harbors another type of interneuron defined by the Ca^{2+} binding protein expression of parvalbumin (*140*). The cell bodies of PV cells lie in EPL and form inhibitory connections with MTCs over a large area and are broadly tuned to odors (*172, 173*). Thus, PV cells can bring about inhibition on a global scale. Further studies on understanding the role of PV cells in modulating MTC activity are warranted. These studies will also throw light on whether GCs and PVs work in a coordinated manner or are their roles mutually exclusive. Along with PV cells, there is another population of interneurons located in EPL, and these are axon-less cells that are immunoreactive to somatostatin (SST cells). These SST neurons are GABAergic in nature and extend their dendrites in deep EPL and connect specifically to MTC secondary dendrites (*174*).

For a long time, it was known that GCs receive GABAergic inputs; however, the intrabulbar source of such inhibition was unknown (*139, 162*). A study from the last decade demonstrated that GCs receive GABA$_A$ receptor-mediated inhibition from a sub-population of SA cells, known as Blanes cells (*175*). This opened up an avenue to find more such cell types that can contribute to GABAergic control of GCs. One subpopulation of SAs, called deep short-axon cells (dSA), has been found in inframitral layers, which are also GABAergic in nature. The dSA can be sub-classified depending on axonal projections across the different layers of OB. The axon terminals

of dSA selectively innervate GABAergic GCs and PGs and evoke GABA$_A$ receptor-mediated IPSCs (*176*). One subclass of GL projecting dSA has been demonstrated to receive feed-forward sensory input from ET and tufted cells to inhibit apical dendritic tufts of ET and tufted cells across widespread glomeruli (*177*).

1.1.2.5 The output neurons of OB

The mitral cell bodies (20-30 μm in diameter) lie in a thin mitral cell layer (MCL) 200-400 μm from the bulb's surface. Tufted cells are smaller (15-20 μm in diameter) and are classified depending on the soma localization (*139*). The middle-tufted cells lie in EPL, and internal tufted cells are located in MCL. The lateral dendrites of tufted cells extend mainly to the middle and superficial layers in EPL. The lateral dendrites of mitral cell (type-I) project tangentially in EPL's deeper regions and spread in a radius of about 850 μm (*138*). There is a subpopulation of mitral cells, type-II mitral cells, which send their lateral dendrites to the middle layer of EPL. MTC responses are characterized by prolonged bursts of action potentials lasting >100 ms separated by equally long intervals in response to odor stimulation (*178*). On cessation of odor stimulus, these activities persist in the post-stimulus period and are shown to carry odor-specific information (*33, 34*). The firing activities of MTCs can be heterogenous in several ways. On odor presentation, tufted cells exhibit high firing rates (>100 Hz), while mitral cells respond with relatively low firing rates (<100 Hz) (*179*). *In vitro* studies have shown that tufted cells exhibit short-latency responses that are maintained across a concentration gradient, whereas mitral cells respond only to stronger stimuli (*180*). Tufted cells increase their firing response amplitude as odor concentration rises, while mitral cells display phase progression with increasing concentration (*171*) (Figure 1-3 C). MTCs also exhibit respiration-phase-locked spontaneous spiking behavior. During exhalation, mitral cells are activated, while tufted cells become active during inhalation (*171*) (Figure 1-3 A and B). The MTCs also differ in the nature of lateral inhibition they receive in response to glomerular activation *in vitro*. On separating the early (<250 ms after glomerular stimulation) and late (>250 ms after glomerular stimulation) components of inhibitory currents, it is observed that the amplitude of these inhibitory currents is larger in mitral cells than in tufted cells (*170*).

The morphological and functional variations indicate that MTCs differ substantially in their ability to decode odor information. When a specific odor is mixed with a structurally identical odor that activates neighboring glomeruli, mitral cell units are normally inhibited. On the other hand, the tufted cell units show a relatively weak inhibitory response to such odor mixtures activating similar sets of glomeruli (*179*). The differential inhibition can be explained by mitral cell's extensive dendrodendritic synaptic contacts with neighboring glomerular columns, while tufted

cells have limited lateral inhibition. These observations suggest that the output of mitral cells is determined by the combined excitatory input from its glomerulus and the surrounding glomeruli's activity. The differential processing of odor information via these two cells may explain the fast but stimulus-dependent odor discrimination times observed in rodents. For dissimilar odors that evoke glomerular activity with little overlap, short-latency responses in tufted cell units may provide reliable information to make an accurate decision. In contrast, when odors evoke similar glomerular activities, accurate decisions would depend on the contrast in the activity of mitral cell units in neighboring glomeruli.

The MTCs also have distinct axonal projections in different cortical regions along with the functional differences in firing activities between mitral and tufted cells (Figure 1-3 D). The axons of these cells travel via the lateral olfactory tract (LOT) and primarily terminate on several olfactory cortical areas, including anterior olfactory nucleus (AON), olfactory tubercle (OT), piriform cortex (PCx), orbitofrontal cortex (OFC), amygdala and rostral entorhinal cortex (*181*). The tufted cells project densely to specific regions in anterior areas of olfactory cortex, while mitral cells project to all olfactory cortical areas (*180*, *181*). In each of the anterior areas that receive both mitral and tufted cell inputs, axons of these cells project to distinct, non-overlapping areas.
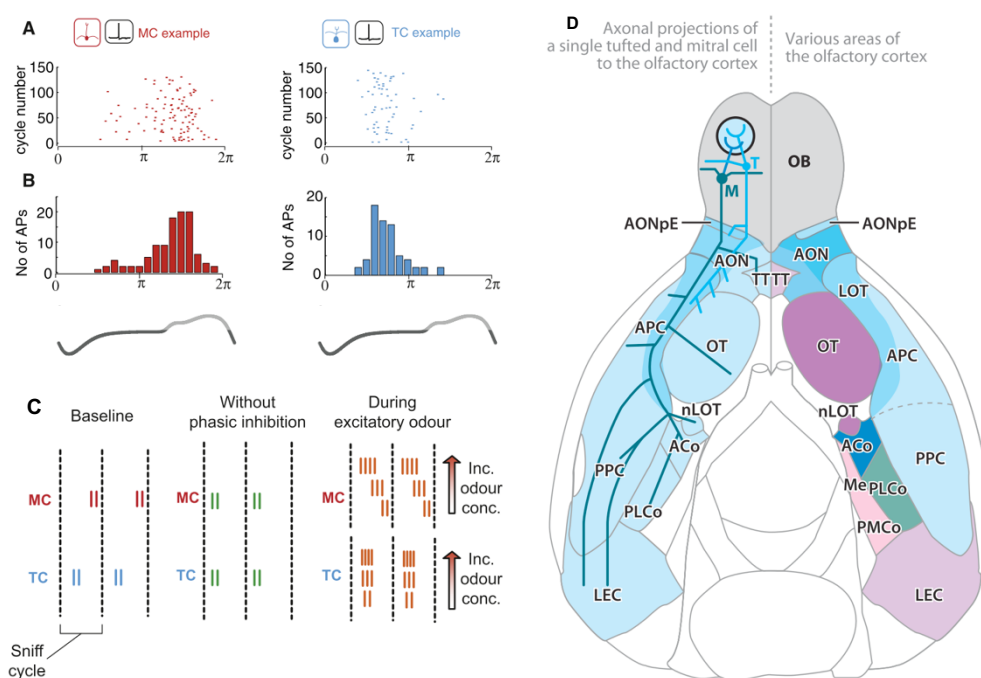
Figure 1-3: Schematic illustration of distinct functional properties and axonal projection of mitral and tufted cells.

A and B. Example of mitral and tufted cells show that firing activities are coupled to sniff phases. While tufted cells preferentially fire during inhalation, mitral cells fire during the exhalation of a breathing cycle.

C. The phase-locked activities of MTCs are abolished when the inhibition on MTCs is blocked. In such a scenario, mitral cells start to fire during the inhalation phase while there is no change observed in the phasic properties of tufted

cells. The phase advancement in the firing of mitral cells is also observed when odor concentration is increased. On the other hand, increasing the odor concentration increases the firing rate of tufted cells.

D. The mitral and tufted cells also differ in its axonal projections to different olfactory cortical areas. While mitral cells broadly project to all olfactory cortical areas, tufted cell projection is restricted to anterior areas of the cortex, specifically to anterior areas of AON, anterior PCx, and the cap region of OT. *Adapted from Mori and Sakano 2011, Annual review of Neuroscience and Fukunaga I., 2012, Neuron (104, 171).*

1.1.3 Odor processing in olfactory cortex

1.1.3.1 Structural organization of olfactory cortex

Out of the different cortical areas receiving axonal projections from MTCs, PCx forms the most extensive area (*182, 183*). The PCx is a laminar structure with three distinct layers. Layer I receives afferent fibers from OB, which spread across the surface (Layer Ia). Here they form synapses with dendrites extending from cells in the deeper layers. Layer II is a dense layer of pyramidal cells and neurons lacking basal dendrites known as semilunar cells. Layer III is the innermost moderately dense layer, with pyramidal cells situated in superficial areas. The association fiber system emerges within PCx and terminates primarily in deeper parts of layer I (layer Ib), and in layer III (*182, 184*). The pyramidal cells' axons form synaptic contacts with < 1% of other pyramidal cells. Nonetheless, many pyramidal cells in PCx ensure that each cell receives excitatory inputs from thousands of other pyramidal cells (*185*). In fact, MTC input accounts for a small fraction of input to pyramidal cells, and the majority of odor-evoked responses are brought about by excitatory dendrodendritic contacts amongst pyramidal cells (*186*). In contrast, semilunar cells receive more robust afferent excitatory inputs from OB (*187*). The PCx also receives associational fibers from AON, OT, entorhinal cortex, and certain areas within the amygdala (*188, 189*). In addition to afferent fibers and associational fibers, the brainstem, thalamus, hypothalamus, and basal forebrain are other regions that send inputs to PCx.

AON is one region of the olfactory cortex that mediates interbulbar connections. It receives inputs from MTCs in the ipsilateral OB and sends feedback to GCL in the contralateral OB (*190, 191*). AON is one of the initial recipients of odor information and stores odor engrams needed for behavioral expression of odor memories (*192*). Another cortical structure having direct connectivity with OB is OT. The OT is a cortical structure in the ventral striatum with extensive anatomical connections with brain reward areas (*193, 194*). Owing to this feature of OT, one can hypothesize its role in odor reward categorization. Indeed, it has been found that micro-stimulation of OT can regulate odor hedonics without modulating odor perception (*195*). It has been observed recently that neurons in OT are activated within 50-100 ms of inhalation and carry explicit representation of the reward category, independent of odor identity (*196*). The OFC, another

cortical region essential in odor characterization that receives direct olfactory information from PCx. OFC neurons show activity during trial initiation, odor sampling, and consumption of rewards (*197*).

The AON and PCx, along with sending projections to other cortical areas, also send dense projections in the GC layer and periglomerular layer in OB (*188, 198–200*). The cortical feedback is dominated by inhibitory responses, which suppresses the firing rates of MTCs both *in vitro* and during *in vivo* odor stimulation. The inhibition is mediated by a disynaptic pathway wherein cortical projections excite inhibitory interneurons, thereby inhibiting MTC responses (*199, 200*). Along with GC and PG cells, SA cells in GL and GCL receive excitatory input from pyramidal cells in PCx. Since SA cells primarily inhibit GC and PG cells, cortical feedback projections can also disinhibit MTC responses. Further, Ca^{2+} imaging has revealed that wakefulness enhances both the magnitude and duration of cortical feedback projections compared to anesthetized conditions (*201*). Also, the feedback activity is odor-specific and can vary in the latency with respect to odor onset, and can persist long after the withdrawal of odor onset (*202*).

Along with cortical feedback projections, OB also receives significant noradrenergic input from locus coeruleus (LC) (*86, 87*), cholinergic projection from the horizontal limb of the diagonal band of Broca (HDB) (*139*), and serotonergic input from the dorsal and medial raphe nuclei (*88*). Noradrenergic fibers terminate densely in IPL and GCL and moderately in EPL and MCL (*203*). Both GCs and MTCs express α1 and α2 receptors, and the direct application of norepinephrine (NE) in OB can hyperpolarize GABAergic GCs and thus inhibit mitral cell responses to weak OSN inputs (*86, 204–206*). Further, blocking noradrenergic receptors in OB reduces odor discrimination accuracies between similar odorant mixtures (*87*). Similarly, cholinergic inputs to OB have been demonstrated to potentiate olfactory habituation, improve short-term olfactory memory and increase the discriminability of bulbar responses generated by very similar odorants (*85, 207*). The third neuromodulatory input to OB is from the serotonergic system. Although OB receives dense serotonergic inputs, very little is understood about the serotonergic system's specific role in olfactory information processing.

1.1.3.2 Odor representation in olfactory cortex

The odor information on reaching PCx loses the spatially segregated chemotopic map observed in GL. A single pyramidal neuron receives overlapping inputs from axonal terminals of MTCs receiving sensory information from different glomeruli (*208, 209*). Also, MTCs from a single glomerulus sends their projection across the PCx without apparent spatial preference (*210, 211*). Typically, an individual odorant activates only 3-15% of cells in PCx. Moreover, neurons

that respond to dissimilar odors often fail to respond to similar odors. Thus, the odor representation in PCx exhibit discontinuous receptive fields (*210*). Evidence for these overlapping clusters (individual neurons responding to structurally dissimilar odorants) is primarily observed in the posterior PCx and entorhinal cortex but not in OT and anterior PCx (*212*). As the neural activity in PCx is sparse in response to odor stimuli, it becomes interesting to determine how a limited set of neurons decodes odor information. One hypothesis relies on the Hopfield model, explaining the mechanism of encoding and decoding of odorant information in different olfactory cortical areas (*213*). This model predicts that the earliest activated MTCs and the ensemble of cells in PCx broadly define odor identity, while MTCs activated later are required for fine discriminations. Consistent with this prediction, it was observed that neurons in layer II/III of PCx respond reliably to early MTC activity. The late MTC activity is reduced due to the global inhibition brought about in PCx (*211*, *214*, *215*). Further, odor intensity is encoded within firing latencies in these early responsive MTCs.

To understand how olfactory cortical areas conduct the balancing act of odor generalization and odor discriminations, in two separate studies, rats were trained to complex odor mixtures under different contexts (*216*, *217*). In the first study, rats learned to discriminate between two odor mixtures containing ten odorants. It was observed that rats could discriminate between a target mixture of ten odorants (10C) with the other mixture in which one odorant was replaced with a novel odorant (10CR1). On the contrary, rats faced difficulties in discriminating the same target mixture (10C) from the other mixture in which one of the odorants was deleted (10C-1) (*217*). Single-unit recordings from the anterior piriform cortex (APC) showed that the extent of decorrelation was the governing factor in the discriminability of odors. When one of the components was replaced (10C vs. 10CR1), two mixtures formed decorrelated patterns in APC ensembles. On the other hand, 10C and 10C-1 formed very similar activity ensembles in APC, which was the cause of poor discrimination displayed by rats. In the second study (*216*), the authors trained rats to a difficult discrimination of 10C vs. 10C-1. Although animals had poor performance early on, accuracies increased significantly with time. APC recordings revealed that the activities were highly correlated initially; however, after the animals learned the task, activities for the two odors showed significant decorrelation. Following it up, they designed another task wherein rats had to discriminate 10C or 10CR1 from a third odor, vanillin. Like previously, 10C and 10CR1 formed dissimilar ensemble activities in APC. However, on training rats on this task, a high correlation in the activities of 10C and 10CR1 was observed. These studies elegantly demonstrated that cortical systems could efficiently carry out odor generalization and discriminations in a context-dependent manner, with cortical network plasticity playing a pivotal role.

1.2 Approaches to assess functional relevance of odor representations: from molecules to behavior

In recent years, interest has grown in determining how olfactory representations change under different contexts. Technologies have helped open new horizons to study these representations from molecular to behavioral levels. At a molecular level, using Cre-lox and Clustered regularly interspaced short palindromic repeats (CRISPR)-Cas9 systems to achieve gene manipulations in a spatially and temporally regulated manner has been crucial in studying single gene function in circuit activity and behavior (*218*, *219*). Recombinant viral vectors such as adeno-associated virus (AAV), and rabies virus (RV) have made efficient exogenous gene transfer possible. When these techniques are combined, a powerful tool for labeling, imaging, and genetically modifying cells can be developed. For example, by injecting AAV carrying a floxed gene into a specific brain area, it is possible to express gene-of-interest in a Cre-dependent manner (*220–222*). Prevalence of several OB-specific Cre-driver lines like GAD65-Cre (*221*), PV-Cre (*223*), Sst-Cre (*221*), CCK-Cre (*221*), Pcdh21-Cre (*224*), Tbx21-Cre (*225*), *et cetra* offer a robust approach to study odor-evoked activities in different cell types. Next-generation transcriptomic studies, in addition to molecular methods, have aided the identification of cell-type-specific markers in OB (*226–228*). Such studies have revealed transcriptionally diverse neuronal cell types and allowed us to track molecular changes during development and maturation. *In vivo* electrophysiological experiments have facilitated recording of odor-evoked activities across different olfactory areas with high temporal resolution (*20*, *215*, *229*, *230*). Computational models have been developed on published human psychophysical data to predict how novel odor molecules would smell (*231*). All these approaches have contributed to a better understanding of circuit mechanisms of odor representations and its relevance in health and disease. However, covering all these methodologies is beyond the scope of this thesis. Thus, approaches to assess olfactory function that is relevant to this thesis's goals are elaborated.

1.2.1 Visualizing odor representations

In vivo neural imaging has been instrumental in understanding the neural basis of olfactory functions due to its capability to record neuronal dynamics distributed in space and time. It provides an opportunity to study:

1. Different stages of OB circuit development (*125*, *232–234*).
2. Changes in real-time activity in response to odor stimulations (*13–17*, *22*).
3. Plasticity changes in response to odor learning (*19*, *20*, *32*, *235*, *236*).
4. Changes due to infections or disease-associated degeneration (*237–239*).

Analyzing neural basis of olfactory function using imaging methods widely include:

1. Measuring glucose uptake with radiolabeled 2-deoxyglucose (2DG) to examine neuronal activity.

2. Measuring intracellular Ca^{2+} dynamics using chelators like 1,2-bis(o-aminophenoxy)ethane-N,N,N',N'-tetraacetic acid (BAPTA), fluorescent Ca^{2+} indicators such as fura-2, fluo-2, and indo-1, or protein-based genetically encoded Ca^{2+} indicators like GCaMP6f.

3. Measuring transmembrane voltage using fluorescent voltage-sensitive dyes.

4. Measuring intrinsic optical properties of the tissue.

2-DG uptake patterns from glomerular units across hundreds of odors have revealed that odors with similar molecular characteristics activate glomeruli in specific zones of OB (*15*, *16*). However, 2-DG imaging requires prolonged odor stimulation and is not suitable for measuring real-time odor-evoked activities. Intrinsic Optical Signal (IOS) imaging has been extensively used in several brain regions, including OB (*13*, *22*, *32*, *240*, *241*). In OB, following action potential propagation in OSNs, hemodynamic changes cause light scattering that is sensed by IOS imaging. Although IOSs can accurately map neuronal activity, this technique is limited to imaging superficial layers of the brain. Two-photon (2-P) Ca^{2+} imaging mitigates this problem as it allows super-resolution *in vivo* fluorescence microscopy in highly scattering brain tissues (*242*). 2-P microscopy is characterized by the incidence of two low-energy, short, near Infrared (IR) pulses on the biological sample. As excitation wavelength is within the IR spectrum, tissue penetration is better, and the stray fluorescence signal is very low. For these reasons, 2-P Ca^{2+} imaging is a favored technique for visualizing neuronal activities in deeper brain areas (*243*). Another promising way of capturing Ca^{2+} dynamics from deep brain regions involves inserting optical fibers and gradient refractive index (GRIN) lenses (*244*, *245*). Custom designed microendoscope GRIN lens system enables chronic population recording from hundreds of neurons. By increasing effort to miniaturize the head-mounted imaging device, neural activity can be recorded from freely behaving mice (*245*, *246*). Finally, the technological evolution of imaging techniques like magnetic resonance imaging (MRI), positron emission tomography (PET), computed tomography (CT), *et cetra* has been advantageous to track abnormalities in OB and cortex during the progression of different neurodegenerative diseases (*247–249*).

1.2.2 Optogenetics: A powerful tool to establish a causal relationship between neuronal activity with odor perception.

In 1979, Nobel laureate Francis Crick suggested a need to selectively target one neuronal type to better understand how the brain works. He noted that electric stimuli using electrodes might

not be suitable as they non-selectively stimulate cells in its vicinity, and drugs are slow to act. Subsequently, he speculated that light could be used to precisely control the activity of selected neurons. Years later, this idea became a reality when scientists succeeded in exciting *Drosophila melanogaster* neurons with light flashes (*250*). Since then, this technique of photostimulating neurons, namely optogenetics, has been widely used in the neuroscience field. Optogenetics involves the exogenous expression of light-sensitive ion channels in neuronal membranes. When the light of a specific wavelength is flashed on such channels, there is a change in the membrane potential of the targeted neuronal population. Over the years, various photosensitive channels have been developed with distinct response kinetics or excitation wavelengths. The most commonly used excitatory channel, namely, Channelrhodopsin-2 (ChR2) was isolated from a marine organism, *Chlamydomonas reinhardtii,* in 2002 (*251*). ChR2 was the first ionotrophic transmembrane microbial opsin used to excite neurons by Deisseroth's lab at Stanford University (*252*). ChR2 can rapidly open in response to optical stimulation, with its spectral response peaking at 480 nm, corresponding to blue light. It is a non-specific cation channel, permeable to Na^+, K^+, and Ca^{2+}, resulting in a reversal potential near to 0 mV in neurons. Similarly, other opsins like chloride transporter halorhodopsin isolated from *Natronomonas pharaonis* and proton pump archeorhodopsin (Arch) isolated from *Halobacterium salinarum* have been used to silence neuronal activities.

The main advantage of optogenetics has been the possibility of precise control over the stimulation. Since the discovery in 2002, advancements have been directed towards improving the photocurrent properties, reducing deactivation and desensitization time (*253*). All of these features together have allowed exceptional spatiotemporal control over neural circuit stimulations. In recent years, studies have employed optogenetic tools to study the link between olfactory circuits and behavior. This is primarily due to the ease of access to the olfactory circuit and laminar organization of OB. Owing to this property, researchers are using optogenetics to imitate neuronal excitation or inhibition that is likely generated by odor stimuli. Optogenetic stimulation of a single glomerulus has shown that each glomerulus can transmit odor-related information that can be processed during odor discrimination tasks (*254*). In a recent study, patterned optogenetic stimulation has allowed researchers to create 'synthetic' odors. Such stimulations helped identify different spatiotemporal features of glomerular response contributing to odor perception (*255*).

However, while utilizing optogenetics as an investigative tool, researchers must also keep in mind a few drawbacks of the technique. First of all, the efficiency in controlling neural activity is dependent on light penetration across the brain. Thus, depending on the area which needs to be stimulated, one needs to wisely choose between dorsal surface illumination or deep tissue

stimulations using optical fibers. Secondly, odor representations formed in OB are pretty complex, and they change depending on factors such as the sniffing phase, odor concentration, and time. As a result, mimicking natural odor representations with light stimulation has limitations. Lastly, it is possible to get asymmetric effects of activation versus inhibition of the same subsets of neurons (*256*). However, this limitation can be overcome by being aware of their existence while interpreting results and having appropriate controls while designing experiments.

1.2.3 Psychophysical measurement of odor perception

Psychophysics quantitatively measures the relationship between sensory stimulus and perception. In olfaction, psychophysical measurements can reveal (a) the relationship between odorant chemical structure and its perceived smell; (b) how olfactory stimuli of varying complexities can be discriminated against, and how this is accomplished in nose and brain; (c) what effect does odor have on our perception? The answer to these questions is uncomplicated in humans as we have acquired language. Human subjects can verbally express if they can detect a smell, characterize the smell, or decide if two odors are discriminable. There are certain constraints on experimentation performed on humans, such as genetic manipulation, invasive imaging, and electrophysiology, which raises the need for utilizing animal models. To study psychophysics of odor discrimination in mice, different conditioning paradigms are designed. In one such paradigm, namely, Go/No-go olfactory operant conditioning tasks, rodents discriminate between two odorants with different reward associations (e.g., one is rewarded and the other is not) (*257*). By measuring odor discrimination times, discrimination accuracies, and memory performance, the effect of task difficulty on neural processing can be studied in detail. A constant effort is directed towards developing automated behavioral paradigms based on temporally precise stimulus delivery (*17, 25, 258, 259*). The technological advancement has permitted coupling high-throughput behavioral paradigms with fast imaging techniques and optogenetics. These methodologies have been instrumental in establishing how neural representations are formed in rodent OB and lay down the causal relationship of such representations with different behavioral outputs.

Human olfactory psychophysics has traditionally relied on odor detection thresholds, odor identification, and discrimination using minimalistic instrumentation, for instance, semi-static olfactometry developed by Zwaardemaker in 1888 or blast olfactometry developed in 1935 (*260*). The modern-day olfactometry tests that are widely used are the University of Pennsylvania Smell Identification Test (UPSIT), Connecticut Chemosensory Clinical Research Center (CCCRC) Test, Sniffin' Sticks (SS) test *et cetra*. The UPSIT is a multiple-choice odor identification test consisting of a booklet with forty suprathreshold concentration odorants embedded in

microencapsulated crystals. On each page, an odorant is accompanied by four alternative options naming the odor, and each subject chooses from one of these responses even if the smell is not detected (*61*). On similar lines, CCCRC evaluates odor identification skills and odor detection threshold. The SS test utilizes felt-tip pens (sticks) dipped in odorants to investigate olfactory detection and discrimination performance (*62*). First, the threshold is assessed, then odors are presented in triplets to test odor discrimination. The total score from these tests classifies participants as normosmic, hyposmic or anosmic, and has proved to be useful as screening measures to identify many neurodegenerative disorders. However, these tests have shortcomings; (a) most odor identification and discrimination tests deliver odor at suprathreshold concentrations. However, odor perception changes with odor concentration (*261*); (b) due to lack of instrumentation, there is no control on stimulus delivery. Moreover, if these tests are self-administered by subjects in the absence of a physician, it creates variability in the way the result is interpreted; (c) these tests have limitations in probing the cognitive skills of subjects. This is very critical as most of these tests are used to determine the olfactory loss in patients with neurodegenerative disorders who face challenges with cognitive abilities. Thus, there is a dire need to engineer olfactory tests that overcome existent olfactory tests' limitations.

1.3 Goals and achievements

To summarize the previous sections, many questions are still open concerning functional relevance of odor representations in health and disease:

1. How do overlapping odor representations elicited by complex odors influence discrimination times?
2. Do animals modulate their sampling behavior for different odorants during a decision-making task?
3. What is the functional relevance of post-odor representations? How does it compare with the information coded during odor representations?
4. Developing a method to precisely control stimulus delivery to quantitate human olfactory dysfunctions.

The main achievement of this thesis is to unravel the role of olfactory stimulus and post-stimulus representations in health and disease, which are:

1. By using odors of different chemical classes, our study revealed that the similarity and strength of glomerular activity patterns define the degree of olfactory processing required for odor discrimination. Apart from glomerular patterns, we observed a temporal relationship between breathing behavior and decision-making independent of odor identity.

2. By varying stimuli durations for different odor complexities, we studied the influence of neural representations in odor discrimination learning and long-term memory formation. Optogenetically modulating the inhibitory strength of OB circuitry unveiled differential mechanisms modulating odor discrimination learning and long-term memory formation. Precisely, decorrelation in MTC activities during stimulus duration controls odor discrimination learning, while post-odor MTC firing activities assist in the formation of long-term odor memories.

3. We developed a tool by which we can precisely control odor delivery pulses. Using such sophisticated instrumentation helped us understand how odor representations are formed under different stimuli conditions and their relevance at a behavioral level. Expanding that knowledge to human olfaction, we developed a quantitative way to probe human olfactory dysfunctions. Using our custom-built olfactory-action meter, we identified olfactory loss in 82% of the total asymptomatic COVID-19 patients assessed.

CHAPTER 2
Materials and methods

All experimental procedures common to multiple chapters are outlined in this chapter. The section-wise material and methods explains experimental procedures specifically performed for those studies.

The experimental protocols used in this thesis have been approved by the Institutional Animal Ethics Committee (IAEC) at IISER Pune, and the Committee for the Purpose of Control and Supervision of Experiments on Animals (CPCSEA), Government of India (animal facility CPCSEA registration number 1496/GO/ReBi/S/11/CPCSEA). The usage of mice in the study described in chapter 3 was licensed under (IISER/IAEC/2017-02/003), and study described in chapter 4 was licensed under (IISER/IAEC/2017-02/007).

2.1 Maintenance of mice used in the study

Adult male mice (4-6 weeks old) were used for all experiments. Mice were maintained on a 12 hrs day-light cycle (light phase: 9 A.M. till 9 P.M.; dark phase: 9 P.M. till 9 A.M.) and housed in individually ventilated cages (IVC). Each cage had a floor area of 800 cm^2 and housed 3-5 mice. Mice were provided with standard rodent bedding and nesting material. The mouse holding room temperature was maintained at 22-25°C, and relative humidity was maintained at 45-55%. All behavioral experiments were performed during the light cycle. On behavioral training days, mice had *ad libitum* access to food but were on a water deprivation schedule designed to keep them at $\geq$ 80% of their body weight. The water restriction schedule never extended beyond 12 hrs.

2.2 Odors used in the study

Odors used were Methyl benzoate (MB), Amyl acetate (AA), Ethyl butyrate (EB), 1,4-Cineole (CI), Eugenol (EU), (+)-Carvone (C+), (-)-Carvone (C-), (+)-Octanol (O+), (-)-Octanol (O-), Hexanal (HX), 2-Pentanone (PN) and binary mixtures of these odorants (containing different relative fractions of two odors, e.g., 40% AA and 60% EB). MB was used in the task habituation phase for both the freely-moving and head-restrained behavioral paradigm. The odors were procured from Sigma-Aldrich and had high purity (>99%). For behavioral training, liquid dilution of odors was done in mineral oil (Paras Pharmaceuticals) and was further diluted by airflow.

2.3 Olfactory behavior

2.3.1 Olfactory behavioral training using Go/No-Go (GNG) operant conditioning paradigm

For studying olfactory behavior, mice were trained on the GNG paradigm as described previously (*22*, *257*). In brief, mice were trained to discriminate between two different odorants. One of the odorants was associated with a water reward (S+ odor), while the other was without a water reward (S- odor). The water reward of 3-4 µl was given if mice continuously licked at the lick port for S+ odor presentation. Mice weren't supposed to lick for S- odor presentation. However, even if they licked during S- odor presentation, neither a reward nor any form of punishment was given. In our paradigm, the response time window coincided with the onset of odor presentation. The response time window was virtually segregated into four equal time bins. The criterion for a correct S+ trial was set as follows; mice had to lick at least once in 3 out of 4 time bins. For S- odor, if mice registered a lick in less than or equal to two-time bins, the trial was recorded as a correct trial. In all experiments, mice were either trained under freely-moving or hear-restrained conditions. The training rules were identical in both conditions, but mice were restrained on a platform when conducting the task under head-restricted conditions, as the name implies. The instrumental and experimentation details are described in the following sections.

2.3.2 Behavioral training under Freely-Moving (FM) conditions

2.3.2.1 Apparatus

All the FM olfactory behavioral training was performed using four 8-channel olfactometers (Knosys, Washington, USA) (*257*) controlled by a custom-written program in IgorPro (Wavemetrics, OR). The olfactometer comprises of the following components: 1. An operant chamber, 2. Flowmeters, 3. Solenoid valves, 4. Combined odor sampling/reward port, 5. Final Valve/Diversion Valve (DV), 6. Water valve, 7. Manual control box, and 8. Digital I/O board (Figure 2-1 A and B). The operant chamber was constructed from plexiglass and had a metallic platform. On one side of the chamber, a circular cutout opened into a sampling port, and on the opposite side, a fan was placed, which blew air inside the chamber. This inward flow of air prevented odorized air from entering the operant chamber. An IR beam and a photodiode guarded the sampling port entrance that helped us monitor head insertion by mice. Two flowmeters independently controlled the flow of clean and odorized air which was distributed to eight solenoid pinch valves. The S+ and S- odors were randomly connected to different valves. In a trial, odor from one of the channels was presented to mice in a combined odor sampling and reward port. Combining the odor and lick port ensured a tight association between water reward and presented odors. On trial initiation by mice, one of the odor valves opened along with a DV that diverted

odorized air away from the mouse to an exhaust chimney for an initial 500 ms. After 500 ms, DV closed, and the odor was presented to the mouse. Thus, DV minimized odor traveling time between odor onset and the first contact with the mouse's nose. The lick responses were measured using a lick circuit connected to the lick port. When the mouse licked on the lick port, its body acted as a conductor, completing the circuit between the metallic platform and lick port. The licking and sampling behavior were recorded in microsecond resolution. However, data was stored as Igor waves in 125 time-bins (was set prior to the start of an experiment) with 20 ms resolution. The program written in IgorPro controlled all parameters and received all state changes in the circuit using a digital I/O peripheral board.
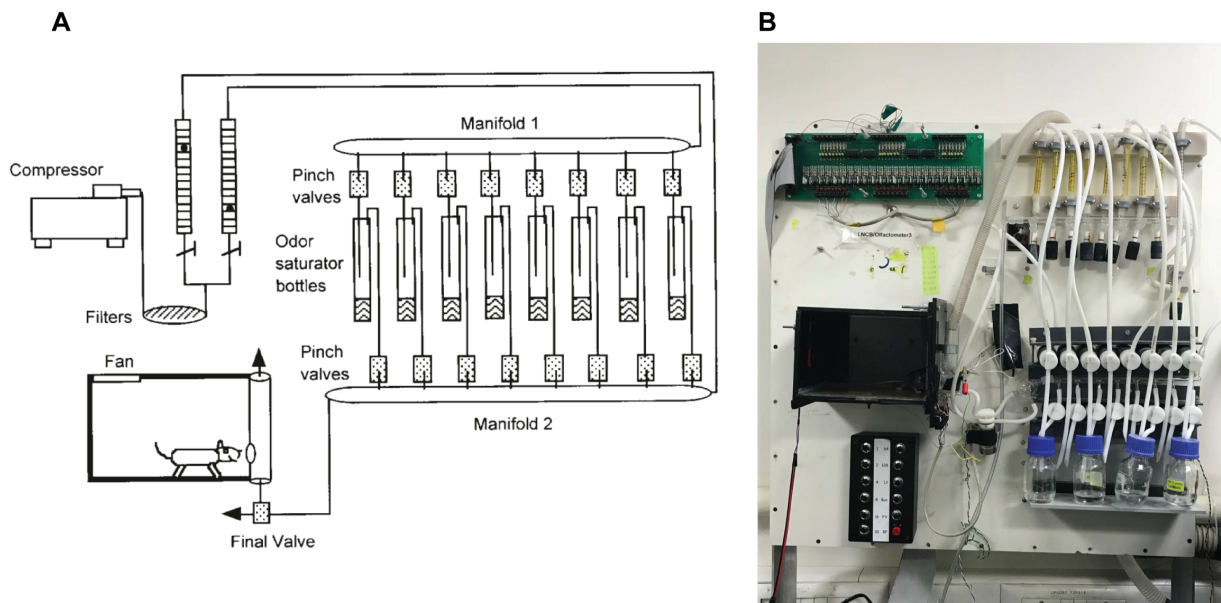
Figure 2-1: Automated olfactometer for behavioral training under freely-moving condition.

A. Schematic representation of an olfactometer with different components. In brief, air is pumped into the olfactometer by a compressor. Two flowmeters control the airflow and distribute air across different channels using a manifold. A mouse is placed in the operant chamber, where it samples the odor and registers an appropriate response depending on odor's reward contingency. *Adapted from Bodyak and Slotnick 1999. Chem. Senses (257).*

B. One of the olfactometers used for behavioral training sessions.

2.3.2.2 Task habituation training

After beginning a water restriction schedule, mice were pre-trained to make them learn procedural rules during the first 2-3 days. In first phase, mice received water reward after poking their nose in the sampling port. After 15-20 such nose pokes, second phase started wherein the mouse had to initiate a lick at the lick port to receive a water reward. After 20 trials, a third phase began wherein head insertion opened one of the odor valves for 2 s, during which water reward was provided upon a successful lick. The 'odor' used in this phase was mineral oil used for odor dilutions. From fourth phase, 1% MB was used as a detection odor. Within this phase, the lick

criterion was progressively increased to train the mouse to lick continuously during odor presentation. Mice usually learned this task within 2-3 days (4-6 sessions of 20 min each).
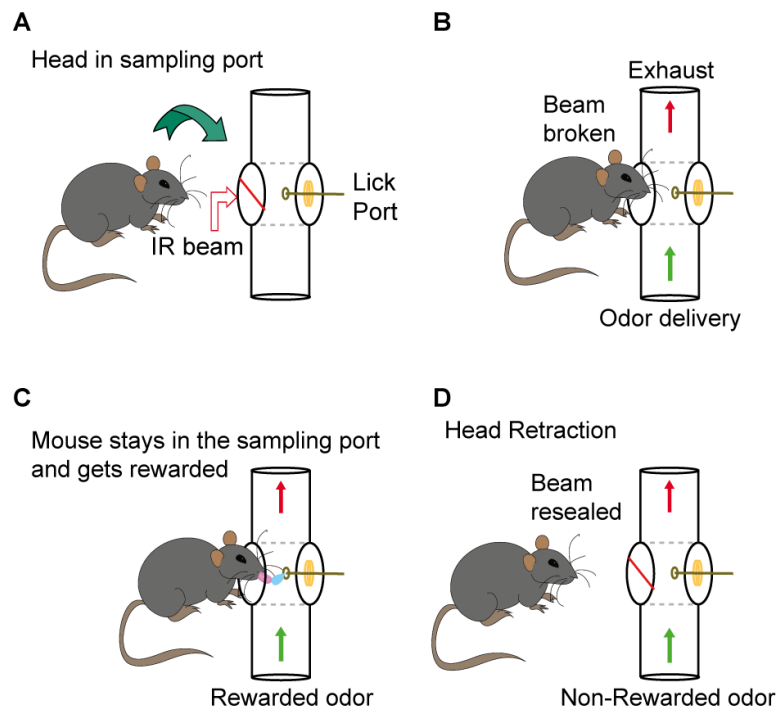
Figure 2-2: Schematic of an individual trial during behavioral training under freely-moving conditions.
(1) A trial is initiated as mouse enters the sampling port and the IR beam is broken. (2) Mouse samples the presented odor. (3) If S+ odor is presented, correct licking response triggers water delivery. (4) For S- odor, a trained mouse retracts its head from the sampling port and the IR beam is resealed.

2.3.2.3 Olfactory behavioral training

During odor discrimination training, a trial was initiated when the mouse broke the IR beam guarding the sampling port opening (Figure 2-2 A). After a 500 ms delay, an odor was delivered through the sampling port for a variable duration (odor presentation duration varied with experiments and is indicated in chapter-wise methods) (Figure 2-2 B). If the mouse continuously licked for the S+ trial satisfying the criteria set, it received a 3 µl water reward at the end of stimulus delivery (Figure 2-2 C). S- trials were marked correct if the mouse refrained from licking upon an S- odor presentation (Figure 2-2 D). A subsequent trial did not initiate unless an inter-trial interval (ITI) of at least 5 s had elapsed. The set ITI was sufficiently long to allow the mouse to retract quickly at the end of a trial. No rules were implemented to force the mouse to sample the odor for a minimal time before deciding. Further, no rules were set to prevent licking during the pre-odor period. Trials were grouped in blocks of 20 trials. Odors in each block were presented in a pseudo-randomized order to avoid more than two successive delivery of the same odor. Also, all blocks contained an equal number of S+ and S- odor presentations. Each mouse was allowed to perform

150-250 trials each day across two sessions to maintain optimum motivation despite being on a water restriction schedule. Each mouse's motivation was continuously monitored by measuring ITI and licking frequency.

2.3.2.4 Measurement of behavioral parameters
2.3.2.4.1 Measurement of learning progression

To analyze the progression of learning across different sessions we computed block-wise accuracies (20 trials/block). Next, by averaging accuracies across five blocks, we calculated the percentage of correct trials across 100 trials. We plotted these values to see if learning accuracies varied across different experimental conditions.

2.3.2.4.2 Measurement of discrimination time

We defined odor discrimination time (ODT) as the time point after odor onset when the mouse's response for S+ and S- odors significantly diverged. The sampling behavior of each mouse was monitored by tracking the status of the IR beam to determine ODT. The mouse's sampling behavior evolved with learning and could be easily distinguished between untrained and well-trained mice. With a trained mouse, after S+ odor onset, the IR beam was continuously broken as it remained inside the sampling chamber to lick on the lick port. During S- odor presentation, a mouse familiar with the odor usually retracted its head from the sampling port. The average difference in sampling response towards S+ and S- odor followed a sigmoidal curve and yielded a sensitive measure of odor discrimination performance. The ODT was determined as follows: First, we combined 300 successive trials (150 S+ and 150 S- trials) from blocks with ≥80% accuracy. For each time bin, the IR beam status for S+ and S- odors were compared using a paired one-tailed t-test. The last time point yielding a statistically significant value ($p = 0.05$) was determined as ODT. In few cases, when this value did not correspond to the point of largest curvature in the log (p) vs. time plot, ODT was manually corrected.

2.3.3 Behavioral training under Head-Restrained (HR) condition
2.3.3.1 Preparation of animals for the experiment - Surgical implantation of head-post

For the head-restrained GNG task, mice were mounted in a Polyvinyl chloride (PVC) tube and restrained on it using a custom-made stainless steel bracket. This assembly was fixed on an articulating arm with a magnetic base. To restrain the mouse, a stainless steel head-post was surgically implanted on top of each mouse's skull. The entire surgical procedure is explained below:

1. Mice were anesthetized by I.P. injection of a cocktail of Ketamine (50 μg/g body weight) and Xylazine (10 μg/g body weight). The extent of anesthesia was examined by checking the toe pinch reflex.

2. Once the mouse reached an anesthetized state, the scalp was washed with sterile distilled water, and fur was shaved using a hair clipper. During the period of surgery, the eyes were continuously rehydrated by applying artificial tears.

3. The mouse was then mounted on the stereotaxic instrument as follows; (i) ear bars were placed behind the arches of the ears, (ii) incisor teeth were placed on the incisor bar, and (iii) nose clamp was secured over the mouse's nose.

4. A local anesthetic gel (Lignocaine hydrochloride) was applied over the skin.

5. A circular cut of skin over the skull was made using a scissor (Figure 2-3 A). The area was cleaned with artificial cerebrospinal fluid (ACSF composition: 125 mM NaCl, 5 mM KCl, 10 mM Glucose, 10 mM HEPES, 2 mM $CaCl_2$, 2 mM $MgSO_4$, in 1 litre sterile Distilled water, pH = 7.4) using a cotton swab (Figure 2-3 B). A scalpel blade was used to gently scrape off periosteum on the skull and exposed muscles at the sides of the wound. This step aided dental cement to adhere to the skull.

6. The skull was allowed to air dry. In case of minor bleeding, Gelfoam® (soaked in ACSF) was used to accelerate clotting.

7. The skull was chemically etched using a dental etching agent to increase the surface's roughness, which is critical for dental cement to adhere to the skull. The excess etching agent was cleaned with ACSF, and the surface was air-dried.

8. A thin coat of cyanoacrylate gum was applied on the surface of the exposed skull and wound margins to prevent seepage of *sero sanguinous* fluid. This base of cyanoacrylate gum reinforced the skull surface to provide a better base for adherence to dental acrylic cement.

9. A dental primer was applied to the skull and wound margin. After air-drying for 15 s, the primer was polymerized by flashing U.V. light for 10 – 20 s. The primer acts as an adhesive for U.V. polymerizing cement to attach onto the bone.

10. A thin layer of U.V. polymerizing cement was spread over the skull, and the periphery of the cement layer was fused with the skull using a flat bottomed spatula (Figure 2-3 C). The cement layer was polymerized using U.V. light for 20 – 30 s (Figure 2-3 D).

11. The U.V. polymerizing cement was applied onto the base of the head-post and was placed upright on the basal cement layer (Figure 2-3 E). The two layers of cement were properly fused using a spatula. The position of the head-post was adjusted accordingly. The cement layer was polymerized using U.V. light for 40 – 50 s.

12. The dental acrylic cement (DPI RR Cold Cure) was mixed with a polymerizing agent and a drop of cyanoacrylate gum and used to seal exposed areas on the skull (Figure 2-3 F). This mixture provided the best results in terms of stability and allowed experiments to be conducted over 2-3 months. Once the cement dried, the mouse was unmounted from the stereotaxic instrument and was placed in the home cage.

13. The cage was placed over a heating pad till the mouse recovered from anesthesia and moved freely in the cage. During this period, body temperature was continuously monitored.

14. As post-operative care, mice were fed moistened food for one day after the surgery. Signs of inflammation were closely monitored for two days. Carprofen (5 µg/g body weight) was administered through water in case of any inflammation around the operated area.

2.3.3.2 Apparatus

At the beginning of a training session, each mouse was mounted in the PVC tube. The PVC tube had a removable plexiglass platform wrapped in a metallic mesh. The mouse rested on this platform and the metallic mesh aided in providing electrical contact when it licked on the lick tube. The olfactory discrimination tasks under head-restrained conditions were performed using a custom-built 10-channel olfactometer that was integrated with a lickometer and a breathing detector. The lickometer is an interface between all individual components, which recorded and digitized lick and breath responses of mice toward different odorants. The olfactometer housed eleven mass flow controllers (10 mini MFC and 1 main MFC, Pneucleus Technologies LLC, Hollis, NH) and electromagnetic solenoid valves (SMC Pneumatik AG, Switzerland), which allowed us to achieve temporal precision during odor delivery. A manifold installed in the olfactometer split a clean air stream and diverted air to different MFCs. Air through mini MFCs entered odor bottles while air from the main MFC was controlled by solenoid valves and used as a dilution air stream. The dilution air stream and odorized air stream merged at the output through a T-tube before entering the odor delivery nozzle. The odor delivery nozzle used was a customized glass nozzle with seven channels and an exhaust outlet. Before the odor presentation, a set pre-loading time of 3.2 s wherein odorized air passed through the nozzle into the exhaust to ensure that the odor plume attained a steady state (Figure 2-4 A). After 3.2 s, the exhaust switched off, allowing odorized air to be delivered to the mouse. This allowed us to obtain a sharp odor pulse with concentration stability during stimulus presentation. To minimize odor travel time, the nozzle was placed next to the nostrils. The lick tube was positioned near the mouse's mouth. Water reward was delivered through this lick tube. A lick circuit was connected to the lick tube, which allowed us to record lick responses during behavioral training sessions. An airflow sensor (AWM2300V,

Honeywell) coupled with a custom-made digitizer was used to monitor breathing cycles during behavioral experiments continuously.

2.3.3.3 Task habituation

Like the FM paradigm, after beginning the water restriction schedule for 2-3 days, mice were trained to acquaint themselves with the task's procedural aspects. On the first day, the mouse was placed inside the PVC tube and fed free water to acquaint them with the setup. On the next day, the first phase of pretraining began (20 trials). In this phase, each trial's onset was marked by a tone of 200 ms. Immediately after the tone, a water drop (3 µl) was given to the mouse. The delay between tone and water reward gradually increased to 1 s (15 trials) and 2 s (15 trials) in the next phase. This helped to train mice to wait for water rewards. The number of trials was varied depending on the motivation shown by mice. Once mice learned to wait for the reward, an odor pulse (mineral oil) was introduced for 2 s. A lick response during odor presentation was rewarded. Following the tone, a baseline licking was recorded for 1 s before odor presentation during the next stage. In this phase, mineral oil was replaced by 1% MB. If the mouse refrained from licking during the baseline period, water delivery criteria were based on the licking time during odor presentation. During odor presentation, the total licking time required for mice to receive water reward gradually increased from 40 ms to 240 ms (*17*). If mice licked during the baseline, a lick penalty was introduced, and the required licking time kept increasing from 100% to 200%. Most of the mice picked up the task's procedural rules in 2-3 days (4-6 sessions of 20 min each).

2.3.3.4 Olfactory behavioral paradigm

The odor discrimination task was carried out with a constant ITI of 13.2 s, including a preloading time of 3.2 s. The trial onset was marked with a tone of 200 ms (Figure 2-4 A). The onset of odor delivery was determined on the breath synchronization parameter. When breath synchronization was not implemented, odor onset was immediately after 3.2 s of preloading time. With breath synchronization, the program monitored an ongoing breathing cycle after preloading time and triggered the odor delivery in the middle of the exhalation period. This was done so that the odor reaches the mouse's nose during the next inhalation phase. The duration of odor presentation was varied depending on experimental conditions. However, the reaction window was always set at 2 s, and its onset coincided with odor delivery (Figure 2-4 A). The total lick duration needed to earn a reward (3 µl) at the end of an S+ trial was determined by licking activity during the baseline period. The mouse had to lick twice the amount of time during the reaction window to receive a water reward if it licked during the baseline period. If the mouse refrained licking during

the baseline period, it had to lick for a total time of 80 ms in any of the three out of four time-bins to receive a water reward. Trials were recorded as correct if mice met the criteria as mentioned earlier for S+ odors. If mice did not lick during baseline in S- trials, a cumulative lick period of 80 ms in two out of four time-bins was the qualification for a correct trial. If mice licked during the baseline, the S- trial was considered right if the total licking time during odor presentation did not exceed 25% of the baseline licking. The incorrect trials were not punished.
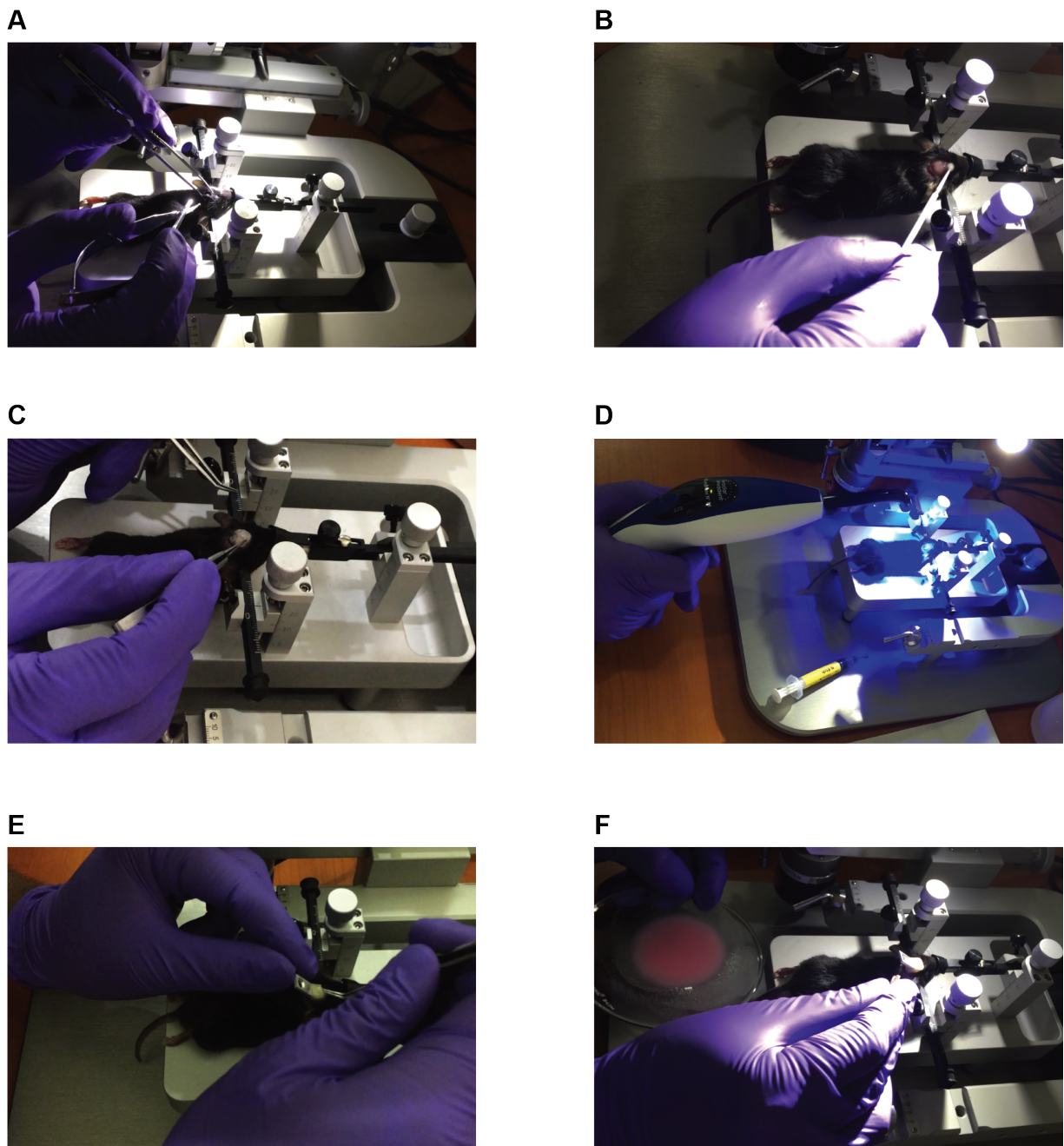
Figure 2-3: Surgical procedure for head-post implantation.

A. Mouse is mounted on the stereotaxic apparatus. B. The skin over the skull is removed, and the surface is cleaned. C. Base layer of U.V. polymerizing cement is applied. D. Polymerization of the cement using U.V. light. E. Head-post is fixed on the skull. E. The surrounding area is covered with acrylic dental cement.

In a block of 20 trials, the odor sequence was pseudo-randomized. The pseudo-randomization ensured that a given odor was not presented in more than two successive trials, and S+ and S- trials were equally presented within each block of 20 trials. Also, the order of presentation for two odors differed in consecutive blocks of trials. For different odors used in this study, mice did not show any intrinsic preference towards the odors. However, to exclude any bias caused by odor preferences, we counterbalanced S+ and S- trials amongst mice within a set. In total, mice performed 200-300 trials spanned across two sessions every day. The motivation of mice was controlled by monitoring the licking frequency. When mice lost motivation, they stopped licking for rewarded trials.
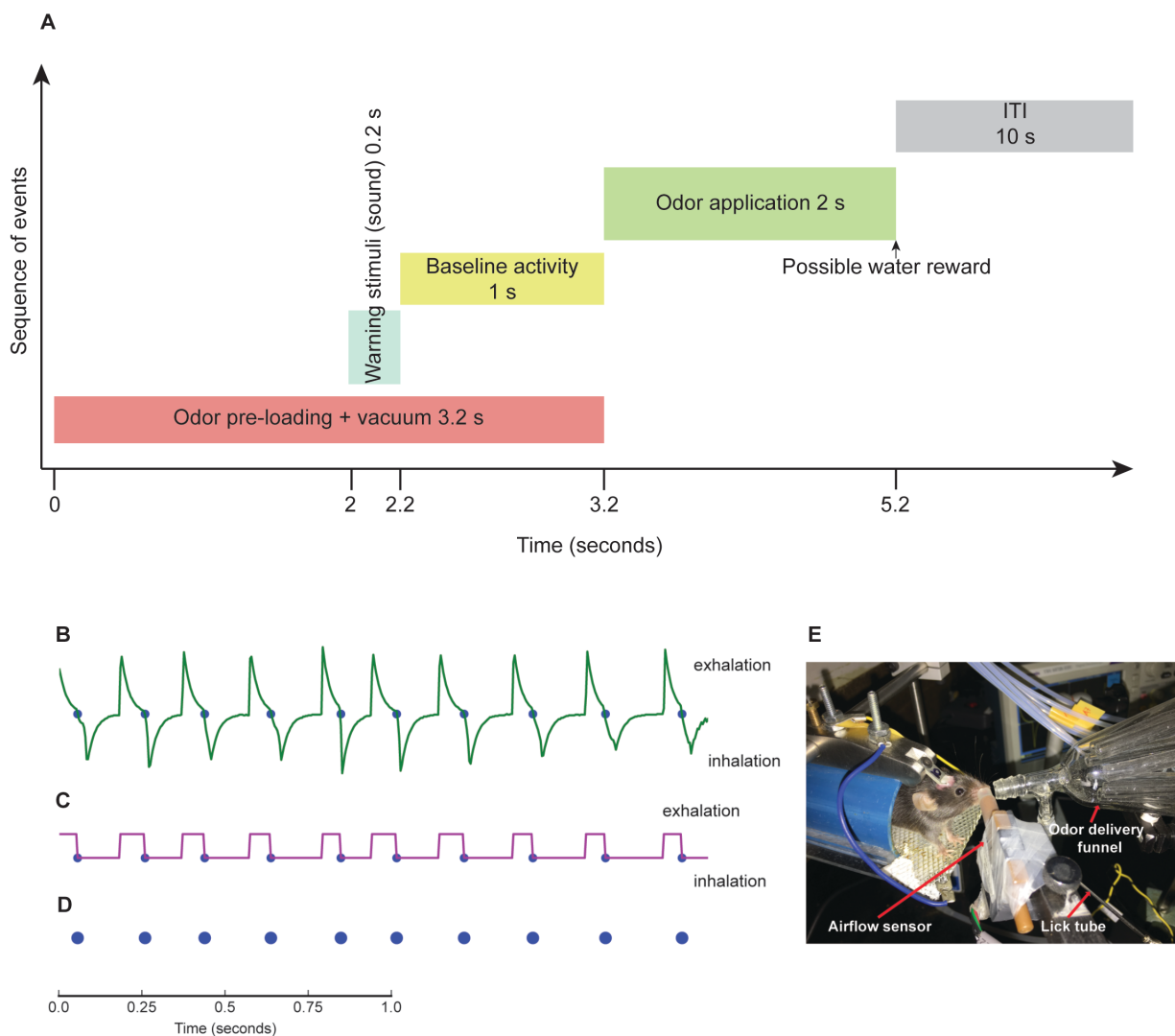
Figure 2-4: Experimental set-up to study olfactory behavior under head-restrained condition.

A. Structure of an individual trial when mice are trained under head-restrained conditions. B. Representative breathing trace acquired using a non-invasive airflow sensor placed near one nostril of the mouse. C. A threshold function converts the analog breathing pattern to a digital signal where a value of 0 corresponds inhalation and a value of 1 represents exhalation. D. Breath initiations points are marked as blue dots. E. A mouse engaged in olfactory behavior experiment.

2.3.3.5 Measurement of breathing parameters

During behavioral training, the mouse's respiratory rhythm was continuously acquired using a non-invasive airflow pressure sensor placed near the nostrils (Figure 2-4 E). The sensor fed real-time analog signals to the breathing circuit with a temporal resolution of 4 µs (Figure 2-4 B). The breathing circuit converted the raw analog signals to a digital signal by applying a threshold function. This converted the raw traces to a binary signal where a value of 0 corresponds to an inhalation and a value of 1 corresponded to an exhalation (Figure 2-4 C and D). The filtered traces were recorded continuously using the lickometer software. The breathing circuit parallelly relayed unfiltered traces to an oscilloscope (TBS 1072B-EDU, Tektronix) for visualization.

2.3.3.6 Calculation of breathing frequencies and plotting histograms

For every trial, the breathing frequency was measured for the entire stimulus period. All breath initiation time-points were marked in a raster plot. The inhalation onset distribution over all trials across different animals was visualized by plotting a histogram with a bin resolution of 20 ms. The mode of distribution of breath initiations was defined as the sniffing peak. Custom written codes in MATLAB and Python were used for analysis.

2.3.3.7 Measurement of discrimination time

The licking response was acquired at a high temporal resolution and averaged into time bins of 2 ms resolution. When mice learned odor discrimination, upon S+ odor delivery, they continuously licked during the reaction window, whereas upon S- odor delivery, mice abstained from licking during the reaction window (Figure 2-5 A). Similar to behavioral experiments under FM conditions, only the blocks ≥80% accuracy were considered for discrimination time measurements. The discrimination time was determined as the first time point wherein lick response towards S+ and S- trials diverged significantly (Figure 2-5 B). In few cases, when this value did not correspond to the point of largest curvature in the log (p) vs. time plot, ODT was manually corrected.
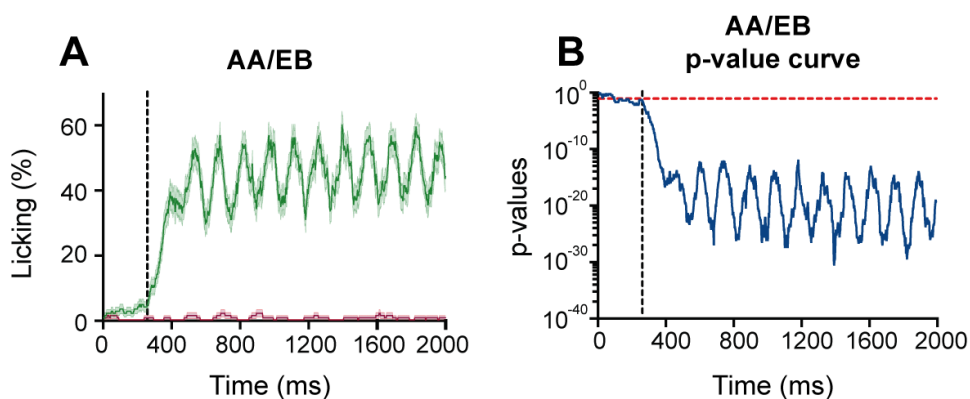
Figure 2-5: ODT measurements from the licking behavior of mice towards S+ and S- odorants.

A. Representative lick responses (averaged over 150 S+ and 150 S- trials) for AA vs. EB odor pair discrimination observed for an individual animal. Green traces represent licking responses for S+ odorants and magenta traces represent S- trials.

B. Statistical difference calculated between 150 S+ and S- trials. The red dotted line represent a p-value of 0.05, while the black dotted line represents where the trace crosses the p-value of 0.05 and corresponds to the measured ODT.

2.4 *In vivo* imaging of odor-evoked activities in GL and GCL

2.4.1 Intrinsic optical imaging of glomerular activity

The detailed methodology is described in section 3.2.2. In brief, a cranial window was implanted over the surface of OB. During imaging sessions, the dorsal surface of OB was illuminated at 700 nm using a halogen lamp and a light guide system. Images were acquired at (i) 5 Hz for 10 s using a Navitar macroscope with a 3001 Imager optical system, or (ii) 6.5 Hz for 9.3 s using a modified Fuji camera with 2001VSD+ Imager controller. All images were realigned for analysis by comparing the blood vessel pattern and filtered using a custom MATLAB script. Further, the Euclidean distance between points on activity maps was calculated using a Pythagorean formula.

2.4.2 Microendoscopic imaging of GCs

The procedure for chronic imaging of GC interneurons is described in section 4.2.11. In brief, a 1 mm cranial window was drilled at the center above one hemisphere of OB. A track of 1 mm was created by inserting a blunt Hamilton needle. We then lowered the GRIN lens (1 mm protrusion) vertically until it reached the GCL (Figure 2-6 A and B). We used a combination of cyanoacrylate gum and acrylic dental cement to fix lens assembly on the skull surface. A head-post implanted posterior to the implanted lens allowed us to record the Ca^{2+} dynamics in head-restrained mice (Figure 2-6 C). Mice were given 3-4 weeks to recover. Imaging was done in naive anesthetized and awake mice. During imaging sessions, images were acquired at 10 Hz for 10 s. An external TTL signal from the olfactometer was used to synchronize the recording of Ca^{2+} signals. Images were acquired at a spatial resolution of 350 μm × 350 μm, which was further binned 2×2 times. For analysis, images that had frame drops were detected and excluded. The relative change in fluorescence was measured and compared across different stimuli conditions. All image analyses were done using custom-written MATLAB scripts.
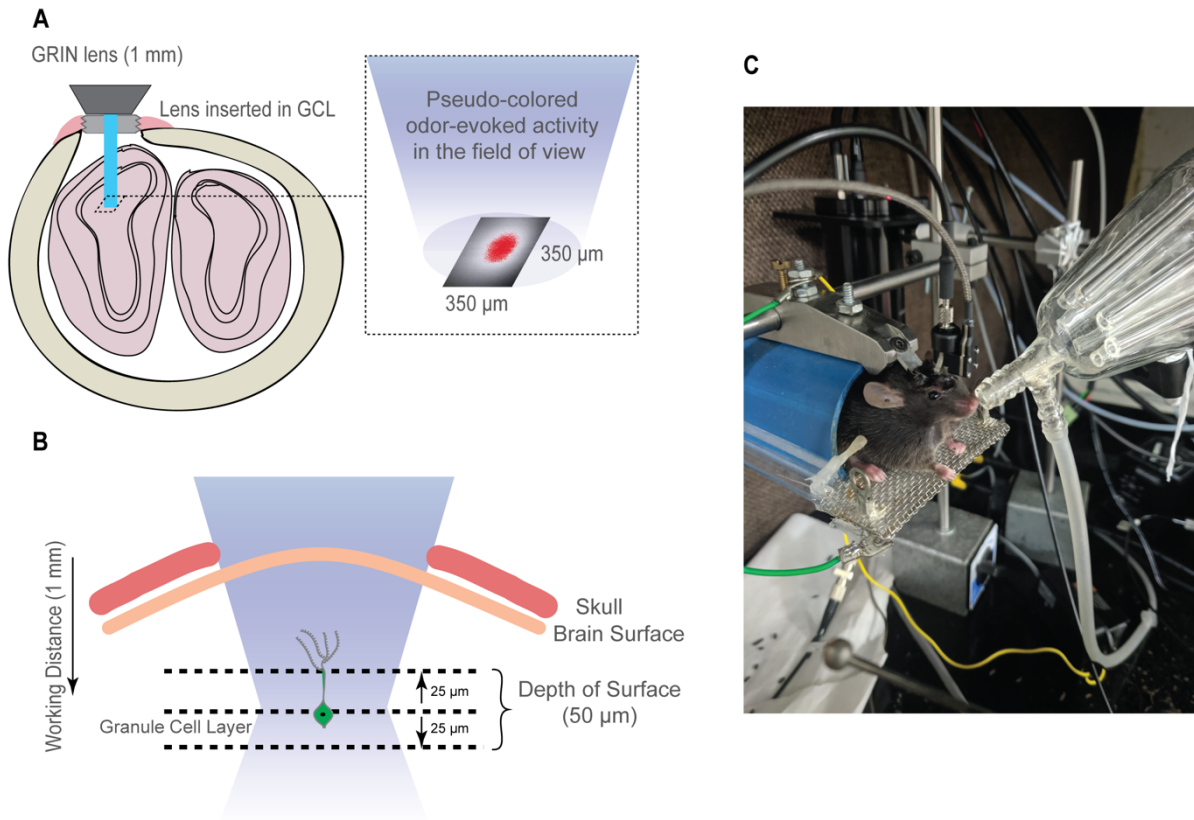
Figure 2-6: Illustration of microendoscopic imaging session.

A. Field of view obtained using the microendoscope. B. Depth range of the imaging canula used for imaging GCs. C. Representation of an imaging session with an anesthetized mouse.

2.5 Optogenetic modification of olfactory learning and long-term memory

In Chapter 4, one of the principal aims was to evaluate the influence of inhibition on MTCs in olfactory learning and long-term memory formation. To establish such a causal relationship, we took advantage of modulating the activity in a majority of OB's inhibitory interneurons by expressing either ChR2 or Arch under the GAD65 promoter. We photostimulated/photoinhibited GAD65 +ve interneurons while mice were performing odor discrimination tasks to investigate the role of inhibition in olfactory learning and long-term memory formation. To activate the interneurons, we flashed pulses of blue light (473 nm) of 5 ms at 40 Hz frequency. We used 1000 ms pulses of amber light (595 nm) at 1 Hz frequency to inhibit the interneurons. The light stimulations were synchronized to odor onset for these sets of experiments. Another important aim was to see whether light-driven modulation of MTC ensemble activities during the post-stimulus period could help form long-term memories. To study this, we manipulated MTC activity by controlling the activity of GAD65 interneurons. We overstimulated inhibitory interneurons in ChR2-expressing mice to fully shut down MTC activity during the post-stimulus period. To accomplish this, we timed the start of light pulses to correspond with the end of odor stimulation.

The pulse width and frequency were kept similar to the previous condition. However, the duration of light stimulation was increased to 4 s. We inhibited interneuron activity in a separate batch of Arch expressing mice in order to sustain MTC ensemble activities in the post-stimulus period. We achieved this by giving four 1 s pulses of amber light at 1 Hz frequency at the end of odor stimulation. The detailed protocol for surgical preparation and light-driven olfactory behavior is described in sections 4.2.7 to 4.2.9 of this thesis.

CHAPTER 3

Similarity and strength of glomerular odor representations define a neural metric of sniff-invariant discrimination time

Adapted from: **A. S. Bhattacharjee***, S. Konakamchi*, D. Turaev, R. Vincis, D. Nunes, A. A. Dingankar, H. Spors, A. Carleton, T. Kuner, N. M. Abraham, Similarity and Strength of Glomerular Odor Representations Define a Neural Metric of Sniff-Invariant Discrimination Time. *Cell Rep.* **28**, 2966-2978 (2019).

3.1 Introduction

3.1.1 Sense of smell and odor reaction times

The olfactory system constantly processes complex odor mixtures in the environment, assisting in decision-making and, ultimately, guiding behavior. However, understanding the mechanisms involved in the neural processing of these odor mixtures is still an ongoing investigation. Odor mixture perception is influenced by relative intensities of different components (*262*), mixture complexity (*263*), and chemical structure (*264, 265*). Odor mixtures can exhibit either elemental, configurational, or overshadowing properties. Odor mixtures wherein each component is easily identifiable by an animal are considered elemental mixtures (*264*). Configurational mixtures are perceived as novel and distinct from each component, and animals fail to identify the mixture's individual components (*265, 266*). When one odorant dominates and overshadows the other odorant in some mixtures, animals detect the dominant odorant but not the other odorants (*264*). To understand the neural mechanisms underlying processing of different kinds of odor mixtures, it is critical to employ psychophysical paradigms that quantitatively measures different behavioral readouts (*14, 25, 30, 267*). Reaction times and accuracy have proven successful across various species and sensory systems as sensitive behavioral readouts reflecting stimulus and task complexities. For difficult tasks such as discrimination between perceptually similar objects, if quick decisions are demanded, one would expect poor performance in discrimination of similar objects. Likewise, if high performance is to be maintained, one would take longer reaction times to make discriminations (*268*). In nature, animals make these speed-accuracy tradeoffs in various ecologically important tasks, such as detecting prey and predators, pollinators choosing between flower species, and nest site exploration strategies (*269*).

In the context of olfaction, the concept of speed-accuracy tradeoff has been a subject of debate. Igniting this debate was a study to measure rats' reaction times using a two-alternative

forced-choice olfactory discrimination task. Using odor mixtures of varying complexities, the study concluded that odor discrimination speed was independent of odor similarity (*29*). On the contrary, an odor discrimination study using a GNG paradigm showed that accurate decisions were significantly faster for simple odor discriminations than difficult discriminations (*22*). From the time of these two studies, few studies have found that olfactory performance depends on the stimulus properties (*23–27*). In contrast, other studies demonstrated uncoupling of decision-making accuracy from stimulus complexities (*30*, *31*).

One reason for such contradictory conclusions can be attributed to a limited number of odorants used in studies uncoupling accuracy from stimulus complexity. This severely limits our interpretation as the high dimensionality of odor stimulus space was disregarded as a potential criterion influencing olfactory decision-making. In OB, odorants from different chemical classes evoke complex patterns of glomerular activity (*166*). While monomolecular odorants produce distinct glomerular activity patterns, their binary mixtures evoke similar activity patterns (*22*, *270*). Mice can accurately discriminate monomolecular odor within hundreds of milliseconds, while binary mixture discrimination takes a longer duration (*22–24*). These observations raise the question of whether glomerular map similarity correlates to odor discrimination times for different classes of odorants. Establishing such a relationship would link odor representations to the degree of neural processing required to make well-informed decisions.

3.1.2 Odor sampling behavior and sense of smell

The sense of smell is also influenced by odor sampling behavior. The volatile odor molecules are transported by air, and therefore, their location depends on air turbulences. For instance, in the moth, *Manduca sexta*, a change of odor plume direction in a turbulent air stream drastically impacts the response of OSNs and downstream neurons in the olfactory pathway (*271*, *272*). The constant change in odor stream is not ideal for optimally sampling odorant molecules. To counteract this problem, animals have developed strategies. For instance, lobster ORs are located on the flagellum of antennules, which form a dense brush layer. Under low flow conditions, this layer shields ORs from odorants, rendering its detection virtually impossible. Lobster flicks their antennules at around 4 Hz to drive water through the brush and allow odorants to be detected by OSNs (*273*). Similarly, rodents display high breathing frequency or sniffing while detecting novel odors in their surroundings, engaging in social interactions, or detecting and discriminating different odorants (*230*, *274–276*).

It has been observed that rodents can vary their sniff frequency, and rapid changes in sniff frequencies can alter OSN's response towards odorants. At low frequencies (< 3 Hz), OSN fire in

brief bursts that rapidly returns to baseline with each inhalation. On the contrary, at high-frequency sniffing (> 4 Hz), OSN firing appears mainly as tonic signals (*277*). At postsynaptic terminals, it has been shown that respiration can synchronize MTC activities (*278*), and the absence of nasal respiration can reduce mitral cell firing activities and abolish rhythmic spiking in tufted cells (*279*). At high sniffing frequencies, MTC excitability is reduced due to a combined outcome from the adaptation of sensory neuron responses (*277, 280, 281*) and an increase in the strength of inhibitory inputs onto MTC via GCL inhibitory circuits (*147, 282*). Such modulations in sniff frequencies thus bring about a significant change in odor responses in MTCs. Calculating Euclidean distances between MTC response vectors indicated a better discriminability when there is a positive change in breathing frequencies. Despite these results, less is known about whether sampling behavior in awake animals changes OB responses contributing towards olfactory decision-making.

This study investigated how glomerular activity and sampling behavior patterns relate to ODT. We selected odors that either specifically activated glomeruli on the dorsal surface (*22, 283, 284*) or activated overlapping glomerular patterns (*16, 29, 284*). This facilitated odor-evoked functional activity imaging in anesthetized and awake mice. The correlation of IOS imaging data with behavioral measurements revealed that ODT is inversely correlated to the measured Euclidean distances between activated glomeruli patterns across different chemical classes. These results suggested that the strength and similarity of glomerular activity patterns can predict ODT for different chemical classes. Further, we observed a significant increase in sniff frequency during the decision-making period. However, the increase in ODT for binary mixtures compared to monomolecular odors did not depend on the sniffing frequency. This suggests that odor representations are invariant of the sampling behavior, thus allowing a stable percept formation.

3.2 Materials and methods

In this chapter of thesis, mice were either trained to olfactory behavioral training using the GNG paradigm under FM or HR conditions. The detailed methodologies for these behavioral paradigms are explained in materials and methods chapter (2.3.2 and 2.3.3).

3.2.1 Measurement of olfactory discrimination times for different odor pairs

The detailed procedure to calculate odor discrimination time is stated in sections 2.3.2.4 and 2.3.3.7. Briefly, ODT measurement was done from tasks (blocks of 300 trials) with ≥ 80% accuracy. For mice trained under HR conditions, task-wise ODT was calculated by comparing lick responses towards 150 S+ and 150 S- trials. The time point where the licking response significantly

diverged for S+ and S- trials was defined as the odor discrimination time. ODT was calculated for mice trained under FM conditions by comparing odor sampling behavior towards S+ and S- trials.

The first three sets of mice were trained under FM conditions. The sequence of odorants used in set 1 was as follows (Figures 3-1 A-D, 3-2 A and B, numbers reflect the total number of trials performed): 1200 CI vs. EU, 600 AA vs. EB, 900 AA/EB 60/40 vs. AA/EB 40/60, 600 AA vs. EB, 900 AA/EB 60/40 vs. AA/EB 40/60, 600 CI vs. EU, 900 CI/EU 60/40 vs. CI/EU 40/60, 600 CI vs. EU, 900 CI/EU 60/40 vs. CI/EU 40/60, 900 C+ vs. C–, 900 C+/C– 60/40 mix, 600 C+ vs. C–, 900 C+/C– 60/40 mix (n = 9-10 mice).

In the second set of experiments, odor pair sequences were as follows (Figures 3-1 E–H, 3-2 A and B): 900 O+ vs. O–, 900 O+/O– mix, 600 O+ vs. O–, 900 O+/O– mix (n = 7 mice). In this set of experiments, 0.1% odor dilution was used. The 3rd set of mice (n = 6 mice) were trained on CI vs. EU (1200 trials), followed by O+/O- (900 trials) and O+/O- mix (1200 trials). In these experiments, 1% odor dilution (in mineral oil) was presented to mice. Learning performance and ODT were similar to those reported for set 2 (data pooled in Figure 3-3).

The 4th batch of mice was trained under HR conditions to investigate the sniffing behavior while mice were actively involved in behavioral training tasks (n = 7-8 mice, set 4). A noninvasive airflow pressure sensor was used to record the sampling behavior of mice. The detailed methodology for the measurement of breathing is provided in section 2.3.3.5 and 2.3.3.6. Mice were trained to the following sequence of odorants: CI vs. EU, CI/EU 60/40 vs. CI/EU 40/60, AA vs. EB, AA/EB 60/40 vs. AA/EB 40/60, C+ vs. C–, C+/C– 60/40 mix, O+ vs. O, O+/O– 60/40 mix. We trained the 5th batch of naive mice on MO vs. MO task to study sampling behavior in the absence of odors (Figure 3-6, n = 8 mice, set 5). To identify the role of anticipation in controlling the sniffing behavior, a separate batch of mice was trained without a tone demarcating the onset of a trial (Figure 3-7, n = 8 mice, set 6). The odor sequence was identical to that used for the fourth batch of mice.

To study glomerular activity patterns for odorants used for behavioral training, another batch of naive mice (n = 5 mice, set 7) was used for IOS imaging. The eighth set of mice (n = 5 mice) was trained on different dilutions of CI/EU and AA/EB ranging from 10^0 to 10^{-10} (% dilution in mineral oil). These mice were used for imaging under awake conditions (Figure 3-11).

3.2.2 *In Vivo* Optical Imaging (This experiment was done by Dr. Nixon and our collaborators at the University of Heidelberg, Germany and University of Geneva, Switzerland)

The detailed protocol is mentioned in our published report (*17*). Briefly, using Intrinsic Optical imaging, glomerular activity patterns were recorded from awake and anesthetized mice (5

mice in each set). Odorants were presented using olfactometers used for behavioral experiments, or a GC PAL robot system (CTC Analytics, Switzerland) was used. A light guide system with a halogen lamp and 700 nm interference filter was used to illuminate the OB surface. During each imaging session, a reference image of blood vessels was acquired using a 546 nm interference filter. This image allowed us to focus on the same field of view across multiple imaging sessions. Images were taken with a Navitar macroscope with a 3001 Imager optical system or a modified Fuji camera with a 2001VSD+ Imager controller. For a 10 s imaging window, sampling was done at 5 Hz, and for a 9.3 s imaging window, sampling was at 6.5 Hz. Irrespective of the imaging duration, a trial initiated with a short baseline followed by odor presentation for 4-5 s. A minimum of 60 s of ITI was provided between the trials to prevent adaptation and desensitization effects. The sequence of odor presentation was varied between experiments to minimize the influence of odor sequence on the analysis outcome. The image analysis was performed using custom-written scripts in MATLAB. To pre-process the images, all image frames were normalized to the reference frame, and a Gaussian filter was applied to remove non-specific signal and high-frequency artifacts. Regions surrounding the bulb were masked using a single exclusion mask. For each odor, images across different trials were averaged to obtain a single activity map. This was done to increase the signal-to-noise ratio. The Euclidean distance between points on the activity maps was calculated using a Pythagorean formula. The maps were compared only between the same mouse. However, for directly comparing activity maps for awake and anesthetized mice, Euclidean distance measured for a common odor pair (CI vs. EU) was used as a normalization factor. This was done to minimize the variability introduced by different imaging systems and movement artifacts that were more prominent in awake mice.

3.2.3 Quantification and statistical analyses

For this chapter, all statistical analyses were performed using GraphPad Prism 7 and 8, Microsoft Excel, and MATLAB. We used one-way and two-way ANOVA and associated post-hoc tests, student's t-test, and different non-parametric tests. The normality of data sets was determined using the Shapiro-Wilk test. To establish the relationship between Euclidean distance and measured ODTs for different odors, the following equation was applied: $A1*exp(-x/t1) + y0$.

3.3 Results

3.3.1 Stimulus-dependent olfactory discrimination time for odor pairs of different chemical classes

To assess if odors of varying complexities exhibit stimulus-dependent ODTs, we trained mice on a GNG operant conditioning task using an automated olfactometer (*22*, *23*, *257*). Details of task habituation training and two-odor discrimination training are described in the materials and methods chapter (Section 2.3.2). Mice were sequentially trained to discriminate monomolecular odorants and binary mixtures across different chemical classes. Following task habituation, we first trained a group of mice for AA/EB, CI/EU, and C+/C- (set 1; see materials and methods). On training mice on CI/EU, within 600 trials, their performance stabilized at ≥90% accuracies, which continued till the end of 1200 trials (Figure 3-1 A). Next, we tested AA vs. EB following a previously published training scheme (*22*). Mice started performing AA vs. EB discrimination with >80% accuracy within 200 trials and reached asymptotic performance within 600 trials (Figure 3-1 A and B). Learning AA/EB binary mixture discrimination, a more complex task, took longer. However, mice attained 95% accuracy by the end of the second task (end of 600 trials, figure 3-1 A and B). ODTs were measured from the last 300 trials of each odor discrimination training paradigms (Figure 3-1 C). In 255 ± 16 ms, mice could discriminate between AA/EB monomolecular odor pair; nonetheless, they took significantly longer time for binary mixture discrimination (359 ± 16 ms; one-way repeated measures [RM] ANOVA, F = 31.2, p = 6.4×10^{-9}).
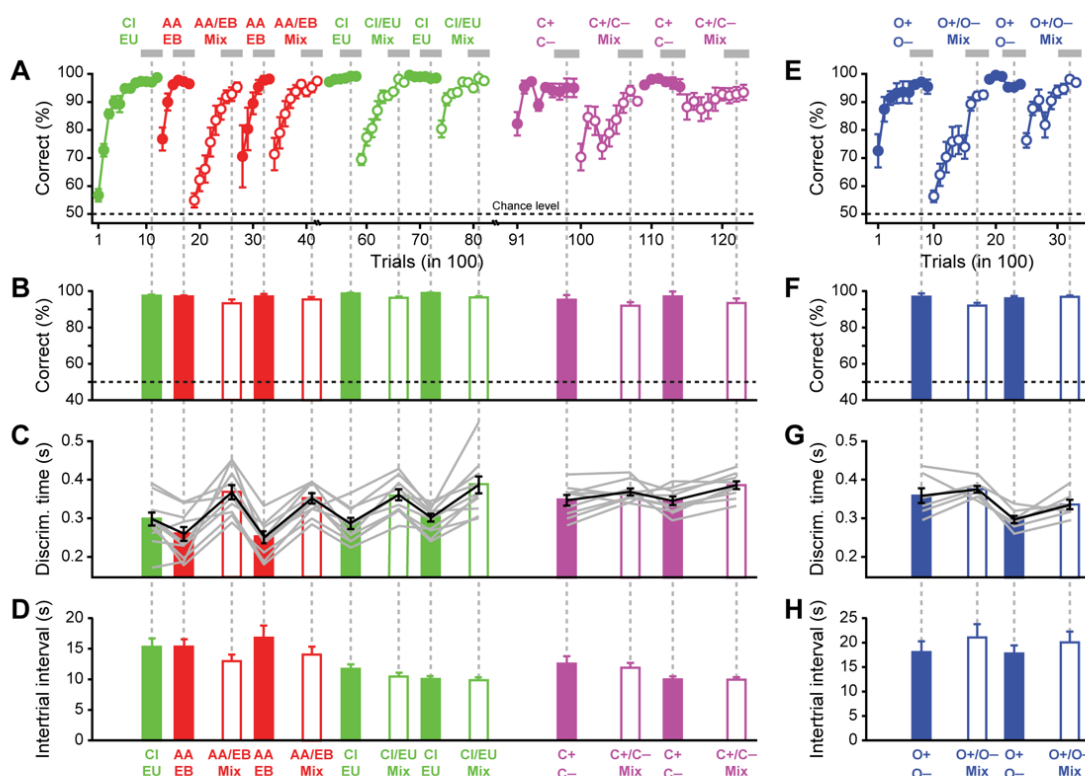
Figure 3-1: Odor discrimination time varies for odors pairs belonging to different chemical classes.

(A) Training schedule and odor discrimination learning accuracies measured for different monomolecular odors and binary mixtures.

Discrimination accuracies are shown as percentage correct responses averaged over 100 trials. Each data point is the average of nine or ten animals. The x-axis indicates the progression of time. The trials highlighted with a gray bar were used for ODT analysis. Odor pairs used were 1% CI vs. 1% EU, 1% AA vs. 1% EB, 1% C+ vs. 1% C-, and mixtures of these odorants as indicated (60/40 mixtures were used; e.g., the AA/EB mix is 0.6% AA + 0.4% EB vs. 0.4% AA + 0.6% EB; all odor pairs were counterbalanced as described in materials and methods). The black dotted line running parallel to the x-axis indicates chance level.

(B) Learning accuracies measured from blocks of trials indicated in (A) (gray bars).

(C) ODTs measured from experimental blocks as in (B) for individual mice and for the population (gray and black lines, respectively). The ODTs were found to be longer for binary mixture odor pairs compared to monomolecular pairs of odorants (between AA/EB and their binary mixtures: one-way RM ANOVA, $F = 31.2$, $p = 6.4 \times 10^{-9}$, n = 10 mice; CI/EU and their binary mixtures: one-way RM ANOVA, $F = 17.5$, $p = 4.7 \times 10^{-8}$, n = 10 mice; C+/C– and their binary mixtures: one-way RM ANOVA, $F = 3.4$, $p = 0.03$, n = 9 mice).

(D) Inter-trial interval (ITI), a measure of motivation was not correlated odor similarity (AA/EB, CI/EU and their binary mixtures: $R^2 = 0.2$, ANOVA $F = 1.8$, $p = 0.2$, n = 10 mice; C+/C– and their binary mixtures: $R^2 = 0.1$, ANOVA, $F = 0.6$, $p = 0.4$, n = 9 mice).

(E) Training schedule for O+/O- and its binary mixtures. Odor discrimination accuracy shown as percentage correct responses averaged across 100 trials. Each data point is an average of seven animals (different sets of mice as shown in A). Odor pairs used were 0.1% O+ vs. 0.1% O- and mixtures of O+ and O- (0.06% O+ and 0.04% O- vs. 0.04% O+ and 0.06% O-).

(F) Learning accuracy was averaged for the blocks of trials indicated by gray bars.

(G) ODTs corresponding to experimental blocks indicated in (E) (one-way RM ANOVA, $F = 9.2$, $p = 6.3 \times 10^{-4}$, n = 7 mice).

(H) ITI calculated for O+/O- monomolecular odor and binary mixtures tasks ($R^2 = 0.4$, ANOVA, $F = 1.4$, $p = 0.4$, n = 7 mice). Data are presented as mean ± SEM.

The training then continued with monomolecular discrimination of CI/EU and their binary mixtures. As this set of mice had been previously trained to CI/EU, mice discriminated CI/EU monomolecular discrimination with ≥90% accuracy (Figure 3-1 A). The performance transiently reduced upon the introduction of the CI/EU binary mixture. However, mice learned to perform with a ≥90% success rate by the second task (Figures 3-1 A and B). The ODTs were consistently longer for binary mixtures than monomolecular discrimination even after training mice to alternating tasks of these odors (Figure 3-1 C; n = 10 mice; one-way RM ANOVA, $F = 17.5$, $p = 4.7 \times 10^{-8}$). Averaging ODT across the tasks, we observed that mice took 295 ± 10 ms to discriminate CI/EU monomolecular odor pair (mean ± SEM; n = 10 mice; data averaged over three blocks of 300 trials). However, mice took approximately 80 ms more to discriminate CI/EU binary mixture (373 ± 17 ms; data averaged over two blocks of 300 trials). The motivational states of mice

while engaged in discrimination tasks were monitored by measuring ITI. The ODT and ITI for different odor discriminations were not correlated ($R^2 = 0.2$; ANOVA, F = 1.8, p = 0.2), indicating that ODT differences are independent of motivational factors.

We trained mice for C+/C- monomolecular discrimination and their binary mixtures to further increase the task complexity. This was specifically done as enantiomer pairs elicit overlapping patterns of OB activity. On measuring ODTs, we again observed a significantly faster reaction time for C+/C- monomolecular odorants compared to binary mixtures (345 ± 7 and 377 ± 7 ms for C+/C- monomolecular and binary mixtures, respectively [mean ± SEM]; n = 9 mice; data averaged over two blocks of 300 trials; one-way RM ANOVA, F = 3.4, p = 0.03). The ITI for these discriminations was found to be similar, suggesting that the ODT difference between monomolecular odors and binary mixtures was unrelated to motivational levels in mice (Figure 3-1 D; $R^2 = 0.1$; ANOVA, F = 0.6, p = 0.4). Next, to examine if odor concentration affects ODT and test another class of odor, we trained mice to the enantiomer pair of O+/O-, and their binary mixtures at a lower dilution of 0.1%. This experiment was performed with a new batch of mice to reduce the confounding effects of previous training with 1% odor concentration. After pre-training, mice were trained for monomolecular discrimination of CI/EU, followed by O+/O- monomolecular odor discrimination and their associated binary mixtures. Mice quickly learned to perform O+/O- monomolecular discriminations and attained accuracies >90% by the end of 400 trials (Figure 3-1 E). Given the complexity of binary discriminations, mice required 900 trials to reach a 90% performance level (Figures 3-1 E and F). Moreover, the learning performance for O+/O- binary mixture was similar to the previous mixture discriminations (Figures 3-1 A and B). Upon retraining mice to binary mixtures, there was a brief dip in learning performance. However, mice performed above the chance level, and accuracies peaked >95% in the last 300 trials (Figures 3-1 E and F). ODT calculated for O+/O- binary mixtures (355 ± 7 ms [mean ± SEM]) was significantly longer by ~30 ms compared to O+/O- monomolecular discriminations (Figure 3-1 G. 327 ± 13 ms; n = 7 mice; data averaged over two blocks of 300 trials; one-way RM ANOVA, F = 9.2, p = 6.3×10^{-4}). Stimulus complexity-dependent increase in ODT was independent of motivational levels of mice (Figure 3-1 H; $R^2 = 0.4$; ANOVA, F = 1.4, p = 0.4). These experiments reliably reveal that mice need excess time for accurate discrimination of complex binary mixtures than simple monomolecular odorants. Also, the magnitude of ODT increase measured at a lower odor concentration and a higher concentration was similar. To summarize, our results show that stimulus-dependent ODT is a general property of odor discrimination in mice.

3.3.2 Extent of stimulus dependency of ODTs varies for different odor pairs

Training mice to different odor classes, we observed that monomolecular odorant pairs were discriminated with discrete ODTs. The ODTs were measured from different batches of FM and HR mice. When comparing ODTs of each odor discrimination from the last 300 trials from the same number of mice, FM and HR mice did not show significant differences in ODTs (Figure 3-2). Thus, we pooled ODTs across FM and HR mice to compare them across different odor classes (Figure 3-3).
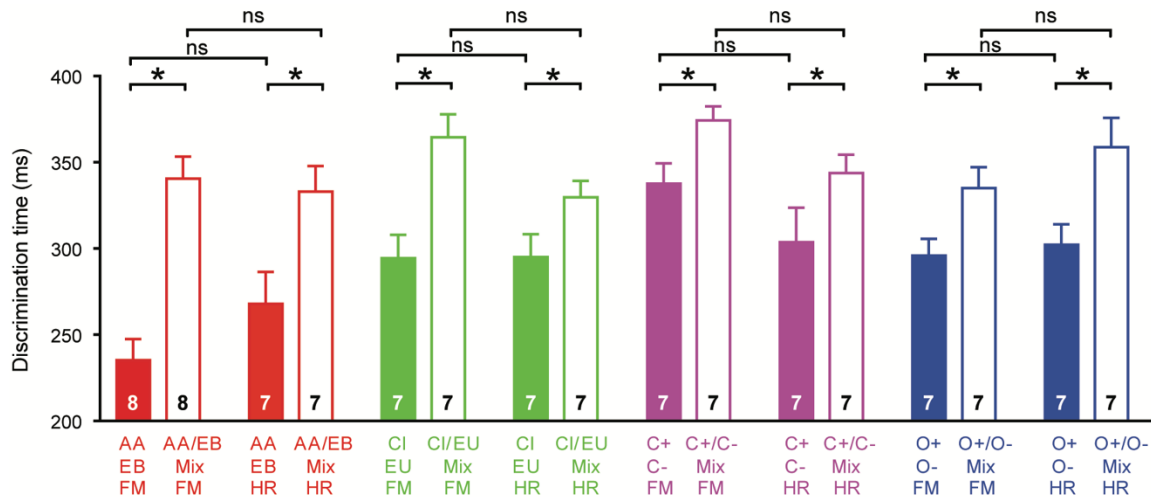
Figure 3-2: Comparison of ODTs for monomolecular odorants and binary mixtures measured under FM and HR conditions.

Mice showed increased ODTs for binary mixtures compared to corresponding monomolecular odor discriminations for all odor pairs tested under FM and HR conditions. The ODTs are averaged across different experiments. Data are presented as mean ± SEM. $DT_{AA/EB(FM)} = 235 \pm 14$ ms, $DT_{AA/EBmix(FM)} = 341 \pm 14$ ms, $DT_{AA/EB(HR)} = 268 \pm 19$ ms, $DT_{AA/EBmix(HR)} = 333 \pm 15$ ms, $DT_{CI/EU(FM)} = 294 \pm 14$ ms, $DT_{CI/EUmix(FM)} = 365 \pm 13$ ms, $DT_{CI/EU(HR)} = 295 \pm 13$ ms, $DT_{CI/EUmix(HR)} = 330 \pm 10$ ms, $DT_{C+/C–(FM)} = 338 \pm 13$ ms, $DT_{C+/C–mix(FM)} = 374 \pm 9$ ms, $DT_{C+/C–(HR)} = 304 \pm 20$ ms, $DT_{C+/C–mix(HR)} = 344 \pm 11$ ms, $DT_{O+/O–(FM)} = 296 \pm 10$ ms, $DT_{O+/O–mix(FM)} = 335 \pm 12$ ms, $DT_{O+/O–(HR)} = 302 \pm 12$ ms, $DT_{O+/O–mix(HR)} = 359 \pm 17$ ms. Number of mice trained to different odor pairs is indicated on each bar. * Comparison of ODTs for monomolecular odorants with corresponding binary mixtures: Paired t-test, $p < 0.05$. Comparison of ODTs for monomolecular odorants and binary mixture discriminations under FM and HR conditions: Unpaired t-test, $p > 0.05$.

We observed that AA/EB and CI/EU could be discriminated faster than monomolecular discriminations of carvone and octanol enantiomer pairs. In general, all monomolecular odor pair discrimination required distinct ODTs except the enantiomers, which showed similar ODTs (Figure 3-3 A. Comparison between the monomolecular odorants, ANOVA, $F = 11.09$, $p < 0.0001$; Fisher's LSD: AA/EB vs. CI/EU, $p < 0.05$; AA/EB vs. C+/C-, $p < 0.0001$; AA/EB vs. O+/O, $p < 0.0001$; CI/EU vs. C+/C-, $p < 0.01$; CI/EU vs. O+/O-, $p < 0.05$; C+/C- vs. O+/O-, $p = 0.34$). The results show that ODT is an odorant-specific property, with each odorant requiring a specific time to differentiate when performed with high accuracy. We further noticed a consistent increase in

ODT for binary mixtures tested compared to monomolecular odorants. However, the magnitude of increase in ODT differed between individual odor class (Figure 3-3 A; ANOVA, monomolecular odorants vs. binary mixtures, F = 12.81, p < 0.0001; Fisher's LSD: AA/EB vs. AA/EB 60/40 mix, p < 0.0001; CI/EU vs. CI/EU 60/40 mix, p < 0.0001; C+/C- vs. Carvones 60/40 mix, p < 0.05; O+/O- vs. Octanols 60/40 mix, p < 0.01).
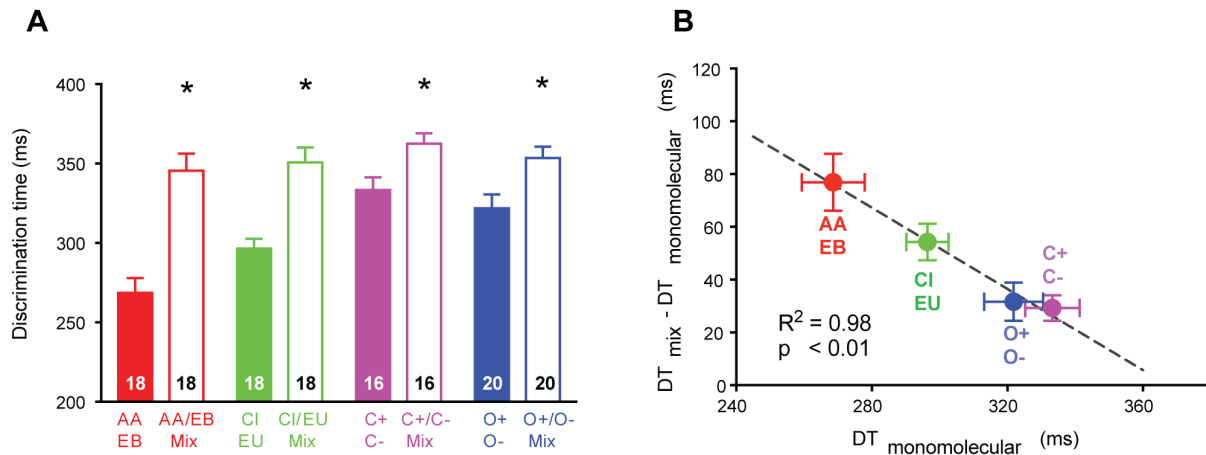
Figure 3-3: Comparison of ODTs for monomolecular odorants and binary mixtures across different classes of odor molecules.

(A) Average ODTs measured across different odor pair discriminations. Data are presented as mean ± SEM. $DT_{AA/EB}$ = 269 ± 9 ms, $DT_{AA/EBmix}$ = 346 ± 11 ms, $DT_{CI/EU}$ = 296 ± 6 ms, $DT_{CI/EUmix}$ = 351 ± 9 ms, $DT_{C+/C-}$ = 333 ± 8 ms, $DT_{C+/C-mix}$ = 363 ± 7 ms, $DT_{O+/O-}$ = 322 ± 9 ms, $DT_{O+/O-mix}$ = 353 ± 7 ms. Number of mice is indicated inside each bar. The monomolecular odors are represented by filled bars while binary mixtures are represented by empty bars. *Comparison of ODTs for monomolecular odorants vs. binary mixtures: ANOVA, F = 12.81, p < 0.0001; Fisher's LSD, p < 0.05. Data are presented as mean ± SEM.

(B) The difference in ODT for binary mixtures and related monomolecular odors is inversely correlated to ODT for monomolecular odorants (linear regression: R^2 = 0.98; ANOVA, p < 0.01).

To identify the pattern of increase in binary mixture ODTs compared to monomolecular ODTs, we plotted the difference in ODT between binary mixtures and monomolecular odorants against the ODT of monomolecular odorants. All data points were equally distributed near the regression line (Figure 3-3 B, R^2 = 0.98, p < 0.01). This relation indicates that the increase in ODT for binary mixture from monomolecular odors is inversely correlated to the monomolecular ODTs. Furthermore, the point of crossing of the regression line with the x-axis may be defined as maximal ODT (~400 ms), within which the olfactory system is forced to process odor information in a decision-making task. This signifies that no excess time would be consumed for binary mixtures at maximal accuracies if the discrimination time of a monomolecular odor pair approaches 400 ms. This observation indicates a probable upper limit for decision-making time for odor discriminations.

3.3.3 Sampling behavior does not influence the increase in ODT during binary mixture discrimination

Our results demonstrated an increase in ODT for binary mixtures compared to monomolecular odorants across different odor classes. We next explored the possibility of animals' sampling behavior influencing the difference in ODT towards stimuli of varying complexities. To probe this question, we trained a batch of naive mice (set 4; see materials and methods) on different monomolecular odorants and their binary mixtures and measured their breathing frequency while involved in an odor discrimination task. Breathing patterns were measured non-invasively in HR mice using an airflow pressure sensor placed near one of the nostrils (refer to section 2.3.3.5).
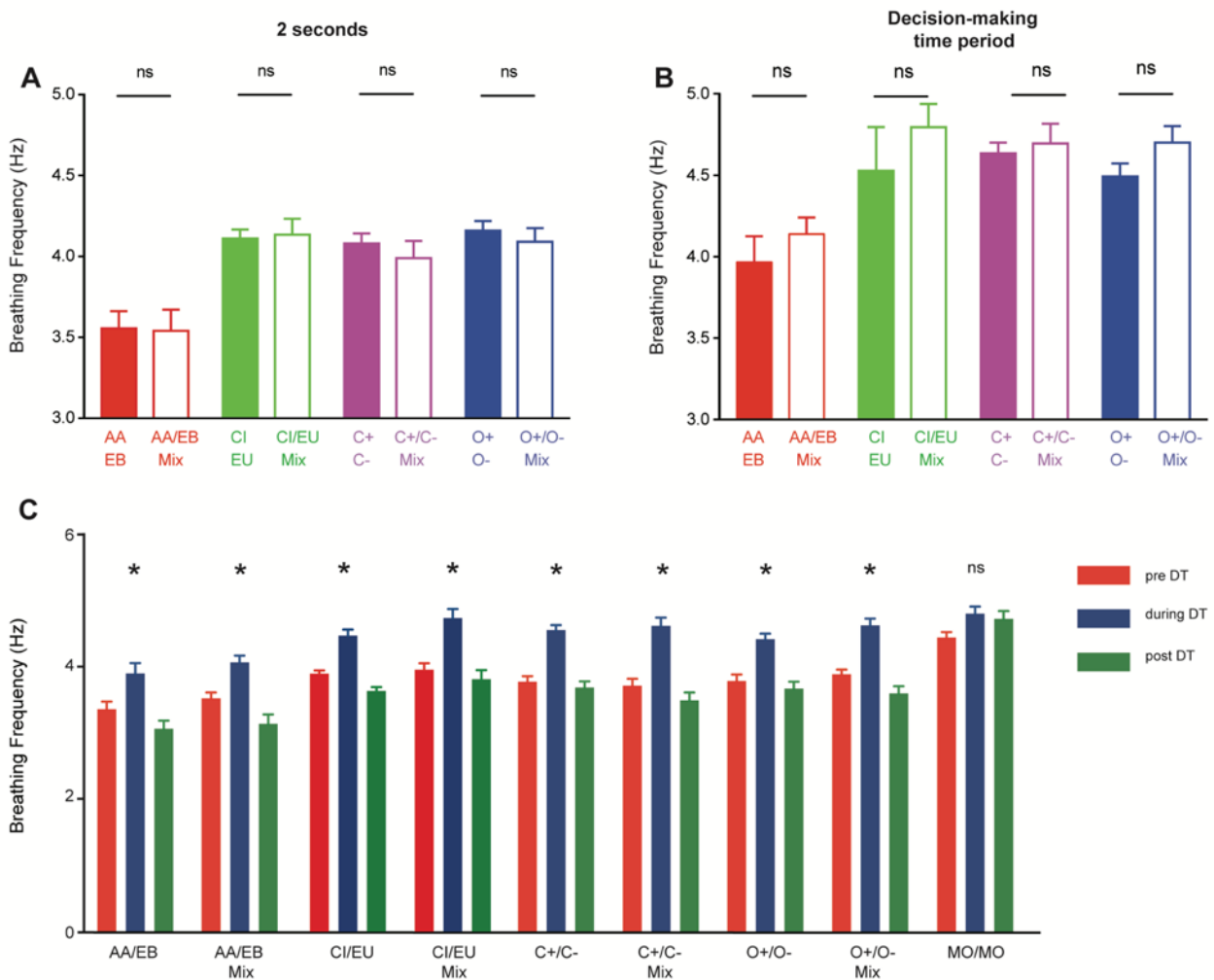
Figure 3-4: Sniffing behavior modulation during decision-making window.

(A) Sniffing frequencies (SFs) were measured during the entire stimulus duration (i.e., for 2 s). We did not observe any difference in SF across the different odor chemical classes. Data are presented here as mean ± SEM. $SF_{AA/EB} = 3.56 \pm 0.1$ Hz, $SF_{AA/EBmix} = 3.54 \pm 0.12$ Hz, $SF_{CI/EU} = 4.11 \pm 0.05$ Hz, $SF_{CI/EUmix} = 4.13 \pm 0.09$ Hz, $SF_{C+/C-} = 4.08 \pm 0.06$ Hz, $SF_{C+/C-mix} = 3.99 \pm 0.1$ Hz, $SF_{O+/O-} = 4.15 \pm 0.06$ Hz, $SF_{O+/O-mix} = 4.09 \pm 0.08$ Hz. Comparison between monomolecular odors and binary mixtures (same odor pairs were used as in Figures 3-1, 3-2 and 3-3, but

behavioral training was done under HR conditions) was done using t-test with Welch's correction; $p > 0.05$ for all odor pairs tested (n = 7 or 8 mice).

(B) No difference in sniffing frequencies was observed during the decision-making window.

The ODTs and corresponding SFs were calculated for each task (300 trials) where learning accuracy was ~80%. Data are presented as mean ± SEM. $SF_{AA/EB} = 3.97 \pm 0.15$ Hz, $SF_{AA/EBmix} = 4.14 \pm 0.1$ Hz, $SF_{CI/EU} = 4.53 \pm 0.1$ Hz, $SF_{CI/EUmix} = 4.79 \pm 0.14$ Hz, $SF_{C+/C-} = 4.63 \pm 0.06$ Hz, $SF_{C+/C-mix} = 4.70 \pm 0.12$ Hz, $SF_{O+/O-} = 4.49 \pm 0.08$ Hz, $SF_{O+/O-mix} = 4.70 \pm 0.1$ Hz. SFs from decision-making periods for monomolecular odors and associated binary mixtures were compared using t-test with Welch's correction, $p > 0.05$ for all odor pairs tested (n = 7 or 8 mice).

(C) SFs calculated during, pre-, and post-decision-making periods.

The SF increased specifically during the decision-making period for different odor pairs tested. *Comparison between pre-, during, and post-decision-making period: one-way ANOVA, $p < 0.05$; n = 7 or 8 mice. For naive mice trained on MO/MO discrimination task, we did not observe any significant differences during the three periods (one-way ANOVA, $p > 0.05$; n = 8 mice).

The average breathing frequency across different odors was 3.9 ± 0.05 Hz during the entire 2 s odor application and 4.5 ± 0.05 Hz during the decision-making period (Figures 3-4 A and B; average ± SEM). Thus, the breathing frequency increased significantly during the decision-making window (Figure 3-4 C; comparison between pre-, during, and post-decision-making periods, one-way ANOVA, $p < 0.05$; n = 7 or 8 mice). To check if this increase in breathing frequency is specific to odor discrimination, we trained another batch of naive mice to MO vs. MO discrimination task. Mineral oil is used as a solvent to dilute odorants for odor discrimination tasks. When breathing frequencies were measured in these mice, we did not observe any instances of stimulus-related increase in frequencies (one-way ANOVA, $p > 0.05$; n = 8 mice). Further, breathing frequencies for monomolecular odorants and associated binary mixtures were found to be similar (t-test with Welch's correction, $p > 0.05$). This suggests that changes in sampling strategies can be confidently eliminated as a mechanism contributing to the increased ODT when discriminating two highly similar stimuli. Lastly, we did not find a difference in sniffing frequencies between different chemical classes except AA/EB monomolecular discrimination (ANOVA, F = 7.62, $p < 0.0001$; Fisher's LSD: comparison of AA/EB and AA/EB 60/40 binary mixture vs. all other chemical classes, both monomolecular and binary mixtures, highest $p < 0.01$). In conclusion, sniffing frequency modulations during odor discrimination occur independently of odor complexity and do not contribute to enhanced ODT observed for binary mixtures compared to monomolecular odorants.
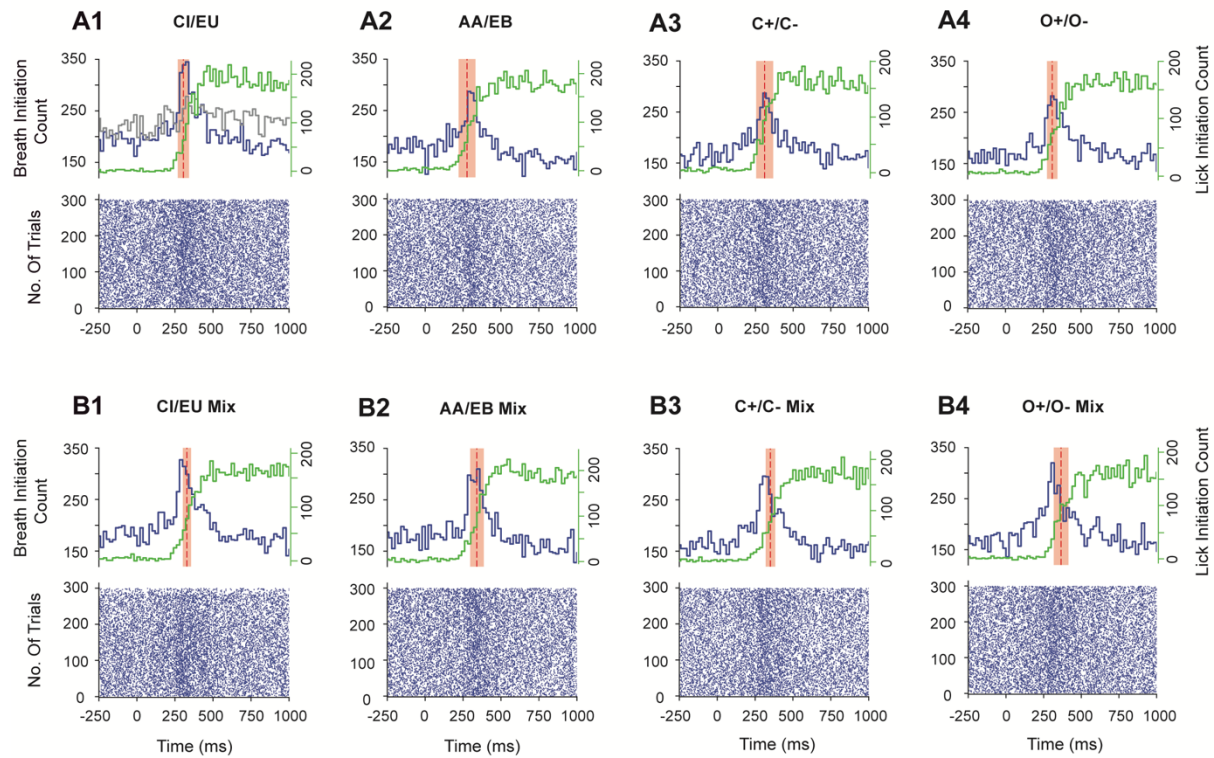
Figure 3-5: Sniffing, licking, decision-making, and ODT under HR conditions.

(A1–B4) The bottom half of each panel (raster plots of A1–B4) shows breathing initiation events of mice during the last 300 trials of training when performance accuracy was ≥80%. The top half of each panel (A1–B4) shows a histogram calculated by averaging data points with 20 ms bin resolution. The red dotted line and shaded region represent the mean ODT ± SD. Histograms for each odor pair have been compared with the histogram obtained from MO vs. MO task, which is shown for comparison in (A1) (gray line). Comparison between odor and MO histograms was made using Kolmogorov-Smirnov (K-S) test (p < 0.0001 for all odor pairs). The licking responses towards different odorants are represented as histogram distribution in green (combined from S+ and S- trials).

3.3.4 Temporal relationship of sniffing and decision-making

On analyzing breathing frequencies throughout 2 s, we observed an increase in frequencies during the decision-making window. To probe the modulatory effect of breathing behavior on decision-making, we looked at inhalation onset incidences during the odor application period (Figure 3-5). By plotting all breath initiation events for the last 300 trials across all mice, a raster graph was plotted for different odor pairs. Each point in the raster was transformed into a histogram with a bin resolution of 20 ms. The breath initiation counts increased consistently for all odor discriminations around 250 ms after odor presentation (Figure 3-5, blue histogram). To identify if this increase in breath initiations is odor dependent, we compared it with a breath initiation histogram recorded from a naive batch of mice trained on MO vs. MO (Figure 3-6 A; ANOVA, F = 1.66, p = 0.16). On comparing the MO vs. MO breath initiation histogram (Figure 3-6 B, gray histogram) with odor discrimination task breath histogram, we observed a significant difference

(Figure 3-6 C; K-S test, p < 0.0001 for all odor pairs), implying that breath synchronization developed when mice were actively discriminating odors. To examine how breath synchronizations evolved during different learning phases, we categorized learning in low to high accuracy blocks (low accuracy blocks - ≤60% accuracy, mid accuracy blocks - 61-79%, high accuracy blocks - ≥80%). To account for differences in the number of trials in different categories, we pooled monomolecular odors and binary mixtures and randomly plotted an equal number of trials. We observed that for a given odor discrimination, in the initial phase of training, when accuracies are low, multiple peaks are seen in the breath initiation count histogram (Figures 3-6 D and E). As the accuracies increase, mice learn to synchronize their breathing during the decision-making window.
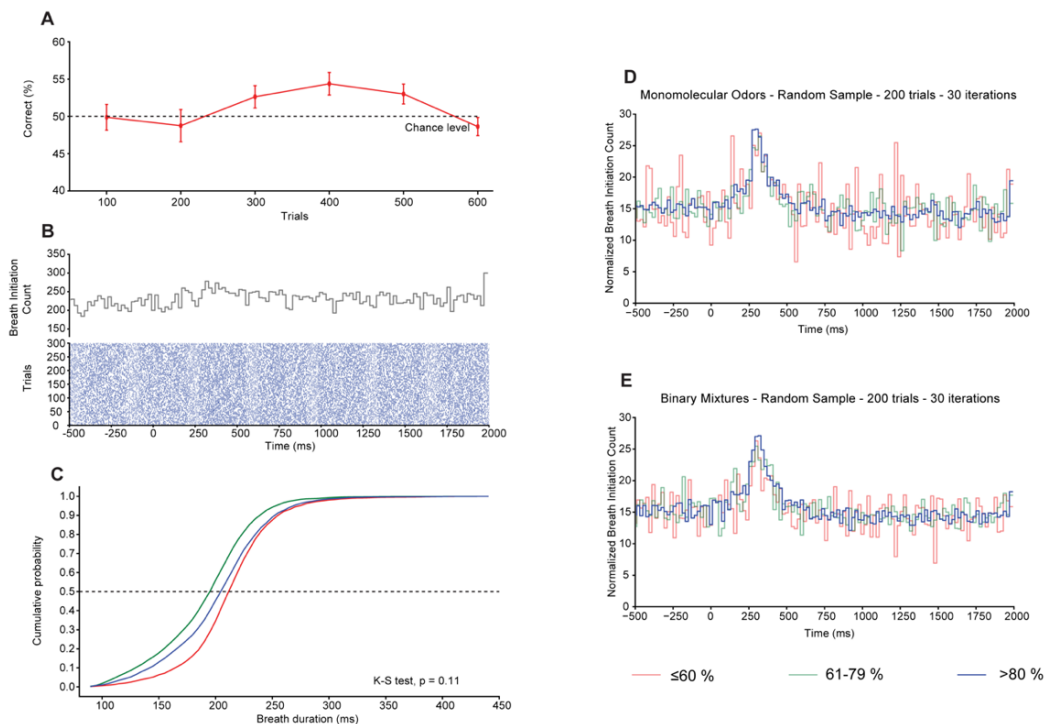
Figure 3-6: Naive mice show no specific sniffing peak but quickly learn to refine their breathing behavior when involved in an odor discrimination task.

(A) Animals showed no learning for a MO vs. MO discrimination task (ANOVA, F = 1.66, p = 0.16). Odor discrimination learning accuracy is shown as percentage correct choices averaged over 100 trials. Each data point is an average of 8 animals. The x-axis reflects a progression of time. Data are presented as mean ± SEM.

(B) Raster plot and histogram calculated and plotted from the last 300 trials of MO vs. MO discrimination task (n = 8 mice).

(C) Cumulative probability distribution plot of breath duration measured for pre- (red), post- (blue), and decision-making period (green). Breath duration remains unaltered during the three phases (K-S test, p = 0.11).

(D and E) Normalized breath initiation histograms for monomolecular odors and binary mixtures. Normalization was done by randomly sampling 200 trials across three different accuracy blocks. The sampling was iterated over 30 times, and histograms for low accuracy (red), mid accuracy (green), and high accuracy (blue) blocks are plotted.

A rapid switch in sniffing behavior can happen in awake animals in anticipation of odor and reward delivery (*285, 286*). We trained another set of mice (n = 8 mice, set 6) to different odor pairs in the absence of tone marking a trial's onset. Without the tone, mice did not have any non-olfactory cues to anticipate the beginning of odor delivery. By analyzing breathing behavior from the last 300 trials, we observed a consistent increase in breath initiation count similar to the previous experiment, which was conducted with tone (Figures 3-7 A1 and A2; a representative figure is shown for one monomolecular odor and a binary mixture). To check whether reward association influences the breathing behavior, we calculated breathing frequencies separately for S+ and S- odors. By pooling all odors, we observed that the breathing frequency was higher for S+ compared to S- odor trials. The increase was evident for the entire duration of odor presentation (Figure 3-7 C1, cumulative probability, K-S test, $p < 0.0001$, n = 64) and during the decision-making window (Figure 3-7 C2, cumulative probability, K-S test, $p < 0.0001$, n = 64). Nevertheless, mice learned to increase their breathing frequency during the decision-making period for both odors independent of reward association (Figures 3-7 B1 and B2; representative breathing raster separately plotted for S+ and S- odors. Figure 3-7 D1 and D2, breathing frequencies calculated during, pre-, and post-decision-making periods for S+ and S- odors. For S+ odors; one-way ANOVA, $p < 0.0001$; For S-odors; one-way ANOVA, $p < 0.0001$; n = 8 mice).
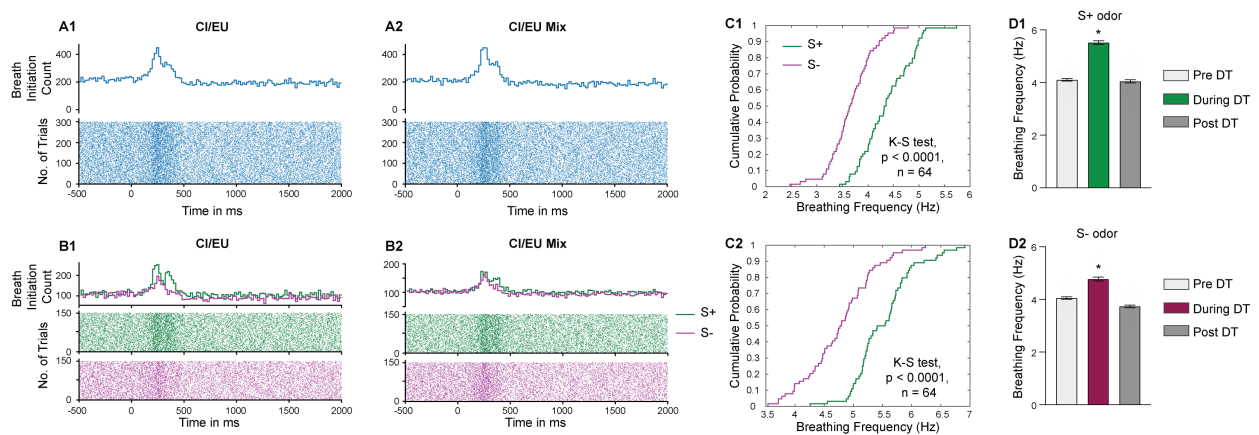
Figure 3-7: Active modulation of breathing behavior during the decision-making window is not due to anticipation of odor or reward.

(A1 and A2). Representative raster and histogram showing the breathing cycle pattern of mice during the last 300 trials of training for CI/EU monomolecular odor and binary mixture discriminations. Odor discrimination training was done in the absence of tone marking the start of a trial.

(B1 and B2). Representative raster and histogram plotted separately for S+ and S- stimulus. For both monomolecular odor and binary mixtures, breathing cycle patterns show increased breath initiation counts for both rewarded and non-rewarded stimuli. Green colored dots and histogram represent rewarded trials and magenta dots and histogram represent non-rewarded trials.

C1. Comparison of sniffing frequency between S+ and S- odor trials during 2 s of odor presentation. The cumulative probability curve was plotted by combining all the odors. K-S test, $p < 0.0001$, n = 64.

C2. Comparison of sniffing frequency between S+ and S- odor trials during the decision-making period. The cumulative probability curve was plotted by combining all the odors. K-S test, p < 0.0001, n = 64.

(D1 and D2). Breathing frequencies were calculated during, pre-, and post-decision-making periods for S+ and S- odors. The breathing frequencies increased specifically during the decision-making window during all S+ and S- odor trials. *Comparison between pre-, during, and post-decision-making period: one-way ANOVA, p < 0.0001; n = 8 mice.

Further, to probe for the temporal relationship between sniffing and licking, we analyzed lick responses towards rewarded and non-rewarded stimuli. The findings show that random lick responses contribute only a small increase prior to the decision-making window while licking frequency peaks after the decision-making window. Thus, there is no obvious temporal relationship between sniffing and licking (Figures 3-5 and 3-8, green histogram; K-S test, p < 0.0001 for all odor pairs).
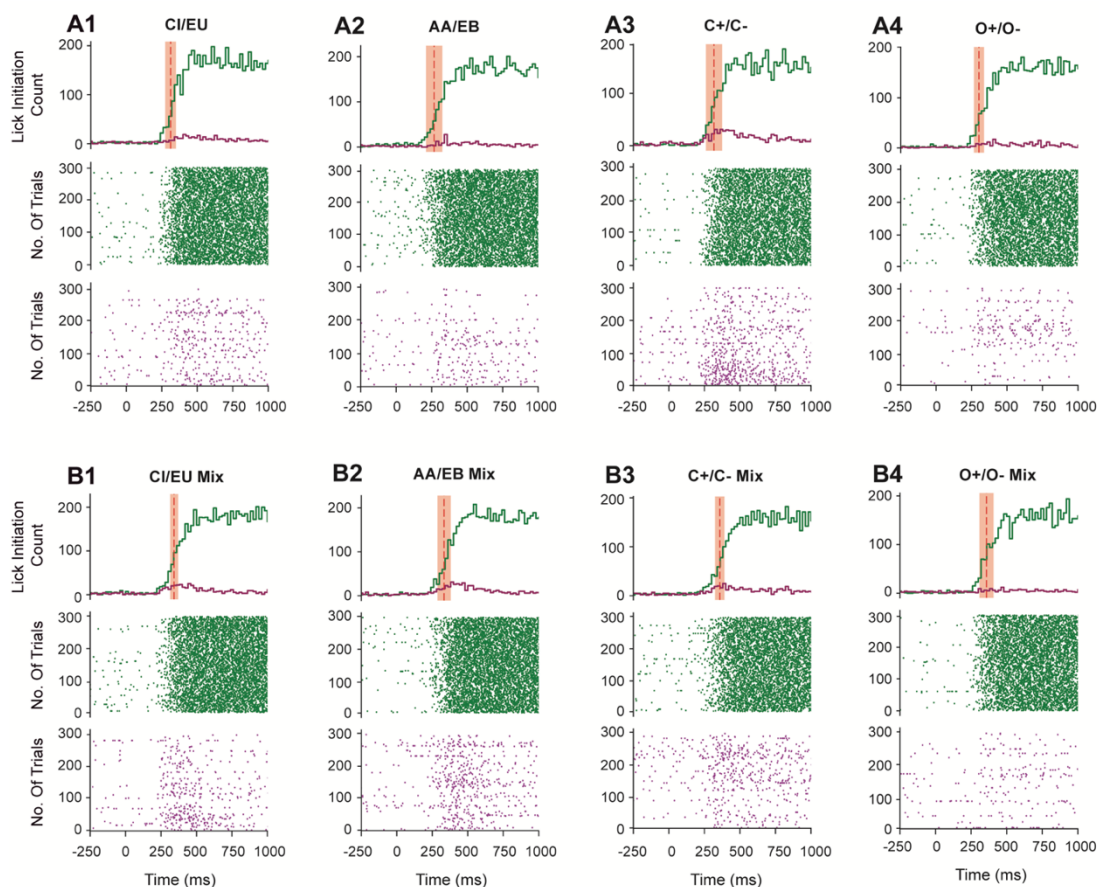
Figure 3-8: Licking behavior of mice towards rewarded and non-rewarded odorants in a discrimination task.

(A1-A4) Lick onset pattern for monomolecular odorants

(B1-B4) Lick onset pattern for binary mixtures. Raster plots (bottom two rows of each panel, A1 – B4, n = 7-8 mice) show lick onset events during the last 300 trials of training across all mice, where performance accuracy was ≥80%. Histograms were (top row of each panel, A1 – B4, n = 7-8 mice) calculated from all trials with a bin resolution of 20 ms. The red dotted line and shaded region represent mean ODT ± SD. Green colored dots and histogram represents lick onset events for rewarded trials, and magenta dots and histogram represent non-rewarded trials. K-S test comparing

Interestingly, breath histograms reveal that breath initiation count peak coincides with the decision-making window for monomolecular odor discriminations and precedes the window for binary mixture discriminations. To investigate this, we analyzed and compared ODTs with sniffing peak latency (SPL) for each task when mice performed with ≥80% accuracy (for all tasks, mice had an overall accuracy ≥80 %. However, for one mouse, in one task of CI/EU he performed with 76% accuracy). For all odor classes, binary mixture ODTs were considerably higher than monomolecular odorants but, the SPL remained unaltered (Figure 3-9 A, comparison between ODTs for monomolecular odors and related binary mixtures, paired t-test, p < 0.05; comparison between SPL for monomolecular odors and related binary mixtures, paired t-test, p > 0.05; Figure 3-9 B, cumulative probability, K-S test, p = 0.8, n = 61). This indicates a substantial shift in ODTs compared to SPL for binary mixtures (Figure 3-9 D, cumulative probability, K-S test, p < 0.05, n = 61) but not for monomolecular odor discriminations (Figure 3-9 C, cumulative probability, K-S test, p = 0.8, n = 61). The difference between SPL to ODT for binary mixtures amounts to ~30 ms
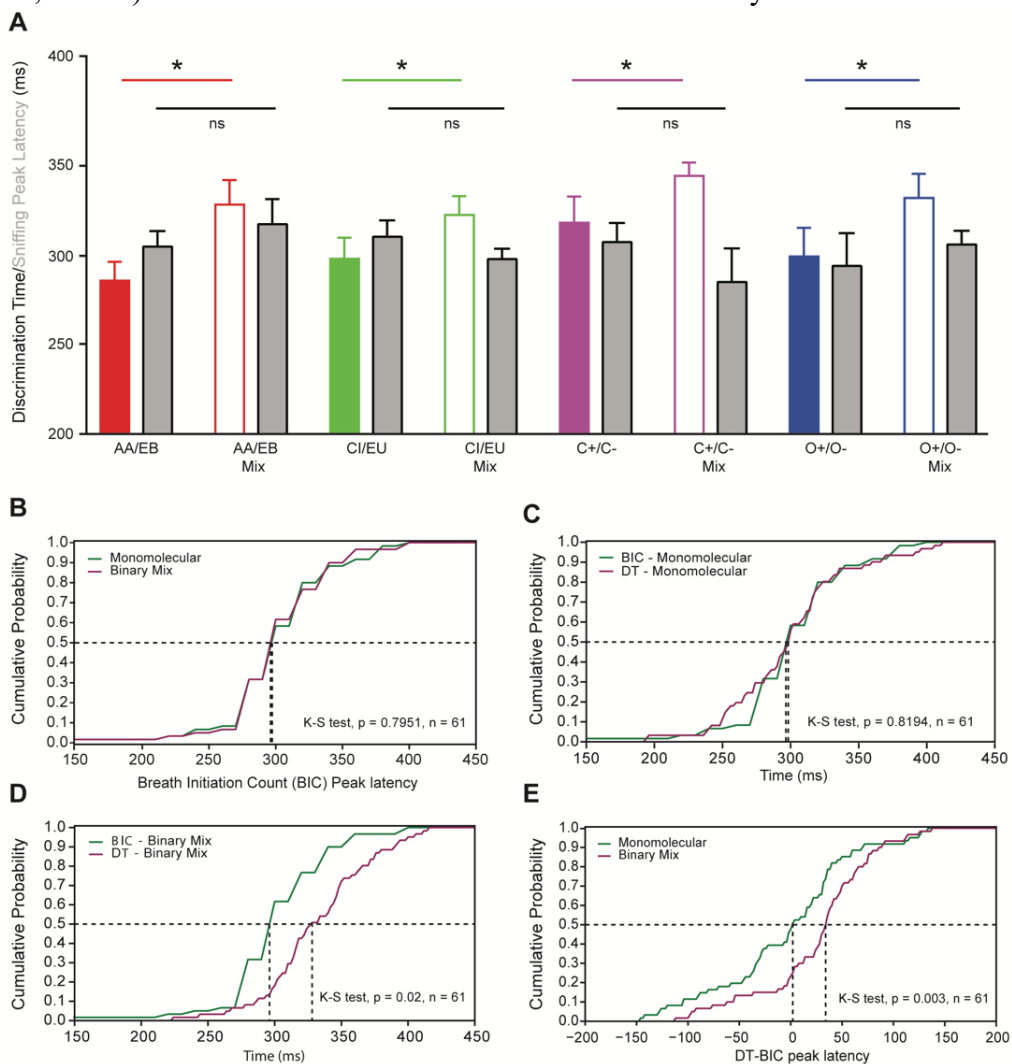
Figure 3-9: Sniff-invariant odor discriminations for odor pairs of varying complexity.

(A) Comparison between ODTs and SPL for odor pairs of varying complexity.

The colored bars (filled – monomolecular odors, and empty – binary mixtures) are for ODTs, and gray bars represent the sniffing peak latency values for the corresponding ODTs. Data are presented as mean ± SEM. $DT_{AA/EB} = 286 \pm 11$ ms, $DT_{AA/EBmix} = 328 \pm 14$ ms, $DT_{CI/EU} = 298 \pm 12$ ms, $DT_{CI/EUmix} = 322 \pm 11$ ms, $DT_{C+/C-} = 318 \pm 15$ ms, $DT_{C+/C-mix} = 344 \pm 7$ ms, $DT_{O+/O-} = 299 \pm 16$ ms, $DT_{O+/O-mix} = 332 \pm 13$ ms, $SPL_{AA/EB} = 305 \pm 9$ ms, $SPL_{AA/EBmix} = 317 \pm 14$ ms, $SPL_{CI/EU} = 310 \pm 9$ ms, $SPL_{CI/EUmix} = 298 \pm 6$ ms, $SPL_{C+/C-} = 307 \pm 11$ ms, $SPL_{C+/C-mix} = 285 \pm 19$ ms, $SPL_{O+/O-} = 294 \pm 18$ ms, $SPL_{O+/O-mix} = 306 \pm 8$ ms. Comparison between ODTs for monomolecular odorants and related binary mixtures; paired t-test, $p < 0.05$. Comparison between sniffing peak latency for monomolecular odors and related binary mixtures; paired t-test, $p > 0.05$.

(B) Comparison of SPL between monomolecular odors and binary mixtures by combining all odor pairs. The SPL frequency distribution is similar for monomolecular odors and binary mixtures (K-S test, $p = 0.8$; $n = 61$).

(C and D) Comparison of cumulative probability distributions between ODT and SPL for monomolecular odors and binary mixtures. There is a significant shift in the distribution corresponding to the added time required to discriminate binary mixtures (compared with SPL, D; K-S test, $p = 0.02$; $n = 61$), but the cumulative distribution of ODTs and SPL remains unaltered for monomolecular odors (C; K-S test, $p = 0.82$; $n = 61$).

(E) The difference between SPLs and ODTs for monomolecular odors and binary mixtures represented by cumulative probability distributions. The difference is greater for binary mixtures compared with monomolecular odors (K-S test, $p = 0.003$; $n = 61$).

(Figure 3-9 E, cumulative probability, K-S test, $p < 0.01$, $n = 61$). The extra time needed to initiate a lick response for binary mixture discrimination could indicate the additional time required for OB circuitry to refine odor representations. In our task paradigm, we did not set any rules over the sampling behavior of mice. This meant that they could smell different odors according to their individual sniffing strategies. Due to this relaxed rule, first inhalation latencies ranged from 1 ms to almost the duration of one breathing cycle across different trials. Hence, we measured task-wise medians of first inhalation latencies for different odors, and these vary in the range of 100–200 ms. On a population level, first breath onset latencies were found to be similar for monomolecular odors and binary mixtures (Figure 3-10 A, cumulative probability, K-S test, $p = 0.929$, $n = 61$). For each task, we recalculated ODTs by correcting for first breath latencies. The recalculation again yielded longer ODTs for binary mixtures compared to monomolecular odors, corresponding to the time specifically required for complex odor discriminations (Figure 3-10 B, cumulative probability, K-S test, $p = 0.002$, $n = 61$).
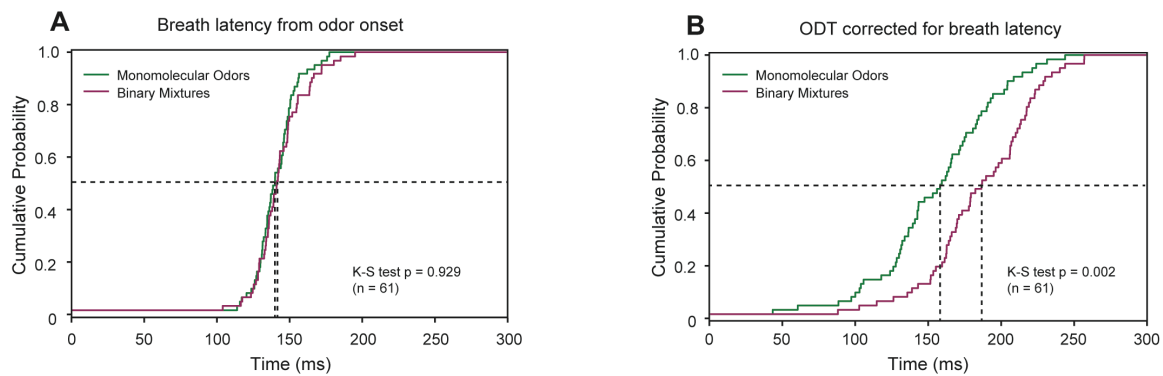
Figure 3-10: Reaction time differences between simple and complex odors are independent of first breath onset delays.

(A) Comparison between first breath onset delays between monomolecular odors and binary mixtures.

(B) Corrected ODT measurements after subtracting the first breath onset delay. Mice showed longer ODTs for binary mixtures than monomolecular odors.

3.3.5 The odor discrimination time is correlated to the similarity and strength of odor-evoked glomerular activity patterns

Our findings show that variations in ODT between monomolecular odorants and their binary mixtures are not due to sampling behavior. Can the increased ODT be related to neural processing mechanisms in the olfactory system? Odors are first represented in the olfactory system as glomerular activity patterns. Thus, we probed if the pattern of glomerular activity with respect to number and activation strength correlates with ODT. We used IOS imaging to visualize glomerular activities in anesthetized mice for all odors used for discrimination tasks (Figure 3-11 A). We calculated the Euclidean distance to measure the similarity between odor-evoked glomerular activity patterns. Across different odor pairs tested, odor-evoked glomerular activities were more overlapping for binary mixtures compared to monomolecular odors as calculated from the Euclidean distance (Figure 3-11 B; paired t-test, $p < 0.0005$; n = 5 mice). Amongst the monomolecular odors, carvones and octanols enantiomers evoked very similar glomerular activities compared to other odors (paired t-test, $p = 0.1$; n = 5 mice). The similarity in activated patterns reflected the longer ODT consumed for these odors during odor discrimination tasks. Overall, the high correlation between Euclidean distance measurements and corresponding ODTs establishes a robust relationship between glomerular activity patterns and discrimination times for monomolecular odors and binary mixtures. A strong negative correlation (Figure 3-11 C; $R^2 = 0.96$; ANOVA, $p < 1 \times 10^{-12}$) suggests that the time required for odor discrimination is based on the overlap observed for odor-evoked patterns of glomerular activity.
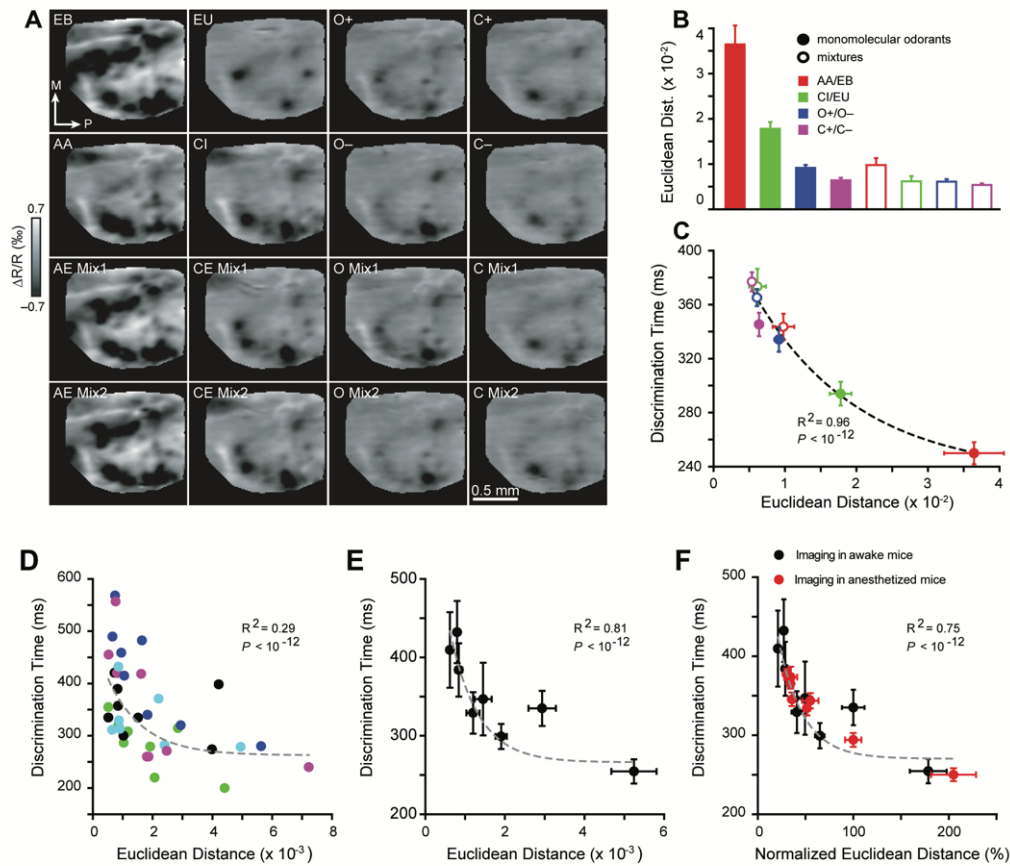
Figure 3-11: The Euclidean distance measured for odor-evoked glomerular activity maps in naive and awake trained mice correlates with the corresponding ODT measured for different odors.

(A) The glomerular activity maps imaged for four pairs of monomolecular odors and related binary mixtures using IOS.

(B) ED measured for glomerular activity patterns evoked by different odor pairs (comparison of monomolecular odorants with binary mixtures: paired t-test, p < 0.0005, n = 5 mice).

(C) ODT measured for monomolecular odorants and binary mixtures are plotted as a function of ED for different odor pairs. Data were best fitted with a single exponential function ($R^2 = 0.96$, ANOVA, $p < 1 \times 10^{-12}$) (see materials and methods).

(D) ODTs measured during different discrimination tasks (10^{-6} IAA vs. 10^{-6} EB, 10^{-4} IAA vs. 10^{-4} EB, 10^{-2} IAA vs. 10^{-2} EB, 10^0 IAA vs. 10^0 EB, 10^{-3} CI vs. 10^{-3} EU, 10^{-2} CI vs. 10^{-2} EU, 10^{-1} CI vs. 10^{-1} EU, 10^0 CI vs. 10^0 EU) are plotted against Euclidean distances measured for corresponding odor pairs for individual mice ($R^2 = 0.29$, ANOVA, $p < 1 \times 10^{-12}$). The high odor dilutions generated sparse representations in OB. Filled color bars indicate data collected from monomolecular odors, while empty bars correspond to binary mixtures for each individual mouse (n = 5).

(E) The correlation between ODTs and ED averaged across mice ($R^2 = 0.81$, ANOVA, $p < 1 \times 10^{-12}$, n = 5 mice).

(F) ODTs measured for different odor pairs are plotted as a function of normalized ED, from both awake and anesthetized mice (normalized to 1% CI vs. EU, the common odor pair for both sets of experiments, $R^2 = 0.75$, $p < 1 \times 10^{-12}$, n = 10 mice). Data are presented as mean ± SEM.

As we measured Euclidean distances for different odors in untrained anesthetized mice, we further tested if odor discrimination training influences this correlation. This is particularly

important as ODTs are generally measured when animals achieve high learning accuracies. Further, activation of a few glomeruli can assist mice in detecting and discriminating odorants (*254*). Therefore, we decided to test the discrimination abilities of mice across a wide range of odor concentrations designed to activate different numbers of glomerular units. We trained naive mice on different dilutions of CI/EU and IAA/EB ranging from 10^0 to 10^{-10}. At the lowest concentration, these odors activated one or two glomeruli on the dorsal surface of OB. The training commenced from the lowest concentration for both odors. Mice started to learn to discriminate between the odors from 10^{-3} odor dilution of CI/EU and 10^{-6} odor dilution of IAA/EB. Once mice reached threshold accuracies, we acquired IOS images and measured the ODT for each dilution. We observed a negative correlation between the measured Euclidean distances and ODT on a single animal basis (Figure 3-11 D; $R^2 = 0.29$; ANOVA, $p < 1 \times 10^{-12}$) and when averaged across all mice used for imaging (Figure 3-11 E; $R^2 = 0.81$; ANOVA, $p < 1 \times 10^{-12}$). To substantiate the Euclidean distance measurements done under anesthetized and awake conditions, we normalized the measurements to a common odor pair 1% CI vs. EU. The negative correlation between Euclidean distances and ODTs occurred regardless of whether the imaging was performed in an anesthetized or awake state (Figure 3-11 F; $R^2 = 0.75$; $p < 1 \times 10^{-12}$). These results indicate that the glomerular activity map similarity measured by Euclidean distance can accurately predict the time required for odor discrimination.

3.4 Discussion

In this study, using odorants of varying physico-chemical properties, we show that mice take additional time to discriminate binary mixtures compared to monomolecular odors accurately. The sniff-invariant time taken by mice to discriminate between two odors is defined by the degree of similarity as well as the number and strength of glomerular representations in OB. Further, Euclidean distances measured between activated glomerular patterns established a metric to define odor pair specific ODTs. For odors evoking similar glomerular activity patterns, we predict an upper threshold limit of ~400–500 ms for the ODTs. This indicates that investing more time in sampling the odor may not improve discrimination performance. Overall, a time difference of 100-150 ms was observed when comparing monomolecular odors with shortest and longest discrimination times or when comparing monomolecular odors and their associated binary mixtures. This difference alludes to the time needed to refine and integrate odor representations for complete percept formation, facilitating accurate odor discriminations. Interestingly, this processing time is independent of the sampling behavior for different odors. However, within a trial, mice learn to increase their sniffing frequencies independently of stimulus complexities

during the decision-making window. The results establish a neural metric of odor reaction time and define the temporal window for olfactory information processing while mice are involved in sniff-invariant decision-making.

3.4.1 Stimulus-dependent odor discrimination times

The stimulus dependency of odor reaction times remains an intensely debated topic (*22, 23, 27–31, 287–289*). Using GNG behavioral paradigm, ODTs were determined for different odors. The ODTs varied in a stimulus-specific manner, with esters being discriminated considerably faster compared to enantiomers. The odor discrimination times or sampling times have been found to be malleable to multiple factors like reinforcement structure and motivation in decision tasks (*290*). The ITI is a parameter that indicates the urgency of animals to initiate the next trial. Animals had identical ITIs for all odor pairs, indicating that their motivational states had little effect on the variations in ODTs. The behavioral experiments under FM and HR conditions differ in motor responses shown by mice towards rewarded and non-rewarded odors. Discrimination times were measured in an FM behavioral task by comparing odor sampling patterns towards rewarded and non-rewarded odors. In contrast, for behavioral experiments under HR conditions, a difference in licking response towards rewarded and non-rewarded odors is used to calculate ODTs. Even with differences in motor response, our results show similar ODTs across FM and HR behavioral experiments. Further, in both experiments, mice were given the liberty to initiate a lick response within 1000 ms of odor presentation, allowing ample time to respond. Hence, our ODT measurements are not affected by the influence of urgency during decision-making.

3.4.2 Speed-accuracy tradeoff in olfaction

Previously, studies reporting odor reaction times have argued both for and against stimulus-dependent changes in odor sampling times. The speed-accuracy tradeoff concept in olfactory decision-making was recently challenged (30). Studying rats performing an odor categorization task, it was observed that accuracy improved with stimulus sampling time in a finite time window independent of the task complexity. Intriguingly, a difference of 30 ms was observed between the easiest and the most difficult mixture of octanol enantiomer pairs. In the paradigm we propose here, using different classes of olfactory stimuli, we observed a similar difference of ~30 ms in discrimination time between the monomolecular pairs and corresponding binary mixtures of enantiomers, revealing the time-window of olfactory information processing needed to make odor discrimination. In the study reported by Zariwala et al., 2013 (30), results were based on a binary mixture of a single odor pair of octanols. The use of a single odor pair limits the conclusion on the

existence of a speed-accuracy tradeoff in olfaction. Our study overcomes this limitation by demonstrating stimulus-dependent ODTs across different odor classes. In another recent study, results indicate that animals make speed-accuracy tradeoffs in odor-guided decision-making tasks when the task difficulty is increased either by lowering stimulus concentration or by introducing difficult odor mixtures (*291*). With these findings, there is enough evidence to conclude that odor reaction times in olfaction are stimulus complexity dependent.

3.4.3 Sniff-invariant olfactory decisions

Rodents adjust their breathing behavior under different contexts as a strategy to collect maximum information for better odor discrimination. They show an increase in their breathing frequency when investigating a novel odor source or when involved in an odor operant task (*275*). The behavioral context in which animals are challenged determines the degree of such a change in sniff frequency. In a Two-Alternative Choice task, animals realize the possibility to receive a reward for all trials on performing the task accurately. In such a task, the transition in sniffing frequency is possibly driven by odor anticipation as animals enter into the odor-sampling port or by an expectation to obtain a reward (*285*). In the GNG paradigm, we observed that mice increase their sniffing frequency while making decisions, and then sniffing frequency returns to baseline (Figures 3-5 and 3-7). On comparing sniffing frequencies for S+ vs. S- odor trials, we observed increased sniffing frequencies during S+ odor presentation. The licking responses during S+ odor presentation may be one reason for increased sniffing frequency for S+ trials compared to S-trials. Further in-depth studies are needed to determine factors that influence sniffing behavior. However, synchronization of breathing during the decision-making window was not driven by odor or reward anticipation. The modulation of sniffing was invariant of the chemical class of odors, and in the absence of odor discrimination, sniff modulations did not occur (Figure 3-6). Thus, ODT for odors of varying similarity is independent of the sniffing behavior and places our result in agreement with a growing consensus of sniff independent odor coding in rodents (*274, 280, 292*).

3.4.4 Determinants of the olfactory system governing discrimination time

The odor reaction time includes the time required for odor plumes to travel across the olfactory epithelium to bind onto odor receptors, odor processing in OB and olfactory cortical areas, decision-making, and execution of motor output. Although it is difficult to define the time required for each of these steps, odor-specific differences in ODT can arise from any single or combination of these steps. Although we used odors varying in their physicochemical properties, our results prove that animals' sniffing behavior is not correlated with ODT differences between

monomolecular odors and binary mixtures (Figures 3-9 and 3-10). Hence, investigating odor sampling behavior in combination with ODT allowed us to precisely identify the time exclusively required for olfactory processing, as depicted in Figure 3-12. In the breath histogram example of AA vs. EB mixture (60/40) discrimination, breath initiations begin to rise at 250 ms and reach the peak around 280-300 ms. Considering that signal transduction in OSNs could start as late as the breath initiation curve peak (~280 ms), the time difference between monomolecular odor and binary mixtures ODTs (~290 ms for AA vs. EB to ~350 ms for Carvones mix; see Figure 3-10) stipulates the time needed to complete (1) odorant representation in OB and other olfactory cortical centers, (2) decision-making, and (3) execution of motor response. In that scenario, from the point of BIC rise, monomolecular discriminations take ~10–40 ms, and binary mixture discriminations need an additional 60–70 ms to attain high accuracy in odor discrimination tasks. Although it is hard to ascertain the time frame for different processes, subtracting the extreme ODT values provide the time exclusively needed for odor processing in OB and higher olfactory centers while discriminating complex stimuli. Based on the previous reports (*14, 27*), we predict that the bulk of this time is consumed by feed-forward and reciprocal inhibitory activities in OB. As a result, this means that processing in olfactory cortical areas happens on very short timescales. To conclude, the results indicate that odor representations are formed and refined in OB on a fast timescale ranging from 10-70 ms, consistent with a previous report (*25*).
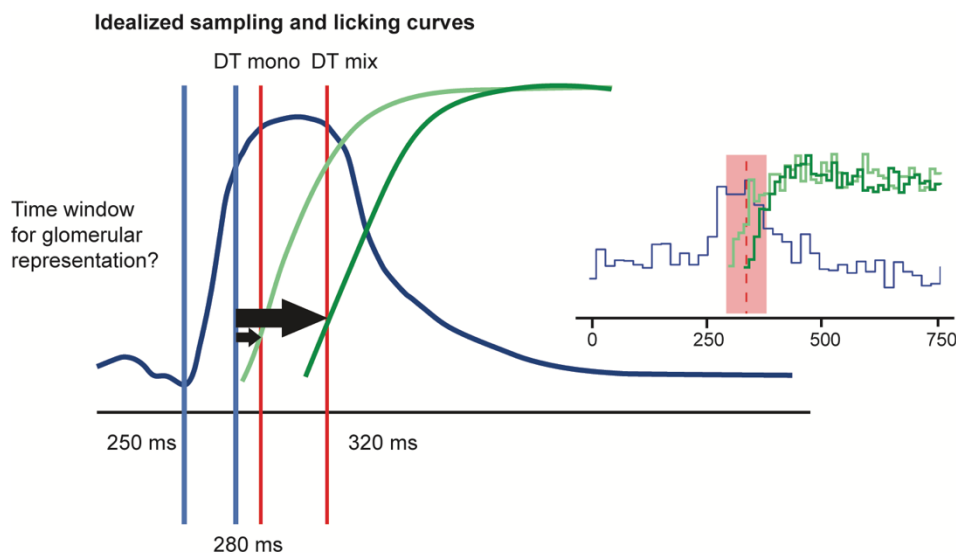
Figure 3-12: Odor discrimination on a fast timescale is supported by sniffing and licking behavior.
An idealized sniffing curve derived from breath initiations (blue curve) and lick curves for monomolecular odors and binary mixtures (light and dark green curves, respectively). The first vertical blue line demarcates the time of sniffing increase, and the second line delineates the time for the sniffing curve to the peak. The red vertical lines depict monomolecular odor and binary mixtures ODT. The black arrows illustrate the times needed for odor representations to be formed and refined in OB, assuming that odor has activated OSNs latest by the time of peak sampling. The small black arrow illustrates a very brief decision-making time window for discriminating monomolecular odors (~10 ms),

while the large black arrow represents the increased time window for discriminating binary mixtures (~30 ms). Finally, the time difference between the two arrows reflects only odor processing in OB and downstream olfactory regions since other processes like motor initiation, programming, and execution should be identical for all tasks, regardless of task complexity.

3.4.5 A neural metric based on glomerular map similarity predicts ODT

The similarity of odor-evoked glomerular activity maps determines how two similar odorants are perceived. For different odors in our experiments, we used IOS imaging to record glomerular activity patterns formed on the dorsal surface of OB in awake and anesthetized mice. The similarity between glomerular activity patterns was quantified by measuring Euclidean distances (less distance reflects high similarity). This parameter reflects both geometrical distributions and the number and activation strength of patterns of glomerular activity. For different odor pairs used in this study, we observed that ODT differences lay within a range of up to 150 ms (Figure 3-11 C). Based on behavioral ODT measurements and patterns of glomerular activities, we introduce a neural metric, which describes an inverse relation between ODT and Euclidean distances measured for activity patterns (Figure 3-11 F). To test if the olfactory metric also applies to odors eliciting sparse glomerular patterns, we used diluted odorants activating only a few glomeruli. Even with these sparse odor representations, mice learned the discrimination task, and the measured ODTs were inversely correlated with Euclidean distance measurements (Figure 3-11 D). Thus, the findings validate the neural olfactory metric that was implemented.

The increase in ODTs between binary mixtures and monomolecular odors was negatively correlated to the monomolecular ODT. Thus, the added time consumed for ODTs was more considerable for binary mixtures whose monomolecular components evoked dissimilar glomerular responses and were discriminated on a fast time scale (e.g., AA/EB). Alternatively, the increase in ODT was smaller for those odorant pairs that evoked highly similar maps (e.g., C+/C-) (Figure 3-3). This result can seem implausible at first glance, but monomolecular odors, such as enantiomers, that elicit similar glomerular activity patterns require long discrimination times, and a small increase in the glomerular map similarity of associated binary mixtures will slightly increase the ODT. Subsequently, one can estimate an ODT of ~400–500 ms for odors activating identical glomerular patterns with small Euclidean distances (Figure 3-11 C). Within this time window, the olfactory system can make highly accurate decisions. For odor discrimination with many components such as white odors (*293*), the olfactory circuitry may fail to decorrelate activity patterns within the maximal ODT window. In such situations, behavioral responses are initiated on incomplete percepts, leading to more wrong decisions. Functionally, the upper threshold limit of

ODT may reflect a maximum processing time allotted towards neuronal mechanisms of pattern formation and decorrelation in OB and higher olfactory cortical areas before committing a decision.

3.5 Future direction

One of the significant accomplishments of this work has been establishing a metric correlating glomerular activity map with ODTs. Although we used a panel of 16 odor pairs across different chemical classes, this falls short of the vast number of odors rodent olfactory system can detect and discriminate. To get around this constraint, an ideal situation would be to conduct chronic imaging of glomerular activity with a wide repertoire of odors and assess the corresponding ODTs. Patterned stimulation of discrete sets of glomeruli using optogenetics can create synthetic odor representations (*254*, *255*, *294*). Even though such artificial stimulation may not capture the full complexity of odor-evoked glomerular maps, this approach nevertheless offers a well-controlled method to precisely modulate odor maps and can be used to establish basic principles of the olfactory code.

CHAPTER 4

Post-odor neural activities in the olfactory bulb control long-term memory formation

4.1 Introduction

When sensory systems are presented with a stimulus, neural representations are formed that dynamically change over time. These representations can persist for several seconds after stimulus cessation and are referred to as post-stimulus neural activity. Post-stimulus activities have been studied in many sensory systems, including mammalian olfaction (*33–39*, *295*). The maintenance of post-stimulus activities depends either on intrinsic neuronal properties or on neural circuit connectivity (*296*). Even though these experiments have revealed features of post-stimulus responses, the physiological significance of such persistent post-stimulus activities is yet unknown.

In mammalian olfaction, MTCs receive odor-specific information from OSNs and transmit it to different olfactory cortical areas. MTC responses are dynamically modulated by inhibition from juxtaglomerular interneurons and lateral or dendro-dendritic inhibition in EPL and GCL (*156*, *282*, *297*, *298*). The reformatting of MTC ensemble activities helps separate overlapping odor inputs during odor discrimination learning, allowing animals to discriminate similar odors (*14*, *20*). MTC odor responsiveness is not limited to the odor presentation period but persists even after cessation of the stimulus. Population analysis reveals that post-odor MTC responses are stimulus duration-dependent and are speculated to be primarily maintained by centrifugal inputs from the cortex (*33*, *34*). However, it's still unclear whether prolonged odor-induced MTC spiking activities facilitate olfactory-guided behavior. We hypothesized that sustained post-odor MTC activities might be a mechanism for regulating memory formation by strengthening odor representations as a function of time.

To investigate the relevance of stimulus and post-stimulus MTC activities in odor discrimination learning and long-term memory formation, we first trained mice to discriminate odorants of varying complexities by presenting stimuli for different durations. We found that reducing stimulus duration for complex odor stimuli led to impairment in odor discrimination learning and long-term memory formation. Microendoscopic imaging of GCL interneuron activities in awake and anesthetized mice revealed stimulus duration-dependent differences in interneuron activity. These differences, in part, can influence the firing activities of MTC ensembles during the stimulus and post-stimulus periods. We further developed a framework to manipulate stimulus and post-stimulus OB representations optogenetically and compared the

effects of these modulations on olfactory learning and long-term memory formation. Specifically, optogenetic modulation of OB inhibitory circuits proved that MTC spiking during odor stimulus controls discrimination learning while the information encoded by post-stimulus MTC spiking influences long-term memory formation. In conclusion, our results direct towards a novel mechanism for olfactory long-term memory formation, which depends on spiking activities of MTCs during the post-odor period.

4.2 Materials and methods

4.2.1 Animals used

Male C57BL6/J mice were used in behavioral experiments under FM conditions. Mice were 6-8 weeks at the beginning of behavioral experiments. For optogenetic experiments under HR conditions, B6N.Cg-Gad2$^{tm2(cre)Zjh}$/J line was crossed with B6.Cg-Gt(ROSA)$^{26Sortm32(CAGCOP4*H134R/EYFP)Hze}$/J or B6.129SGt(ROSA)$^{26Sortm35.1(CAGaop3/GFP)Hze}$/J (The Jackson Laboratory) line to express ChR2 and Arch specifically in GAD2 (GAD65) positive cells. For GCL Ca^{2+} imaging, B6N.Cg-Gad2$^{tm2(cre)Zjh}$/J line was crossed with B6.129SGt(ROSA)$^{26Sortm95.1(CAGGCaMP6f)Hze}$/J for expression of GCaMP6f in GAD65 positive cells (Figure 4-1).
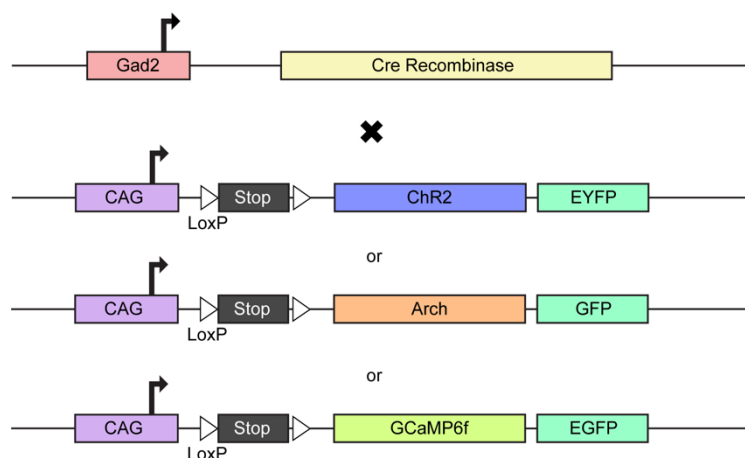
Figure 4-1: Schema of genetic crosses used for experiments.
Homozygous GAD65-Cre mice were crossed with homozygous loxP-flanked mouse lines to attain a stable expression of ChR2, Arch, and GCaMP6f in GAD65 +ve neurons in different sets of animals.

4.2.2 Genotyping details

The GAD65-cre, ChR2-floxed, Arch-floxed, and GCaMP6f-floxed mice were maintained in homozygous conditions (as advised by Jackson Laboratories). Primer sequences for the mouse lines mentioned above were obtained from the Jackson Laboratories website and used for genotyping. Tail clips (2-3 mm in length) were collected from young mice (during weaning) for

genotyping, and homozygous mice were set for breeding. The F1 generation was genotyped, and one mouse from each litter was phenotyped to check for ChR2, Arch, and GCaMP6f expression by visualizing fluorescent signal under Leica SP8 confocal microscope.

For genotyping, we isolated DNA from tissue using the KAPA Express Extract Kit (Kapa Biosystems), as recommended by Jackson Laboratories. We then used the KAPA2G Fast Genotyping Mix for setting PCR reactions (Kapa Biosystems).

4.2.3 Gel electrophoresis

2% agarose gel was prepared in standard TAE (Tris base, acetic acid, and EDTA) buffer. Each well of the gel was loaded with PCR product (14 µl) + loading dye (6x, 1 µl). 3-4 µL DNA ladder, with 100 base pair (bp) separation, was loaded into one of the wells. Since expected bands were far apart, operating the power unit at 100-120V for about 30-45 mins resolved the bands.

4.2.4 Phenotyping details

GAD65-Cre mice were crossed with either ChR2-floxed or Arch-floxed mice, and one mouse from F1 generation was phenotyped for ChR2 or Arch protein expression in GAD65 +ve cells. Essentially, the brain was dissected following transcardial perfusion with 4% paraformaldehyde (PFA) in a 0.1 M phosphate buffer (PBS) (First, chilled PBS was injected throughout the system to flush out the blood. Then, 4% PFA was injected to fix the tissue). The dissected brain was stored overnight in 4% PFA for further fixation. The following day, the tissue was embedded into 2% low melting agarose (LMA, Sigma), and 50 µm free-floating coronal sections were taken using a vibratome (Leica VT 1200S). The sections were stained with DAPI (Sigma, 1:500), and confocal images were acquired to confirm the expression of ChR2 or Arch protein in GAD65 +ve neurons in OB (Figure 4-2 A1 and A2).

To check the expression of GCaMP6f, adult GAD65-GCaMP6f mice were perfused with 20 ml chilled Dulbecco's phosphate-buffered saline (DPBS), followed by fixing the tissue with 4% PFA. The saturating concentration of Ca^{2+} (0.9 mM) in DPBS enhances the fluorescence of GCaMP6f (*299*). After perfusion, the dissected brain was stored overnight in 4% PFA. Next, it was embedded in 2% low melting agarose in DPBS and cut into 50 µm free-floating coronal sections using a vibratome. To check co-localization with nuclei, sections were stained with 4',6-diamidino-2-phenylindole (DAPI) (Sigma, 1:500). Confocal images were acquired to confirm the expression of GCaMP6f in GAD65 +ve neurons in OB (Figure 4-2 B1 and B2).
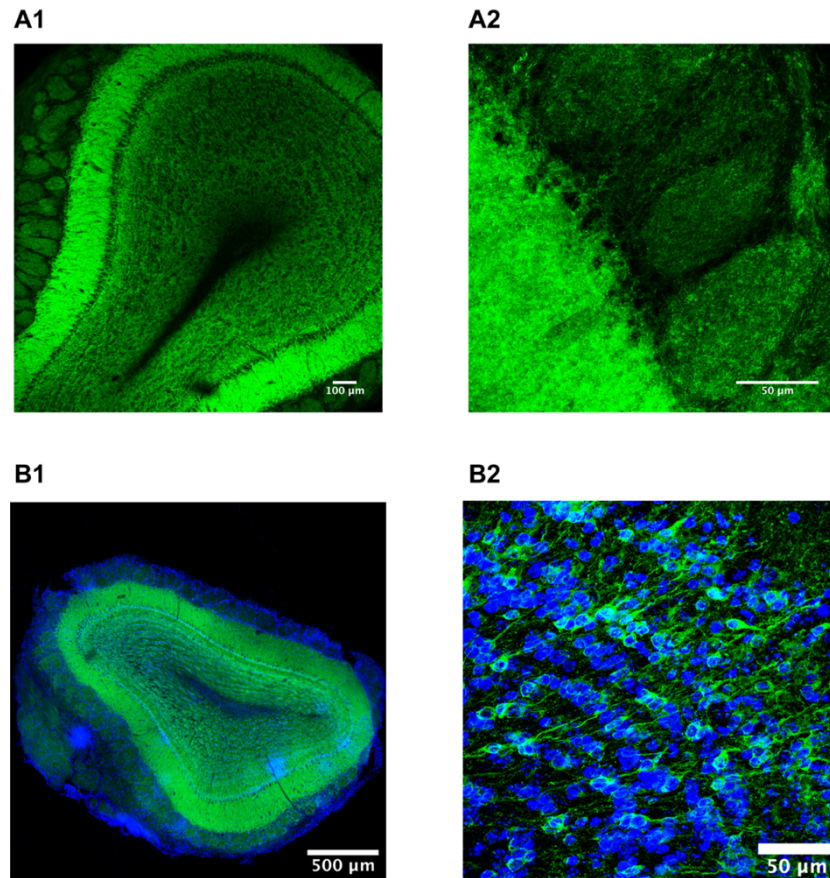
Figure 4-2: Specific expression of transgenes in GAD65 +ve interneurons.

A1 and A2. Example images of opsin expression in GAD65 +ve interneurons across different layers of OB.

B1. Example image of GAD65 +ve interneurons in OB expressing GCaMP6f. Cell nuclei are stained with DAPI (blue).

B2. GCaMP6f expression in GAD65 interneurons (green) in GCL.

4.2.5 Training schemes for behavioral training under FM conditions

For behavioral training under FM conditions, mice (n = 21, divided into three groups containing seven mice) were trained on different stimuli duration (Figure 4-6 A). Irrespective of the stimulus duration, odor concentration was maintained at 1%. Odors were freshly prepared after each task (300 trials). Initially, mice were trained to discriminate AA vs. EB monomolecular odor to make them aware of the procedural rules of the task. For this experiment, stimulus duration was kept at 2 s across the groups. Because training parameters were kept constant, it allowed us to detect any cohort-specific differences in their olfactory abilities. Next, mice were trained to HX vs. PN monomolecular odor discrimination followed by binary mixture (60/40 mix) discrimination of three odor pairs (HX/PN, C+/C-, O+/O-).

4.2.6 Olfactory memory assessment

Once mice had attained maximal learning accuracy, they performed a partial reinforcement task that incorporated partial reinforcement theory guidelines. This task was carried out immediately following the completion of odor pair discrimination training. The partial reinforcement task helps to stabilize the reward association for a corresponding odor in a specific pair. This task comprised of 100 trials with 50 trials for S+ and S- odor each, and only 50% of S+ trials were reinforced. This was unlike the normal training paradigm in which each S+ trial is reinforced if performed correctly. The combination of reinforced and unreinforced trials increased the attention of mice. This is mainly due to the fact that the results of trials are unexpected for mice. The uncertainty introduced by the task in obtaining reward increases the association strength and allows memory to be more persistent (*300*). The long-term odor memory was checked for each odor pair one month post the partial reinforcement task. Before commencing the memory task, mice were trained to an unrelated odor pair of CI vs. EU until they reached high accuracy. This odor pair served as a background for memory assessment. The memory task was carried out once the CI vs. EU odor pair discrimination accuracy was consistently over 90% across all mice in the experimental set. The memory task comprised of 200 trials. In the first three blocks of 20 trials each, the background odor pair of CI vs. EU was presented. These trials allowed us to estimate the motivation levels of mice. In the following blocks of trials, odors whose memory was to be ascertained were interleaved (2 S+ and 2 S- trials) in each block of 20 trials of the background odor pair. In total, 14 S+ and 14 S- memory trials were presented across seven blocks of trials. None of the memory trials were rewarded. We monitored mice's lick responses towards memory trials to calculate the memory score.

4.2.7 Cranial window and light-emitting diode (LED) implantation

For optogenetic manipulation of olfactory behavior, LED was implanted on top of OB. This was done by implanting a cranial window to avoid direct contact of LED with brain tissue. Detailed surgical procedure for implanting cranial window and LED is explained below:

1. Mice were anesthetized and prepared for surgery as described in section 2.3.3.1 (Steps 1-6).
2. A circular area (window) on top of OB was marked using a 2.5 mm biopsy punch.
3. A circular slit in the skull was made around the marked area using a blunt-ended dental drill bit. While thinning the skull, ACSF was regularly applied to avoid heating of the tissue underneath. Thinning continued till the cortical circuit vasculature became visible under the circular groove.

4. Once the slit was of desired depth, further cutting of the skull was continued using a 2.5 mm biopsy punch. This ensured a perfectly circular cut on the skull.

5. Next, the tip of a sharp forcep was gently inserted on the exposed side of the slit. A sharp needle was kept in a horizontal position, and the central island was slowly lifted from the skull, exposing dura. Next, the brain surface was cleaned with ACSF.

6. A drop of dexamethasone, a glucocorticoid steroid, was applied to the dura surface to reduce inflammation.

7. The exposed dura was covered with a circular coverslip (3 mm round, #1 thickness, Thomas Scientific). Dura was kept moist using ACSF, but the surrounding skull was dried using a cotton swab. The coverslip was sterilized with 70% isopropyl alcohol before use.

8. The optical window was sealed to the skull with acrylic dental cement (mixed with one drop of cyanoacrylate gum) by covering coverslip edges.

9. The cement was allowed to dry completely for 5-10 mins. The coverslip was then covered with hot-melt adhesive to avoid the mouse scratching on it.

10. Following cranial window implantation, a head-post was implanted posterior to the window. For detailed protocol, refer to section 2.3.3.1 (Steps 7-12).

11. Upon completing the surgery, the mouse was unmounted from the stereotaxic instrument and placed in the home cage. The cage was placed over a heating pad till the mouse regained senses and moved freely in the cage. During this period, body temperature was continuously monitored.

12. As post-operative care, mice were fed moistened food for one day after the surgery. After a 7-10 days recovery period, the mouse was anesthetized again using a mild dose of anesthesia. The mouse was mounted on the stereotaxic apparatus, and transparency of the cranial window was assessed and noted.

13. The walls surrounding the cranial window was flattened using a dental drill and a ~2 mm LED (either blue LED (473 nm), NFSB036BT or amber LED (595 nm), NJSA172, Nichia Corp.) with the connector (ED11100 - ND, connector socket .207 100POS 0.050SMT, Digikey, and ED8250-ND Connector strip header 50POS, 0.050) was fixed on top of the cranial window with dental acrylic cement (Figure 4-3). Once cement dried, the mouse was unmounted from the stereotaxic instrument and was placed in the home cage. The same postoperative care was taken as mentioned previously.
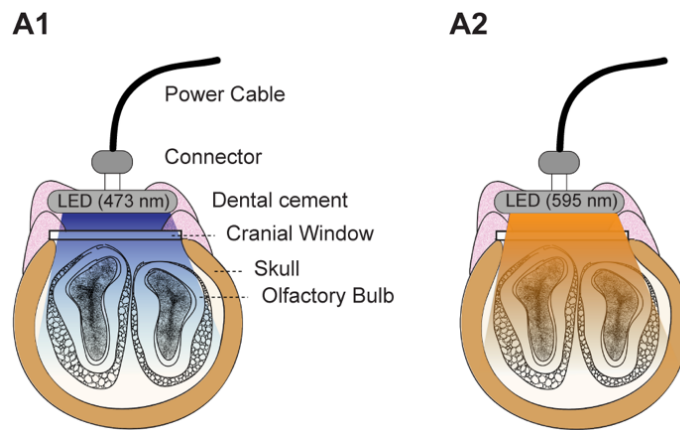
Figure 4-3: LED implantation over the OB.

A1. Schematic of a 473 nm blue LED with a connector fixed on top of a circular cranial window over OB in GAD65-ChR2 expressing mouse used for optogenetic stimulations during odor discrimination tasks. A2. A 595 nm amber LED with a connector fixed on top of a circular cranial window over OB in GAD65-Arch expressing mouse.

4.2.8 Standardization of LED power

The implanted LEDs were operated using a LED driver (LEDD1B, T-Cube LED Driver, ThorLabs) during optogenetic behavioral tasks. The goal of optogenetic experiments was to assess whether modulation of GAD65 +ve interneurons during different phases of stimulus presentation could influence odor discrimination learning and long-term memory formation. As the degree of transparency of the cranial window could vary amongst mice, optimal power needed to manipulate the majority of GAD65 +ve interneuron activity would also vary. Hence, we standardized the light power separately for each mouse to ensure illumination over a large area without increasing tissue temperature. For every light power setting, we measured the surface temperature of LED and wattage using a laser power and energy meter (LabMax-TOP, Coherent). We selected only those power settings which emitted heat around or below ambient body temperature.

To optimize LED power, mice were first trained to learn procedural aspects of odor detection tasks. We then modulated GAD65 +ve OB interneurons using different light stimulation protocols. Specifically, blocks of 20 trials with light stimulation were interleaved with trials involving no light stimulation. For the first optogenetic experiment with GAD65-ChR2 mice, we optimized the light power to photostimulate GAD65 +ve interneurons during odor stimulus of 0.5 s duration. A 40 Hz stimulation of blue LED (473 nm) was synchronized during odor presentation. LED power was selected such that licking response during light trials matched licking response for trials without light stimulation (Figure 4-4 A1). In contrast, for experiments wherein we desired post-stimulus inhibition of MTC activities, the light stimulation protocol was modified. In this case, 40 Hz stimulation of blue LED was paired with a 2 s odor presentation. Overstimulating inhibitory

activity has previously been shown to completely inhibit MTC activity, which in turn shuts down licking behavior (*14*). By progressively increasing the light power, we overstimulated GAD65 +ve interneurons. With increasing LED power, we saw a decrease in licking probabilities, and at the highest power, mice stopped licking (Figure 4-4 A2). For odor discrimination tasks to study the relevance of post-odor inhibition of MTC activities, we selected the highest light power, which preserved the licking response in mice.

The LED optimization protocol for GAD65-Arch mice was the same for both sets of experiments. Similar to previous experiments, mice were trained to odor detection tasks. Once they were aware of the procedural rules, light power was optimized by interleaving light trials with no light trials. During the light trials, 1 Hz stimulation of amber LED (595 nm) was synchronized during odor presentation for 2 s. The LED power was selected such that the licking response during light trials matched the licking response for trials without light stimulation (Figure 4-4 B1 and B2).
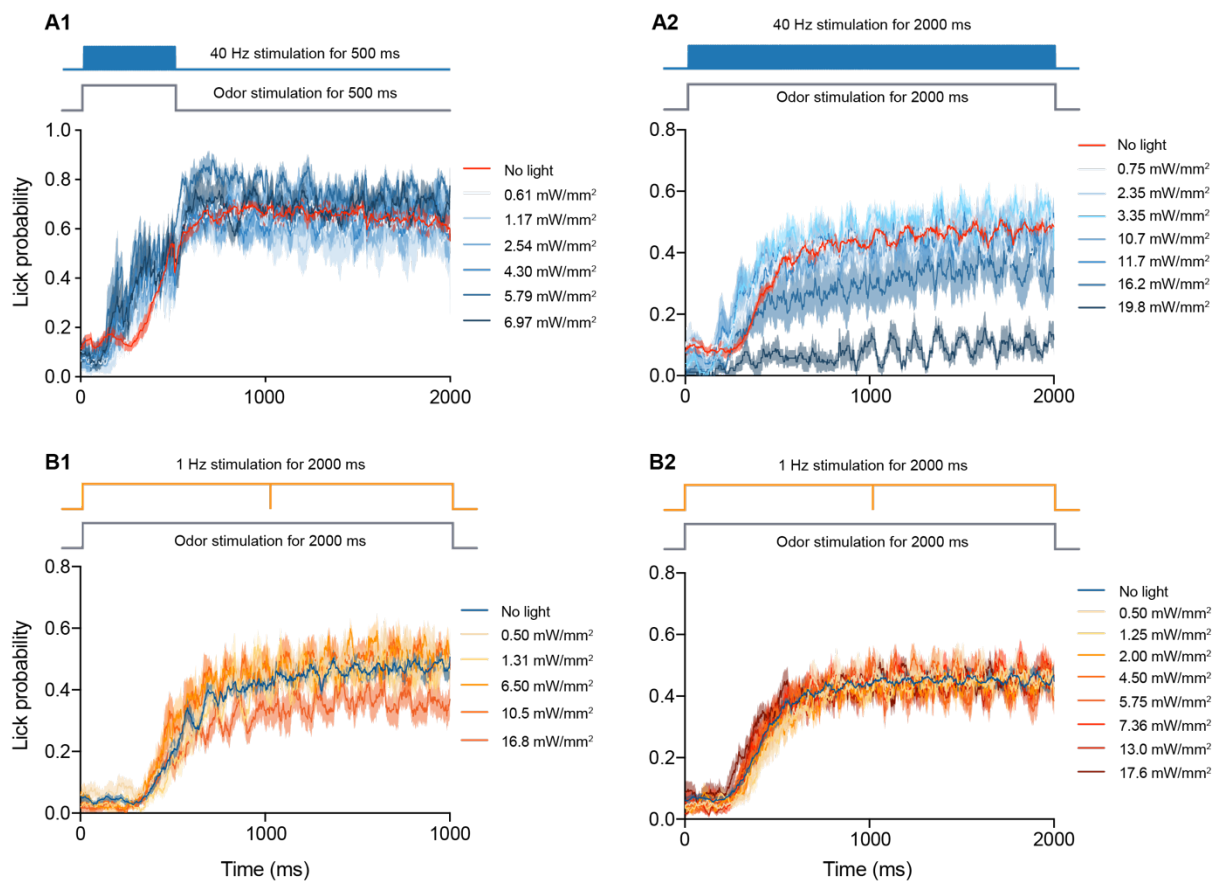
Figure 4-4: Optimization of LED power for optogenetic modification of GAD65 +ve interneurons during odor discrimination behavior.

A1. Licking response evoked by odor presentation (beginning at time 0) for GAD65-ChR2 expressing mice (n = 5 mice). The scheme for odor and photostimulation is provided above the graph. The LED power eliciting licking similar to no light trials was chosen for the odor discrimination experiment (red trace with the red shaded area). Note that licking response was averaged across mice. Each mouse exhibited differential licking at different LED powers; thus, LED power was individually determined. The solid lines and shaded areas represent mean and s.e.m., respectively.

A2. Adjustment of LED power for optogenetic inhibition of post-odor MTC firing activities in GAD65-ChR2 expressing mice. Licking patterns evoked by odor presentation with different light intensities for all mice (n = 7-8 mice for different powers). We observed that increasing LED power progressively suppressed licking behavior compared to the licking during no light trials (red trace). For each mouse, the highest power which preserved licking response during odor presentation was selected for odor discrimination tasks.

B1. Licking response evoked by odor presentation (beginning at time 0) for GAD65-Arch expressing mice. The scheme for odor and photostimulation is provided above the graph. The LED power eliciting licking similar to no light trials is chosen for the odor discrimination experiment (blue trace with the blue shaded area). The licking response was subdued at higher light powers and avoided for optogenetic modulations.

B2. Adjustment of LED power for optogenetic stimulation of post-odor MTC firing activities in GAD65-Arch expressing mice. The scheme for odor and photostimulation is provided above the graph. The power was selected such that licking remains similar to no light trials (blue trace with the blue shaded area). The lowest power, which evoked a licking response similar to light trials, was chosen to avoid heating issues as photostimulation during odor discriminations would subsequently be for 4 s at 1 Hz frequency.

4.2.9 Optogenetic modulation of odor discrimination behavior

For optogenetic experiments, different photostimulation schemes were utilized for different experiments. In brief, for experiments with photostimulation during odor presentation, the breathing rhythm was monitored using a non-invasive airflow sensor to synchronize odor and light onset according to the respiratory cycle. Thus, for ChR2 expressing mice (n = 5) trained to 0.5 s odor stimulus, light stimulation and odor delivery initiated at the middle of an exhalation cycle and lasted for 0.5 s. In total, 20 pulses of 5 ms duration at a frequency of 40 Hz were flashed during the odor period. An external blue LED lit with tone and stayed lit until the odor stimulus ended to obscure light flashed on the mouse's skull. The discrimination training paradigm was similar to previous chapters.

For photoinhibition of GAD65 +ve OB interneurons, Arch expressing mice (n = 7) were trained to 2 s odor stimulus. The amber LED pulses and odor delivery initiated at the middle of an exhalation cycle and lasted for 2 s. During the odor period, two 1000 ms pulses at a frequency of 1 Hz were flashed in total. Light flashes were concealed by using an external amber LED that lit up with a tone and shut off when the odor stimulus was over.

For post-odor stimulations, LED was flashed at the end of odor stimulus and sustained for 4 s. The stimulation frequency was kept the same as in previous experiments. The external LED turned on with tone and remained lit till the end of photostimulation. In ChR2 mice (n = 7-8), odor stimulus was for 2 s followed by 4 s post-odor stimulation. For Arch mice (n = 9), one discrimination task (HX vs. PN binary mixture task) was performed with 0.5 s stimulus and the other with 2 s odor stimulus (Octanols binary mixture task). In both cases, post-odor stimulation was for 4 s.

4.2.10 Scheme of training for optogenetic experiments

For all optogenetic experiments, the sequence of odor training was kept constant. First, mice were trained to HX vs. PN monomolecular odor discrimination task without any photostimulation. This task ensured that mice across different batches have similar olfactory abilities. Next, mice were trained to HX vs. PN binary mixture task with photostimulation. To assess if the behavior observed in this task was specific to photostimulation, Carvones binary mixture discrimination task was performed in the absence of light stimulation. To reaffirm the effects of photostimulation on olfactory behavior, Octanols binary mixture discrimination task was performed with photostimulation.

4.2.11 Microendoscopic Ca^{2+} imaging

For Ca^{2+} imaging, two new sets of naive GAD65-GCaMP6f mice were used (5 mice used for imaging under anesthetized conditions while 7 mice used for imaging under awake conditions).

4.2.11.1 Implantation of Imaging Canula

1. The barrel on top of the dummy microscope body was rotated clockwise till resistance was felt, and then an additional ¼ turns were made. The left and the right clamp were pulled outwards using a snapping tool. Then the protective cannula was removed.

2. To secure an imaging cannula on the dummy microscope body, it was inserted onto the dummy microscope body. The left and right clamps were clipped into place using the snapping tool. Next, the barrel was rotated anti-clockwise until it became loose. This ensured that clamps were tightly holding the cannula. The barrel was never unscrewed completely.

3. Next, a Fluorescent microscope holder (FMH) was installed as follows; Connector caps from microscope M3 optical connector and FMH ferrule were removed. The ferrule was inserted into the M3 optical connector. This connection was secured by screwing the FMH extremity. The FMH was then attached to the stereotaxic apparatus using FMH clamps. When ready for use, the output protective cap was removed from the canula by unscrewing it.

4. The surgical preparation and craniotomy were performed as described previously. A 1 mm circular piece of bone was removed over one hemisphere of the OB.

5. To prepare for implantation, an adjustment ring was first screwed to the lens assembly. This was done by placing a couple of drops of slow-drying cyanoacrylate glue to secure the ring to the metal thread of the imaging cannula. Care was taken to avoid the application of glue on the imaging lens. The ring is used to stabilize the system on the skull when the implanted cannula is at an appropriate depth. For imaging OB, a reduced footprint adjustment ring was used.

6. A path was created for lens implantation to a desired depth by slowly lowering a blunt Hamilton needle using the stereotaxic arm for canula installation.

7. Next, the imaging cannula attached to the dummy microscope was placed above the cranial window. The dummy microscope assembly was lowered into the craniotomy hole at an approximate velocity of 1 μm/sec to allow proper penetration.

8. To secure the cannula on skull, a mixture of cyanoacrylate gum and dental acrylic cement was applied between the protrusion ring and surface of the skull. Once the cement dried, a head-post was implanted posterior to the implanted lens (detailed protocol in section 2.3.3.1).

9. After the surgery, the dummy microscope was unclamped from the imaging cannula. This was done by rotating the barrel in an anti-clockwise direction. Next, cannula clamps were unclipped using the snapping tool, and the dummy microscope was removed. The protective cap was placed onto the implanted cannula to protect the rod lens.

10. A recovery time of at least three weeks was provided to mice after surgery and before beginning the imaging sessions.

4.2.11.2 Image acquisition and image processing

A snap-in fluorescence microscope body (OSFM model L, Doric lenses Inc., Canada) mounted on the implanted GRIN cannula (1 mm length) was used to image GAD65 +ve interneurons in the GCL of OB. The working distance of the cannula was 80 μm, with a focal range of 50 μm. The CE:YAG fluorescence source (465 nm output, Doric Lenses Inc.) was tuned to 250-700 mA. The field of view corresponding to 350 μm × 350 μm (further binned 2 × 2 times) was imaged at a frame rate of 10 Hz. For imaging in an anesthetized condition, an I.P. injection of Ketamine (50 mg/Kg body weight) and Xylazine (10 mg/Kg body weight) was administered before every session. In each session, 60-80 odor trials were presented to mice at an interval of 13.2 s. The sequence of odor presentation was pseudorandomized. For imaging under awake conditions, mice were pretrained to odor detection tasks mentioned in materials and methods. After pretraining, imaging was done while mice were passively exposed to different odors. Each odor was presented for 20 trials in this task, and each session consisted of 80 trials. The sequence of odor delivery was randomized. The imaging session spanned over two weeks, with one session a day. Ca^{2+} imaging was synchronized to the trial onset by an external TTL signal from the olfactometer. Specifically, a tone at the beginning of a trial triggered the microendoscope. The imaging continued for 10 s. Within this 10 s, the first 1.2 s was a baseline, followed by odor delivery either for 0.5 s or 2 s. The trial-by-trial imaging data was annotated by comparing the trial sequence generated by the olfactometer result file.

Image analysis was done using custom scripts in MATLAB (Mathworks Inc.). Pre-processing of images was performed by cropping images to 300 μm × 300 μm frames. This was done to remove vignettes that had developed around the edges of raw images. The whole image was considered as a global region-of-interest (ROI) to analyze population activity within the frame. In few images, the microscope dropped frames within a trial. Such trials were detected and excluded from the analysis. The relative changes in fluorescence for each frame were calculated by $F_{(t)}/F_0 = [F_{(t)} - F_0]/F_0$, where F_0 is the mean activity during the baseline. F_0 was calculated separately for each trial. The latency to the peak was calculated by measuring the time to attain maximum amplitude from odor onset for a given trace. The maximum change in fluorescence was calculated by averaging the trials for a given odor. The overall activity for a single trial was measured by calculating the total area under curve (AUC).

4.2.12 Immunohistochemical estimation of Arc protein in different areas of olfactory cortex

A new batch of WT, GAD65-ChR2, and GAD65-Arch mice (n = 4-5 mice) were trained to HX vs. PN monomolecular odor discrimination followed by binary mixture discrimination of Octanols enantiomer. For octanols binary mixture discrimination, odor stimulus was followed by post-odor photostimulation. To keep the conditions the same, even WT mice were trained with photostimulation. At the end of the training, three mice were randomly processed for immunohistochemical analyses. Mice were perfused using 4% PFA, and the dissected brain was stored in 4% PFA at 4°C for 16-18 hrs. Using a vibratome (Leica VT 1200S), 50 μm floating sagittal sections were taken. Three washes of 15 mins each were given to these sections using 1X Tris Buffered Saline (TBS). The sections were then incubated in blocking solution (5% Bovine Serum Albumin [BSA] in 1% Triton-X in TBS [TBST]) and placed on a rocker for 1.5 hrs. Following incubation, sections were transferred in 1° antibody (Rabbit anti-Arc, 156003, Synaptic Systems) diluted to 1:1250 in blocking solution (1% BSA in 0.1% TBST) for 12-14 hrs at 4°C. After the incubation, three washes of 15 mins with TBS were given to sections. Next, sections were incubated with a 2° antibody (Anti-Rabbit Alexa Fluor 594, Jackson Immunoresearch), diluted to 1:500 in 1% BSA, and kept for incubation at RT for 2 hrs. After incubation with 2° antibody, sections were washed three times with TBS (15 mins each). In the last wash, DAPI (Sigma, 1:500) was added to TBS to label cell nuclei. Following the washes, sections were transferred to fresh TBS till they were mounted on slides. Vectashield® anti-fade mounting medium (Vector Labs, H-1000) was used to retain the fluorescence for an extended period. Confocal imaging was done to visualize Arc labeled nuclei across different olfactory areas. Quantification of Arc +ve cells was done using FIJI software (US National Institutes of Health). Briefly, a 5 × 5 median filter was

applied to image stacks. Cells were then segmented from the background using a robust automatic threshold selection plugin. In the case of clustering, a watershed algorithm was applied. The total percentage of Arc +ve cells was estimated by comparing it with the total number of cells in the area labelled with DAPI.

4.3 Results

4.3.1 Olfactory stimulus duration influences odor discrimination learning and long-term memory formation

To investigate how odor representations and olfactory discriminability change with stimulus time, we designed our behavioral paradigms by training mice to three different odor stimuli duration – 2 s, 1 s, and 0.5 s (Figure 4-6 A). The shortest stimulus duration of 0.5 s was chosen by considering the predicted upper limit of ODT at maximal accuracies (Figure 3-3 B). A set of 21 male mice were first trained to AA vs. EB monomolecular odor discrimination task with 2 s stimulus duration. On training mice on AA vs. EB task, within 900 trials, their performance stabilized at ≥ 90% accuracies, which continued till the end of 1200 trials. Mice were then divided into three groups of seven mice each (to be conditioned on different stimuli durations). On random assignment, groups had similar learning accuracies for monomolecular discrimination of AA vs. EB (Figure 4-5, one-way ANOVA, p = 0.9384). The three groups of mice were then trained on a monomolecular odor discrimination task of HX vs. PN with different stimuli durations. All groups of mice started performing HX vs. PN discrimination with > 80% accuracy within 200 trials and reached asymptotic performance by the end of 400 trials. Overall, we observed that changing the stimulus duration did not influence learning accuracies for monomolecular odor discrimination task (Figure 4-6 B, a pairwise comparison made between each time point across three groups using two-way ANOVA and Tukey's multiple comparison test, $F_{(22,216)} = 0.5819$, p = 0.9330). On the other hand, reducing the stimulus duration affected the learning efficiency for HX vs. PN binary mixture discrimination. Mice trained on 0.5 s stimulus displayed a slow learning pace compared to groups trained with 1 s and 2 s stimulus duration (Figure 4-6 C1, two-way ANOVA; for HX vs. PN binary mix, p = 0.0004). To increase the complexity of the task further, mice were trained on two different enantiomer mixtures. As shown in the previous chapter, enantiomer mixtures represent a class of odor with overlapping patterns of glomerular activity. Mice were sequentially trained to binary mixtures of C+/C- and O+/O-. With increasing complexity, learning deficits were observed in groups trained with shorter stimulus duration compared to the 2 s group. The extent of learning deficit was more severe for mice trained with 0.5 s stimulus with the accuracies reaching

~80% only after 1000 trials (Figure 4-6 C2 and C3, two-way ANOVA; for Octanols binary mix, p = 0.0157; for Carvones binary mix, p < 0.0001).
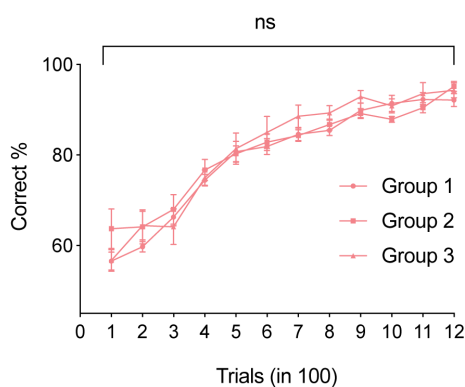
Figure 4-5: Similar learning accuracies across different cohorts of mice.
Training accuracies were measured for AA vs. EB monomolecular odor pair discrimination. Mice were trained with a stimulus duration of 2 s. After the completion of 1200 trials, mice were randomly segregated into different groups. On forming the groups, each group had similar learning accuracies (ordinary one-way ANOVA, p = 0.9384).

Our results demonstrate a decrease in the learning performance with short stimulus duration. Does odor discrimination training with different stimulus duration also influence the way animals form a memory of rewarded and non-rewarded stimulus? To investigate this, we assessed olfactory memory after thirty days of training in the same batch of mice. To assess memory, mice were trained to a non-related odor pair (CI vs. EU). Once mice reached asymptotic accuracies, memory trials were interleaved within CI/EU trials, and the response towards memory trials was assessed (Please refer to materials and methods). For the monomolecular odor (HX vs. PN), mice correctly responded towards memory trials, and all groups had a memory accuracy of > 90% (Figure 4-6 B2, one-way ANOVA, p = 0.3606, R^2 = 1.08). Next, the memory for binary mixtures was checked and compared between the groups. For both the binary mixtures, we observed a significant reduction in long-term memory performance for mice trained with shorter stimuli durations (Figure 4-6 D1-3, one-way ANOVA; for HX vs. PN binary mix, p < 0.0001; for Octanols binary mix, p < 0.0001; for Carvones binary mix p < 0.0001). This observation suggests that a longer duration of odor stimulus during odor discrimination training helps in stabilizing long-term memory formation.
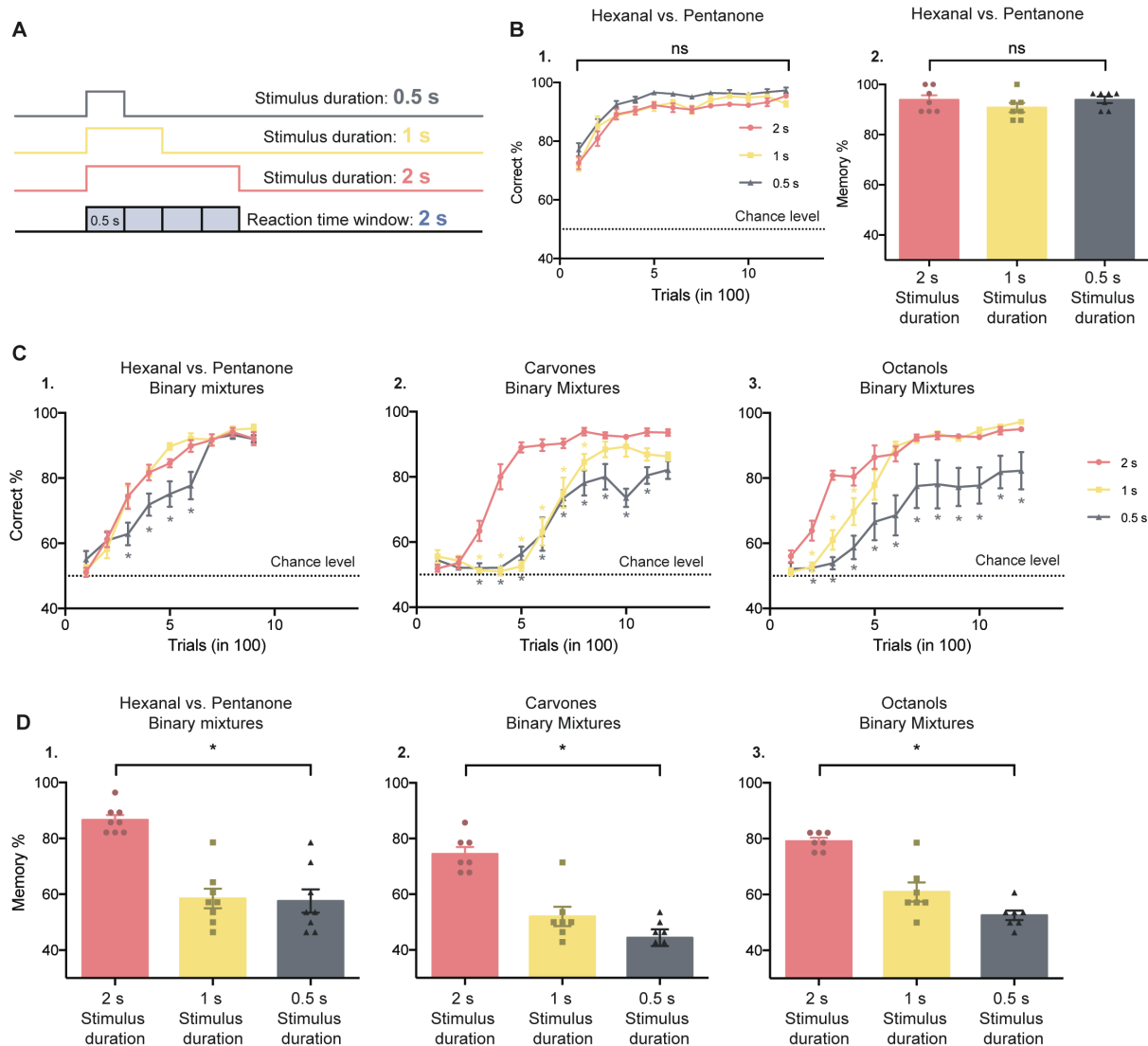
Figure 4-6: Olfactory learning and long-term memory formation are critically dependent on stimuli durations.

A. Scheme of odor presentation for variable stimuli durations. Irrespective of the stimulus duration, the reaction time window was set at 2 s. Mice registered their lick response towards a rewarded odor during this reaction time window.

B. For monomolecular odor discriminations, mice across three groups had similar learning accuracies and long-term memory performance. (1) Learning accuracies were measured for three different stimuli durations (2 s, 1 s, 0.5 s represented by red, yellow, and gray lines, respectively). Discrimination learning accuracy is shown as percentage correct choices averaged across 100 trials. Each data point is an average of 7 mice. A pairwise comparison was made between each time point across three groups using two-way ANOVA with Tukey's multiple comparison test, $F_{(22,216)} = 0.5819$, $p = 0.9330$. Comparisons were made keeping the 2 s group as a reference group. Each point indicates mean ± sem. (2) Memory responses were calculated for groups of mice presented with stimuli of different durations. No significant difference was observed for monomolecular odor discrimination of HX vs. PN (one-way ANOVA, $F = 1.08$, $p = 0.3606$, $R^2 = 1.08$).

C. With increasing odor complexities, mice trained on 1 s and 0.5 s stimuli durations showed slower learning as compared to mice trained on 2 s stimulus (two-way ANOVA; (1) for HX vs. PN binary mix, $F_{(16,162)} = 2.861$, $p = 0.0004$; (2) for Carvones binary mix, $F_{(22,216)} = 8.219$, $p < 0.0001$; (3) for Octanols binary mix, $F_{(22,216)} = 1.831$, $p = 0.0157$).

D. For binary mixtures, the memory was significantly low for mice trained with 1s and 0.5s odor stimulus as compared to the 2 s group (one-way ANOVA; (1) for HX vs. PN binary mix, $F = 24.86$, $p < 0.0001$, $R^2 = 0.7031$; (2) for Carvones binary mix, $F = 26.78$, $p < 0.0001$, $R^2 = 0.7485$; (3) for Octanols binary mix, $F = 34.14$, $p < 0.0001$, $R^2 = 0.7914$). (n = 7 mice).

4.3.2 The OB GABAergic interneuron activity is dependent on odor stimulus duration

Having identified major differences in olfactory behavior with changing stimuli durations, we next asked how olfactory representations change with odor presentation time. The mice' ability to discriminate between two similar odors depends on the extent of pattern separation in MTC activity ensembles ([14, 20, 41]). On odor stimulation, OB interneurons are activated with widely distributed firing responses which inhibit MTCs, decorrelating stimulus representations. We sought to elucidate OB inhibitory interneuron activity in response to odor stimuli of varying durations. To record from the majority of OB GABAergic interneurons, we expressed genetically encoded Ca^{2+} indicator GCaMP6f in GAD65 +ve interneurons. To record Ca^{2+} dynamics from GAD65 +ve interneurons, we implanted a microendoscopic GRIN lens in GCL of OB at a depth of -1 mm. Taking advantage of the dense expression of GCaMP6f throughout GCL, we recorded population activity within the field of view. We imaged Ca^{2+} transients from OB in separate batches of anesthetized and awake mice while passively exposing them to six odorants presented for either 0.5 s or 2 s duration. In both sets of mice, each odor was presented for 20 trials in a pseudorandomized manner. This was done to minimize the effects of habituation, and we observed robust responses across different trials in both sets of mice when presented with different stimuli (Figure 4-7 A, B, C, and D). When GAD65 +ve interneuron activity was recorded under anesthesia, we routinely observed a slow rise and decay in Ca^{2+} transients independent of the stimulus duration (Figure 4-7 C). For 0.5 s stimulus, Ca^{2+} signals consistently peaked in the post-stimulus period (~850 ms, averaged across six different odors), while Ca^{2+} signals peaked at around 1900 ms when the odor was presented for 2 s. In comparison, the increase in Ca^{2+} signals was instantaneous in response to odor presentation in awake animals (Figure 4-7 D, E, and F. For 0.5 s stimulus, peak latency between awake and anesthetized mice, two-tailed t-test, $p < 0.0001$, $t = 11.04$, $df = 10$. For 2 s stimulus, peak latency between awake and anesthetized mice, two-tailed t-test, $p < 0.0001$, $t = 21.69$, $df = 10$). The fast kinetics of Ca^{2+} signals in awake conditions is probably due to higher breathing frequencies compared to basal breathing rates under anesthetized states. For 2 s stimulus, additionally, we observed a difference in the maximum fluorescence change of Ca^{2+} signals between awake and anesthetized animals (Figure 4-7 G. For 0.5 s stimulus, peak amplitude between awake and anesthetized mice, two-tailed t-test, $p = 0.4843$, $t = 0.7264$, $df = 10$. For 2 s stimulus, peak latency between awake and anesthetized mice, two-tailed t-test, $p = 0.0017$, $t = 4.26$, $df = 10$).

Further, the overall activity was compared by measuring the AUC. For the two stimuli duration, activity was found to be greater when imaged in mice under anesthesia compared to awake mice (Figure 4-7 H1 and H2. For 0.5 s stimulus, AUC between awake and anesthetized mice, K-S test, $p = 5.15 \times 10^{-30}$. For 2 s stimulus, AUC between awake and anesthetized mice, K-S test, $p = 2.09 \times 10^{-17}$).
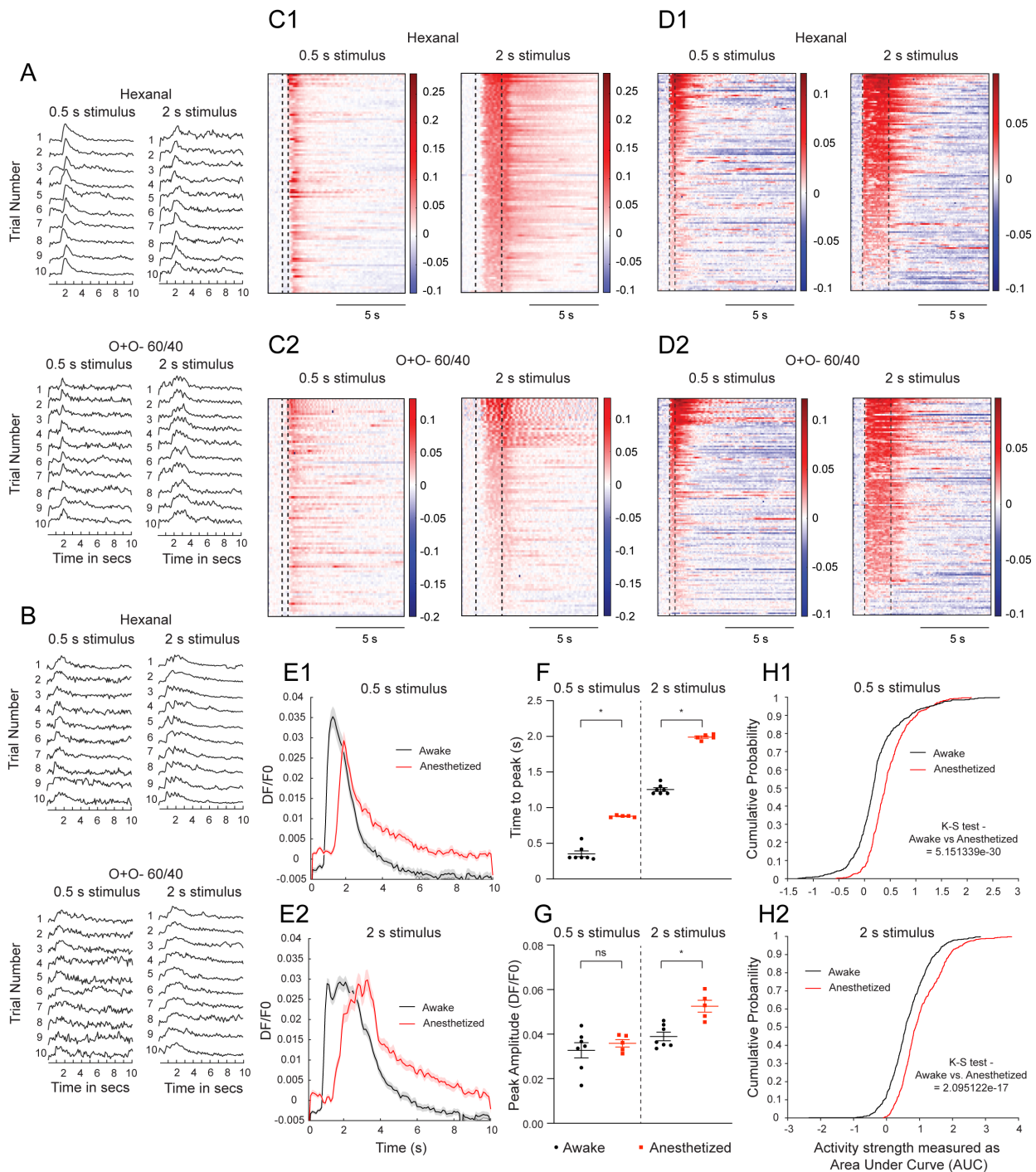
Figure 4-7: The response kinetics of GAD65 +ve OB interneurons under awake and anesthetized conditions.

A and B. Example of GAD65 +ve OB interneuron response to a monomolecular odor and a binary mixture presented for two different stimuli duration under anesthetized (A) and awake (B) conditions. Each individual trace represents an odor-evoked GCaMP6f response to the odor stimulus. The trials are arranged in the sequence of odor presentation to the mouse.

C1 and C2. Pseudo-color heatmaps of Ca^{2+} dynamic responses evoked by either 0.5 s or 2 s odor application (black dotted lines) for a monomolecular odor and a binary mixture under anesthetized condition. Data were acquired from 5 mice with 20 odor presentations. Data from all trials are arranged in decreasing order of Ca^{2+} response during odor application.

D1 and D2. Pseudo-color heatmaps of Ca^{2+} dynamic responses evoked by either 0.5 s or 2 s odor application (black dotted lines) for a monomolecular odor and a binary mixture under awake condition. Data were acquired from 7 mice with 20 odor presentations. Data from all trials are arranged in decreasing order of Ca^{2+} response during odor application.

E1 and E2. Average Ca^{2+} responses were used to measure response kinetics under different stimuli conditions. The different parameters calculated are the latency to peak, peak amplitude, and total response by measuring AUC.

F. The latency to peak was calculated by measuring the time to reach the maximum signal after odor presentation. The latencies are calculated by averaging the response for each odor (Total odors used = 6). For 0.5 s stimulus, peak latency between awake and anesthetized, two-tailed t-test, $p < 0.0001$, $t = 11.04$, $df = 10$. For 2 s stimulus, peak latency between awake and anesthetized, two-tailed t-test, $p < 0.0001$, $t = 21.69$, $df = 10$.

G. The peak amplitudes were measured for each odor and compared between awake and anesthetized mice across different stimuli durations. For 0.5 s stimulus, peak amplitude between awake and anesthetized, two-tailed t-test, $p = 0.4843$, $t = 0.7264$, $df = 10$. For 2 s stimulus, peak latency between awake and anesthetized, two-tailed t-test, $p = 0.0017$, $t = 4.26$, $df = 10$.

H1 and H2. The total interneuron activity was compared between awake and anesthetized mice for two different stimuli durations. The AUC is plotted in the form of a cumulative probability curve. For 0.5 s stimulus, AUC between awake and anesthetized, K-S test, $p = 5.15 \times 10^{-30}$. For 2 s stimulus, AUC between awake and anesthetized, K-S test, $p = 2.09 \times 10^{-17}$.

We next investigated the kinetics of Ca^{2+} signals for different stimuli durations in awake mice. For all odors tested, differences in interneuron activities were consistently observed between 0.5 s and 2 s stimulus duration (Figure 4-8 A1-6). To quantify stimuli duration-dependent differences, we measured AUC and peak amplitudes for different odors across seven mice. In awake conditions, OB inhibitory interneuron activity was higher when the stimulus duration was 2 s. Both AUC and peak amplitudes were greater for 2 s stimulus when averaged across the different odors (Figure 4.8 B and C. For AUC between 2 s and 0.5 s stimulus, K-S test, $p = 1.72 \times 10^{-50}$. For peak amplitude between 2 s and 0.5 s stimulus, K-S test, $p = 0.0031$). In summary, odor-evoked activities of GAD65 +ve interneurons are much stronger with longer stimuli durations, indicating the role of stimuli duration in driving inhibitory activity within OB and thereby modulating olfactory representations.
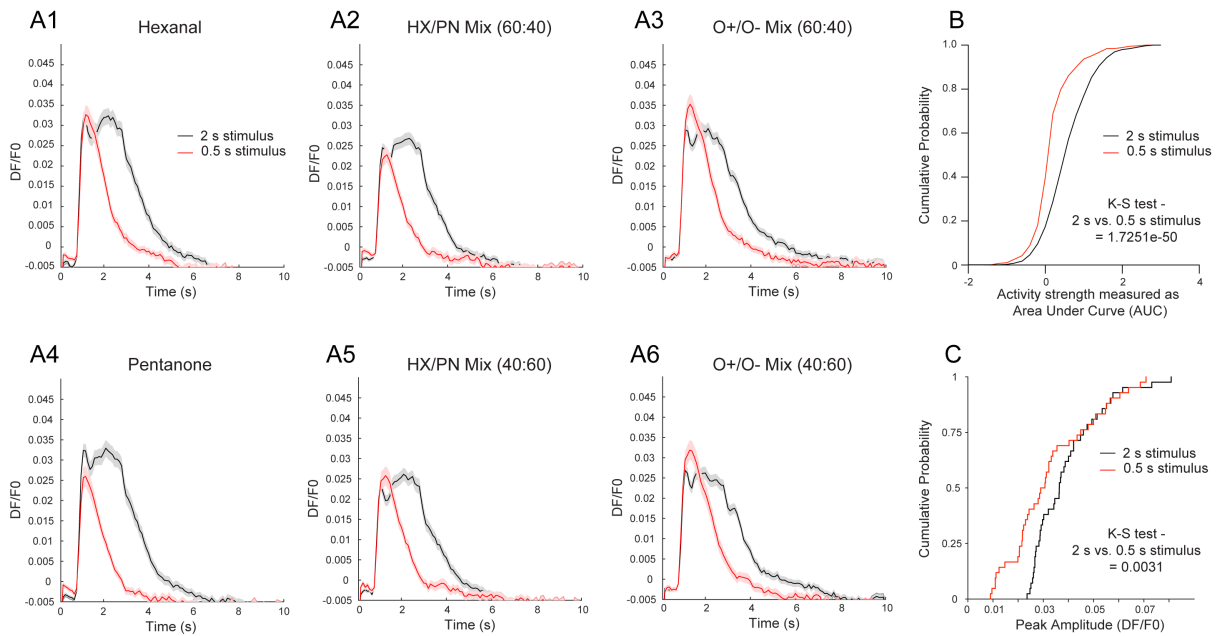
Figure 4-8: Comparison of GAD65 +ve interneuron activity in awake animals for 0.5 s and 2 s stimulus.

A1-6. Average Ca^{2+} responses for the six odors presented either for 0.5 s or 2 s stimulus (red and black traces, respectively). Irrespective of odor class and duration of the stimulus, onset latencies are very similar across different conditions.

B. The total interneuron activity was compared between 0.5 s and 2 s stimulus durations. The AUC is plotted in the form of a cumulative probability curve (K-S test, p = 1.72×10^{-50}).

C. The peak amplitudes were measured for each odor and compared between 0.5 s and 2 s stimulus (K-S test, p = 0.0031).

4.3.3 Modulating OB inhibitory activity during stimulus presentation influences odor discrimination learning without affecting long-term memory formation

Our Ca^{2+} imaging data suggest considerable differences in the interneuron activity during odor application in response to a short and long stimulus. Can this difference in synaptic inhibition explain the olfactory discrimination learning and long-term memory deficits we observed under different stimuli conditions? We trained two sets of head-restrained mice (expressing either ChR2-EYFP or Arch-GFP in the GAD65 +ve interneuron population) to study the causality between odor discrimination performance and synaptic inhibition on the same odor discrimination tasks. By expressing ChR2 and Arch in separate sets of mice, the aim was to increase the inhibitory strength when stimulus duration was short while reducing the inhibitory strength when stimulus duration was long. Initially, both the groups were trained to HX vs. PN monomolecular odor discrimination to assess their olfactory abilities. Both sets of mice performed with similar accuracy compared to WT control mice (Figure 4-9 A1, two-way ANOVA, p = 0.9006). Mice were next trained on two different binary odor mixture discrimination tasks. Specifically, ChR2 expressing mice were trained to 0.5 s stimulus duration, and Arch expressing mice were trained to 2 s of stimulus duration

(See materials and methods for detailed protocol). In either case, photostimulation was restricted to the period of odor presentation. Photostimulating GAD65 +ve interneurons during short odor presentation improved the learning efficacy in ChR2 expressing mice. Additionally, they learned complex odor discriminations with the same efficiency as the control WT mice trained to 2 s stimulus (Figure 4-9 B, two-way ANOVA, (1) for HX vs. PN binary mix, p = 0.0004; (2) for Octanols binary mix, p = 0.0012). On the other hand, Arch expressing mice had difficulties in learning complex discrimination tasks even with 2 s of odor stimulus and managed to reach accuracies similar to WT animals only in the last task. The specificity of photostimulation was assessed by training mice to Carvones binary mixture task without photostimulation. Without light stimulation, ChR2 animals had slower learning compared to WT and Arch animals (Figure 4-9 B3, two-way ANOVA, p < 0.0001). In conclusion, optogenetically controlling the inhibitory strength during odor presentation resulted in bidirectional modulation of olfactory learning performance.
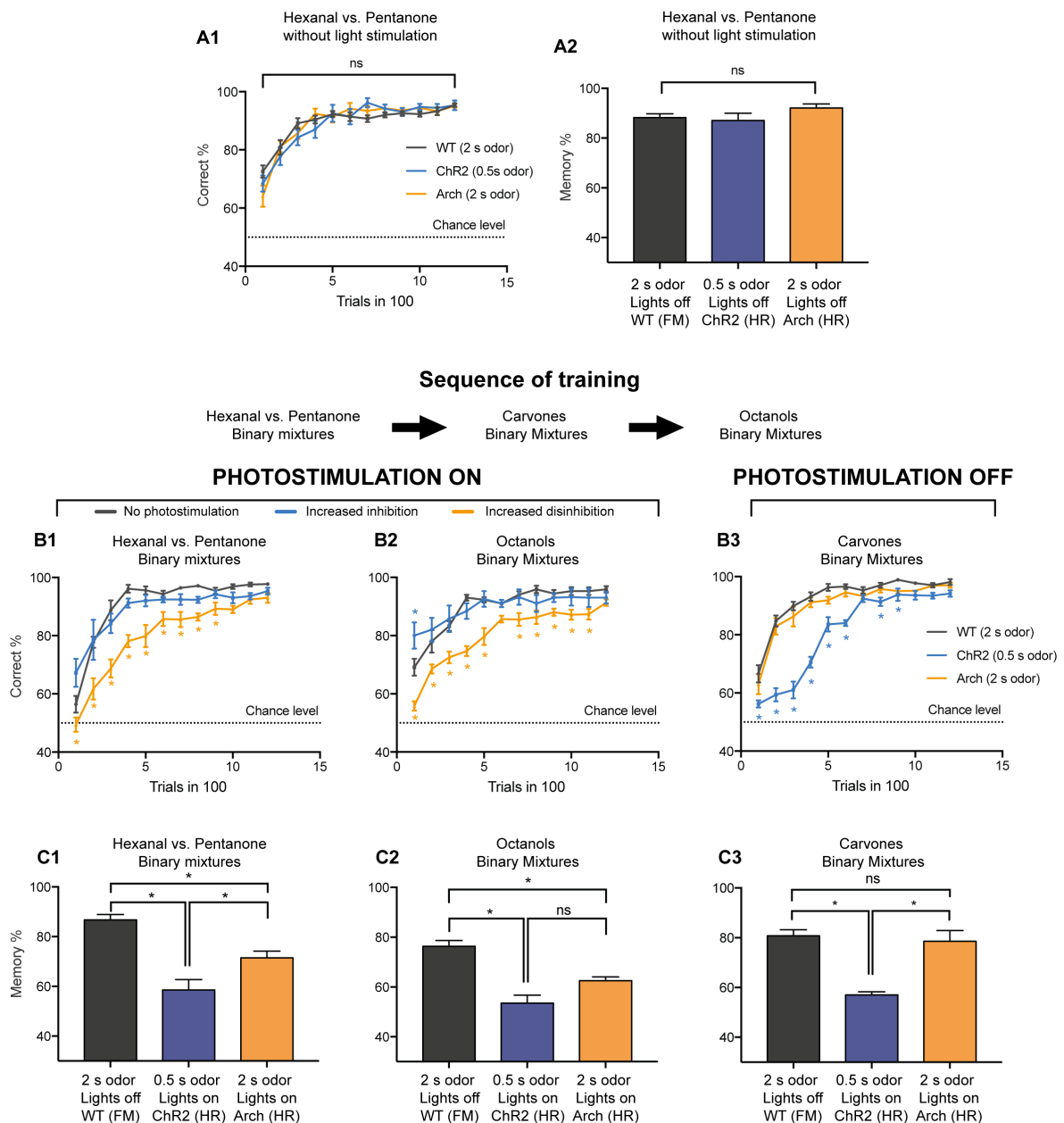
Figure 4-9: Optogenetic manipulation of GAD65 +ve interneurons during stimulus presentation influences odor discrimination learning without affecting long-term memory formation.

A. (1) Training ChR2 and Arch expressing mice to HX vs. PN monomolecular odor discrimination without photostimulation. ChR2 animals were trained to 0.5 s odor (blue trace, n = 5) while Arch animals were trained to 2 s odor duration (amber trace, n = 7). The performance was compared with WT control mice trained to 2 s odor application (gray trace, n = 7). All three groups of mice had similar learning efficiencies (two-way ANOVA, $F_{(2, 192)} = 0.1047$, p = 0.9006). (2) Memory responses were similar across the groups (one-way ANOVA, F = 1.714, p = 0.2136).

B. Increasing the inhibition on MTCs by photostimulating GAD65 +ve interneurons increased the learning pace in ChR2 expressing mice while disinhibiting the MTCs led to learning impairment as compared to control WT mice. *Pairwise comparison was made between each time point across three groups using two-way ANOVA and Tukey's multiple comparison test ((1) for HX vs. PN binary mix, $F_{(22, 192)} = 2.523$, p = 0.0004; (2) for Octanols binary mix, $F_{(22, 180)} = 2.341$, p = 0.0012).

B3. In the absence of photostimulation, an opposite trend was observed wherein ChR2 expressing mice had learning impairment while Arch expressing animals had learning efficiencies similar to WT mice (ordinary two-way ANOVA, $F_{(22, 192)} = 8.431$, p < 0.0001).

C. Despite the rescue of learning deficits, no improvement was observed in memory responses with optogenetic stimulation as compared to the control WT mice (one-way ANOVA, (1) for HX vs. PN binary mix, F = 22.93, p < 0.0001, $R^2 = 0.7535$; (2) for Octanols binary mix, F = 23.62, p < 0.0001, $R^2 = 0.747$).

C3. Without photostimulation, Arch expressing mice had memory similar to WT mice while ChR2 expressing mice had memory impairment (one-way ANOVA, F = 16.84, p = 0.0001, $R^2 = 0.6779$).

We next examined whether modulating synaptic inhibitory strength during odor presentation controls long-term memory formation. First, memory for HX vs. PN monomolecular odors was assessed across the groups. All the groups had similar memory performance for monomolecular odor trained with different stimuli duration (Figure 4-9 A2, one-way ANOVA, F = 1.714, p = 0.2136). Interestingly, photostimulation of GAD65 +ve interneurons during short odor presentation did not influence long-term memory formation. For binary mixtures, ChR2 expressing mice displayed long-term memory deficits although they learned odor discrimination with high accuracies (Figure 4-9 C, one-way ANOVA, (1) for HX vs. PN binary mix, p < 0.0001; (2) for Octanols binary mix, p < 0.0001). When the memory was assessed in Arch expressing animals, it was observed that these mice had a poor memory performance for these mixtures (Figure 4-9 C, comparison with WT mice, one-way ANOVA, (1) for HX vs. PN binary mix, p < 0.0001; (2) for Octanols binary mix, p < 0.0001). Memory loss following slow learning in odor discrimination tasks is congruent with the previous data (Figure 4-6 D). However, Arch animals had a high memory performance for Carvones binary mixture task in the absence of photostimulation (Figure 4-9 C3, one-way ANOVA, p = 0.0001). These findings show that modifying neural representations formed during odor presentation can regulate odor discrimination learning while having no effect on long-term memory formation.

4.3.4 Post-stimulus neural activity in OB circuitries controls long-term memory formation

Despite improvement in learning, long-term memory impairment indicates the possibility for separate neural mechanisms controlling odor discrimination learning and long-term memory formation. Within a general scheme, memory formation happens by stabilizing neural activities as a function of time (*301*). As odor-induced neural responses outlast the stimulus duration, it raises a question of whether post-odor responses are involved in memory formation. To probe the relevance of post-odor responses in memory formation, we trained a new batch of ChR2 and Arch expressing mice. To achieve global silencing of MTC activities, we adopted an approach to increase the inhibitory strength of GAD65 +ve interneurons in ChR2 expressing mice. Thus, we calibrated LED intensities to overstimulate GAD65 +ve interneurons to shut down MTC activities. On the contrary, by inhibiting OB interneurons, we aimed to disinhibit MTC responses in the post-stimulus period using Arch expressing mice. Combining these two experiments, we investigated the role of post-odor responses in olfactory long-term memory formation.

Post-stimulus firing activities in MTC ensembles show a correlation with odor activities elicited by the stimulus for up to 10 breaths (*34*). To target post-odor responses, we photo-stimulated ChR2 and Arch for 4 s following odor stimulation (For ChR2 activation – 40 Hz stimulation for 4 s. For Arch activation – 1 Hz stimulation for 4 s). Mice were first trained to discriminate HX vs. PN monomolecular odor with a 2 s stimulus duration. Mice achieved >80% accuracy within the first 300 trials, and the accuracy was comparable to previous data sets. After assessing the olfactory competence of mice, ChR2 expressing mice were sequentially trained to discriminate two complex binary mixtures with post-odor stimulation of GAD65 +ve interneurons. The odor stimulus duration was set to 2 s. Although Arch expressing mice were trained to the same odor, the stimulus duration was 0.5 s for HX vs. PN binary mixture while the stimulus duration was 2 s for Octanols binary mixture. Training ChR2 expressing mice with post-stimulus inhibition of MTC firing activity did not affect the learning efficacy in binary mixture discriminations when compared to the control WT group (Figure 4-10 A1 and A2, for HX vs. PN binary mix, two-way ANOVA, $p = 0.6126$. For Octanols binary mix, two-way ANOVA, $p = 0.0921$). When these mice were trained to discriminate Carvones binary mixture without photostimulation, we observed a reduced performance in the discrimination task compared to WT mice (Figure 4-10 A3, comparison between ChR2 and WT mice, two-way ANOVA, $p < 0.0001$). However, by the end of the third task, their accuracies reached >90 % and matched with the other groups. Reduced performance in initial trials may be a result of cohort-specific differences in the learning performance. Comparing learning accuracies with a previous batch of WT mice trained on the same odor pair under head-restricted conditions (set 4 used in chapter 3), we observed similar learning in both the groups (two-

way ANOVA, p = 0.1073). Further, comparing learning performances across all the groups (ChR2, Arch, and WT control mice), we did not find any difference in their learning accuracies (Figure 4-10 A3, two-way ANOVA, $F_{(2, 240)} = 1.335$, p = 0.1495). Next, the effect of disinhibiting MTC firing activities in the post-stimulus period on the learning performance was evaluated. Training Arch expressing mice with post-stimulus disinhibition of MTC firing activity did not impact the learning efficacy for HX vs. PN and Octanols binary mixtures when compared with the control WT group (Figure 4-10 A, (1) for HX vs. PN binary mixture, two-way ANOVA, p = 0.3588; (2) for Octanols binary mixture, two-way ANOVA, p = 0.3241). Also, in the absence of any stimulation, Arch expressing mice had similar learning accuracies for Carvones binary mixture task compared to WT animals (Figure 4-10 A3, two-way ANOVA, p = 0.9230).
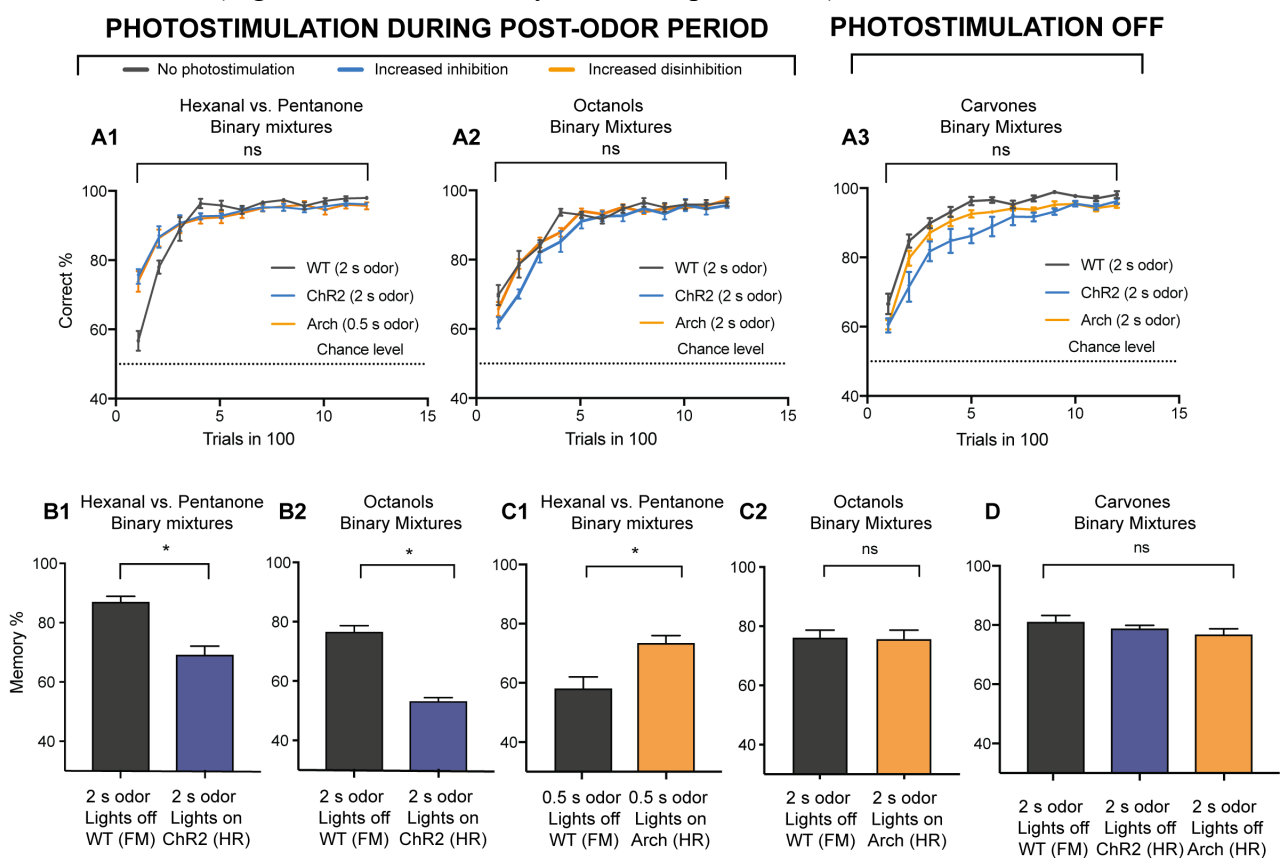
Figure 4-10: Post-odor MTC spiking activity controls long-term memory formation.

A. Modulating post-odor MTC firing activities do not influence olfactory learning accuracies. On comparing learning accuracies of ChR2 and Arch expressing mice with WT control mice, we observed that bidirectional modulation of post-odor MTC firing activities did not affect binary mixture discriminations ((1) For HX vs. PN binary mixtures, ordinary two-way ANOVA, $F_{(2, 240)} = 1.133$, p = 0.3238. (2) For Octanols binary mixture, ordinary two-way ANOVA, $F_{(2, 228)} = 1.426$, p = 0.1033). (3) Learning accuracies of three groups of mice (ChR2, Arch, and WT control mice) were similar for Carvones binary mixture discrimination without photostimulation (two-way ANOVA, $F_{(2, 240)} = 1.335$, p = 0.1495).

B. The long-term memory was degraded for ChR2 expressing mice trained under conditions wherein post-odor MTC firing activities were inhibited (two-tailed t-test, (1) for HX vs. PN binary mix, p = 0.0006; (2) for Octanols binary mix, p < 0.0001).

C. (1) Post-odor disinhibition of MTC firing activities following 0.5 s of odor stimulus improved long-term memory as compared to WT control mice trained to 0.5 s odor stimulus (two-tailed t-test, p = 0.0077). (2). With post-odor disinhibition of MTC firing activities following 2 s of odor stimulus, long-term memory performance was similar to WT mice (two-tailed t-test, p = 0.9030).

D. Without photostimulation, long-term memory performance was similar across three groups of mice (one-way ANOVA, p = 0.362).

We finally examined whether modulating post-odor MTC firing activities would have any influence on long-term memory formation. Inhibiting post-odor MTC firing activities in ChR2 expressing mice during training resulted in degradation of long-term memory formation for complex odor discriminations (Figure 4-10 B, two-tailed t-test, (1) for HX vs. PN binary mix, p = 0.0006; (2) for Octanols binary mix, p < 0.0001). This effect was specific to tasks with light stimulation, as the memory performance of Carvones binary mixtures in the absence of light stimulation was comparable to control WT mice (Figure 4-10 D, ordinary one-way ANOVA, p = 0.362). Further, disinhibiting post-odor MTC activities in Arch expressing mice facilitated long-term memory formation with a 0.5 s stimulus (Figure 4-10 C1, two-tailed t-test, p = 0.0077). For a 2 s stimulus, a high memory score was observed in WT mice. To check if post-odor disinhibition of MTC firing activities can further improve memory performance, we examined Arch expressing mice's memory performance for Octanols binary mixture with 2 s stimulus. We observed that these mice had memory performance similar to WT animals (Figure 4-10 C2, two-tailed t-test, p = 0.9030). The result suggests a possible upper limit for memory performance towards complex mixtures beyond which the memory performance doesn't improve further. Collectively, these results revealed the role of post-odor MTC activities in controlling long-term memory formation.

In conclusion, our results establish that bidirectional modification of OB GABAergic GAD65 +ve interneurons influences the degree of decorrelation in MTC ensemble activity patterns. Such manipulations during stimulus delivery control the ability of mice to learn to discriminate similar odorants while the information coded by post-stimulus firing activity of projection neurons controls the formation of long-term olfactory memories.

4.3.5 Olfactory performance-dependent refinement in sniffing behavior

One of the key findings from this work was the bidirectional modulation of olfactory learning and long-term memory performance by manipulating OB inhibitory activity during different stimuli presentation phases. In the previous chapter, we observed a refinement in sniffing behavior with learning. Thus, we were interested in studying whether modulation of olfactory performance by the inhibitory network influenced sniffing behavior in mice. We analyzed sniffing

frequencies during the decision-making period while mice were trained with optogenetic stimulations. When the learning speed was improved by photostimulating GAD65 +ve interneurons, mice displayed higher sniffing frequencies during the decision-making period (Figure 4-11 A, for HX vs. PN binary mix, two-tailed t-test, p = 0.0097, t = 3.268, df = 9. For Octanols binary mix, two-tailed t-test, p = 0.0088, t = 3.329, df = 9). Further, sniffing frequencies were measured during memory trials for mice trained to odor discrimination tasks with post-odor manipulation of MTC activities. When the memory performance was high, mice exhibited higher sniffing frequencies during memory trials (Figure 4-11 B, for HX vs. PN binary mix, two-tailed t-test, p = 0.004, t = 4.827, df = 12. For Octanols binary mix, two-tailed t-test, p = 0.0026, t = 3.872, df = 11). For Carvones binary mix, when mice were trained without photostimulation, we did not observe any difference in breathing frequencies during memory trials irrespective of the stimulus duration (two-tailed t-test, p = 0.4156, t = 0.8432, df = 12). In conclusion, our results suggest a strong association between OB network activity, olfactory performance, and sniffing behavior. The learning and memory-dependent modulation of sniffing behavior also hint towards a neural pathway connecting olfactory centers with respiratory centers.
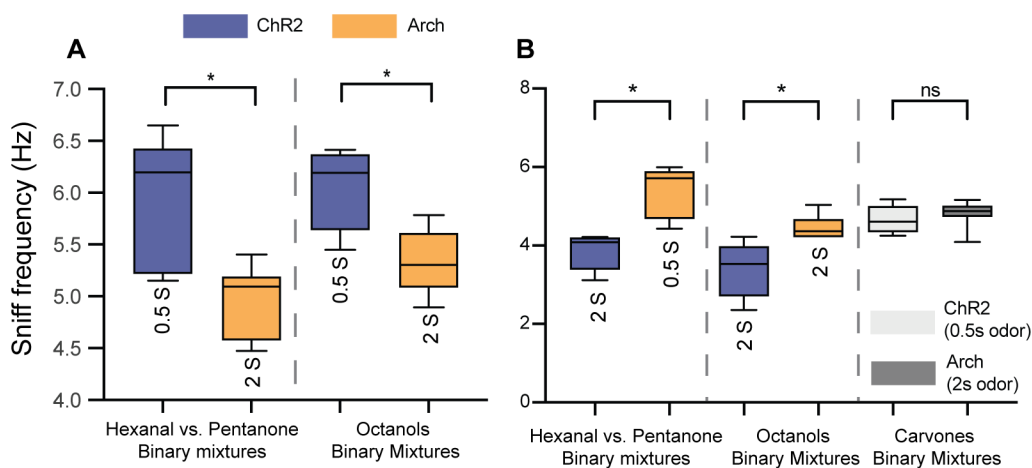
Figure 4-11: Modulation of sniffing frequencies with learning and memory.

A. Increase in sniffing frequencies observed during the decision-making window when learning pace was accelerated by stimulating GAD65 +ve interneurons (for HX vs. PN binary mix, two-tailed t-test, p = 0.0097, t = 3.268, df = 9. For Octanols binary mix, two-tailed t-test, p = 0.0088, t = 3.329, df = 9). The stimulus duration is mentioned beneath the box and whiskers.

B. During memory trials, breathing frequencies during odor presentation was higher when the memory performance was high (for HX vs. PN binary mix, two-tailed t-test, p = 0.004, t = 4.827, df = 12. For Octanols binary mix, two-tailed t-test, p = 0.0026, t = 3.872, df = 11). For Carvones binary mix, when both groups of mice are trained without photostimulation, no difference in breathing frequencies was observed during memory trials (two-tailed t-test, p = 0.4156, t = 0.8432, df = 12).

4.4 Discussion

Although it has been shown that olfactory discriminations can take place within 350-400 ms, no study has focused on the relevance of extra stimulus information in different facets of olfactory behavior. We trained mice on freely-moving odor discrimination tasks with different stimuli durations. Our results show the critical role of odor stimulus duration in setting the pace of discrimination learning and forming long-term odor memories. To understand the mechanistic differences, using Ca^{2+} imaging, we recorded from GCL interneurons in anesthetized and awake head-restrained animals by presenting odors for varying durations. Between short and long stimuli durations, we observed critical differences in interneuron responses. At a population level, this indicates that the degree of reformatting of MTC ensembles varies when stimulus duration is reduced, thereby influencing odor-driven behaviors. While odor representations formed during stimulus presentation guide discrimination learning, post-odor MTC activities help in stabilizing these representations leading to the formation of long-term olfactory memories. Thus, our results provide a novel MTC activity-dependent mechanism controlling odor discrimination learning and long-term memory formation.

4.4.1 Stimulus duration sets the pace of odor discrimination learning and long-term memory formation

Learning an olfactory discrimination task requires a comparison between alternating odor cues and the reward value of odors, and acquisition of rule learning. With repeated odor experience, there is a reduction of both excitatory and inhibitory MTC responses and dynamic reformatting of ensemble odor representations that accumulate over days (*20, 235*). This sort of plasticity enhances pattern separation, which is observed during active learning (*20*). When a stimulus is provided for 2 s, animals quickly learn odor discriminations independent of task complexities. In the previous chapter, we have shown that animals can perform odor discriminations within 350-400 ms when performing at maximal accuracy (Figure 3.3B). Whether this time is sufficient to make accurate decisions during the initial phases of odor discrimination learning is yet unclear. We trained mice to novel odor discriminations by shortening the stimulus duration. On reducing the time of odor presentation, mice efficiently performed monomolecular odor discriminations. However, when the odor similarity was increased, mice made more mistakes in the early stages of learning. With repetitive odor exposure, mice slowly picked up odor discriminations; however, maximal accuracies reached by these mice were significantly lower compared to mice trained on long stimulus duration. The results presented here illustrate that there is a temporal limit to the neural reformatting in MTC ensembles. As a consequence, when the stimulus length is reduced for

complex odors, the pattern separation process may be incomplete, resulting in animals making incorrect decisions. With repetitive odor presentations, neural responses sharpen within OB circuitry, which primes the system for faster temporal patterning of MTC spiking (*19*, *235*). This allows for learning at a later stage of training when an odor is presented for short durations.

The refinement in MTC activities can be attributed to the circuit within and beyond OB. Within a glomerulus, the OSN-MTC synapse formed is capable of undergoing long-term potentiation (LTP) (*302*). Following high-frequency OSN stimulation, N-methyl-D-aspartate (NMDA) receptors on MTCs get activated, and cells display prolonged, increased spiking. At the same time, low-frequency OSN stimulation can exhibit long-term depression (LTD) on the same synapse (*303*). The interaction between MTCs and GABAergic interneurons within OB has been shown to improve pattern separation and aid in odor discrimination learning (*14*, *41*, *304*). Along with these changes, feedback from PCx can enhance the separation between overlapping MTC ensemble responses (*202*). Indeed paired stimulation on proximal synapses formed between piriform cortical neurons and GCs has been shown to release Mg^{2+} block from NMDA receptors at distal dendrodendritic synapses formed between MTCs and GCs (*305*, *306*).

The changes in OB odor representations with learning (*20*, *32*, *235*, *307*) have been shown to stabilize over time (*40*, *308*). Once mice had learned the task, retrieval of memories of the previously learned task was checked thirty days post-training. Mice trained with a short stimulus duration had a consistent deficit in long-term memory formation for all complex odors tested. One may argue that this deficit is attributed to poor learning performance with short stimuli durations. To analyze this, we compared learning accuracies from the last 100 trials with memory scores. The percentage reduction in olfactory performance was determined by calculating the difference in percentage correct responses between the last 100 trials of training with memory trials. The percentage reduction was ~40% for mice trained to short stimuli compared to 5-15% reduction observed for mice trained to 2 s stimulus (Figure 4-12). This showcases an explicit deficit in memory performances with short stimuli.
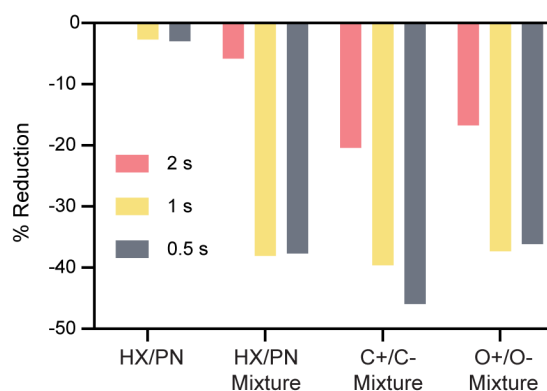
Figure 4-12: The reduction in olfactory performance is aggravated with a lowering of stimuli duration.

To quantify the reduction in olfactory performance, learning accuracy from the last 100 trials of training was subtracted from the memory score, and the percentage difference was measured. For a simple odor, across different stimuli durations, the percentage reduction was less than 5%. On the other hand, for binary mixtures, the percentage reduction in olfactory performance was ~40% for mice trained to short stimuli compared to 5-15% reduction observed for mice trained to 2 s stimulus.

4.4.2 Enhanced activity of inhibitory GCs with increasing odor duration

On odor stimulation, widely distributed granule cell activities provide an intuitive mechanism for increasing temporal variability in MTC ensembles that promote discriminability (*41*). We used a microendoscopic imaging technique to record population GAD65 +ve interneuron activity. This technique offers a possibility to image from a large field, which is difficult with two-photon Ca^{2+} imaging. On comparing GAD65 +ve interneuron activity under anesthetized and awake conditions, we found differences in the kinetics of odor-evoked interneuron responses. For the two stimuli durations across different odors, the rise in activity was slow in anesthetized mice, and the activity sustained for a longer duration in the post-stimulus period. Further, we observed a slight attenuation in odor-evoked interneuron activities under awake conditions compared to the anesthetized state. In awake mice, passive sensory experiences have shown to recruit non-responsive MTCs, thus causing a reorganization of MTC ensemble activities (*20*). The robust odor-evoked reformatting in MTCs under awake condition, at least in part, can explain the weakening of interneuron activity that we observe under awake state.

In awake animals with 0.5 s stimulus presentation, Ca^{2+} dynamics measured from GCL interneurons showed a subdued interneuron activity compared to 2 s stimulus duration. Strikingly, in these naive animals, interneuron activity peaked at the same time for 0.5 s and 2 s stimulus; however, the maximum fluorescence change was less for 0.5 s stimulus when averaged across six different odors. Further, in comparison with a 2 s stimulus, overall activity was less when the stimulus was presented for 0.5 s (Figure 4-8 B). Thus, time-dependent differences in interneuron activities were observed both under anesthesia and awake states. Overall, reduced interneuron activity in response to short stimulus presentation provides solid evidence supporting the lack of temporal refinement in MTC ensembles, thereby leading to slow learning and impairments in memory formation.

4.4.3 Optogenetic modulation of odor discrimination learning

To improve the extent of pattern separation in MTC ensembles during short stimulus presentation, we optogenetically stimulated the activity of OB GABAergic interneurons using GAD65-ChR2 mice. Genetically targeted light-gated ChR2 allows optical activation of neurons

with high spatial and temporal resolution (*252, 309, 310*). Consistent with previous results (*14*), we observed that optogenetic stimulation improved the learning of binary odor mixtures. In a separate set of experiments, using GAD65-Arch mice, in which all GAD65 +ve interneurons expressed Arch, we hyperpolarized OB interneurons while odors were presented for a long duration. Notably, under these conditions, mice had difficulties in performing odor discriminations which were reflected in their learning accuracy (Figure 4-9 B1 and B2). The internal control experiment with Carvones binary mixture ensured that the effect we observed was specific to optogenetic modification of neural representations (Figure 4-9 B3). Our results suggest that GAD65-ChR2 photostimulation forces a global, yet specific, GABA release mimicking an increase in synaptic inhibition (*21*), favoring pattern separation in MTC ensembles, thus improving odor discrimination accuracies. In contrast, upon Arch photostimulation, MTCs receiving sparse inhibition may tend to fire more regularly (*41*). When two similar odors are presented under these conditions, population responses of MTCs are identical, and odor discrimination becomes difficult. In conclusion, our findings support the functional importance of OB-mediated pattern separation during odor presentation in the processing of similar odorants.

4.4.4 Post-stimulus firing activity controls long-term memory formation

Rodents display a change in behavior towards rewarded and non-rewarded stimuli in response to odor experience. The persistence of neural network changes leading to a behavioral shift with time can be defined as odor memory. Previous studies have implicated the role of hippocampus (*311, 312*), amygdala (*313*), PCx (*314, 315*), AON (*192*), and OFC (*197*) in odor memories. In addition, considerable efforts are being made to elucidate mechanisms contributing to odor memories within OB. There is evidence to prove that turnover of GCs in OB by the process of adult neurogenesis and its survival is sensitive to learning and memory (*316–318*). The impact of adult-born neurons in olfactory processing has been demonstrated by selectively expressing ChR2 in adult-born neurons. Activating adult-born GCs accelerated complex odor discrimination learning and improved memory (*319*).

In mouse OB, following odor presentation, a fraction of MTCs maintain their odor-evoked responses even after stimulus delivery cessation. Using optogenetic manipulations, we developed a novel way to manipulate post-odor MTC activities and study its role in memory formation. Using optogenetic tools to artificially manipulate memory formation processes has been progressively used by neuroscientists. In a recent study, optogenetic manipulation of the experience-tagged neuronal population within AON has revealed that odor engrams are stored within AON, and their activity is necessary for the behavioral expression of odor memories (*192*). Another study used

paired optogenetic stimulation of specific subsets of glomeruli and distinct inputs into the ventral tegmental area to create fully artificial memory in the absence of stimuli in mice (*320*).

Our optogenetic manipulations of MTC activities during the post-odor period showcase that attenuation of MTC output during this period can negatively impact long-term memory formation. In an attempt to promote long-term memory formation, we disinhibited MTC activities during the post-odor period. Such manipulation led to improvement in long-term memory compared to animals trained without photostimulation. Hence, our results delineate the role of post-odor neural representations in long-term memory formation. Our study now raises an important question. How do post-odor MTC activities store long-term memories? It is likely that MTC post-odor activities might be accelerating the long-term plasticity of synapses formed between (1) OB interneurons and MTCs, and (2) cortical neurons and OB interneurons.

4.4.5 Sustained high-frequency sampling correlates with odor discrimination learning and long-term memory formation

We now know that animals learn to increase their sniffing frequency, specifically during the decision-making period (Figure 3-4 C). There exists a close relationship between respiration and intrinsic network functioning in OB (*321–323*). Active respiration can synchronize MTC activities (*278*), and the absence of nasal airflow in double tracheotomized rats can abolish respiration-coupled spiking in MTCs (*279*). Further, odor sampling at sustained higher frequencies can lead to increased decorrelation of MTC population activities over time (*280*). At the population level, nasal respiration drives neural activity oscillations in OB that reaches PCx and further downstream to the hippocampus (*321*, *324–326*). These oscillations have been implicated in linking sensory and memory networks that underlie cognitive functioning (*325*). Direct evidence has been provided by studies in human subjects that correlate nasal respiration to memory encoding and recall (*326*, *327*). Using optogenetic modulation of inhibitory interneuron activity during the stimulus and post-stimulus period, we observed specific differences in discrimination learning and memory formation. Strikingly, improvement in learning and long-term memory performance coincided with increased sniffing frequency (Figure 4-11 A and B). When taken together, these findings establish a connection between breathing and neural activity patterns associated with olfactory learning and long-term memory formation.

4.5 Limitations

This study has some limitations. First, we modulated the firing activities of MTC by manipulating inhibitory interneurons in OB. Although we targeted the majority of the interneuron

population, this approach fails to consider the role of other interneurons in tuning MTC responses. A more direct approach would be to manipulate MTCs directly using cell-type-specific markers like Pcdh-21 and Tbet-21, specific to mitral and tufted cells. Direct manipulation of MTC activities during different odor presentation phases may improve our understanding of these responses in different odor-related behaviors. Secondly, while imaging Ca^{2+} dynamics of inhibitory interneurons, we could not distinguish individual cells due to a high expression of Ca^{2+} sensors in the densely populated GCs in GCL. Although such imaging provides us with the knowledge of the population dynamics of these neurons in response to odor presentation, it is difficult to know how odor information is coded in individual cells.

4.6 Future direction

This study demonstrates that post-odor responses aid in the formation of long-term odor memories. However, how these post-odor activities are maintained remains unanswered. With little or no contribution from sensory neurons, maintenance of MTC post-odor activities may be attributed to intrinsic mechanisms within the bulb (*33*, *34*) and top-down centrifugal inputs from olfactory cortical areas. As post-odor activities are stronger and persist longer in awake mice than anesthetized mice, the role of cortical inputs in maintaining such activities can be strongly hypothesized. As a preliminary study to locate synaptic plasticity events in different areas of the olfactory cortex, Activity-regulated cytoskeleton-associated protein (Arc) expression was checked after training mice to protocols that either attenuated or enhanced post-stimulus MTC activities. Following an increase in synaptic activity, Arc expression is upregulated in a range of behavioral paradigms (*328–330*). Arc, therefore, provides a means to identify cells undergoing synaptic plasticity, a process essential for memory consolidation. Training mice to odor discrimination task with post-odor inhibition of GAD65 +ve interneurons significantly increased the Arc expression in PCx, OT, and OFC compared to mice trained with post-odor stimulation of GAD65 +ve interneurons (Figure 4-13 C2, one-way ANOVA with Tukey's multiple comparison test. Between Control vs. Post-odor stimulation, p = 0.1577. Between Control vs. Post-odor inhibition, p < 0.0001. Between Post-odor inhibition vs. Post-odor stimulation, p < 0.0001. (E2). One-way ANOVA with Tukey's multiple comparison test. Between Control vs. Post-odor stimulation, p = 0.2348. Between Control vs. Post-odor inhibition, p < 0.0001. Between Post-odor inhibition vs. Post-odor stimulation, p = 0.0002). PCx sends out most of the centrifugal inputs to OB and maybe one of the potential sites controlling MTC activities following odor stimulation (*180*, *331*). Specifically, PCx has direct projections to widespread portions of the prefrontal cortex and OFC (*180*, *189*, *210*). Such reciprocal connections of PCx with higher cognitive areas make it a potential

site contributing to memory formation. OT is an important center for decoding the odor reward category and relaying this information to higher cognitive areas (*196*). OFC is strongly and reciprocally connected with perirhinal and entorhinal areas and is involved in odor identification and memory representations of specific stimuli (*197, 332–334*). Hence, it would be interesting to study and compare the neural activities in PCx, OT, and OFC during and after odor presentation.
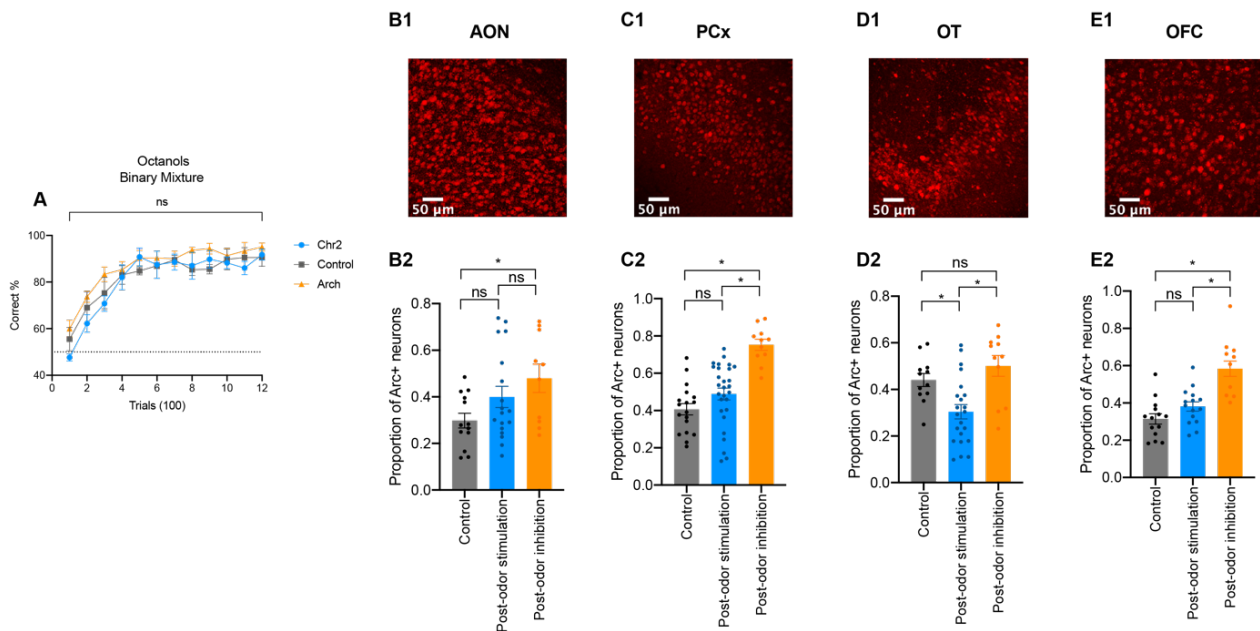
Figure 4-13: Expression of Arc protein in different areas of olfactory cortex following odor discrimination training coupled with post-odor manipulation of GAD65 +ve interneurons.

A. Learning accuracies for Octanols binary mixture show that manipulating the post-odor GAD65 +ve OB interneuron responses does not influence the learning efficacy (two-way ANOVA, $F_{(22,108)} = 0.4884$, $p = 0.9723$) (n = 4-5 mice).

B1. Representative image of Arc protein expression in AON.

B2. The expression profile of Arc protein in AON shows a noticeably increase when post-odor responses are inhibited compared to control mice. However, no difference is observed when GAD65 +ve interneurons are stimulated in the post-odor period (one-way ANOVA with Tukey's multiple comparison test. Between Control vs. Post-odor stimulation, $p = 0.2456$. Between Control vs. Post-odor inhibition, $p = 0.042$. Between Post-odor inhibition vs. Post-odor stimulation, $p = 0.4730$).

C1. Representative image of Arc protein expression in PCx.

C2. The expression profile of Arc protein in PCx shows a noticeably increase when post-odor responses are inhibited compared to control mice and in mice where post-odor responses are stimulated (one-way ANOVA with Tukey's multiple comparison test. Between Control vs. Post-odor stimulation, $p = 0.1577$. Between Control vs. Post-odor inhibition, $p < 0.0001$. Between Post-odor inhibition vs. Post-odor stimulation, $p < 0.0001$).

D1. Representative image of Arc protein expression in OT.

D2. The expression profile of Arc protein in OT shows a significant decrease when post-odor responses are stimulated compared to control mice and in mice where post-odor responses are inhibited. The Arc expression of animals trained with post-odor inhibition was similar to control mice (one-way ANOVA with Tukey's multiple comparison test. Between Control vs. Post-odor stimulation, $p = 0.02$. Between Control vs. Post-odor inhibition, $p = 0.5283$. Between Post-odor inhibition vs. Post-odor stimulation, $p = 0.0008$).

E1. Representative image of Arc protein expression in OFC.

E2. The expression profile of Arc protein in OFC shows a noticeably increase when post-odor responses are inhibited compared to control mice and in mice where post-odor responses are stimulated (one-way ANOVA with Tukey's multiple comparison test. Between Control vs. Post-odor stimulation, $p = 0.2348$. Between Control vs. Post-odor inhibition, $p < 0.0001$. Between Post-odor inhibition vs. Post-odor stimulation, $p = 0.0002$).

Another important observation from this work is the modulation of sampling behavior with learning and memory formation. Till date, there is no information available regarding direct connectivity between olfactory centers with respiratory centers. However, our results strongly suggest a link between these centers. Although the proposition of a direct link between the respiratory and olfactory center is alluring, we propose the existence of an intermediate locus linking these two regions (Figure 4-14). Such a neural locus should receive olfactory information and also have direct input from respiratory centers. As our behavioral paradigm is reward-oriented, Lateral Hypothalamus (LH) emerges as a potential site as it is a vital feeding center (*335*). The preBötzinger Complex, a structure in the medial medulla responsible for respiratory rhythm generation, has projections throughout the hypothalamus, including LH (*336*). Further, projection neurons in the olfactory cortex send inhibitory output to LH, modulating odor-guided behaviors (*337*). Additional work is demanded to study this circuit in detail.
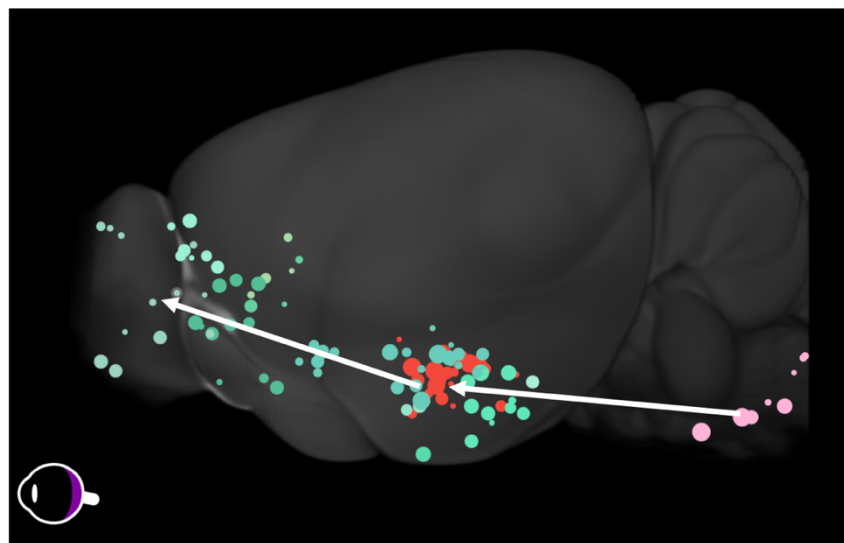
Figure 4-14: Putative pathway connecting respiratory centers with olfactory centers via LH.

To identify the pathway connecting respiratory centers to olfactory centers, a projection mapping image atlas provided by Allen Brain atlas was used. This tool provides serial two-photon tomography data detailing axonal projections labeled by rAAV tracers. Pink spots in the above figure represent areas in respiratory centers which have axonal connectivity with LH. The red spots are loci within LH which have connectivity with olfactory cortex and respiratory centers. The green spots represent areas of olfactory circuit receiving axonal projections from LH.

CHAPTER 5

Quantitative assessment of olfactory dysfunction accurately detects asymptomatic COVID-19 carriers

Adapted from: **A. S. Bhattacharjee**, S. V. Joshi, S. Naik, S. Sangle, N. M. Abraham, Quantitative assessment of olfactory dysfunction accurately detects asymptomatic COVID-19 carriers. *EClinicalMedicine*. **28**, 1-13 (2020).

5.1 Introduction

In humans, olfactory dysfunctions have been described in several neurodegenerative diseases like Alzheimer's disease (*71*), Down syndrome (*73*), and dementia (*74*); motor diseases like Parkinson's disease (*72*), and amyotrophic lateral sclerosis (*338*); and other disorders like depression (*339*) and Wilson's disease (*340*). Some obstructive or inflammatory processes triggered by upper respiratory tract viral and bacterial infections can also impair olfactory function (*4*). The occurrence and severity of olfactory dysfunctions may be related to changes in sensory perception and cognitive abilities that occur during the progression of these diseases. For precise quantification of olfactory fitness in these patients, there is a need to develop methodologies that test sensory as well as cognitive skills in human subjects.

In December 2019, SARS-CoV-2 triggered an outbreak in Wuhan, China. COVID-19 subsequently spread rapidly to several countries, and as of April 27th, 2021, 147,539,302 cases have been confirmed worldwide, and over 3,116,444 deaths have been attributed to the virus (https://covid19.who.int/). A plethora of symptoms characterize COVID-19 ranging from serious complications such as pneumonia with respiratory failure, mild-to-moderate flu-like symptoms, and asymptomatic forms of the disease (*341*, *342*). While it is easy to identify people who have flu-like symptoms, the lack of widespread population testing makes identifying a large number of asymptomatic COVID-19 carriers difficult (*343*). With an increasing number of cases, reports suggested smell loss as a predominant symptom for COVID-19 (*49*, *50*, *54*, *77*, *78*, *344*, *345*).

How does SARS-CoV-2 infection cause olfactory dysfunction? As discussed in chapter 1, odor sensation begins when odorants bind to ORs expressed on OSNs in the olfactory epithelium. The supporting (sustentacular) cells in the olfactory epithelium express high levels of angiotensin-converting enzyme 2 (ACE2) and Transmembrane Protease Serine 2 (TMPRSS2), two proteins needed for SARS-CoV-2 cellular entry (*55*, *56*, *346*). Damage to supporting cells in the olfactory epithelium results in inflammatory changes (*57*) that may indirectly impair OSN functioning and

cause subsequent OSN damage. The virus-induced disruption of OSN activity through the malfunctioning of supporting cells can attribute to smell loss in COVID-19 patients.

In light of reports indicating the onset of anosmia as a prevalent symptom in COVID-19 patients (*77, 79, 347, 348*), testing olfactory dysfunctions can be an effective method for detecting and isolating these patients. Assessing minor dysfunctions may not be feasible using conventional approaches, owing to the lack of accuracy in administering odor stimuli to individuals (*62, 349*). Therefore, we custom-built an olfactory-action meter with mass-flow controllers to provide well-defined odor pulses to human subjects. Our olfactory-action meter, which was designed initially to quantitate the olfactory function of healthy subjects, was modified to meet the safety requirements for usage in COVID-19 clinics. Using this olfactory-action meter, we designed a quantitative olfactory function test to assess olfactory capabilities in asymptomatic COVID-19 patients. Considering the virus-induced impairments of the olfactory epithelium, we assessed the detection threshold for various odorants to estimate olfactory sensitivity in asymptomatic COVID-19 patients. Further, we developed a novel test paradigm that evaluated olfactory matching accuracy, reflecting neurophysiological problems diagnosed in COVID-19 patients (*63, 64, 67, 350, 351*). By refining the test parameters with healthy subjects, we optimized the duration of the olfactory function test to twenty minutes. On evaluating sensory-cognitive olfactory defects, we observed that 82% of asymptomatic COVID-19 patients displayed distinct olfactory dysfunctions compared to normal healthy subjects. Therefore, this method can efficiently provide a systematic sensitive evaluation that can be used in clinics to quantify the extent of olfactory dysfunction in asymptomatic carriers.

5.2 Materials and methods

5.2.1 Study population

Our study had distinct cohorts of normal healthy subjects (Table 5-1) and asymptomatic COVID-19 patients (Table 5-2). The healthy subjects who participated in this study were residents of the IISER-Pune campus. These individuals did not manifest any symptoms of COVID-19 when they were tested for olfactory functioning. The inclusion criteria for normal healthy subjects were:

1. Subjects' willingness to participate in the study without any monetary expectations. Participants were fully briefed about the study's design and signed a consent form to participate in the study.
2. No travel history or movement outside the city 14 days before the test session.
3. No inadvertent interaction with COVID-19 positive patients.
4. No active respiratory tract infection or any nasal blockage.

5. No signs of COVID-19 (fever, rhinorrhea, dry cough, sore throat, and dyspnea) were observed (Table 5-3).

The asymptomatic COVID-19 patients were individuals with an active infection of SARS-CoV-2 who were admitted to Byramjee Jeejeebhoy Government Medical College and Sassoon General Hospitals' (BJGMC & SGH) COVID-19 isolation wards. The SARS-CoV-2 infection was confirmed by real-time reverse-transcriptase polymerase chain reaction (RT-PCR) based detection of the virus from nasal and throat swab. The confirmatory test protocol for detection of COVID-19 was approved by the Indian Council of Medical Research (ICMR). Patients who registered for the test became infected as a result of inadvertent contact with COVID-19 patients in their neighborhood or at work, or as healthcare workers (clinicians and support staff) who became infected while on the job. At the time of the test, none of these patients were diagnosed with Parkinson's disease, Alzheimer's diseases, or other neurological disorders, as smell dysfunctions are an early indicator of these diseases.

Inclusion/exclusion criteria for asymptomatic COVID-19 patients were:

1. Patients who were asymptomatic on the day of olfactory function test (Table 5-3).

2. The patients who were willing to participate in the research study were included. Before the study began, participants signed a consent form.

3. Patients with persistent symptoms were excluded from the study.

4. One patient (BJMC P24) took part in the study, but on the day of the olfactory function test, the patient received a negative RT-PCR result. As a result, patient's data was not included in the study.

5. One patient (BJMC P4) was not eager to participate for the entire duration of the test. Hence, detectability at 50% (v/v) concentration was first evaluated. Due to good detection at 50 % concentration (Refer to Table 5-2 for details), the patient was requested to participate in the olfactory matching test. The patient declined further participation. Due to incomplete data points, patient's data were excluded from the analysis.

In total, thirty-seven normal healthy subjects and thirty-four asymptomatic COVID-19 patients enlisted for olfactory function test. To prevent any bias arising due to subject's lack of interest, only the individuals who willingly enrolled in the study were called for the olfactory function test.

Median of detection indices measured for normal healthy subjects (%)	0.5	0.7	0.8	1		
Concentration tested (% v/v)	9.1	16.6	23.1	50	Normalized olfactory matching performance index	Olfactory deficits
Subject ID						
NS1	0.6	1	1	1	1.04	No
NS2	0.3	0.9	0.9	1	1.19	No
NS3	0.5	0.8	0.9	1	1.19	No
NS4	0.4	0.6	0.6	1	0.74	Yes
NS5	0.8	1	1	1	0.74	No
NS6	0.4	0.8	0.5	1	1.04	No
NS7	0.2	0.3	0.8	1	1.04	No
NS8	0.1	0.8	0.8	1		No
NS9	0.1	0.8	0.5	0.8	1.34	No
NS10	0.9	0.7	0.9	1	0.89	No
NS11	0.7	0.6	1	1	1.19	No
NS12	0.8	0.9	1	1	0.89	No
NS13	0.4	0.7	0.7	1	0.74	Yes
NS14	0.5	0.7	1	1	1.04	No
NS15	0.5	0.7	1	1	1.04	No
NS16	0.6	0.5	0.6	1	1.19	No
NS17	0.7	0.9	1	1	1.19	No
NS18	0.5	0.5	0.8	1	0.59	No
NS19	0.5	0.5	0.5	1	0.89	Yes
NS20	0.5	0.6	0.7	0.9	0.74	Yes
NS21	0.7	0.8	1	1	0.74	No
NS22	0.6	0.7	0.8	1	0.89	No
NS23	0.7	0.7	1	1	0.89	No
NS24	0.8	0.8	1	1	1.04	No
NS25	0.6	0.5	0.7	1	1.19	No
NS26	0.7	0.7	0.8	1	0.74	No
NS27	0.8	1	1	1	1.04	No
NS28	0.5	0.5	0.7	0.9	1.04	No
NS29	0.5	0.5	0.6	0.6	1.49	No
NS30	0.1	0.4	0.5	0.9	0.89	Yes
NS31	0.6	0.4	0.3	1	1.04	No
NS32	0.5	0.9	1	1	1.04	No
NS33	0.3	0.2	0.2	1	1.04	No
NS34	0.7	0.9	0.9	1	1.04	No
NS35	0.4	0.6	0.9	0.9	1.34	No
NS36	0.6	0.9	1	0.9	0.89	No
NS37	0.5	0.7	0.8	1	0.74	No

Table 5-1: Tabulation of olfactory function scores calculated from normal healthy subjects.

5.2.2 Ethics committee approval information

The experimental protocols used in this study were authorized by the IISER Ethics Committee for Human Research (IECHR/Admin/2020/001), Biosafety Committee at IISER-Pune, and the Ethics Committee at BJGMC & SGH, Pune, India (BJGMC /IEC/Pharmac/ND-Dept 0420053-053).

Median of detection indices measured for normal healthy subjects	0.5	0.7	0.8	1		
Concentration tested (% v/v)	9.1	16.6	23.1	50	Normalized olfactory matching performance index	Olfactory deficits
Patient ID						
BJMC P1	0.0	0.0		0.1		Yes
BJMC P2	0.0	0.0	0.0	0.0		Yes
BJMC P3	0.0	0.0	0.0	0.3		Yes
BJMC P4[*]				0.9		Not evaluated
BJMC P5	0.0	0.0	0.0	0.0		Yes
BJMC P6	0.0	0.0	0.0	0.4		Yes
BJMC P7	0.5	0.5	0.6	0.6	0.66	Yes
BJMC P8	0.4	0.6	0.6	0.4		Yes
BJMC P9	0.8	0.6	0.6	1.0	0.89	Yes
BJMC P10	0.4	0.4	0.6	0.7	0.44	Yes
BJMC P11	0.7	0.9	1.0	1.0	0.89	No
BJMC P12	0.0	0.3	0.3	0.5		Yes
BJMC P13				0.0		Yes
BJMC P14	0.1	0.1	0.2	1.0	0.44	Yes
BJMC P15	0.0	0.0	0.0	0.0		Yes
BJMC P16	0.0	0.2	0.1	0.8	1.12	Yes
BJMC P17	0.1	0.6	0.2	0.7	0.56	Yes
BJMC P18	0.6	0.6	1.0	1.0	1.30	No
BJMC P19	0.0	0.2	0.3	0.8	0.89	Yes
BJMC P20	0.8	0.8	0.7	0.8	0.89	Yes
BJMC P21	0.6	1.0	1.0	1.0	0.89	No
BJMC P22	0.1	0.2	0.3	0.1		Yes
BJMC P23	0.0	0.5	0.7	0.8	1.30	Yes
BJMC P25	0.0	0.0	0.0	0.0		Yes
BJMC P26	0.0	0.0	0.0	0.4		Yes
BJMC P27	0.4	0.6	0.5	0.7	0.66	Yes
BJMC P28	0.6	0.5	0.4	0.7	0.82	Yes
BJMC P29	0.4	0.3	0.8	1.0	1.32	No
BJMC P30	0.4	0.8	0.8	1.0	0.74	No
BJMC P31	0.8	0.7	0.7	0.9	0.89	Yes
BJMC P32	0.8	0.7	0.9	1.0	1.04	No
BJMC P33	0.0	0.1	0.2	0.5		Yes
BJMC P34	0.0	0.0	0.1	0.7	0.18	Yes
BJMC P35	0.0	0.0	0.0	0.8	0.56	Yes

* The data for BJMC P4 was not analyzed because the subject refused to take part in the entire test.

Table 5-2: Tabulation of olfactory function scores calculated from asymptomatic COVID-19 patients.

5.2.3 Sample size determination

To determine the sample size needed to detect some effect with inferential statistics, we performed *a priori* power analysis. We hypothesized that the detectability at different threshold concentrations and olfactory matching accuracy would return a minimum difference of 10% between the study groups. On running the analysis, we realized a minimum of twenty subjects are required in each cohort to expect a 10% difference for the different readouts we propose here.

	Healthy subjects	COVID-19 patients
Age (Years)	36±8	35±12
Sex		
Male	23 (62.2%)	21 (61.8%)
Female	14 (37.8%)	13 (38.2%)
Symptoms during testing		
Fever	0 (0%)	0 (0%)
Rhinorrhea	0 (0%)	0 (0%)
Dry cough	0 (0%)	0 (0%)
Sore throat	0 (0%)	0 (0%)
Dyspnoea	0 (0%)	0 (0%)
Reason for hospitalization		
Mild symptoms	N.A.	7 (21%)
Contact tracing	N.A.	17 (50%)
Contact with COVID-19 patients	N.A.	10 (29%)

Table 5-3: Details of normal healthy subjects and asymptomatic COVID-19 patients included in the study.

5.2.4 Study location

Instrumentation, standardization, and PID measurements were performed at the Laboratory of Neural Circuits and Behavior (LNCB) at IISER Pune. The olfactory function test for healthy subjects was performed in the common area of the IISER Pune Biology Department, which matched the indoor environment of COVID-19 isolation wards at BJGMC & SGH. This was deliberately done to minimize the variability of odor profiles with differing temperatures and humidity. The olfactory function test for healthy subjects was carried out between 22nd April 2020 and 10th May 2020. To assess olfactory abilities of asymptomatic COVID-19 patients, we relocated the instrument to the COVID-19 isolation ward at BJGMC & SGH. Here, the study was conducted between 12th May 2020 and 21st May 2020. During this time, asymptomatic COVID-19 patients admitted in two separate wards were tested for olfactory proficiency.

5.2.5 Olfactory-action meter design

We developed a novel ten-channel olfactory-action meter that allows participants to smell different odors through a low-cost disposable odor delivery unit. High-efficiency particulate air (HEPA) is pumped at a rate of 5 l/min in the olfactory-action meter. The sterile air passes through a filter that traps residual background odor before reaching the olfactory-action meter. The sterile air on entering the olfactory-action meter is divided into eleven channels by a metallic manifold, and the channels are attached to ten mini Mass Flow Controllers (MFC) (Pneucleus Inc.) and one Main MFC. The functioning of these MFCs is software-driven, and the experimenter can independently control the amount of air flowing through each of them. The main MFC output is bifurcated into ten channels with a solenoid valve assembly (one valve for each odor channel). The software can regulate sterile air distribution using these solenoid valves. Each of the ten mini MFCs is connected to ten different odor tanks. 15 ml borosilicate glass bottles were used as odor tanks with a customized glass cap filled with 4 ml of pure, undiluted odorants. The glass cap has separate

channels for the input of sterile air and output of odorized air. The odorized air from the odor tank passes through an inert Tygon tube and mixes with a channel of deodorized sterile air (controlled by the main MFC) before entering the glass nozzle. The total air output from the nozzle is the sum of the volume of odorized and deodorized sterile air. The concentration of odor in the output air stream can be calculated by taking a ratio of the volume of odor vapors to the volume of total odorized airflow and is defined as volumetric odor concentration (% v/v). Hence, by changing the volumetric concentration ratio, we selected a concentration range between 9.1% to 50% (v/v). The odor delivery unit is a 15 cm long and 0.8 cm wide tube with a suction outlet. Four separate layers of a surgical mask-grade filter are placed along the odor delivery unit's length, and the suction outlet is guarded by a 0.2 µm Polyethersulfone (PES) filter membrane (Whatman Uniflow). A vacuum pump operating at ~450 mbar was attached to the PES filter at the suction outlet of the odor delivery unit. The exhaust from suction outlet passes through two 0.2 µm HEPA filters and one 0.2 µm PES filter before getting discharged to a 60 cm long activated carbon filter. The risks of cross-contamination between participants and contamination of the instrument are nullified by the combined effect of vacuum suction and use of a sterile odor delivery unit for each subject. During a trial, air through the odor delivery unit is diverted to the exhaust for the entire duration, except during the odor delivery period. During odor presentation, vacuum switches off, enabling odorized air to pass from the odor nozzle to the tip of the odor delivery unit. A plexiglass separating wall is wrapped around the instrument to prevent a patient from making physical contact with the instrument. A port is designed for the tip of the odor delivery unit to emerge from the separating wall. The height of this port is fixed at 160 cm, which is the average height found in the Indian population. Participants always wore surgical masks while performing olfactory function tests. We reduced the risk of any viral particle entering the device through these safety measurements and made it ideal for use in clinical settings (See Results, Figure 5-1A).

5.2.6 Odors used

The odors used in olfactory function tests were monomolecular odorants, widely used in human olfactory psychophysical studies (*293*, *352*). Odors used were Acetophenone, (-)-Carvone, 1,4-Cineole, Ethyl butyrate, Eugenol, Hexanal, Isoamyl acetate, (+)-Limonene, (-)-Limonene, and Octanal. All these odors were purchased from Sigma Aldrich and had ~99% purity. The odor profiles were measured using miniPID (Aurora Scientific) at 50% concentration (v/v). Measurements were made by placing the miniPID probe at the tip of odor delivery unit.

5.2.7 Olfactory function test

At the beginning of the test session, subjects were briefed about the study paradigm and were asked to read the consent form carefully. Consent forms were available in three different languages (English, Hindi, and Marathi). Once subjects were acquainted with the test's procedural aspects, odor detection indices measurements were obtained from them, followed by the olfactory matching test.

5.2.8 Measurements of odor detection indices

For measuring odor detectability at threshold concentration, we delivered different odors in ascending order of concentration, and the odor sequence was pseudo-randomized at each concentration level. The measurements were repeated until the odor was detected for two successive concentrations in normal healthy subjects, with the lower concentration being reported as a detection threshold for that odor. We also checked the detectability at 50% (v/v) odor concentration. It was observed that the majority of participants detected all odors at the lowest three concentrations (9.1%, 16.6%, and 23.1% [v/v]). For asymptomatic COVID-19 patients, these three dilutions were used to probe their detection abilities at threshold concentrations.

In a given trial, odors were presented for 4 s, followed by an ITI of 17.2 s. During the preloading time of 3.2 s before odor presentation, odorized air passed through the odor delivery unit's suction line into the exhaust. At the end of the preloading period, vacuum was turned off, allowing odorized air to be delivered to the subject. The preloading time minimized the odor delivery delay, and a well-defined pulse was obtained. At the time of odor presentation, subjects were asked to breathe normally and assess whether they could detect the odors. The participants were specifically instructed to detect and avoid identifying the odors. A 200 ms tone was played 1 s prior to odor delivery to alert participants of trial onset. At the end of odor delivery, the participant verbally responded 'YES' or 'NO' depending on whether they detected any odor. After delivering odors at three different concentrations, a short interval of two minutes was provided to each participant. After the interval, the detection abilities of the participant were examined at 50% odor concentration. However, the participant was unaware of the increased odor concentration, which prevented any preconceived responses towards odorants at higher concentrations. We calculated the detectability index for each odor and overall detection accuracy at each concentration level at the end of the tests. Detection accuracy was calculated by measuring the fraction of odors detected at a given concentration level. The percentage reduction in detection abilities of asymptomatic COVID-19 patients was evaluated by calculating the AUC measured for different concentrations of ten odorants. For 38.2% of the patients (13 out of 34), the detection accuracy was found to be

≤50% at 50% v/v odor concentration. To check the detectability for pure odorants, these thirteen patients were requested to further participate in detecting pure, undiluted odors. Ten patients agreed to participate, and we proceeded to measure detection accuracies by presenting paper strips dipped in pure odors. This additional step was not conducted for healthy participants as all of them were able to detect more than five odors at a 50% concentration level.

The median detectability indices at each concentration level were calculated for healthy participants. The median scores were then used as threshold values with which the patient's detection indices were compared. To categorize patients with 'olfactory deficits', stringent criteria were applied as follows: Condition 1 – detection scores of patients were less than median scores at all four concentrations tested. Condition 2 – detection scores were less for two or more concentrations and normalized olfactory matching performance index of less than 100 (explained in the next session). To check the sensitivity of our classification scheme, we performed receiver operating characteristic (ROC) analysis on detection indices measured from healthy subjects and asymptomatic COVID-19 patients.

5.2.9 Measurements of odor matching performance index

Participants were asked to participate in the olfactory matching test if they attained ≥60% detection accuracy at 50% v/v odor concentration level (1 out of 21 COVID-19 patients declined participation). The odor matching test measured how well participants remembered the first odor in order to compare it to the second. The olfactory matching test consisted of ten trials. Each odor was presented at 50% odor concentration, and the trial sequence was randomized. The trial was initiated with a 200 ms tone, and the first odor was delivered after 1 s. Two odors were delivered for 4 s, with an inter-stimulus interval (ISI) of 5 s. In a trial, two odors introduced may either be the same or different, and participants were required to determine whether the odor sequence was 'same' or 'different.' The participants were given 10 s to register a verbal response after the second odor delivery onset. The response was recorded in a data book after the experimenter entered it into a response console.

Two pairs of odors were used for the olfactory matching test. Out of the two pairs, one pair had a significant difference in their PID response amplitudes (Hexanal vs. Acetophenone) while the other pair had identical response amplitudes (Isoamyl acetate vs. 1,4-Cineole) (Figure 5-3 A). All healthy participants completed the olfactory matching test with these two odor pairs. The majority of COVID-19 patients carried out the test with these two odor pairs. If any of these odors were undetected by patients at 50 % (v/v), another odor with similar PID response amplitudes was substituted.

We calculated the average olfactory matching accuracy of healthy subjects for analyzing the olfactory performance index. The individual olfactory matching score of each participant (including normal subjects and patients) was then normalized to this average value (transformed to 100), and the data was plotted as normalized matching accuracy (Figure 5-3 B).

5.2.10 Calculation of olfactory function score (OFS)

We pooled the measured detection and olfactory matching performance index to quantify the degree of olfactory dysfunctions in COVID-19 patients relative to normal healthy subjects (Table 5-1 and Table 5-2). We assigned equal weighting to olfactory detection and olfactory matching performance index to measure the olfactory function score. OFS was determined by combining the detection scores measured at all four concentrations (9.1%, 16.6%, 23.1%, and 50% v/v) and the normalized olfactory matching index. For patients who did not qualify for the olfactory matching test, their OFS was calculated on the basis of the average value of their detection indices obtained at various concentration levels. The efficiency of using OFS to detect individuals with olfactory deficits was evaluated by performing ROC analysis. Separate analyzes were conducted to assess the impact of confounding variables such as age and gender (see Results, Figure 5-5) and incomplete variables (see Results, Figure 5-7).

5.2.11 Statistical analyses

All statistical analyses were done using Microsoft Excel, GraphPad Prism 8, and MATLAB. We used ANOVA and associated post-hoc tests, Student's t-tests, ROC analysis for sensitivity and specificity, and other sensitivity analyses to assess the influence of confounding variables and incomplete variables on the dataset.

5.3 Results

5.3.1 Optimization of olfactory-action meter and designing quantitative olfactory function test for COVID-19 patients

The establishment of a diagnostic test for an infectious disease involves optimizing the test parameters to make it sensitive, specific, user-friendly, rapid, and cost-effective. The challenge is to achieve this by preventing cross-contamination between patients. We developed an advanced olfactory-action meter with a removable low-cost odor delivery unit. The odor delivery unit was fabricated by introducing multiple layers of filters, ensuring utmost safety (Figure 5-1 A, see materials and methods). We used a 3.2 s pre-loading period during which odorized air was redirected from the odor delivery tube to exhaust, resulting in a well-defined odor pulse. The

vacuum was turned off at the end of the pre-loading period, and a precise odor pulse was delivered to the participant's nose. We selected ten monomolecular odorants of varying volatilities to record olfactory responses of healthy subjects and asymptomatic COVID-19 patients. PID measurements at 50% odor concentration confirmed the varying physical properties of these odorants (Figure 5-1 B, PID amplitudes, two-way ANOVA, $F_{(9,40)} = 18.49$, $p < 0.0001$). These measurements also revealed that this olfactory-action meter could reliably generate two odor pulses in rapid succession with an ISI of 5 s (Figure 5-3 A).

We collected olfactory responses from 37 normal healthy subjects (23 males and 14 females, check Table 5-1 for details of the subjects) towards different odorants to determine criteria for a clinically appropriate olfactory function test. First, we assessed detectability of ten different odorants at various concentrations (9.1%, 16.6%, 23.1% and 50% v/v) in these subjects. On testing the detectability, as a group, normal healthy subjects detected eight out of ten odorants at 16.6% concentration, and the remaining two odorants were detected at 23.1% concentration (Figure 5-1 C and Table 5-1). These results established criteria for asymptomatic COVID-19 patients' olfactory fitness examination.
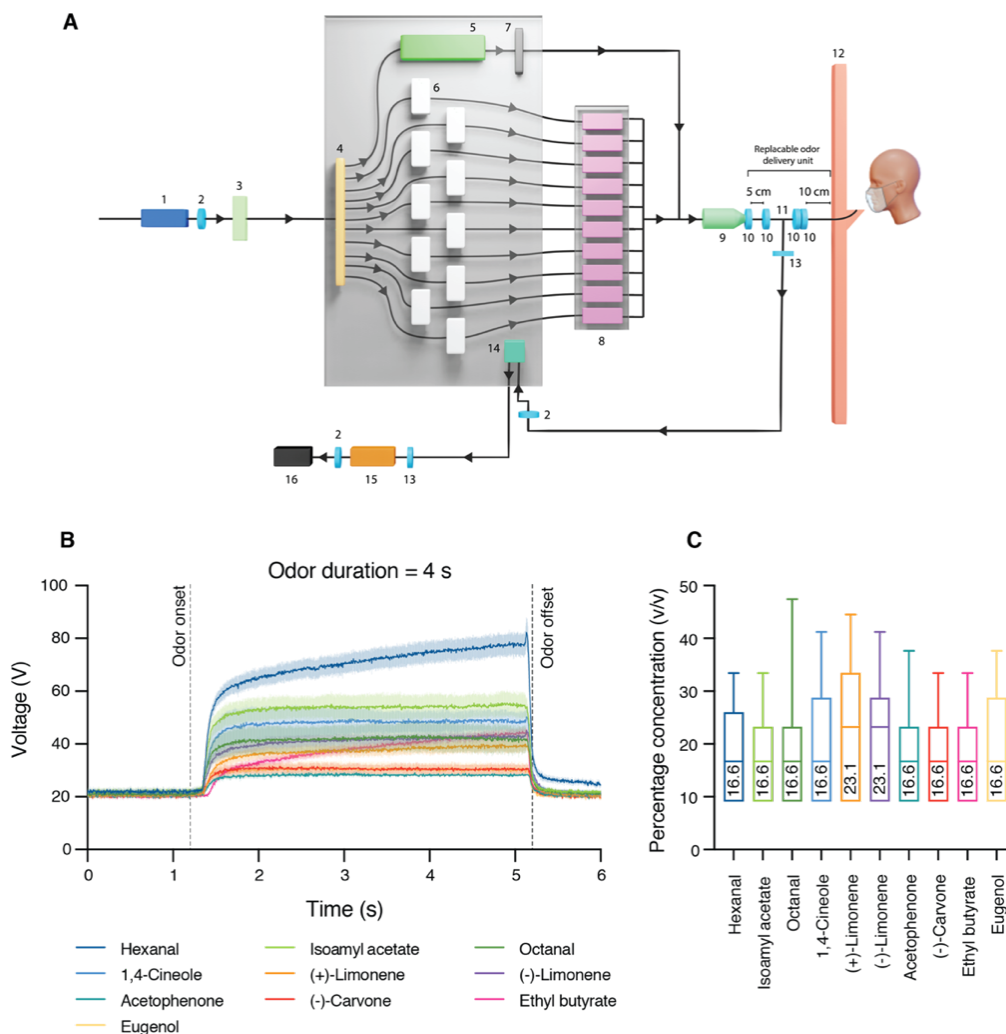
Figure 5-1: Fabrication of olfactory-action meter and optimization of olfactory function test parameters for use in COVID-19 clinics.

A. Schema of the olfactory-action meter.

The different components of the olfactory-action meter are as follows: 1. Air Pump (5 L/min). 2. 0.2 μm HEPA filter. 3. Air filter. 4. Manifold. 5. Main Mass flow controller (200 uccm). 6. Mini Mass flow controller (for each odor line, 20-200 uccm). 7. Solenoid valves. 8. Odor box containing ten odor bottles. 9. Glass odor nozzle. 10. Filter made from surgical mask material. 11. T-joint (Replaceable odor delivery unit consists of 10, 11, and 13). 12. Separating wall. 13. 0.2 μm PES filter (Whatman uniflow). 14. Electromagnetic valve. 15. Vacuum pump (~450 mbar). 16. Carbon filter (60 cm in length). To ensure optimal safety requirements for use in COVID-19 clinic, HEPA-sterilized air was pumped into the instrument. The sterile air was bifurcated into eleven channels (into ten mini MFCs and to main MFC) using a metallic manifold. Using custom-written software, the experimenter controlled the volumetric airflow through these MFCs. The main MFC's output was distributed into ten channels, using a battery of solenoid valves (one for each odor channel). The precise timing of sterile air delivery was made possible using these solenoid valves. During the preloading time, odorized air from odor bottles traveled through the odor nozzle and into the odor delivery unit. A vacuum suction (~450 mbar) attached to the odor delivery unit extracted odorized air through a series of three 0.2 μm filters (refer to materials and methods for details) into a carbon filter. The vacuum was turned off during odor presentation, and the odorized air was presented to subjects via the odor delivery unit. During the test, participants wore surgical masks, and the odor delivery unit was changed after each session to avoid cross-contamination. The multiple layers of filters that ran the length of the odor delivery unit prevented virus particles from entering the instrument.

B. Ten odorants with varying physicochemical properties were chosen for the olfactory function test.

We chose odors that are commonly used in human psychophysical studies. To assess the kinetics of odor pulses, PID measurements were taken for each of the ten odorants. The use of vacuum during the preloading period ensured a well-defined odor pulse with minimal delay (100-200 ms onset latency). Depending on the physicochemical properties of each odor, amplitude and rise time varied across different odors (PID amplitudes, two-way ANOVA, $F_{[9,40]} = 18.49$, $p < 0.0001$). Traces averaged across five trials and represented as mean ± SEM.

C. Odor detection thresholds of healthy subjects for all the odorants.

Healthy subjects detected eight out of ten odors at 16.6 % odor concentration. For the enantiomer pair of limonene, the detection threshold was found to be 23.1 %. The line within the box plot shows the median detection value for each odorant. Whiskers represent the highest detection thresholds for different odorants in healthy subjects (n = 37 subjects).

5.3.2 Olfactory detection abilities are significantly weakened in asymptomatic COVID-19 patients

To test olfactory function in asymptomatic COVID-19 patients, we registered 34 patients (21 males and 13 females) admitted in two COVID-19 isolation wards at BJGMC & SGH. These patients either contacted the disease due to their inadvertent interaction with COVID-19 patients or were healthcare workers involved in managing COVID-19 in the city (For details of patients: Table 5-3). All the patients were positive for COVID-19 infection, confirmed by their RT-PCR testing. To perform the olfactory function test, the patients' medical history was documented to

ensure that none of these patients had any symptoms of COVID-19 (see materials and methods, Table 5-3). The test paradigm was thoroughly explained, and signed consent was obtained before starting the olfactory function test with a patient. Before carrying out the olfactory function test, we enquired about the patient's general ability to smell and taste. In response to the enquiry, 85% of the total patient population stated that their smelling abilities were intact, and 91% indicated that they had not experienced taste loss post-infection.
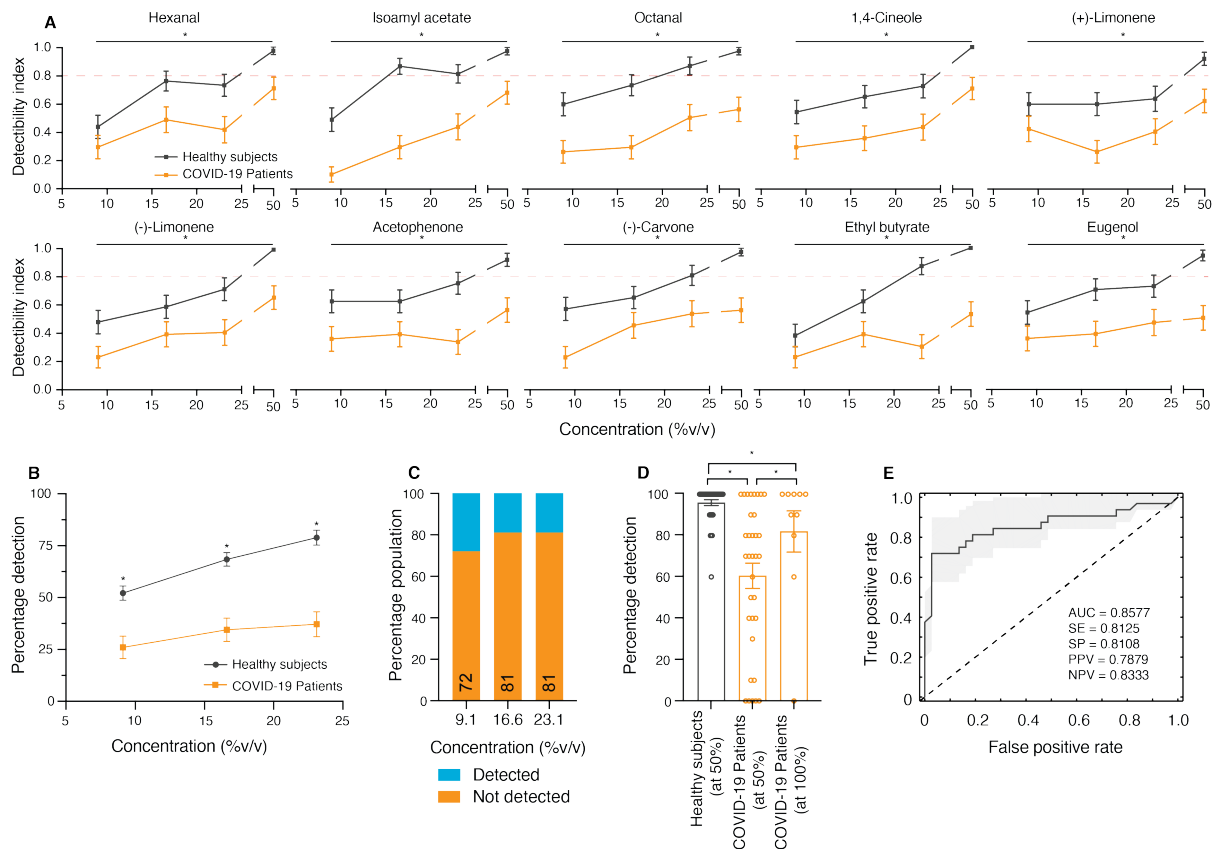
Figure 5-2: Asymptomatic COVID-19 patients show severely compromised olfactory detection abilities.

A. Asymptomatic COVID-19 patients displayed reduced olfactory detectability for all odorants. The fraction of odors detected by subjects at a given concentration was used to measure the detectability index. For different odors tested, healthy subjects had better detection at lower concentrations than asymptomatic COVID-19 patients (two-way ANOVA; for Hexanal, $F_{(1, 260)} = 20.72$, $p < 0.0001$, for Isoamyl acetate, $F_{(1, 265)} = 68.21$, $p < 0.0001$, for Octanal, $F_{(1, 258)} = 52.74$, $p < 0.0001$, for 1,4-Cineole, $F_{(1, 257)} = 26.2$, $p < 0.0001$, for (+)-Limonene, $F_{(1, 258)} = 20.62$, $p < 0.0001$, for (-)-Limonene, $F_{(1, 260)} = 26.84$, $p < 0.0001$, for Acetophenone, $F_{(1, 260)} = 31.64$, $p < 0.0001$, for (-)-Carvone, $F_{(1, 259)} = 30.82$, $p < 0.0001$, for Ethyl butyrate, $F_{(1, 259)} = 45.22$, $p < 0.0001$, for Eugenol, $F_{(1, 261)} = 28.45$, $p < 0.0001$). Data is represented as mean ± SEM.

B. Estimation of olfactory dysfunctions at threshold odor concentration. Detectability indices were pooled for all odorants to probe the extent of olfactory dysfunction in asymptomatic COVID-19 patients (two-way ANOVA, $F_{(1,200)} = 82.8$, $p < 0.0001$). Data is represented as mean ± SEM.

C. Asymptomatic COVID-19 patients show olfactory deficits at threshold concentrations.

The detection indices of asymptomatic patients were compared with the median detectability index calculated from healthy subjects. Asymptomatic patients showed 72%, 81%, and 81% reduction in scores compared to normal healthy subjects.

D. Comparison of detectability at 50% odor concentration and with pure, undiluted odorants.

Measurement of detectability index at 50% odor concentration showed that healthy subjects had an overall detectability of 96%. However, the detectability was considerably compromised in the COVID-19 patient cohort, with an average detection of 61%. (two-tailed t-test, $p < 0.0001$, $t = 5.8$, $df = 69$). Patients who were unable to detect at 50% concentration were presented with paper strips saturated in pure, undiluted odors. These patients displayed a high detection rate of 82% for pure odors. Data is represented as mean ± SEM.

E. ROC analysis for predicting olfactory dysfunction in asymptomatic COVID-19 patients using detection indices measured at different concentrations.

The ROC analysis shows an AUC of 0.86, specificity of 0.81, and sensitivity of 0.81 for prediction based on detection indices measured from healthy subjects and asymptomatic COVID-19 patients. The different values extracted from ROC analyses indicating the sensitivity of the classifier are mentioned in the figure. 95% confidence interval bound is marked by a gray shaded area.

When testing detectability at low concentrations for all odors, we observed that asymptomatic COVID-19 patients had substantially reduced detection capabilities relative to normal healthy subjects (Figure 5-2 A, pooled analysis for all ten odors, two-way ANOVA, $p < 0.0001$). These patients displayed a 38% - 55% reduction in detection indices for the ten odorants tested (Figure 5-2 A, comparison of area under curves, Table 5-4) and a 50% reduction for the combined detection threshold at lower three concentration levels (Figure 5-2 B, comparison of area under curves, Table 5-4). To assess the proportion of patients with olfactory dysfunctions at lower concentrations, pooled detection scores of normal healthy subjects were compared with that of asymptomatic COVID-19 patients for all ten odorants (Figure 5-2 B, two-way ANOVA, $F_{(1, 200)} = 82.77$, $p < 0.0001$). We observed that 81% of the patients showed low detection scores at threshold odor concentration when compared with normal healthy subjects (Figure 5-2 C). Further, 65% (20 out of 31) of these patients showed lower detection scores for all three concentrations tested (Table 5-2).

To explore the degree of olfactory dysfunction in patients, we further assessed their detectability at 50% (v/v) odor concentration. At this concentration, normal healthy subjects showed detection accuracy of 96% (participants could detect on average 9.6/10 odors), while asymptomatic patients demonstrated a significantly reduced detection accuracy of 61% (Figure 5-2 D, comparison of detection accuracies at 50% (v/v) odor concentration, two-tailed t-test, $p < 0.0001$, $t = 5.8$, $df = 69$). We provided patients with paper strips soaked in pure odorants and assessed their detection accuracies if they were unable to detect ≤ 5 odors at 50% odor concentration. At this high concentration, 82% of these asymptomatic patients could detect pure

odorants with high accuracy (Figure 5-2 D, comparison of detection accuracies at 50% (v/v) concentration (n = 34 patients) with pure odorants (n = 10 patients), one-tailed t-test, p < 0.05, t = 1.7, df = 42). To determine the sensitivity of our categorization of subjects with olfactory dysfunction, we performed ROC analysis with detection indices at different concentration levels (at 9.1%, 16.6%, 23.1%, and 50% v/v). The high accuracy of using detection threshold indices as an olfactory diagnostic parameter is reflected in the AUC of 0.86, sensitivity, and specificity at 81% (Figure 5-2 E). These findings demonstrate transient olfactory dysfunctions in asymptomatic COVID-19 patients can be evaluated at low odor concentrations. This emphasizes the importance of using sensitive and accurate methods to diagnose olfactory dysfunctions in COVID-19 patients. Importantly, self-assessment findings or outcomes from crude methods using less defined stimuli such as paper strips dipped in odors at a suprathreshold concentration (see materials and methods, ~100%) must be viewed with caution.

Odorant used	Area under curve (AUC) Normal healthy subjects (unit^2)	AUC Patients (unit^2)	% reduction in detectability observed for patients
Hexanal	2.186	1.362	38%
IAA	2.405	1.086	55%
Octanal	2.38	1.17	51%
1,4-Cineole	2.143	1.257	41%
(+)-Limonene	1.984	1.149	42%
(-)-Limonene	2.057	1.195	42%
Acetophenone	2.141	1.149	46%
(-)-Carvone	2.225	1.342	40%
Ethyl Butyrate	2.182	1.039	52%
Eugenol	2.172	1.248	43%
Combined AUC for lowest three concentrations	1.349	0.6715	50%

Table 5-4: Percentage reduction in the detection abilities of COVID-19 patients compared to normal healthy subjects. AUC analysis done for detection indices measured for different concentrations of ten odorants used in this study.

5.3.3 Asymptomatic COVID-19 patients show impairments in performing olfactory matching test

The nasal epithelium is one of the SARS-CoV-2 entry sites where it binds to and interacts with ACE2 and TMPRSS2 receptors expressed on non-neuronal supporting cells (55, 56). Recent reports suggest that infection is not restricted to the sensory periphery, as many patients display neurological conditions after a COVID-19 diagnosis (63, 66, 237, 351, 353). Although the exact mechanism of viral invasion of the brain is unknown, several brain regions may be affected depending on the severity of infection, potentially increasing the risk of neurological and

psychiatric disorders. Thus, it is quite possible that cognitive skills could be affected due to neurological alterations in higher brain centers of asymptomatic COVID-19 patients.

To assess patients' cognitive abilities, we devised an olfactory matching test that assesses detection and discrimination abilities and working memory while matching two odors presented with a specific delay. The parameters such as stimulus duration, ISI, and ITI for the matching test have been optimized from 265 healthy subjects (Bhowmik et al., unpublished data). These optimized parameters were used to probe olfactory matching skills in asymptomatic COVID-19 patients. Participants were given two consecutive 4 s odor stimulations separated by a 5 s ISI in this matching test. After sampling both stimuli, participants determined whether they were the same or different and gave a verbal response to the experimenter. Only those with a detection index of ≥60% at 50% odor concentration were allowed to participate in the olfactory matching test. The odors used for the matching test were selected by considering patients' detectability towards these odors. Each session consisted of ten trials, and matching accuracy was normalized to the mean accuracy of healthy subjects. Compared to normal healthy subjects, asymptomatic COVID-19 patients showed a significant reduction in olfactory matching accuracy (Figure 5-3 B, comparing normalized olfactory matching accuracy between normal healthy subjects and COVID-19 patients two-tailed t-test, p = 0.015, t = 2.5, df = 54). This necessitates detailed clinical and diagnostic analysis to help identify the signs and severity of neurological disorders caused by SARS-CoV-2.
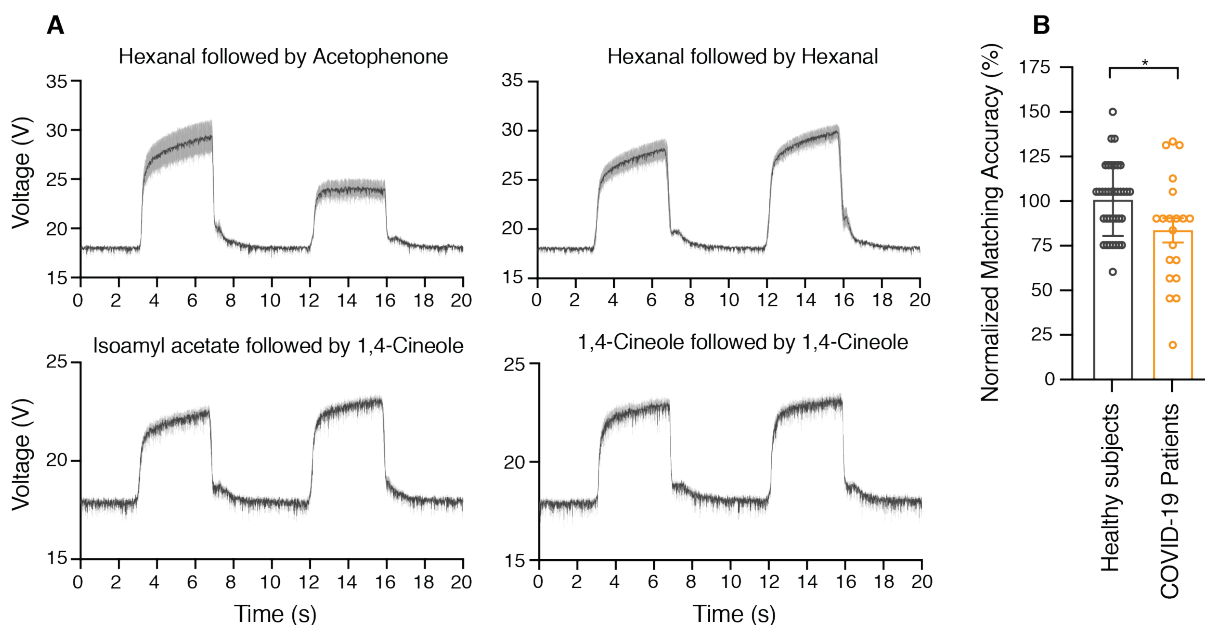
Figure 5-3: Decreased olfactory matching performance is seen in asymptomatic COVID-19 patients.

A. Precise odor delivery pulses achieved in an olfactory matching trial. For the odor matching test, two pairs of odors were picked from the list of odors detected by each patient.

Odors were selected such that one odor pair had a difference in odor profile (Hexanal vs. Acetophenone) while the other odor pair had a similar odor profile (Isoamyl acetate vs. 1,4-Cineole). For the olfactory matching test, the two odors were delivered for 4 s with an ISI of 5 s. For 'same' odor trials, an ISI of 5 s was adequate to saturate the vapor

phase in odor bottles, which is evident from the PID odor profile of the same odor delivered twice in sequence. Representative traces of 'same' and 'different' trials are averaged over 4-5 trials and illustrated. Data are represented as mean ± SEM.

B. Normalized odor matching accuracies.

The odor matching accuracy was normalized to the mean accuracy displayed by healthy subjects. COVID-19 patients demonstrated reduced odor matching accuracies relative to healthy subjects (two-tailed t-test, p = 0.015, t = 2.5, df = 54). Data are represented as mean ± SEM.

5.3.4 Asymptomatic COVID-19 patients show severe olfactory dysfunctions

To arrive at a unitary readout to define olfactory dysfunctions at sensory and cognitive level, a cumulative analysis on detectability scores at 9.1%, 16.6%, 23.1%, and 50% v/v and normalized matching accuracies was performed. Subjects were classified as having olfactory dysfunctions if they had a deficiency in detectability indices for all four concentrations tested or had a deficiency in detectability indices for two or more concentrations and normalized olfactory matching accuracy. Such analysis revealed 82% of the patient population (27 out of 33) and 13% normal healthy subjects (5 out of 37) with olfactory deficits (Figure 5-4 A, B, Tables 5-1 and 5-2). Further, to check the efficiency of our categorization, we calculated the sensitivity, specificity, and accuracy by calculating the number of true positives (TP), false positives (FP), true negatives (TN), and false negatives (FN). This analysis revealed a sensitivity [TP/(TP+FN)] of 82%, specificity [TN/(TN+FP)] of 87%, and accuracy [(TP+TN)/(TP+TN+FP+FN)] of 85%.

Further, we formulated OFS by assigning equal weightage to all behavioral readouts. OFS was calculated by averaging detectability indices and normalized olfactory matching performance index. One patient (BJMC P13) declined to participate for the entire duration of the test. We, therefore, measured detection indices at 50% (v/v) concentration and for pure odorants wherein the patient had 0 and 0.6 detectability indices, respectively. Thus, OFS was not calculated for this patient but was classified as a patient with an olfactory deficiency. By calculating OFS for healthy subjects and asymptomatic COVID-19 patients, we show significantly reduced OFSs in the patient cohort relative to healthy subjects. Further, the OFS of 85% of the patient population (28 out of 33) was found to be lower than the median score shown by healthy subjects (Figure 5-4 C, two-tailed unpaired t-test, p < 0.0001, t = 6.4, df = 68). ROC analysis with OFS values provides a good predictive AUC value of 0.83, revealing the applicability of OFS as a good olfactory fitness indicator for the diagnosis of COVID-19 (Figure 5-4 D). Also, ROC analysis returned a sensitivity and specificity above 70% and 90%, respectively. This signifies the effectiveness of different behavioral readouts and strategies we recommend for assessing olfactory function across individuals.

To test the dependency of olfactory function scores towards different variables, we analyzed various confounding factors. To ensure optimal motivation of subjects while performing the olfactory function test, we evaluated only those willing to participate in the study. Before beginning the test, care was taken to ensure that participants completely understood the paradigm. Moreover, none of the participants had any experience of smell loss. To determine whether the gender and age of participants affected test readings, we analyzed the association of these variables with olfactory detection indices and OFS. Our analyses revealed no correlation between these confounding variables and test readouts and thus confirmed the robustness of the data (Figure 5-5).
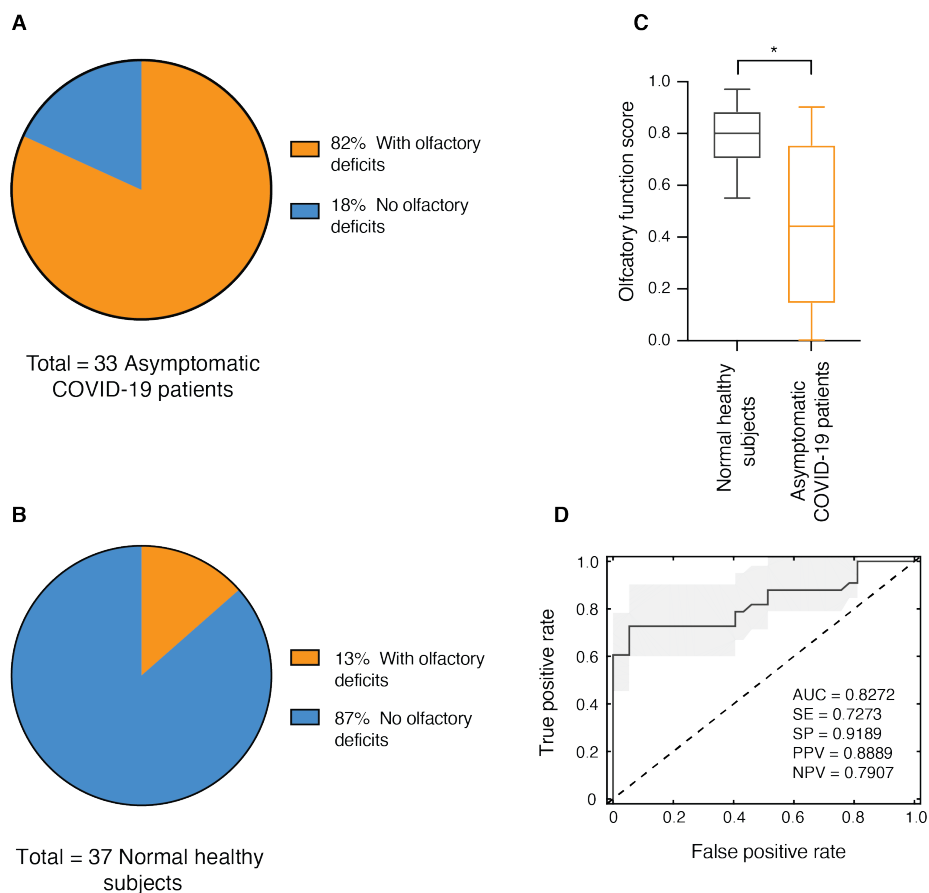
Figure 5-4: Quantification of olfactory function can accurately identify asymptomatic COVID-19 carriers.

A. Majority of asymptomatic COVID-19 patients have an olfactory deficiency.

To measure the number of patients with olfactory deficits, we compared their detectability indices at 9.1%, 16.6%, 23.1%, and 50% odor concentrations and the normalized matching accuracy with normal healthy subjects. If patients had a deficiency in detectability indices at all the concentration levels or showed deficiency in detectability indices at two or more concentrations and decreased olfactory matching score, they were classified as 'with olfactory deficits.' With such strict criteria, 82% of asymptomatic patients were found to be experiencing olfactory dysfunctions.

B. Most normal healthy subjects did not have olfactory deficits.

The criteria for classifying subjects with olfactory deficits was applied to the normal healthy subject cohort. The analysis revealed that 87% of the healthy subject population did not show any olfactory deficits.

C. Olfactory function scores reflect a broad spectrum of olfactory deficits in COVID-19 patients.

In order to establish a robust readout representing olfactory dysfunctions, the OFS for each participant was determined by averaging detectability indices and normalized olfactory matching performance index. Asymptomatic COVID-19 patients have substantially decreased OFS relative to normal healthy subjects (median for normal subjects = 0.8, and median for patients = 0.44, two-tailed unpaired t-test, $p < 0.0001$, $t = 6.4$, $df = 68$).

D. ROC analysis was used to test the sensitivity of using olfactory function scores to predict olfactory deficits in asymptomatic COVID-19 patients.

ROC analysis indicates an AUC of 0.83, specificity of 92%, and sensitivity of 73% for the classifier based on OFS for subjects with olfactory dysfunctions. The different values extracted from ROC analyses indicating the sensitivity of the classifier are mentioned in the figure. 95% confidence interval bound is marked by a gray shaded area.

To evaluate the robustness of OFSs as a parameter to determine olfactory fitness, we carried out different sensitivity analyzes. Firstly, we tested the existence of outliers in our data by doing a box-plot analysis. None of the data points were present beyond a 1.5-fold interquartile range, suggesting no outliers in the dataset for healthy subjects and patients. (Figure 5-4 C) (*354*). Simultaneously, even the Grubb's test to identify outliers revealed the absence of outliers in normal healthy subjects and patients' dataset (Alpha = 0.05, Normal healthy subjects: Mean OFS = 0.794, SD = 0.1, Critical value of Z = 3.002, G = 2.250; Patients: Mean OFS = 0.426, SD = 0.32, Critical value of Z = 2.952, G = 1.482) (*355*). Since our data contains no outliers, the measured OFS is a fair representation of the sample set and is not skewed by a few data points. Further, as we observed a wide range of detection indices at 50% odor concentration in asymptomatic COVID-19 patients, the association between detection indices at 50% concentration and OFS was evaluated. There is a strong correlation between these variables, indicating that changes in detection indices are very well represented in OFS (Pearson Correlation coefficient r = 0.8). This is evident from the logistic growth function curve plotted for OFS and detection indices (Figure 5-6, $R^2 = 0.8165$).

As mentioned above, OFS was determined by averaging detectability indices and a normalized olfactory matching performance index. However, only subjects with a detectability index of ≥0.6 at 50% (v/v) odor concentration participated in the olfactory matching test. For those participants who were not eligible for the olfactory matching test, OFS was determined by averaging only the detectability indices. To see if these missing readouts could influence OFS measurement, OFS was re-analyzed only for patients (20 participants) who completed the olfactory matching test. The comparison was made with randomly selected OFS values from twenty healthy subject data. Even after removing the data points with missing variables, the asymptomatic COVID-19 patient cohort displayed substantially reduced olfactory function scores relative to healthy subjects. This finding shows the robustness and sensitivity of OFS used to quantify olfactory function in asymptomatic COVID-19 patients (Figure 5-7, two-tailed unpaired t-test, p <

0.0044, t = 3.031, df = 38). To summarize, the OFS we propose in this study reflects a reliable parameter for the olfactory fitness of subjects. Low OFS can be used to recognize subjects with potential issues arising at the sensory periphery and higher brain centers due to COVID-19 infection.
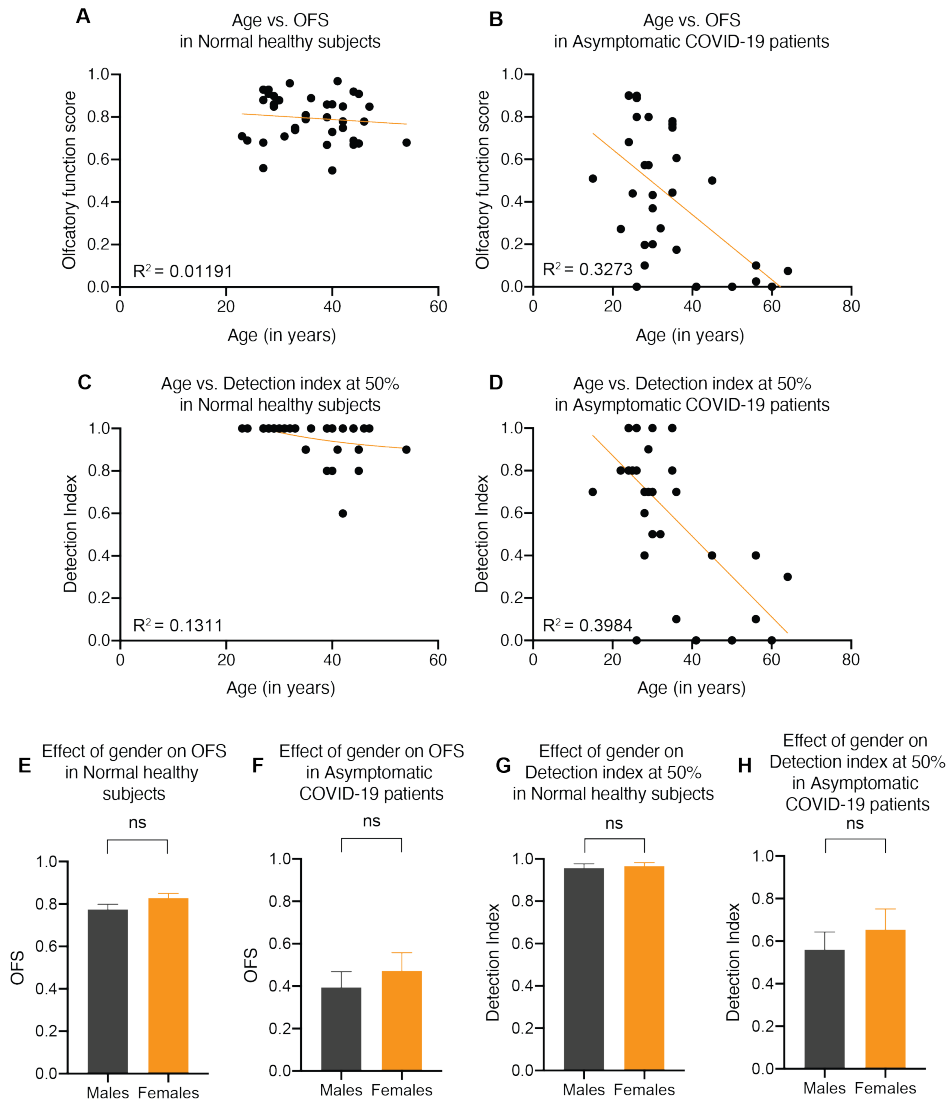
Figure 5-5: The olfactory function score and detection indices are not sensitive to the age and gender of subjects.

(A-D). The olfactory performance of normal healthy subjects and asymptomatic COVID-19 patients was plotted against the age of participants. Linear fit with least square regression (orange lines) on the data shows that olfactory performance does not correlate with the age of subjects (For normal healthy subjects, (A) comparison between age and OFS: $R^2 = 0.01191$ and (C) comparison between age and detection indices at 50% concentration: $R^2 = 0.1311$. For asymptomatic COVID-19 patients, (B) comparison between age and OFS: $R^2 = 0.3273$ and (D) comparison between age and detection indices at 50% concentration: $R^2 = 0.3984$).

(E-H). The olfactory performance was analyzed separately for males and females in normal healthy subjects and asymptomatic COVID-19 patients.

No difference was observed between male and female participants within the two datasets (For normal healthy subjects, (E) comparison of OFS between males and females: two-tailed t-test, p = 0.1504, t = 1.470, df = 35 and (G) comparison

of detection indices at 50% concentration between males and females: two-tailed t-test, p = 0.7953, t = 0.2614, df = 35. For asymptomatic COVID-19 patients, (F) comparison of OFS between males and females: two-tailed t-test, p = 0.5080, t = 0.6697, df = 31 and (H) comparison of detection indices at 50% concentration between males and females: two-tailed t-test, p = 0.4730, t = 0.7261, df = 31).

5.4 Discussion

This chapter aimed to establish a novel strategy for sensitive behavioral assessment of olfactory dysfunctions in human subjects. In the last few years, our lab's collective effort has been instrumental in setting up an innovative 'Olfactory-Action Meter.' Using this instrument, we began estimating the olfactory fitness of the healthy Indian population (Bhowmik et al., manuscript under preparation). In February 2020, anecdotal reports of smell loss associated with COVID-19 started to emerge worldwide, and scientific investigations began in March 2020. We realized that most of these studies relied on subjective self-reports of symptoms that are sensitive to individual bias. To overcome this limitation, we modified our olfactory-action meter to measure the olfactory fitness of asymptomatic COVID-19 patients objectively. We developed an olfactory function test that would challenge subjects' detection abilities at threshold levels and probe olfactory matching skills. As a result, the olfactory function test can detect sensory-cognitive deficits caused by SARS-CoV-2 infection. We realized that 82% of asymptomatic COVID-19 patients had varying degrees of olfactory dysfunctions on performing the olfactory function test. However, only 15% of these patients had self-awareness of their olfactory deficiency before taking the olfactory function test. The disparity between self-reporting and objective assessment accurately shows the urgency of using reliable quantitative olfactory screening tests to diagnose olfactory deficits in unwitting silent spreaders of COVID-19 (*53, 54, 356*).
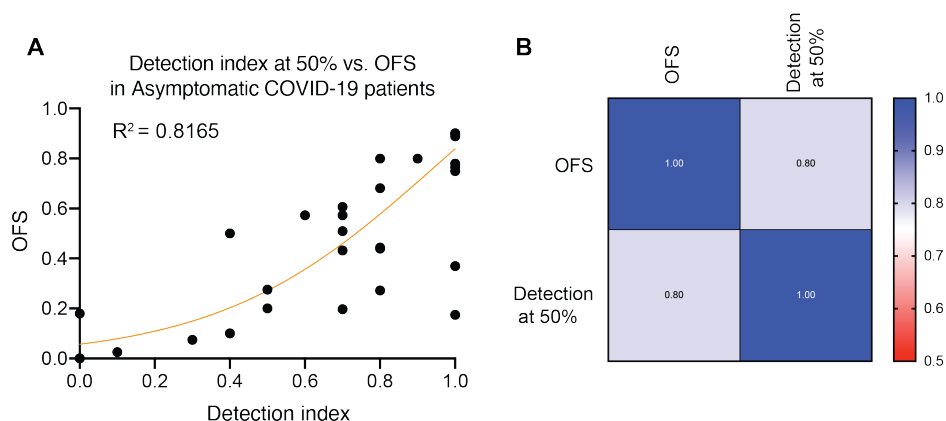

Figure 5-6: Olfactory function score correlates with detection indices measured at 50% concentration for different odors.

A. The olfactory function score is high for asymptomatic COVID-19 patients who perform better in detecting odors at 50% odor concentration. The orange line is a fit of a logistic sigmoidal growth model to the data.

B. Pearson's correlation analysis shows that the olfactory function score and detection indices at 50% odor concentration is highly correlated for asymptomatic COVID-19 patients (Pearson Correlation coefficient r = 0.8).

SARS-CoV-2 infection is characterized by a broad spectrum of symptoms that ranges from extreme cases, including acute respiratory distress syndrome, to mild symptoms like cough, shortness of breath, fever, body ache, and sore throat (*341*, *342*, *357*). To control this infection that spread across the world, it was critical to find a well-defined prognostic marker for early diagnosis and preventive treatment in patients. An online survey conducted in Iran with more than 10,000 individuals found a tight association between anosmia and COVID-19 positivity (*358*). Following this, formal studies conducted in Italy with hospitalized patients found that 19.4-33.9% of the patients reported olfactory disorders, and 60% of these patients had smell loss before hospitalization (*49*, *359*). Subsequent studies suggested a much higher prevalence of olfactory deficits in COVID-19. A multicenter study in Europe with 417 COVID-19 patients found that 85.6% of patients subjectively reported a reduced sense of smell, while 79.6% reported complete loss of smell (*77*). The increasing reports of smell loss that seemed to be more present in asymptomatic or paucisymptomatic subjects made anosmia an important indicator for COVID-19 infection across different countries. In fact, world health authorities believe that anosmia or hyposmia in the absence of other respiratory diseases should be a direct sign of COVID-19 infection. Individuals with these symptoms should seriously consider self-isolation and get themselves tested.
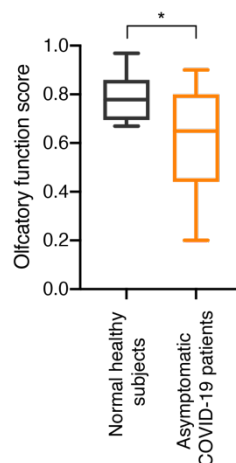
Figure 5-7: Comparison of olfactory function scores from COVID-19 patients who participated in the olfactory matching test with 20 randomly picked healthy subjects.

To establish that inclusion or exclusion of olfactory matching score does not influence OFS measurements, OFS from twenty COVID-19 patients who participated in olfactory matching was compared with twenty randomly picked normal healthy subjects. These asymptomatic COVID-19 patients displayed substantially decreased olfactory function scores relative to normal healthy subjects (two-tailed unpaired t-test, $p < 0.0044$, $t = 3.031$, $df = 38$).

The invasion of the olfactory system had been proven for two other species of virus belonging to the coronavirus family, namely Middle East Respiratory Syndrome-related Coronavirus (MERS-CoV) and Severe Acute Respiratory Syndrome-related Coronavirus (SARS-CoV) (*360–362*). To explain neuronal mechanisms of anosmia associated with COVID-19, several experiments have begun to decode the path of SARS-CoV-2 entry into the olfactory system. The SARS-CoV-2 entry into a host cell relies on the co-expression of two genes, ACE2 and TMPRSS2 receptors. While the ACE2 receptor acts as a docking site for the binding of viral spike protein, TMPRSS2 facilitates cleavage and enables membrane fusion. These two genes are expressed in sustentacular cells of the epithelium but not in OSNs (*55*, *56*, *58*, *363*). In specific individuals, who experience a reduced sense of smell, elevated levels of inflammatory cytokines (*57*), or the possible ionic imbalances in sustentacular cells may affect the functioning of OSNs, contributing to olfactory dysfunctions of differing magnitude (*58*, *59*). Furthermore, as OSNs in the human OE are continuously replaced (*228*, *364*), olfactory dysfunctions due to OSN malfunctions can have a gradual onset and vary in the degree of severity. To assess such wide spectrum of olfactory deficits, precise quantitative methods with better control on stimulus properties are required.

To address the drawbacks of subjective assessment of olfaction, few objective approaches have been implemented to quantify olfactory deficits in COVID-19 patients. These include household odorous object identification (*365*), University of Pennsylvania smell identification tests (*50*), Connecticut Chemosensory Clinical Research Center (CCCRC) Test (*366*), Sniffin' Sticks (SS) test (*367*), and n-butanol threshold tests (*366*). In our study, the quantification of olfactory dysfunction using the olfactory-action meter detected smell deficits of varying degrees in 82% of asymptomatic COVID-19 patients. These objective methods were more efficient in detecting individuals with smell dysfunctions compared to subjective evaluations. In addition to the results we present here, the studies listed above highlight the need for sensitive olfactory tests to be carried out to identify several asymptomatic carriers of COVID-19. Although the application of such a large-scale screening technique presents many logistical challenges, a potential low-cost odor screening test may be carried out using odor arrays with concentrations near detection thresholds. Increasing odor diversity when using such techniques will compensate for precision. Adopting such protocols at workplaces and checkpoints would make it easier to scan large groups of people, and it would be a more sensitive indicator than body temperature monitoring.

Recently neurological complications of COVID-19 have been identified, ranging from mild to severe, in specific case reports and case series (*63–67*). A study using Diffusion Tensor Imaging found microstructural changes in CNS after patients recovered from COVID-19 infection (*237*). While long-term neurological changes attributable to SARS-CoV-2 infection are not specifically

identified, temporary changes in CNS are very worrying. We devised an olfactory matching test that involves detection, discrimination, and memorizing the perceived information of olfactory stimuli. Asymptomatic patients with good detectability indices at 50% odor concentrations were asked to do an olfactory matching test. The COVID-19 patients demonstrated dramatically decreased olfactory matching accuracy relative to normal healthy subjects. The reduced accuracies in the olfactory matching test imply potential cognitive dysfunctions in COVID-19 patients. To create an effective metric representing sensory and cognitive abilities, we proposed OFS, which assumes equal weighting to the various parameters evaluated. When measuring OFS, we found that it may be a strong indicator of olfactory deficiencies in asymptomatic COVID-19 patients. Further, the efficiency of using OFS was determined by performing ROC analysis. The AUC value of 0.83 signifies OFS as an accurate indicator of olfactory deficits in asymptomatic COVID-19 patients. Further analysis has shown that OFS is impervious to missing data points and not biased by the population's mean age and gender ratio. This illustrates the reliability of using an olfactory-action meter for accurate detection of asymptomatic COVID-19 carriers.

To summarize, quantitative estimation of olfactory function using the olfactory-action meter indicates serious olfactory dysfunctions among asymptomatic COVID-19 patients. Such dysfunctions may otherwise remain undetected by conventional approaches due to a lack of sensitivity. As countries are slowly emerging from lockdown policies, contact-tracing of infectious individuals is crucial. Thus, our work provides a blueprint to devise a sensitive, fast, and economic strategy that can be used as an efficient approach for screening large populations to curb the rapid spread of COVID-19.

5.5 Future direction

Using the innovative Olfactory-Action Meter, we successfully screened asymptomatic COVID-19 patients for their olfactory abilities. Our measurements precisely detected olfactory dysfunctions in 82% of these patients, demonstrating the utility of using quantitative methods to assess olfactory fitness in humans. The results provide a great impetus to expand the olfactory-action meter usage to probe the olfactory abilities of patients suffering from various neurodegenerative disorders. As an initial step, we have already begun measuring the olfactory function in a healthy Indian population. These measurements will allow us to estimate olfactory abilities in healthy individuals. The olfactory function of patients suffering from various neurodegenerative disorders will be then compared with healthy individuals' data.

CHAPTER 6

Summary

Optimal decision-making necessitates the ability to respond to different features of sensory stimulus flexibly. In mammalian olfaction, odor representations dynamically change with time and persist even after cessation of the stimulus. In this thesis, we examined how odor representations influence different facets of olfactory behavior by combining automated behavioral assays with optogenetics and *in vivo* imaging techniques. Further, to extend our understanding of circuit mechanisms in human olfactory dysfunctions, we devised a method to probe sensory and cognitive olfactory skills of normal healthy subjects and asymptomatic COVID-19 patients with olfactory deficits. The quantification of olfactory dysfunctions in these patients proved that olfactory fitness could be used to detect diseased conditions with high sensitivity.

1. Sniff-invariant odor discrimination times are correlated to the strength and similarity of glomerular activity patterns.

Active sniffing behavior is a primary step in encoding different features of olfactory stimuli. However, it remained unclear whether mice learn to modulate their sniffing behavior when involved in odor discrimination tasks. We quantified sniffing behavior in mice using a non-invasive breath sensor while they were conditioned to distinguish between odors belonging to different chemical classes. It was observed that mice rapidly learned to increase their sniffing frequency at a fixed latency after odor initiation. This increase was invariant of chemical classes and difficulty of the tasks, and it did not occur in the absence of odor stimuli. With a rise in breathing frequency, monomolecular odorants were discriminated within 10–40 ms, while complex binary mixtures required an additional 60–70 ms. Further, IOS imaging of glomerular activity revealed that Euclidean distances measured between activity patterns are inversely correlated to odor discrimination time. Thus, the similarity and strength of glomerular activity patterns rather than the sampling behavior define the extent of neural processing required for accurate olfactory decision-making.

2. Post-stimulus OB neural activities control olfactory long-term memory formation.

The inhibitory activity of OB interneurons during odor presentation brings about temporal patterning in MTC ensembles that improve odor discrimination. To study how neural representations change with time and their relevance in olfactory processing, we needed a method

to control stimulus properties precisely. Therefore, we designed a behavioral task wherein mice were presented with odor stimulus of varying duration. Equipped with automated behavioral paradigms, we observed that reducing the stimulus duration negatively impacted olfactory performance in mice. Further, *in vivo* Ca^{2+} imaging in awake and anesthetized mice revealed a robust and sustained interneuron activity with long stimulus duration compared to short stimuli. To investigate how this difference in interneuron activity influenced MTC ensemble activities, we employed an optogenetic approach to modulate MTC activities during stimulus presentation and in the post-stimulus period. The optogenetic modulation of OB inhibitory circuits proved that MTC spiking during odor presentation controls discrimination learning while the information encoded by post-stimulus spiking controls long-term memory formation. Now, the challenge lies in dissecting neural mechanisms involved in maintaining firing activities of MTCs during the post-stimulus period.

3. Using olfaction to probe sensory and cognitive deficits

The importance of establishing a precise behavioral paradigm to study odor representations has been one of the major highlights during my graduate studies. In the last chapter of this thesis, we extended our understanding of odor representations to study olfactory functional changes in human subjects. Olfactory dysfunction is one of the primary symptoms observed in individuals suffering from upper respiratory tract infections and many neurodegenerative disorders. Therefore, establishing a paradigm for precise quantification of olfactory deficits in these individuals becomes essential. To quantitatively evaluate olfactory functions in patients, we developed a sophisticated olfactory-action meter that can accurately measure olfactory acumen in human subjects. Global reports suggested loss of smell as an early indicator of COVID-19 infection, and early identification of asymptomatic COVID-19 carriers has been the pressing priority during the ongoing pandemic. To evaluate olfactory dysfunction in asymptomatic COVID-19 patients, we introduced the olfactory function test that probes the subjects' detection abilities at threshold concentrations as well as their olfactory matching skills. Quantification using our method revealed that 82% of the asymptomatic COVID-19 patient population showed olfactory dysfunctions compared to healthy individuals. Thus, the quantification of olfactory function provides a blueprint for developing a rapid and economical strategy to screen large populations efficiently.

To summarize, dissecting neural circuit mechanisms controlling odor discrimination learning and long-term memory formation has provided a range of intriguing observations and new directions for future research. We have been privileged to contribute to society by proposing a

sensitive tool to detect olfactory function in human subjects, which we believe will provide a great impetus to the scientific community in the near future.

Publications

1. **A. S. Bhattacharjee***, S. Konakamchi*, D. Turaev, R. Vincis, D. Nunes, A. A. Dingankar, H. Spors, A. Carleton, T. Kuner, N. M. Abraham, Similarity and Strength of Glomerular Odor Representations Define a Neural Metric of Sniff-Invariant Discrimination Time. *Cell Rep.* **28**, 2966-2978 (2019). [* Equal contributions].

2. **A. S. Bhattacharjee**, S. V. Joshi, S. Naik, S. Sangle, N. M. Abraham, Quantitative assessment of olfactory dysfunction accurately detects asymptomatic COVID-19 carriers. *EClinicalMedicine*. **28**, 1-13 (2020).

Manuscripts under preparation

1. **A. S. Bhattacharjee**, S. Mahajan, M. Pardasani, S. Priyadharshini, and N. M. Abraham, Distinct encoding of odor learning and memory by olfactory bulb projection neurons. In preparation.

Appendix

Copyright forms

References

1. C. Marin, D. Vilas, C. Langdon, I. Alobid, M. López-Chacón, A. Haehner, T. Hummel, J. Mullol, Olfactory Dysfunction in Neurodegenerative Diseases. *Curr. Allergy Asthma Rep.* **18** (2018), doi:10.1007/s11882-018-0796-4.

2. J. Frasnelli, T. Hummel, Olfactory dysfunction and daily life. *Eur. Arch. Oto-Rhino-Laryngology*. **262**, 231–235 (2005).

3. R. I. Mesholam, P. J. Moberg, R. N. Mahr, R. L. Doty, Olfaction in neurodegenerative disease: A meta-analysis of olfactory functioning in Ahlzheimer's and Parkinson's diseases. *Arch. Neurol.* **55**, 84–90 (1998).

4. C. H. Hawkes, R. L. Doty, *Non-neurodegenerative Disorders of Olfaction* (2018).

5. R. L. Doty, Olfaction in Parkinson's disease and related disorders. *Neurobiol. Dis.* **46**, 527–552 (2012).

6. J. F. Morley, J. E. Duda, Olfaction as a biomarker in Parkinsons disease. *Biomark. Med.* **4**, 661–670 (2010).

7. G. L. Bowman, Biomarkers for early detection of Parkinson disease. *Neurology*. **89**, 1432–1434 (2017).

8. M.-E. Lafaille-Magnan, J. Poirier, P. Etienne, J. Tremblay-Mercier, J. Frenette, P. Rosa-Neto, J. C. S. Breitner, Odor identification as a biomarker of preclinical AD in older adults at risk. *Neurology*. **89**, 327–335 (2017).

9. M. E. Growdon, A. P. Schultz, A. S. Dagley, R. E. Amariglio, T. Hedden, D. M. Rentz, K. A. Johnson, R. A. Sperling, M. W. Albers, G. A. Marshall, Odor identification and Alzheimer disease biomarkers in clinically normal elderly. *Neurology*. **84**, 2153–2160 (2015).

10. H. Spors, A. Grinvald, Spatio-Temporal Dynamics of Odor Representations in the Mammalian Olfactory Bulb. *Neuron*. **34**, 301–315 (2002).

11. B. Bathellier, D. L. Buhl, R. Accolla, A. Carleton, Dynamic Ensemble Odor Coding in the Mammalian Olfactory Bulb: Sensory Information at Different Timescales. *Neuron*. **57**, 586–598 (2008).

12. R. M. Carey, J. V. Verhagen, D. W. Wesson, N. Pírez, M. Wachowiak, M. E. Frank, H. F. Goyert, T. P. Hettinger, N. Pirez, M. Wachowiak, Temporal Structure of Receptor Neuron Input to the Olfactory Bulb Imaged in Behaving Rats. *J. Neurophysiol.* **101**, 1073–1088 (2009).

13. R. Vincis, O. Gschwend, K. Bhaukaurally, J. Beroud, A. Carleton, Dense representation of natural odorants in the mouse olfactory bulb. *Nat. Neurosci.* **15**, 537–539 (2012).

14. O. Gschwend, N. M. Abraham, S. Lagier, F. Begnaud, I. Rodriguez, A. Carleton, Neuronal pattern separation in the olfactory bulb improves odor discrimination learning. *Nat. Neurosci.* **18**, 1474–1482 (2015).

15. B. A. Johnson, M. Leon, Chemotopic Odorant Coding in a Mammalian Olfactory System. *J. Comp. Neurol.* **503**, 1–34 (2007).

16. C. Linster, B. A. Johnson, E. Yue, A. Morse, Z. Xu, E. E. Hingco, Y. Choi, M. Choi, A. Messiha, M. Leon, Perceptual correlates of neural representations evoked by odorant enantiomers. *J. Neurosci.* **21**, 9837–9843 (2001).

17. A. S. Bhattacharjee, S. Konakamchi, D. Turaev, R. Vincis, D. Nunes, A. A. Dingankar, H. Spors, A. Carleton, T. Kuner, N. M. Abraham, Similarity and Strength of Glomerular Odor Representations Define a Neural Metric of Sniff-Invariant Discrimination Time. *Cell Rep.* **28**, 2966–2978 (2019).

18. M. Najac, D. de Saint Jan, L. Reguero, P. Grandes, S. Charpak, Monosynaptic and

polysynaptic feed-forward inputs to mitral cells from olfactory sensory neurons. *J. Neurosci.* **31**, 8722–8729 (2011).

19. M. W. Chu, W. L. Li, T. Komiyama, Balancing the Robustness and Efficiency of Odor Representations during Learning. *Neuron.* **92**, 174–186 (2016).

20. Y. Yamada, K. Bhaukaurally, T. J. Madarász, A. Pouget, I. Rodriguez, A. Carleton, Context- and Output Layer-Dependent Long-Term Ensemble Plasticity in a Sensory Circuit. *Neuron.* **93**, 1–15 (2017).

21. M. T. Wiechert, B. Judkewitz, H. Riecke, R. W. Friedrich, Mechanisms of pattern decorrelation by recurrent neuronal circuits. *Nat. Neurosci.* **13**, 1003–1010 (2010).

22. N. M. Abraham, H. Spors, A. Carleton, T. W. Margrie, T. Kuner, A. T. Schaefer, Maintaining accuracy at the expense of speed: Stimulus similarity defines odor discrimination time in mice. *Neuron.* **44**, 865–876 (2004).

23. N. M. Abraham, D. Guerin, K. Bhaukaurally, A. Carleton, Similar Odor Discrimination Behavior in Head-Restrained and Freely Moving Mice. *PLoS One.* **7**, e51789 (2012).

24. D. Rinberg, A. Koulakov, A. Gelperin, Speed-Accuracy Tradeoff in Olfaction. *Neuron.* **51**, 351–358 (2006).

25. A. Resulaj, D. Rinberg, Novel Behavioral Paradigm Reveals Lower Temporal Limits on Mouse Olfactory Decisions. *J. Neurosci.* **35**, 11667–11673 (2015).

26. L. M. Kay, J. Beshel, C. Martin, When Good Enough Is Best. *Neuron.* **51**, 277–278 (2006).

27. N. M. Abraham, V. Egger, D. R. Shimshek, R. Renden, I. Fukunaga, R. Sprengel, P. H. Seeburg, M. Klugmann, T. W. Margrie, A. T. Schaefer, T. Kuner, Synaptic Inhibition in the Olfactory Bulb Accelerates Odor Discrimination in Mice. *Neuron.* **65**, 399–411 (2010).

28. A. T. Schaefer, T. W. Margrie, Spatiotemporal representations in the olfactory system. *Trends Neurosci.* **30**, 92–100 (2007).

29. N. Uchida, Z. F. Mainen, Speed and accuracy of olfactory discrimination in the rat. *Nat. Neurosci.* **6**, 1224–1229 (2003).

30. H. A. Zariwala, A. Kepecs, N. Uchida, J. Hirokawa, Z. F. Mainen, The limits of deliberation in a perceptual decision task. *Neuron.* **78**, 339–351 (2013).

31. A. Kepecs, N. Uchida, Z. F. Mainen, The sniff as a unit of olfactory processing. *Chem. Senses.* **31**, 167–179 (2006).

32. N. M. Abraham, R. Vincis, S. Lagier, I. Rodriguez, A. Carleton, Long term functional plasticity of sensory inputs mediated by olfactory learning. *Elife.* **3**, e02109 (2014).

33. M. A. Patterson, S. Lagier, A. Carleton, Odor representations in the olfactory bulb evolve after the first breath and persist as an odor afterimage. *Proc. Natl. Acad. Sci.* **110**, E3340– E3349 (2013).

34. H. Matsumoto, H. Kashiwadani, H. Nagao, A. Aiba, K. Mori, Odor-Induced Persistent Discharge of Mitral Cells in the Mouse Olfactory Bulb. *J Neurophysiol.* **101**, 1890–1900 (2009).

35. G. Mather, A. Pavan, G. Campana, C. Casco, The motion aftereffect reloaded. *Trends Cogn. Sci.* **12**, 481–487 (2008).

36. I. M. Vogels, A. M. Kappers, J. J. Koenderink, Haptic aftereffect of curved surfaces. *Perception.* **25**, 109–119 (1996).

37. E. Zwicker, "Negative Afterimage" in Hearing. *J. Acoust. Soc. Am.* **36**, 2413–2415 (1964).

38. E. S. Hoke, M. Hoke, B. Ross, Neurophysiological Correlate of the Auditory After-Image ('ZwickerTone'). *Audiol. Neuro Otol.* **1**, 161–174 (1996).

39. G. A. James, X. Li, G. E. DuBois, L. Zhou, X. P. Hu, Prolonged insula activation during perception of aftertaste. *Neuroreport.* **20**, 245–250 (2009).

40. O. Mazor, G. Laurent, Transient dynamics versus fixed points in odor representations by locust antennal lobe projection neurons. *Neuron.* **48**, 661–673 (2005).

41. S. Giridhar, N. N. Urban, Mechanisms and benefits of granule cell latency coding in the mouse olfactory bulb. *Front. Neural Circuits.* **6**, 1–11 (2012).

42. S. Parrish-Aungst, M. T. Shipley, F. Erdelyi, G. Szabo, A. C. Puche, Quantitative Analysis of Neuronal Diversity in the Mouse Olfactory Bulb. *J. Comp. Neurol.* **501**, 825–836 (2007).

43. N. Aguilar Martínez, G. Aguado Carrillo, P. E. Saucedo Alvarado, C. A. Mendoza García, A. L. Velasco Monroy, F. Velasco Campos, Clinical importance of olfactory function in neurodegenerative diseases. *Rev. Médica del Hosp. Gen. México.* **81**, 268–275 (2018).

44. K. Li, F. F. Liu, C. X. He, H. Z. Huang, A. J. Xie, F. Hu, D. Liu, J. Z. Wang, L. Q. Zhu, Olfactory Deprivation Hastens Alzheimer-Like Pathologies in a Human Tau-Overexpressed Mouse Model via Activation of cdk5. *Mol. Neurobiol.* **53**, 391–401 (2016).

45. E. H. Holbrook, D. A. Leopold, An updated review of clinical olfaction. *Curr. Opin. Otolaryngol. Head Neck Surg.* **14**, 23–28 (2006).

46. M. Barresi, R. Ciurleo, S. Giacoppo, V. Foti Cuzzola, D. Celi, P. Bramanti, S. Marino, Evaluation of olfactory dysfunction in neurodegenerative diseases. *J. Neurol. Sci.* **323**, 16–24 (2012).

47. R. L. Doty, Olfactory dysfunction in neurodegenerative diseases: is there a common pathological substrate? *Lancet Neurol.* **16**, 478–488 (2017).

48. A. Welge-Lüssen, M. Wolfensberger, Olfactory disorders following upper respiratory tract infections. *Adv. Otorhinolaryngol.* **63**, 125–132 (2006).

49. A. Giacomelli, L. Pezzati, F. Conti, D. Bernacchia, M. Siano, L. Oreni, S. Rusconi, C. Gervasoni, A. L. Ridolfo, G. Rizzardini, S. Antinori, M. Galli, Self-reported olfactory and taste disorders in patients with severe acute respiratory coronavirus 2 infection: A cross-sectional study. *Clin. Infect. Dis.* **71**, 889–890 (2020).

50. S. T. Moein, S. M. R. Hashemian, B. Mansourafshar, A. Khorram-Tousi, P. Tabarsi, R. L. Doty, Smell dysfunction: a biomarker for COVID-19. *Int. Forum Allergy Rhinol.* **10**, 944–950 (2020).

51. J. R. Lechien, P. Cabaraux, C. M. Chiesa-Estomba, M. Khalife, S. Hans, C. Calvo-Henriquez, D. Martiny, F. Journe, L. Sowerby, S. Saussez, Objective olfactory evaluation of self-reported loss of smell in a case series of 86 COVID-19 patients. *Head Neck.* **42**, 1583–1590 (2020).

52. J. R. Lechien, M. R. Barillari, L. Jouffe, S. Saussez, Anosmia Is a Key Symptom of COVID-19 Infection and Should Be Used as a Diagnostic Tool. *Ear, Nose Throat J.* **99**, 577–578 (2020).

53. K. L. Whitcroft, T. Hummel, Olfactory Dysfunction in COVID-19: Diagnosis and Management. *JAMA - J. Am. Med. Assoc.* **323**, 2512–2514 (2020).

54. A. V. Vroegop, A.-S. Eeckels, V. Van Rompaey, D. Vanden Abeele, M. S. Schiappoli, I. Alobid, T. Hummel, C. De Dorlodot, P. Levie, C. Huart, P. Eloy, O. M. Vanderveken, P. W. Hellings, P. Rombaux, P. Gevaert, COVID-19 and olfactory dysfunction - an ENT perspective to the current COVID-19 pandemic. *B-ENT.* **16**, 81–85 (2020).

55. D. H. Brann, T. Tsukahara, C. Weinreb, M. Lipovsek, K. Van Den Berge, B. Gong, R. Chance, I. C. Macaulay, H. J. Chou, R. B. Fletcher, D. Das, K. Street, H. R. De Bezieux, Y. G. Choi, D. Risso, S. Dudoit, E. Purdom, J. Mill, R. A. Hachem, H. Matsunami, D. W. Logan, B. J. Goldstein, M. S. Grubb, J. Ngai, S. R. Datta, Non-neuronal expression of SARS-CoV-2 entry genes in the olfactory system suggests mechanisms underlying COVID-19-associated anosmia. *Sci. Adv.* **6**, eabc5801 (2020).

56. L. Fodoulian, J. Tuberosa, D. Rossier, M. Boillat, C. Kan, V. Pauli, K. Egervari, J. A. Lobrinus, B. N. Landis, A. Carleton, I. Rodriguez, SARS-CoV-2 Receptors and Entry Genes Are Expressed in the Human Olfactory Neuroepithelium and Brain. *iScience.* **23,** 101839 (2020), doi:10.1016/j.isci.2020.101839.

57. A. Torabi, E. Mohammadbagheri, N. Akbari Dilmaghani, A. H. Bayat, M. Fathi, K. Vakili, R. Alizadeh, O. Rezaeimirghaed, M. Hajiesmaeili, M. Ramezani, L. Simani, A. Aliaghaei, Proinflammatory Cytokines in the Olfactory Mucosa Result in COVID-19 Induced Anosmia. *ACS Chem. Neurosci.* **11**, 1909–1913 (2020).

58.	K. W. Cooper, D. H. Brann, M. C. Farruggia, S. Bhutani, R. Pellegrino, T. Tsukahara, C. Weinreb, P. V. Joseph, E. D. Larson, V. Parma, M. W. Albers, L. A. Barlow, S. R. Datta, A. Di Pizio, COVID-19 and the Chemical Senses: Supporting Players Take Center Stage. *Neuron*. **107**, 219–233 (2020).

59.	F. Vogalis, C. C. Hegg, M. T. Lucero, Ionic conductances in sustentacular cells of the mouse olfactory epithelium. *J. Physiol.* **562**, 785–799 (2005).

60.	X. He, E. H. Y. Lau, P. Wu, X. Deng, J. Wang, X. Hao, Y. C. Lau, J. Y. Wong, Y. Guan, X. Tan, X. Mo, Y. Chen, B. Liao, W. Chen, F. Hu, Q. Zhang, M. Zhong, Y. Wu, L. Zhao, F. Zhang, B. J. Cowling, F. Li, G. M. Leung, Temporal dynamics in viral shedding and transmissibility of COVID-19. *Nat. Med.* **26**, 672–675 (2020).

61.	R. L. Doty, P. Shaman, C. P. Kimmelman, M. S. Dann, University of pennsylvania smell identification test: A rapid quantitative olfactory function test for the clinic. *Laryngoscope*. **94**, 176–178 (1984).

62.	T. Hummel, B. Sekinger, S. R. Wolf, E. Pauli, G. Kobal, "Sniffin" sticks'. Olfactory performance assessed by the combined testing of odor identification, odor discrimination and olfactory threshold. *Chem. Senses*. **22**, 39–52 (1997).

63.	A. Pezzini, A. Padovani, Lifting the mask on neurological manifestations of COVID-19. *Nat. Rev. Neurol.* **16**, 636–644 (2020).

64.	L. Mao, H. Jin, M. Wang, Y. Hu, S. Chen, Q. He, J. Chang, C. Hong, Y. Zhou, D. Wang, X. Miao, Y. Li, B. Hu, Neurologic Manifestations of Hospitalized Patients with Coronavirus Disease 2019 in Wuhan, China. *JAMA Neurol.* **77**, 683–690 (2020).

65.	S. Veronese, A. Sbarbati, Chemosensory Systems in COVID-19: Evolution of Scientific Research. *ACS Chem. Neurosci.* **12**, 813–824 (2021).

66.	M. A. Ellul, L. Benjamin, B. Singh, S. Lant, B. D. Michael, A. Easton, R. Kneen, S. Defres, J. Sejvar, T. Solomon, Neurological associations of COVID-19. *Lancet Neurol.* **19**, 767–783 (2020).

67.	A. Whittaker, M. Anson, A. Harky, Neurological Manifestations of COVID-19: A systematic review and current update. *Acta Neurol. Scand.* **142**, 14–22 (2020).

68.	A. S. Bhattacharjee, S. V. Joshi, S. Naik, S. Sangle, N. M. Abraham, Quantitative assessment of olfactory dysfunction accurately detects asymptomatic COVID-19 carriers. *EClinicalMedicine*. **28**, 100575 (2020).

69.	S. S. Miller, N. E. Spear, Olfactory learning in the rat immediately after birth: Unique salience of first odors. *Dev. Psychobiol.* **51**, 488–504 (2009).

70.	B. Schaal, L. Marlier, R. Soussignan, Human Foetuses Learn Odours from their Pregnant Mother's Diet. *Chem. Senses*. **25**, 729–737 (2000).

71.	C. Murphy, Olfactory and other sensory impairments in Alzheimer disease. *Nat. Rev. Neurol.* **15**, 11–24 (2019).

72.	R. L. Doty, Olfactory dysfunction in Parkinson disease. *Nat. Rev. Neurol.* **8**, 329–339 (2012).

73.	M. P. Cecchini, D. Viviani, M. Sandri, A. Hähner, T. Hummel, C. Zancanaro, Olfaction in people with down syndrome: A comprehensive assessment across four decades of age. *PLoS One*. **11**, 1–13 (2016).

74.	J. Alves, Olfactory dysfunction in dementia. *World J. Clin. Cases*. **2**, 661–667 (2014).

75.	J. Mullol, I. Alobid, F. Mariño-Sánchez, L. Quintó, J. De Haro, M. Bernal-Sprekelsen, A. Valero, C. Picado, C. Marin, Furthering the understanding of olfaction, prevalence of loss of smell and risk factors: A population-based survey (OLFACAT study). *BMJ Open*. **2**, e001256 (2012).

76.	S. Boesveldt, E. M. Postma, D. Boak, A. Welge-Luessen, V. Schöpf, J. D. Mainland, J. Martens, J. Ngai, V. B. Duffy, Anosmia-A clinical review. *Chem. Senses*. **42**, 513–523 (2017).

77.	J. R. Lechien, C. M. Chiesa-Estomba, D. R. De Siati, M. Horoi, S. D. Le Bon, A. Rodriguez,

D. Dequanter, S. Blecic, F. El Afia, L. Distinguin, Y. Chekkoury-Idrissi, S. Hans, I. L. Delgado, C. Calvo-Henriquez, P. Lavigne, C. Falanga, M. R. Barillari, G. Cammaroto, M. Khalife, P. Leich, C. Souchay, C. Rossi, F. Journe, J. Hsieh, M. Edjlali, R. Carlier, L. Ris, A. Lovato, C. De Filippis, F. Coppee, N. Fakhry, T. Ayad, S. Saussez, Olfactory and gustatory dysfunctions as a clinical presentation of mild-to-moderate forms of the coronavirus disease (COVID-19): a multicenter European study. *Eur. Arch. Oto-Rhino-Laryngology*. **277**, 2251–2261 (2020).

78. B. Iravani, A. Arshamian, A. Ravia, E. Mishor, K. Snitz, S. Shushan, Y. Roth, O. Perl, D. Honigstein, R. Weissgross, S. Karagach, G. Ernst, M. Okamoto, Z. Mainen, E. Monteleone, C. Dinnella, S. Spinelli, F. Mariño-Sánchez, C. Ferdenzi, M. Smeets, K. Touhara, M. Bensafi, T. Hummel, N. Sobel, J. N. Lundström, Relationship between odor intensity estimates and COVID-19 prevalence prediction in a Swedish population. *Chem. Senses*. **45**, 449–456 (2020).

79. C. Menni, A. M. Valdes, M. B. Freidin, C. H. Sudre, L. H. Nguyen, D. A. Drew, S. Ganesh, T. Varsavsky, M. J. Cardoso, J. S. El-Sayed Moustafa, A. Visconti, P. Hysi, R. C. E. Bowyer, M. Mangino, M. Falchi, J. Wolf, S. Ourselin, A. T. Chan, C. J. Steves, T. D. Spector, Real-time tracking of self-reported symptoms to predict potential COVID-19. *Nat. Med.* **26**, 1037–1040 (2020).

80. E. E. Morrison, R. M. Costanzo, Morphology of the human olfactory epithelium. *J. Comp. Neurol.* **297**, 1–13 (1990).

81. A. J. Pinching, T. P. Powell, The termination of centrifugal fibres in the glomerular layer of the olfactory bulb. *J. Cell Sci.* **10**, 621–635 (1972).

82. B. J. Davis, F. Macrides, The organization of centrifugal projections from the anterior olfactory nucleus, ventral hippocampal rudiment, and piriform cortex to the main olfactory bulb in the hamster: an autoradiographic study. *J Comp Neurol*. **203**, 475–493 (1981).

83. D. A. Wilson, M. Kadohisa, M. L. Fletcher, Cortical contributions to olfaction: Plasticity and perception. *Semin. Cell Dev. Biol.* **17**, 462–470 (2006).

84. M. Rothermel, R. M. Carey, A. Puche, M. T. Shipley, M. Wachowiak, Cholinergic inputs from Basal forebrain add an excitatory bias to odor coding in the olfactory bulb. *J. Neurosci.* **34**, 4654–64 (2014).

85. C. Linster, T. A. Cleland, Cholinergic modulation of sensory representations in the olfactory bulb. *Neural Networks*. **15**, 709–717 (2002).

86. S. Devore, C. Linster, Noradrenergic and cholinergic modulation of olfactory bulb sensory processing. *Front. Behav. Neurosci.* **6**, 1–12 (2012).

87. W. Doucette, J. Milder, D. Restrepo, Adrenergic modulation of olfactory bulb circuitry affects odor discrimination. *Learn Mem*. **14**, 539–547 (2007).

88. J. H. McLean, M. T. Shipley, Serotonergic afferents to the rat olfactory bulb: II. Changes in fiber distribution during development. *J. Neurosci.* **7**, 3029–3039 (1987).

89. L. Buck, R. Axel, A novel multigene family may encode odorant receptors: a molecular basis for odor recognition. *Cell*. **65**, 175–87 (1991).

90. A. Brochtrup, T. Hummel, Olfactory map formation in the Drosophila brain: Genetic specificity and neuronal variability. *Curr. Opin. Neurobiol.* **21**, 85–92 (2011).

91. Y. Yoshihara, Molecular Genetic Dissection of the Zebrafish Olfactory System, in *Results Probl. Cell Differ.* (2009), pp. 97–120.

92. P. Mombaerts, Seven transmembrane proteins as odorant and chemosensory receptors. *Science*. **286**, 707–711 (1999).

93. X. Zhang, S. Firestein, The olfactory receptor gene superfamily of the mouse. *Nat. Neurosci.* **5**, 124–133 (2002).

94. N. S. Levy, H. A. Bakalyar, R. R. Reed, Signal transduction in olfactory neurons. *J. Steroid Biochem. Mol. Biol.* **39**, 633–637 (1991).

95. T. Nakamura, Cellular and molecular contituents of olfactory sensation in vertebrates. *Comp

Biochem Physiol. **126**, 17–32 (2000).

96. S. Firestein, How the olfactory system makes sense of scents. *Nature*. **413**, 211–218 (2001).

97. K. J. Ressler, S. L. Sullivan, L. B. Buck, Information Coding in the Olfactory System : Evidence for a Stereotyped and Highly Organized Epitope Map in the Olfactory Bulb. *Cell*. **79**, 1245–1255 (1994).

98. B. Malnic, J. Hirono, T. Sato, L. B. Buck, Combinatorial receptor codes for odors. *Cell*. **96**, 713–723 (1999).

99. M. Luo, The necklace olfactory system in mammals. *J. Neurogenet.* **22**, 229–238 (2008).

100. P. L. Greer, D. M. Bear, J. M. Lassance, M. L. Bloom, T. Tsukahara, S. L. Pashkovski, F. K. Masuda, A. C. Nowlan, R. Kirchner, H. E. Hoekstra, S. R. Datta, A Family of non-GPCR Chemosensors Defines an Alternative Logic for Mammalian Olfaction. *Cell*. **165**, 1734–1748 (2016).

101. A. Vassalli, A. Rothman, P. Feinstein, M. Zapotocky, P. Mombaerts, Minigenes Impart Odorant Receptor-Specific Axon Guidance in the Olfactory Bulb. *Neuron*. **35**, 681–696 (2002).

102. A. Magklara, A. Yen, B. M. Colquitt, E. J. Clowney, W. Allen, E. Markenscoff-Papadimitriou, Z. A. Evans, P. Kheradpour, G. Mountoufaris, C. Carey, G. Barnea, M. Kellis, S. Lomvardas, An epigenetic signature for monoallelic olfactory receptor expression. *Cell*. **145**, 555–570 (2011).

103. R. P. Dalton, D. B. Lyons, S. Lomvardas, Co-opting the unfolded protein response to elicit olfactory receptor feedback. *Cell*. **155**, 321–332 (2013).

104. K. Mori, H. Sakano, How is the olfactory map formed and interpreted in the mammalian brain? *Annu. Rev. Neurosci.* **34**, 467–499 (2011).

105. I. Rodriguez, Singular expression of olfactory receptor genes. *Cell*. **155**, 274–277 (2013).

106. R. Pacifico, A. Dewan, D. Cawley, C. Guo, T. Bozza, An olfactory subsystem that mediates high-sensitivity detection of volatile amines. *Cell Rep.* **2**, 76–88 (2012).

107. W. Lin, R. Margolskee, G. Donnert, S. W. Hell, D. Restrepo, Olfactory neurons expressing transient receptor potential channel M5 (TRPM5) are involved in sensing semiochemicals. *Proc. Natl. Acad. Sci. U. S. A.* **104**, 2471–2476 (2007).

108. K. Miyamichi, S. Serizawa, H. M. Kimura, H. Sakano, Continuous and overlapping expression domains of odorant receptor genes in the olfactory epithelium determine the dorsal/ventral positioning of glomeruli in the olfactory bulb. *J. Neurosci.* **25**, 3586–3592 (2005).

109. H. Sakano, Neural Map Formation in the Mouse Olfactory System. *Neuron*. **67**, 530–542 (2010).

110. X. Zhang, M. Rogers, H. Tian, X. Zhang, D. J. Zou, J. Liu, M. Ma, G. M. Shepherd, S. J. Firestein, High-throughput microarray detection of olfactory receptor gene expression in the mouse. *Proc. Natl. Acad. Sci. U. S. A.* **101**, 14168–14173 (2004).

111. J. H. Coleman, X. B. Lin, J. D. Louie, X. J. Peterson, R. P. Lane, X. J. E. Schwob, Spatial Determination of Neuronal Diversification in the Olfactory Epithelium. *J. Neurosci.* **39**, 814–832 (2019).

112. D. J. Rodriguez-Gil, D. L. Bartel, A. W. Jaspers, A. S. Mobley, F. Imamura, C. A. Greer, Odorant receptors regulate the final glomerular coalescence of olfactory sensory neuron axons. *Proc. Natl. Acad. Sci. U. S. A.* **112**, 5821–5826 (2015).

113. J.-F. Cloutier, R. J. Giger, G. Koentges, C. Dulac, A. L. Kolodkin, D. D. Ginty, Neuropilin-2 mediates axonal fasciculation, zonal segregation, but not axonal convergence. *Neuron*. **33**, 877–892 (2002).

114. J. F. Cloutier, A. Sahay, E. C. Chang, M. Tessier-Lavigne, C. Dulac, A. L. Kolodkin, D. D. Ginty, Differential requirements for semaphorin 3F and slit-1 in axonal targeting, fasciculation, and segregation of olfactory sensory neuron projections. *J. Neurosci.* **24**, 9087–9096 (2004).

115. C. Lodovichi, L. Belluscio, L. Belluscio, Odorant Receptors in the Formation of the Olfactory Bulb Circuitry Odorant Receptors in the Formation of the Olfactory Bulb Circuitry. *Physiology*. **27**, 200–212 (2012).

116. H. Takeuchi, H. Sakano, Neural map formation in the mouse olfactory system. *Cell. Mol. Life Sci.* **71**, 3049–3057 (2014).

117. P. Mombaerts, F. Wang, C. Dulac, S. K. Chao, A. Nemes, M. Mendelsohn, J. Edmondson, R. Axel, Visualizing an olfactory sensory map. *Cell*. **87**, 675–686 (1996).

118. J. E. Schwob, Neural regeneration and the peripheral olfactory system. *Anat. Rec.* **269**, 33–49 (2002).

119. E. Blanco-Hernández, P. Valle-Leija, V. Zomosa-Signoret, R. Drucker-Colín, R. Vidaltamayo, Odor Memory Stability after Reinnervation of the Olfactory Bulb. *PLoS One*. **7**, e46338 (2012).

120. N. Ihara, A. Nakashima, N. Hoshina, Y. Ikegaya, H. Takeuchi, Differential expression of axon-sorting molecules in mouse olfactory sensory neurons. *Eur. J. Neurosci.* **44**, 1998–2003 (2016).

121. A. Nakashima, N. Ihara, M. Shigeta, H. Kiyonari, Y. Ikegaya, H. Takeuchi, Structured spike series specify gene expression patterns for olfactory circuit formation. *Science*. **364**, eaaw5030 (2019).

122. S. Serizawa, K. Miyamichi, H. Takeuchi, Y. Yamagishi, M. Suzuki, H. Sakano, A Neuronal Identity Code for the Odorant Receptor-Specific and Activity-Dependent Axon Sorting. *Cell*. **127**, 1057–1069 (2006).

123. P. Lorenzon, N. Redolfi, M. J. Podolsky, I. Zamparo, S. a. Franchi, G. Pietra, A. Boccaccio, A. Menini, V. N. Murthy, C. Lodovichi, Circuit Formation and Function in the Olfactory Bulb of Mice with Reduced Spontaneous Afferent Activity. *J. Neurosci.* **35**, 146–160 (2015).

124. C. R. Yu, J. Power, G. Barnea, S. O'Donnell, H. E. V. Brown, J. Osborne, R. Axel, J. A. Gogos, Spontaneous neural activity is required for the establishment and maintenance of the olfactory sensory map. *Neuron*. **42**, 553–566 (2004).

125. D. F. Albeanu, A. C. Provost, P. Agarwal, E. Soucy, V. N. Murthy, Olfactory marker protein regulates refinement of the olfactory glomerular map. *Nat. Commun.* **9**, 1–12 (2018).

126. C. Lodovichi, Topographic organization in the olfactory bulb. *Cell Tissue Res.* **383**, 457-472 (2021). doi:10.1007/s00441-020-03348-w.

127. M. A. Kerr, L. Belluscio, Olfactory experience accelerates glomerular refinement in the mammalian olfactory bulb. *Nat Neurosci*. **9**, 484–486 (2006).

128. J. Todrank, G. Heth, D. Restrepo, Effects of in utero odorant exposure on neuroanatomical development of the olfactory bulb and odour preferences. *Proc. R. Soc. B Biol. Sci.* **278**, 1949–1955 (2011).

129. P. Valle-leija, E. Blanco-Hernandez, R. Drucker-Colin, G. Gutierrez-Ospina, R. Vidaltamayo, Supernumerary Formation of Olfactory Glomeruli Induced by Chronic Odorant Exposure : A Constructivist Expression of Neural Plasticity. *PLoS One*. **7**, e35358 (2012).

130. J. P. Royet, H. Distel, R. Hudson, R. Gervais, A re-estimation of the number of glomeruli and mitral cells in the olfactory bulb of rabbit. *Brain Res.* **788**, 35–42 (1998).

131. K. Mori, Y. K. Takahashi, K. M. Igarashi, M. Yamaguchi, Maps of Odorant Molecular Features in the Mammalian Olfactory Bulb Maps of Odorant Molecular Features in the Mammalian Olfactory Bulb. *Physiol. Rev.* **86**, 409–433 (2006).

132. N. Uchida, Y. K. Takahashi, M. Tanifuji, K. Mori, Odor maps in the mammalian olfactory bulb: domain organization and odorant structural features. *Nat. Neurosci.* **3**, 1035–1043 (2000).

133. M. Luo, L. C. Katz, Response correlation maps of neurons in the mammalian olfactory bulb. *Neuron*. **32**, 1165–1179 (2001).

134. E. R. Soucy, D. F. Albeanu, A. L. Fantana, V. N. Murthy, M. Meister, Precision and diversity in an odor map on the olfactory bulb. *Nat. Neurosci.* **12**, 210–220 (2009).

135. T. Bozza, J. P. McGann, P. Mombaerts, M. Wachowiak, In vivo imaging of neuronal activity by targeted expression of a genetically encoded probe in the mouse. *Neuron.* **42**, 9–21 (2004).

136. T. A. Cleland, Construction of odor representations by olfactory bulb microcircuits. *Progress in Brain research.* **208**, 177-203 (2014).

137. H. Chae, D. R. Kepple, W. G. Bast, V. N. Murthy, A. A. Koulakov, D. F. Albeanu, Mosaic representations of odors in the input and output layers of the mouse olfactory bulb. *Nat. Neurosci.* **22**, 1306–1317 (2019).

138. K. Mori, K. Kishi, H. Ojima, Distribution of dendrites of mitral, displaced mitral, tufted, and granule cells in the rabbit olfactory bulb. *J. Comp. Neurol.* **219**, 339–355 (1983).

139. G. M. Shepherd, *The Synaptic Organization of the Brain* (Oxford University Press, 2004).

140. T. Kosaka, K. Kosaka, "Interneurons" in the olfactory bulb revisited. *Neurosci. Res.* **69**, 93–99 (2011).

141. M. T. Shipley, M. Ennis, Functional organization of olfactory system. *J. Neurobiol.* **30**, 123–176 (1996).

142. E. Kiyokage, Y. Z. Pan, Z. Shao, K. Kobayashi, G. Szabo, Y. Yanagawa, K. Obata, H. Okano, K. Toida, A. C. Puche, M. T. Shipley, Molecular identity of periglomerular and short axon cells. *J. Neurosci.* **30**, 1185–1196 (2010).

143. M. Wachowiak, M. T. Shipley, Coding and synaptic processing of sensory information in the glomerular layer of the olfactory bulb. *Semin. Cell Dev. Biol.* **17**, 411–423 (2006).

144. R. M. Carey, W. E. Sherwood, M. T. Shipley, A. Borisyuk, M. Wachowiak, Role of intraglomerular circuits in shaping temporally structured responses to naturalistic inhalation-driven sensory input to the olfactory bulb. *J. Neurophysiol.* **113**, 3112–3129 (2015).

145. G. J. Murphy, D. P. Darcy, J. S. Isaacson, Intraglomerular inhibition: signaling mechanisms of an olfactory microcircuit. *Nat. Neurosci.* **8**, 354–364 (2005).

146. Z. Shao, A. C. Puche, E. Kiyokage, G. Szabo, M. T. Shipley, Two GABAergic intraglomerular circuits differentially regulate tonic and phasic presynaptic inhibition of olfactory nerve terminals. *J. Neurophysiol.* **101**, 1988–2001 (2009).

147. D. H. Gire, N. E. Schoppa, Control of on/off glomerular signaling by a local GABAergic microcircuit in the olfactory bulb. *J. Neurosci.* **29**, 13454–13464 (2009).

148. T. A. Cleland, Early transformations in odor representation. *Trends Neurosci.* **33**, 130–139 (2010).

149. A. Hayar, S. Karnup, M. Ennis, M. T. Shipley, External tufted cells: A major excitatory element that coordinates glomerular activity. *J. Neurosci.* **24**, 6676–6685 (2004).

150. D. H. Gire, J. D. Zak, J. N. Bourne, N. B. Goodson, N. E. Schoppa, Balancing extrasynaptic excitation and synaptic inhibition within olfactory bulb glomeruli. *eNeuro.* **6**, 1-21 (2019). doi:10.1523/ENEURO.0247-19.2019.

151. D. De Saint Jan, D. Hirnet, G. L. Westbrook, S. Charpak, External Tufted Cells Drive the Output of Olfactory Bulb Glomeruli. *J. Neurosci.* **29**, 2043–2052 (2009).

152. D. H. Gire, K. M. Franks, J. D. Zak, K. F. Tanaka, J. D. Whitesell, A. A. Mulligan, R. Hen, N. E. Schoppa, Mitral cells in the olfactory bulb are mainly excited through a multistep signaling path. *J. Neurosci.* **32**, 2964–2975 (2012).

153. J. Ma, G. Lowe, Correlated firing in tufted cells of mouse olfactory bulb. *Neuroscience.* **169**, 1715–38 (2010).

154. W. L. Liu, M. T. Shipley, Intrabulbar associational system in the rat olfactory bulb comprises cholecystokinin-containing tufted cells that synapse onto the dendrites of GABAergic granule cells. *J. Comp. Neurol.* **346**, 541–558 (1994).

155. S. Liu, C. Plachez, Z. Shao, A. Puche, M. T. Shipley, Olfactory Bulb Short Axon Cell

Release of GABA and Dopamine Produces a Temporally Biphasic Inhibition-Excitation Response in External Tufted Cells. *J. Neurosci.* **33**, 2916–2926 (2013).

156. J. L. Aungst, P. M. Heyward, a C. Puche, S. V Karnup, a Hayar, G. Szabo, M. T. Shipley, Centre-surround inhibition among olfactory bulb glomeruli. *Nature.* **426**, 623–629 (2003).

157. J. L. Price, T. P. Powell, The morphology of the granule cells of the olfactory bulb. *J. Cell Sci.* **7**, 91–123 (1970).

158. H. Naritsuka, K. Sakai, T. Hashikawa, K. Mori, M. Yamaguchi, Perisomatic-targeting granule cells in the mouse olfactory bulb. *J. Comp. Neurol.* **515**, 409–426 (2009).

159. F. T. Merkle, L. C. Fuentealba, T. A. Sanders, L. Magno, N. Kessaris, A. Alvarez-Buylla, Adult neural stem cells in distinct microdomains generate previously unknown interneuron types. *Nat. Neurosci.* **17**, 207–214 (2014).

160. E. Orona, J. W. Scott, E. C. Rainer, Different granule cell populations innervate superficial and deep regions of the external plexiform layer in rat olfactory bulb. *J. Comp. Neurol.* **217**, 227–237 (1983).

161. V. Egger, Dendrodendritic Synaptic Signals in Olfactory Bulb Granule Cells: Local Spine Boost and Global Low-Threshold Spike. *J. Neurosci.* **25**, 3521–3530 (2005).

162. W. R. Chen, W. Xiong, G. M. Shepherd, Analysis of relations between NMDA receptors and GABA release at olfactory bulb reciprocal synapses. *Neuron.* **25**, 625–633 (2000).

163. B. Halabisky, D. Friedman, M. Radojicic, B. W. Strowbridge, Calcium influx through NMDA receptors directly evokes GABA release in olfactory bulb granule cells. *J. Neurosci.* **20**, 5124–5134 (2000).

164. J. S. Isaacson, B. W. Strowbridge, Olfactory reciprocal synapses: Dendritic signaling in the CNS. *Neuron.* **20**, 749–761 (1998).

165. N. N. Urban, Lateral inhibition in the olfactory bulb and in olfaction. *Physiol. Behav.* **77**, 607–612 (2002).

166. K. Mori, H. Nagao, Y. Yoshihara, The olfactory bulb: Coding and processing of odor molecule information. *Science.* **286**, 711–715 (1999).

167. T. W. Margrie, B. Sakmann, N. N. Urban, Action potential propagation in mitral cell lateral dendrites is decremental and controls recurrent and lateral inhibition in the mammalian olfactory bulb. *Proc. Natl. Acad. Sci. U. S. A.* **98**, 319–324 (2001).

168. M. Leon, B. A. Johnson, Olfactory coding in the mammalian olfactory bulb. *Brain Res. Rev.* **42**, 23–32 (2003).

169. V. Kapoor, N. N. Urban, Glomerulus-Specific, Long-Latency Activity in the Olfactory Bulb Granule Cell Network. *J. Neurosci.* **26**, 11709–11719 (2006).

170. M. A. Geramita, S. D. Burton, N. N. Urban, Distinct lateral inhibitory circuits drive parallel processing of sensory information in the mammalian olfactory bulb. *Elife.* **5**, 1689–1699 (2016).

171. I. Fukunaga, M. Berning, M. Kollo, A. Schmaltz, A. T. Schaefer, Two Distinct Channels of Olfactory Bulb Output. *Neuron.* **75**, 320–329 (2012).

172. K. Miyamichi, Y. Shlomai-Fuchs, M. Shu, B. C. Weissbourd, L. Luo, A. Mizrahi, Dissecting local circuits: Parvalbumin interneurons underlie broad feedback control of olfactory bulb output. *Neuron.* **80**, 1232–1245 (2013).

173. H. K. K. Kato, S. N. N. Gillet, A. J. J. Peters, J. S. S. Isaacson, T. Komiyama, Parvalbumin-expressing interneurons linearly control olfactory bulb output. *Neuron.* **80**, 1218–1231 (2013).

174. G. Lepousez, Z. Csaba, V. Bernard, C. Loudes, C. Videau, J. Lacombe, J. Epelbaum, C. Viollet, Somatostatin interneurons delineate the inner part of the external plexiform layer in the mouse main olfactory bulb. *J. Comp. Neurol.* **518**, 1976–1994 (2010).

175. R. T. Pressler, B. W. Strowbridge, Blanes cells mediate persistent feedforward inhibition onto granule cells in the olfactory bulb. *Neuron.* **49**, 889–904 (2006).

176. M. D. Eyre, M. Antal, Z. Nusser, Distinct Deep Short-Axon Cell Subtypes of the Main

Olfactory Bulb Provide Novel Intrabulbar and Extrabulbar GABAergic Connections. *J. Neurosci.* **28**, 8217–8229 (2008).

177. S. D. Burton, G. LaRocca, A. Liu, C. E. J. J. Cheetham, N. N. Urban, Olfactory bulb deep short-axon cells mediate widespread inhibition of tufted cell apical dendrites. *J. Neurosci.* **37**, 1117–1138 (2016).

178. G. Leng, H. Hashimoto, C. Tsuji, N. Sabatier, M. Ludwig, Discharge patterning in rat olfactory bulb mitral cells in vivo. *Physiol. Rep.* **2**, 1–22 (2014).

179. S. Nagayama, Y. K. Takahashi, Y. Yoshihara, K. Mori, Mitral and tufted cells differ in the decoding manner of odor maps in the rat olfactory bulb. *J. Neurophysiol.* **91**, 2532–2540 (2004).

180. K. M. Igarashi, N. Ieki, M. An, Y. Yamaguchi, S. Nagayama, K. Kobayakawa, R. Kobayakawa, M. Tanifuji, H. Sakano, W. R. Chen, K. Mori, Parallel mitral and tufted cell pathways route distinct odor information to different targets in the olfactory cortex. *J. Neurosci.* **32**, 7970–7985 (2012).

181. S. Nagayama, A. Enerva, M. L. Fletcher, A. V. Masurkar, K. M. Igarashi, K. Mori, W. R. Chen, Differential Axonal Projection of Mitral and Tufted Cells in the Mouse Main Olfactory System. *Front. Neural Circuits.* **4**, 1–8 (2010).

182. J. L. Price, An autoradiographic study of complementary laminar patterns of termination of afferent fibers to the olfactory cortex. *J. Comp. Neurol.* **150**, 87–108 (1973).

183. L. B. Haberly, Neuronal circuitry in olfactory cortex: anatomy and func- tional implications. *Chem Senses.* **10**, 219–238 (1985).

184. L. B. Haberly, Structure of the piriform cortex of the opossum. I. Description of neuron types with golgi methods. *J. Comp. Neurol.* **213**, 163–187 (1983).

185. K. M. Franks, M. J. Russo, D. L. Sosulski, A. A. Mulligan, S. A. Siegelbaum, R. Axel, Recurrent Circuitry Dynamically Shapes the Activation of Piriform Cortex. *Neuron.* **72**, 49–56 (2011).

186. C. Poo, J. S. Isaacson, A Major Role for Intracortical Circuits in the Strength and Tuning of Odor-Evoked Excitation in Olfactory Cortex. *Neuron.* **72**, 41–48 (2011).

187. N. Suzuki, J. M. Bekkers, Two Layers of Synaptic Processing by Principal Neurons in Piriform Cortex. *J. Neurosci.* **31**, 2156–2166 (2011).

188. M. B. Luskin, J. L. Price, The topographic organization of associational fibers of the olfactory system in the rat, including centrifugal fibers to the olfactory bulb. *J. Comp. Neurol.* **216**, 264–291 (1983).

189. L. B. Haberly, Parallel-distributed processing in olfactory cortex: new insights from morphological and physiological analysis of neuronal circuitry. *Chem. Senses.* **26**, 551–576 (2001).

190. T. Imai, H. Sakano, Interhemispheric Olfactory Circuit and the Memory Beyond. *Neuron.* **58**, 465–467 (2008).

191. Z. Yan, J. Tan, C. Qin, Y. Lu, C. Ding, M. Luo, Precise Circuitry Links Bilaterally Symmetric Olfactory Maps. *Neuron.* **58**, 613–624 (2008).

192. A. J. Aqrabawi, J. C. Kim, Olfactory memory representations are stored in the anterior olfactory nucleus. *Nat. Commun.* **11**, 1–8 (2020).

193. S. Ikemoto, Dopamine reward circuitry: Two projection systems from the ventral midbrain to the nucleus accumbens-olfactory tubercle complex. *Brain Res. Rev.* **56**, 27–78 (2007).

194. D. W. Wesson, D. A. Wilson, Sniffing out the contributions of the olfactory tubercle to the sense of smell: Hedonics, sensory integration, and more? *Neurosci. Biobehav. Rev.* **35**, 655–668 (2011).

195. B. J. FitzGerald, K. Richardson, D. W. Wesson, Olfactory tubercle stimulation alters odor preference behavior and recruits forebrain reward and motivational centers. *Front. Behav. Neurosci.* **8**, 1–9 (2014).

196. D. J. Millman, V. N. Murthy, Rapid learning of odor-value association in the olfactory

striatum. *J. Neurosci.* **40**, 4335–4347 (2020).

197. S. J. Ramus, H. Eichenbaum, Neural correlates of olfactory recognition memory in the rat orbitofrontal cortex. *J. Neurosci.* **20**, 8199–8208 (2000).

198. S. Matsutani, Trajectory and terminal distribution of single centrifugal axons from olfactory cortical areas in the rat olfactory bulb. *Neuroscience.* **169**, 436–448 (2010).

199. A. M. Boyd, J. F. Sturgill, C. Poo, J. S. Isaacson, Cortical Feedback Control of Olfactory Bulb Circuits. *Neuron.* **76**, 1161–1174 (2012).

200. F. Markopoulos, D. Rokni, D. H. Gire, V. N. Murthy, Functional Properties of Cortical Feedback Projections to the Olfactory Bulb. *Neuron.* **76**, 1175–1188 (2012).

201. A. M. Boyd, H. K. Kato, T. Komiyama, J. S. Isaacson, Broadcasting of Cortical Activity to the Olfactory Bulb. *Cell Rep.* **10**, 1032–1039 (2015).

202. G. H. Otazu, H. Chae, M. B. Davis, D. F. Albeanu, G. H. Otazu, H. Chae, M. B. Davis, D. F. Albeanu, Cortical Feedback Decorrelates Olfactory Bulb Output in Awake Mice Article Cortical Feedback Decorrelates Olfactory Bulb Output in Awake Mice. *Neuron.* **86**, 1–17 (2015).

203. J. H. McLean, M. T. Shipley, W. T. Nickell, G. Aston-Jones, C. K. H. Reyher, Chemoanatomical organization of the noradrenergic input from locus coeruleus to the olfactory bulb of the adult rat. *J. Comp. Neurol.* **285**, 339–349 (1989).

204. C. Linster, Q. Nai, M. Ennis, Nonlinear effects of noradrenergic modulation of olfactory bulb function in adult rodents. *J. Neurophysiol.* **105**, 1432–43 (2011).

205. A. Hayar, P. M. Heyward, T. Heinbockel, M. T. Shipley, M. Ennis, Direct excitation of mitral cells via activation of α1-noradrenergic receptors in rat olfactory bulb slices. *J. Neurophysiol.* **86**, 2173–2182 (2001).

206. Q. Nai, H. W. Dong, A. Hayar, C. Linster, M. Ennis, Noradrenergic regulation of GABAergic inhibition of main olfactory bulb mitral cells varies as a function of concentration and receptor subtype. *J. Neurophysiol.* **101**, 2472–2484 (2009).

207. M. Ma, M. Luo, Optogenetic activation of basal forebrain cholinergic neurons modulates neuronal excitability and sensory responses in the main olfactory bulb. *J. Neurosci.* **32**, 10105–10116 (2012).

208. A. Apicella, Q. Yuan, M. Scanziani, J. S. Isaacson, Pyramidal cells in piriform cortex receive convergent input from distinct olfactory bulb glomeruli. *J Neurosci.* **30**, 14255–14260 (2010).

209. J. S. Isaacson, Odor representations in mammalian cortical circuits. *Curr. Opin. Neurobiol.* **20**, 328–331 (2010).

210. D. D. Stettler, R. Axel, Representations of Odor in the Piriform Cortex. *Neuron.* **63**, 854–864 (2009).

211. R. L. Rennaker, C.-F. F. Chen, A. M. Ruyle, A. M. Sloan, D. A. Wilson, Spatial and Temporal Distribution of Odorant-Evoked Activity in the Piriform Cortex. *J. Neurosci.* **27**, 1534–1542 (2007).

212. Z. H. Zou, L. F. Horowitz, J. P. Montmayeur, S. Snapper, L. B. Buck, Genetic tracing reveals a stereotyped sensory map in the olfactory cortex. *Nature.* **414**, 173–179 (2001).

213. J. J. Hopfield, Pattern recognition computation using action potential timing for stimulus representation. *Nature.* **376**, 33–36 (1995).

214. M. Stern, K. A. Bolding, L. Abbott, K. M. Franks, A transformation from temporal to ensemble coding in a model of piriform cortex. *Elife.* **7**, e34831 (2018).

215. K. A. Bolding, K. M. Franks, Recurrent cortical circuits implement concentration-invariant odor coding. *Science.* **361**, 1–12 (2018).

216. J. Chapuis, D. A. Wilson, Bidirectional plasticity of cortical pattern recognition and behavioral sensory acuity. *Nat. Neurosci.* **15**, 155–161 (2012).

217. D. C. Barnes, R. D. Hofacer, A. R. Zaman, R. L. Rennaker, D. A. Wilson, Olfactory perceptual stability and discrimination. *Nat. Neurosci.* **11**, 1378–1380 (2008).

218. J. C. Y. Tang, S. Rudolph, O. S. Dhande, V. E. Abraira, S. Choi, S. W. Lapan, I. R. Drew, E. Drokhlyansky, A. D. Huberman, W. G. Regehr, C. L. Cepko, Cell type-specific manipulation with GFP-dependent Cre recombinase. *Nat. Neurosci.* **18**, 1334–1341 (2015).

219. S. Bäck, J. Necarsulmer, L. R. Whitaker, L. M. Coke, P. Koivula, E. J. Heathward, L. V. Fortuno, Y. Zhang, C. G. Yeh, H. A. Baldwin, M. D. Spencer, C. A. Mejias-Aponte, J. Pickel, A. F. Hoffman, C. E. Spivak, C. R. Lupica, S. M. Underhill, S. G. Amara, A. Domanskyi, J. E. Anttila, M. Airavaara, B. T. Hope, F. K. Hamra, C. T. Richie, B. K. Harvey, Neuron-Specific Genome Modification in the Adult Rat Brain Using CRISPR-Cas9 Transgenic Rats. *Neuron.* **102**, 105-119.e8 (2019).

220. H. Zeng, L. Madisen, Mouse transgenic approaches in optogenetics, in *Progress in Brain Research* (Elsevier B.V., ed. 1, 2012; http://dx.doi.org/10.1016/B978-0-444-59426-6.00010-0), vol. 196, pp. 193–213.

221. H. Taniguchi, M. He, P. Wu, S. Kim, R. Paik, K. Sugino, D. Kvitsani, Y. Fu, J. Lu, Y. Lin, G. Miyoshi, Y. Shima, G. Fishell, S. B. Nelson, Z. J. Huang, A Resource of Cre Driver Lines for Genetic Targeting of GABAergic Neurons in Cerebral Cortex. *Neuron.* **71**, 995–1013 (2011).

222. L. Madisen, T. Mao, H. Koch, J. M. Zhuo, A. Berenyi, S. Fujisawa, Y. W. A. Hsu, A. J. Garcia, X. Gu, S. Zanella, J. Kidney, H. Gu, Y. Mao, B. M. Hooks, E. S. Boyden, G. Buzsáki, J. M. Ramirez, A. R. Jones, K. Svoboda, X. Han, E. E. Turner, H. Zeng, A toolbox of Cre-dependent optogenetic transgenic mice for light-induced activation and silencing. *Nat. Neurosci.* **15**, 793–802 (2012).

223. S. Hippenmeyer, E. Vrieseling, M. Sigrist, T. Portmann, C. Laengle, D. R. Ladle, S. Arber, A developmental switch in the response of DRG neurons to ETS transcription factor signaling. *PLoS Biol.* **3**, 0878–0890 (2005).

224. J. Yonekura, M. Yokoi, Conditional genetic labeling of mitral cells of the mouse accessory olfactory bulb to visualize the organization of their apical dendritic tufts. *Mol. Cell. Neurosci.* **37**, 708–718 (2008).

225. R. Haddad, A. Lanjuin, L. Madisen, H. Zeng, V. N. Murthy, N. Uchida, Olfactory cortical neurons read out a relative time code in the olfactory bulb. *Nat. Neurosci.* **16**, 949–957 (2013).

226. Y. I. Kawasawa, A. C. Salzberg, M. Li, N. Šestan, C. A. Greer, F. Imamura, RNA-seq analysis of developing olfactory bulb projection neurons. *Mol. Cell. Neurosci.* **74**, 78–86 (2016).

227. B. Tepe, M. C. Hill, B. T. Pekarek, P. J. Hunt, T. J. Martin, J. F. Martin, B. R. Arenkiel, Single-Cell RNA-Seq of Mouse Olfactory Bulb Reveals Cellular Heterogeneity and Activity-Dependent Molecular Census of Adult-Born Neurons. *Cell Rep.* **25**, 2689-2703.e3 (2018).

228. M. A. Durante, S. Kurtenbach, Z. B. Sargi, J. W. Harbour, R. Choi, S. Kurtenbach, G. M. Goss, H. Matsunami, B. J. Goldstein, Single-cell analysis of olfactory neurogenesis and differentiation in adult humans. *Nat. Neurosci.* **23**, 323–326 (2020).

229. I. Fukunaga, J. T. Herb, M. Kollo, E. S. Boyden, A. T. Schaefer, Independent control of gamma and theta activity by distinct interneuron networks in the olfactory bulb. *Nat. Neurosci.* **17**, 1208–1216 (2014).

230. R. Jordan, I. Fukunaga, M. Kollo, A. T. Schaefer, Active Sampling State Dynamically Enhances Olfactory Bulb Odor Representation. *Neuron.* **98**, 1214-1228.e5 (2018).

231. A. Keller, R. C. Gerkin, Y. Guan, A. Dhurandhar, G. Turu, B. Szalai, J. D. Mainland, Y. Ihara, C. W. Yu, R. Wolfinger, C. Vens, L. Schietgat, K. De Grave, R. Norel, G. Stolovitzky, G. A. Cecchi, L. B. Vosshall, P. Meyer, A. P. Bhondekar, P. C. Boutros, Y. C. Chang, C. Y. Chen, B. W. Cherng, A. Dimitriev, A. Dolenc, A. O. Falcao, A. K. Golińska, M. Y. Hong, P. H. Hsieh, B. F. Huang, L. Hunyady, R. Kaur, M. D. Kazanov, R. Kumar, W. Lesiński, X. Lin, A. Matteson, Y. J. Oyang, B. Panwar, R. Piliszek, A. Polewko-Klim, G. P. S. Raghava,

W. R. Rudnicki, L. Saiz, R. X. Sun, M. Toplak, Y. A. Tung, P. Us, P. Várnai, J. Vilar, M. Xie, D. Yao, M. Zitnik, B. Zupan, Predicting human olfactory perception from chemical features of odor molecules. *Science*. **355**, 820–826 (2017).

232. H. B. Treloar, P. Feinstein, P. Mombaerts, C. A. Greer, Specificity of Glomerular Targeting by Olfactory Sensory Axons. *J. Neurosci.* **22**, 2469–2477 (2002).

233. A. Mizrahi, Dendritic development and plasticity of adult-born neurons in the mouse olfactory bulb. *Nat. Neurosci.* **10**, 444–452 (2007).

234. J. L. Wallace, M. Wienisch, V. N. Murthy, Development and Refinement of Functional Properties of Adult-Born Neurons. *Neuron*. **96**, 883-896.e7 (2017).

235. H. K. K. Kato, M. W. W. Chu, J. S. S. Isaacson, T. Komiyama, Dynamic Sensory Representations in the Olfactory Bulb: Modulation by Wakefulness and Experience. *Neuron*. **76**, 962–975 (2012).

236. A. Wu, B. Yu, Q. Chen, G. A. Matthews, C. Lu, E. Campbell, K. M. Tye, T. Komiyama, Context-dependent plasticity of adult-born neurons regulated by cortical feedback. *Sci. Adv.* **6**, 1–18 (2020).

237. Y. Lu, X. Li, D. Geng, N. Mei, P. Y. Wu, C. C. Huang, T. Jia, Y. Zhao, D. Wang, A. Xiao, B. Yin, Cerebral Micro-Structural Changes in COVID-19 Patients – An MRI-based 3-month Follow-up Study. *EClinicalMedicine*. **25**, 1–12 (2020).

238. A. Campabadal, C. Uribe, B. Segura, H. C. Baggio, A. Abos, A. I. Garcia-Diaz, M. J. Marti, F. Valldeoriola, Y. Compta, N. Bargallo, C. Junque, Brain correlates of progressive olfactory loss in Parkinson's disease. *Park. Relat. Disord.* **41**, 44–50 (2017).

239. R. Barber, C. Ballard, I. G. McKeith, A. Gholkar, J. T. O'Brien, MRI volumetric study of dementia with Lewy bodies: A comparison with AD and vascular dementia. *Neurology*. **54**, 1304–1309 (2000).

240. B. D. Rubin, L. C. Katz, Optical imaging of odorant representations in the mammalian olfactory bulb. *Neuron*. **23**, 499–511 (1999).

241. R. Vincis, S. Lagier, D. Van De Ville, I. Rodriguez, A. Carleton, Sensory-Evoked Intrinsic Imaging Signals in the Olfactory Bulb Are Independent of Neurovascular Coupling. *Cell Rep.* **12**, 313–325 (2015).

242. W. Denk, J. H. Strickler, W. W. Webb, Two-photon laser scanning fluorescence microscopy. *Science*. **248**, 73–76 (1990).

243. K. Svoboda, R. Yasuda, Principles of Two-Photon Excitation Microscopy and Its Applications to Neuroscience. *Neuron*. **50**, 823–839 (2006).

244. M. E. Bocarsly, W. Jiang, C. Wang, J. T. Dudman, N. Ji, Y. Aponte, Minimally invasive microendoscopy system for in vivo functional imaging of deep nuclei in the mouse brain. *Biomed. Opt. Express*. **6**, 4546–4556 (2015).

245. L. Zhang, B. Liang, G. Barbera, S. Hawes, Y. Zhang, K. Stump, I. Baum, Y. Yang, Y. Li, D. T. Lin, Miniscope GRIN Lens System for Calcium Imaging of Neuronal Activity from Deep Brain Structures in Behaving Animals. *Curr. Protoc. Neurosci.* **86**, 1–21 (2019).

246. J. Voigts, J. P. Newman, M. A. Wilson, M. T. Harnett, An easy-to-assemble, robust, and lightweight drive implant for chronic tetrode recordings in freely moving animals. *J. Neural Eng.* **17**, 026044 (2020).

247. P. N. E. Young, M. Estarellas, E. Coomans, M. Srikrishna, H. Beaumont, A. Maass, A. V. Venkataraman, R. Lissaman, D. Jiménez, M. J. Betts, E. McGlinchey, D. Berron, A. O'Connor, N. C. Fox, J. B. Pereira, W. Jagust, S. F. Carter, R. W. Paterson, M. Schöll, Imaging biomarkers in neurodegeneration: Current and future practices. *Alzheimer's Res. Ther.* **12**, 1–17 (2020).

248. S. Tiepolt, M. Patt, G. Aghakhanyan, P. M. Meyer, S. Hesse, H. Barthel, O. Sabri, Current radiotracers to image neurodegenerative diseases. *EJNMMI Radiopharm. Chem.* **4**, 1–23 (2019).

249. A. P. Patterson, S. A. Booth, R. Saba, The Emerging Use of in Vivo Optical Imaging in the

Study of Neurodegenerative Diseases. *Biomed Res. Int.* **2014**, 1–14 (2014).

250. B. V. Zemelman, G. A. Lee, M. Ng, G. Miesenböck, Selective photostimulation of genetically chARGed neurons. *Neuron*. **33**, 15–22 (2002).

251. O. A. Sineshchekov, K. H. Jung, J. L. Spudich, Two rhodopsins mediate phototaxis to low- and high-intensity light in Chlamydomonas reinhardtii. *Proc. Natl. Acad. Sci. U. S. A.* **99**, 8689–8694 (2002).

252. E. S. Boyden, F. Zhang, E. Bamberg, G. Nagel, K. Deisseroth, Millisecond-timescale, genetically targeted optical control of neural activity. *Nat. Neurosci.* **8**, 1263–1268 (2005).

253. J. Mattis, K. M. Tye, E. A. Ferenczi, C. Ramakrishnan, D. J. O'Shea, R. Prakash, L. A. Gunaydin, M. Hyun, L. E. Fenno, V. Gradinaru, O. Yizhar, K. Deisseroth, Principles for applying optogenetic tools derived from direct comparative analysis of microbial opsins. *Nat. Methods*. **9**, 159–172 (2011).

254. M. Smear, A. Resulaj, J. Zhang, T. Bozza, D. Rinberg, Multiple perceptible signals from a single olfactory glomerulus. *Nat. Neurosci.* **16**, 1687–1691 (2013).

255. E. Chong, M. Moroni, C. Wilson, S. Shoham, S. Panzeri, D. Rinberg, Manipulating synthetic optogenetic odors reveals the coding logic of olfactory perception. *Science*. **368**, eaba2357 (2020).

256. E. A. K. Phillips, A. R. Hasenstaub, Asymmetric effects of activating and inactivating cortical interneurons. *Elife*. **5**, 1–22 (2016).

257. N. Bodyak, B. Slotnick, Performance of mice in an automated olfactometer: odor detection, discrimination and odor memory. *Chem. Senses*. **24**, 637–645 (1999).

258. J. K. Reinert, A. T. Schaefer, T. Kuner, High-Throughput Automated Olfactory Phenotyping of Group-Housed Mice. *Front. Behav. Neurosci.* **13**, 1–13 (2019).

259. T. Ackels, A. Erskine, D. Dasgupta, A. C. Marin, T. P. A. Warner, S. Tootoonian, I. Fukunaga, J. J. Haris, A. T. Schaefer, Fast dynamics of the odour landscape are encoded in the mouse olfactory system and guide behaviour. *Nature*. **593,** 558-563 (2021).

260. A. Eibenstein, A. B. Fioretti, C. Lena, N. Rosati, G. Amabile, M. Fusetti, Modern psychophysical tests to assess olfactory function. *Neurol. Sci.* **26**, 147–155 (2005).

261. B. Johnson, R. M. Khan, N. Sobel, Human Olfactory Psychophysics. *Senses A Compr. Ref.* **4**, 823–857 (2008).

262. A. Livermore, D. G. Laing, The influence of odor type on the discrimination and identification of odorants in multicomponent odor mixtures. *Physiol. Behav.* **65**, 311–320 (1998).

263. A. Livermore, D. G. Laing, The influence of chemical complexity on the perception of multicomponent odor mixtures. *Percept. Psychophys.* **60**, 650–661 (1998).

264. L. M. Kay, T. Crk, J. Thorngate, A redefinition of odor mixture quality. *Behav. Neurosci.* **119**, 726–733 (2005).

265. C. Wiltrout, S. Dogra, C. Linster, Configurational and nonconfigurational interactions between odorants in binary mixtures. *Behav. Neurosci.* **117**, 236–245 (2003).

266. C. Linster, T. A. Cleland, Configurational and elemental odor mixture perception can arise from local inhibition. *J. Comput. Neurosci.* **16**, 39–47 (2004).

267. D. Rokni, V. Hemmelder, V. Kapoor, V. N. Murthy, An olfactory cocktail party: figure-ground segregation of odorants in rodents. *Nat. Neurosci.* **17**, 1225–1232 (2014).

268. B. a Reddi, R. H. Carpenter, The influence of urgency on decision time. *Nat. Neurosci.* **3**, 827–830 (2000).

269. L. Chittka, P. Skorupski, N. E. Raine, Speed-accuracy tradeoffs in animal decision making. *Trends Ecol. Evol.* **24**, 400–407 (2009).

270. M. L. Fletcher, Analytical Processing of Binary Mixture Information by Olfactory Bulb Glomeruli. *PLoS One*. **6**, e29360 (2011).

271. N. J. Vickers, T. A. Christensen, T. C. Baker, J. G. Hildebrand, Odour-plume dynamics influence file brain's olfactory code. *Nature*. **410**, 466–470 (2001).

272. M. A. Willis, E. A. Ford, J. L. Avondet, Odor tracking flight of male Manduca sexta moths along plumes of different cross-sectional area. *J. Comp. Physiol. A Neuroethol. Sensory, Neural, Behav. Physiol.* **199**, 1015–1036 (2013).

273. J. Atema, Chemical signals in the marine environment: Dispersal, detection, and temporal signal analysis. *Proc. Natl. Acad. Sci. U. S. A.* **92**, 62–66 (1995).

274. R. Shusterman, Y. B. Sirotin, M. C. Smear, Y. Ahmadian, D. Rinberg, M. C. Smear, Y. Ahmadian, Sniff invariant odor coding. *eNeuro*. **5**, 1–15 (2018).

275. D. W. Wesson, T. N. Donahou, M. O. Johnson, M. Wachowiak, Sniffing behavior of mice during performance in odor-guided tasks. *Chem. Senses*. **33**, 581–96 (2008).

276. D. W. W. Wesson, Sniffing behavior communicates social hierarchy. *Curr. Biol.* **23**, 575–580 (2013).

277. J. V Verhagen, D. W. Wesson, T. I. Netoff, J. a White, M. Wachowiak, Sniffing controls an adaptive filter of sensory input to the olfactory bulb. *Nat. Neurosci.* **10**, 631–639 (2007).

278. R. C. Gerkin, S. J. Tripathy, N. N. Urban, Origins of correlated spiking in the mammalian olfactory bulb. *Proc. Natl. Acad. Sci. U. S. A.* **110**, 17083–17088 (2013).

279. M. E. Phillips, R. N. S. Sachdev, D. C. Willhite, G. M. Shepherd, Respiration drives network activity and modulates synaptic and circuit processing of lateral inhibition in the olfactory bulb. *J. Neurosci.* **32**, 85–98 (2012).

280. M. Díaz-Quesada, I. A. Youngstrom, Y. Tsuno, K. R. Hansen, M. N. Economo, M. Wachowiak, Inhalation frequency controls reformatting of mitral/tufted cell odor representations in the olfactory bulb. *J. Neurosci.* **38**, 2189–2206 (2018).

281. R. M. Carey, M. Wachowiak, Effect of sniffing on the temporal structure of mitral/tufted cell output from the olfactory bulb. *J. Neurosci.* **31**, 10615–10626 (2011).

282. Z. Shao, A. C. Puche, M. T. Shipley, Intraglomerular inhibition maintains mitral cell response contrast across input frequencies. *J. Neurophysiol.* **110**, 2185–2191 (2013).

283. B. A. Johnson, C. C. Woo, M. Leon, Spatial coding of odorant features in the glomerular layer of the rat olfactory bulb. *J. Comp. Neurol.* **393**, 457–471 (1998).

284. B. D. Rubin, L. C. Katz, Spatial coding of enantiomers in the rat olfactory bulb. *Nat. Neurosci.* **4**, 355–356 (2001).

285. A. Kepecs, N. Uchida, Z. F. Mainen, Rapid and Precise Control of Sniffing During Olfactory Discrimination in Rats. *J. Neurophysiol.* **98**, 205–213 (2007).

286. M. Deschênes, J. Moore, D. Kleinfeld, Sniffing and whisking in rodents. *Curr. Opin. Neurobiol.* **22**, 243–250 (2012).

287. M. Ditzen, Odor Similarity Does Not Influence the Time Needed for Odor Processing. *Chem. Senses*. **28**, 781–789 (2003).

288. R. W. Friedrich, Mechanisms of odor discrimination: Neurophysiological and behavioral approaches. *Trends Neurosci.* **29**, 40–47 (2006).

289. N. Uchida, A. Kepecs, Z. F. Mainen, Seeing at a glance, smelling in a whiff: rapid forms of perceptual decision making. *Nat.Rev.Neurosci.* **7**, 485–491 (2018).

290. D. E. Frederick, A. Brown, S. Tacopina, N. Mehta, M. Vujovic, E. Brim, T. Amina, B. Fixsen, L. M. Kay, Task-Dependent Behavioral Dynamics Make the Case for Temporal Integration in Multiple Strategies during Odor Processing. *J. Neurosci.* **37**, 4416–4426 (2017).

291. A. G. Mendonça, J. Drugowitsch, M. I. Vicente, E. E. J. DeWitt, A. Pouget, Z. F. Mainen, The impact of learning on perceptual decisions and its implication for speed-accuracy tradeoffs. *Nat. Commun.* **11**, 1–15 (2020).

292. R. Jordan, M. Kollo, A. T. Schaefer, *eNeuro*, in press, doi:10.1523/ENEURO.0148-18.2018.

293. T. Weiss, K. Snitz, A. Yablonka, R. M. Khan, D. Gafsou, E. Schneidman, N. Sobel, Perceptual convergence of multi-component mixtures in olfaction implies an olfactory white. *Proc. Natl. Acad. Sci.* **109**, 19959–19964 (2012).

294. M. R. Rebello, T. S. McTavish, D. C. Willhite, S. M. Short, G. M. Shepherd, J. V. Verhagen,

Perception of Odors Linked to Precise Timing in the Olfactory System. *PLoS Biol.* **12**, e1002021 (2014).

295. G. Major, D. Tank, Persistent neural activity: Prevalence and mechanisms. *Curr. Opin. Neurobiol.* **14**, 675–684 (2004).

296. J. Zylberberg, B. W. Strowbridge, Mechanisms of Persistent Activity in Cortical Circuits: Possible Neural Substrates for Working Memory. *Annu. Rev. Neurosci.* **40**, 603–627 (2017).

297. Z. Shao, A. C. Puche, S. Liu, M. T. Shipley, Intraglomerular inhibition shapes the strength and temporal structure of glomerular output. *J. Neurophysiol.* **108**, 782–793 (2012).

298. K. M. Cury, N. Uchida, Robust Odor Coding via Inhalation-Coupled Transient Activity in the Mammalian Olfactory Bulb. *Neuron.* **68**, 570–585 (2010).

299. H. Dana, T. W. Chen, A. Hu, B. C. Shields, C. Guo, L. L. Looger, D. S. Kim, K. Svoboda, Thy1-GCaMP6 transgenic mice for neuronal population imaging in vivo. *PLoS One.* **9**, e108697 (2014).

300. M. E. Bouton, C. Sunsay, Contextual control of appetitive conditioning: influence of a contextual stimulus generated by a partial reinforcement procedure. *Q. J. Exp. Psychol. B.* **54**, 109–125 (2001).

301. R. L. Davis, Olfactory learning. *Neuron.* **44**, 31–48 (2004).

302. M. Ennis, C. Linster, V. Aroniadou-Anderjaska, K. Ciombor, M. T. Shipley, Glutamate and Synaptic Plasticity at Mammalian Primary Olfactory Synapses. *Ann. N. Y. Acad. Sci.* **855**, 457–466 (1998).

303. H. Mutoh, Q. Yuan, T. Knöpfel, Long-term depression at olfactory nerve synapses. *J. Neurosci.* **25**, 4252–4259 (2005).

304. S. Giridhar, B. Doiron, N. N. Urban, Timescale-dependent shaping of correlation by olfactory bulb lateral inhibition. *Proc. Natl. Acad. Sci. U. S. A.* **108**, 5843–5848 (2011).

305. R. Balu, R. T. Pressler, B. W. Strowbridge, Multiple Modes of Synaptic Excitation of Olfactory Bulb Granule Cells. *J. Neurosci.* **27**, 5621–5632 (2007).

306. K. A. Sailor, M. T. Valley, M. T. Wiechert, H. Riecke, G. J. Sun, W. Adams, J. C. Dennis, S. Sharafi, G. Ming, H. Song, P.-M. Lledo, Persistent Structural Plasticity Optimizes Sensory Information Processing in the Olfactory Bulb. *Neuron.* **91**, 1–13 (2016).

307. M. L. Fletcher, M. Bendahmane, Visualizing Olfactory Learning Functional Imaging of Experience-Induced Olfactory Bulb Changes. *Prog. Brain Res.* **208**, 89–113 (2014).

308. S. L. Brown, J. Joseph, M. Stopfer, Encoding a temporally structured stimulus with a temporally structured neural representation. *Nat. Neurosci.* **8**, 1568–1576 (2005).

309. G. Nagel, T. Szellas, W. Huhn, S. Kateriya, N. Adeishvili, P. Berthold, D. Ollig, P. Hegemann, E. Bamberg, Channelrhodopsin-2, a directly light-gated cation-selective membrane channel. *Proc. Natl. Acad. Sci.* **100**, 13940–13945 (2003).

310. J. Y. Lin, M. Z. Lin, P. Steinbach, R. Y. Tsien, Characterization of Engineered Channelrhodopsin Variants with Improved Properties and Kinetics. *Biophysj.* **96**, 1803–1814 (2009).

311. P. Alvarez, L. Wendelken, H. Eichenbaum, Hippocampal formation lesions impair performance in an odor-odor association task independently of spatial context. *Neurobiol. Learn. Mem.* **78**, 470–476 (2002).

312. U. Stäubli, T. T. Le, G. Lynch, Variants of olfactory memory and their dependencies on the hippocampal formation. *J. Neurosci.* **15**, 1162–1171 (1995).

313. S. Tronel, S. J. Sara, Mapping of olfactory memory circuits: Region-specific c-fos activation after odor-reward associative learning or after its retrieval. *Learn. Mem.* **9**, 105–111 (2002).

314. D. Saar, Y. Grossman, E. Barkai, Learning-induced enhancement of postsynaptic potentials in pyramidal neurons. *J. Neurophysiol.* **87**, 2358–2363 (2002).

315. C. Martin, N. Ravel, Beta and gamma oscillatory activities associated with olfactory memory tasks: Different rhythms for different functional networks? *Front. Behav. Neurosci.* **8**, 1–13 (2014).

316. C. C. Woo, E. E. Hingco, G. E. Taylor, M. Leon, Exposure to a broad range of odorants decreases cell mortality in the olfactory bulb. *Neuroreport.* **17**, 817–821 (2006).

317. A. V. Kedrov, O. A. Mineyeva, G. N. Enikolopov, K. V. Anokhin, Involvement of Adult-Born and Preexisting Olfactory Bulb and Dentate Gyrus Neurons in a Single-Trial Olfactory Memory Acquisition and Retrieval in Mice. *Neuroscience.* **422**, 75–87 (2019).

318. S. Sultan, N. Mandairon, F. Kermen, S. Garcia, J. Sacquet, A. Didier, Learning-dependent neurogenesis in the olfactory bulb determines long-term olfactory memory. *Faseb j.* **24**, 2355–2363 (2010).

319. M. Alonso, G. Lepousez, W. Sebastien, C. Bardy, M. M. Gabellec, N. Torquet, P. M. Lledo, Activation of adult-born neurons facilitates learning and memory. *Nat Neurosci.* **15**, 897–904 (2012).

320. G. Vetere, L. M. Tran, S. Moberg, P. E. Steadman, L. Restivo, F. G. Morrison, K. J. Ressler, S. A. Josselyn, P. W. Frankland, Memory formation in the absence of experience. *Nat. Neurosci.* **22**, 933–940 (2019).

321. D. Rojas-Líbano, D. E. Frederick, J. I. Egaña, L. M. Kay, The olfactory bulb theta rhythm follows all frequencies of diaphragmatic respiration in the freely behaving rat. *Front. Behav. Neurosci.* **8**, 1–12 (2014).

322. H. Manabe, K. Mori, Sniff rhythm-paced fast and slow gamma-oscillations in the olfactory bulb: Relation to tufted and mitral cells and behavioral states. *J. Neurophysiol.* **110**, 1593–1599 (2013).

323. E. Courtio, C. Amat, M. Thévenet, B. Messaoudi, S. Garcia, N. Buonviso, Reshaping of bulbar odor response by nasal flow rate in the Rat. *PLoS One.* **6**, e16445 (2011).

324. G. Zhou, J. K. Olofsson, M. Z. Koubeissi, G. Menelaou, J. Rosenow, S. U. Schuele, P. Xu, J. L. Voss, G. Lane, C. Zelano, Human hippocampal connectivity is stronger in olfaction than other sensory systems. *Prog. Neurobiol.* **201,** 1-15 (2021).

325. D. H. Heck, R. Kozma, L. M. Kay, The rhythm of memory: how breathing shapes memory function. *J. Neurophysiol.* **122**, 563–571 (2019).

326. C. Zelano, H. Jiang, G. Zhou, N. Arora, S. Schuele, J. Rosenow, J. A. Gottfried, Nasal respiration entrains human limbic oscillations and modulates cognitive function. *J. Neurosci.* **36**, 12448–12467 (2016).

327. A. Arshamian, B. Iravani, A. Majid, J. N. Lundström, Respiration modulates olfactory memory consolidation in humans. *J. Neurosci.* **38**, 10286–10294 (2018).

328. D. P. Daberkow, M. D. Riedy, R. P. Kesner, K. A. Keefe, Arc mRNA induction in striatal efferent neurons associated with response learning. *Eur. J. Neurosci.* **26**, 228–241 (2007).

329. M. P. Kelly, S. A. Deadwyler, Acquisition of a novel behavior induces higher levels of Arc mRNA than does overtrained performance. *Neuroscience.* **110**, 617–626 (2002).

330. Q. Yuan, C. W. Harley, Learning modulation of odor representations : new findings from Arc- indexed networks. *Front. Cell. Neurosci.* **8**, 1–7 (2014).

331. A. J. Giessel, S. R. Datta, Olfactory maps, circuits and computations. *Curr. Opin. Neurobiol.* **24**, 120–132 (2014).

332. D. R. Euston, A. J. Gruber, B. L. McNaughton, The Role of Medial Prefrontal Cortex in Memory and Decision Making. *Neuron.* **76**, 1057–1070 (2012).

333. C. Ranganath, M. K. Johnson, M. D'Esposito, Prefrontal activity associated with working memory and episodic long-term memory. *Neuropsychologia.* **41**, 378–389 (2003).

334. A. Bechara, H. Damasio, A. R. Damasio, Emotion, decision making and the orbitofrontal cortex. *Cereb. Cortex.* **10**, 295–307 (2000).

335. G. D. Petrovich, Lateral hypothalamus as a motivation-cognition interface in the control of feeding behavior. *Front. Syst. Neurosci.* **12**, 1–7 (2018).

336. C. F. Yang, J. L. Feldman, Efferent projections of excitatory and inhibitory preBötzinger Complex neurons. *J. Comp. Neurol.* **526**, 1389–1402 (2018).

337. K. Murata, T. Kinoshita, Y. Fukazawa, K. Kobayashi, K. Kobayashi, K. Miyamichi, H.

Okuno, H. Bito, Y. Sakurai, M. Yamaguchi, K. Mori, H. Manabe, GABAergic neurons in the olfactory cortex projecting to the lateral hypothalamus in mice. *Sci. Rep.* **9**, 1–14 (2019).

338. C. Viguera, J. Wang, E. Mosmiller, A. Cerezo, N. J. Maragakis, Olfactory dysfunction in amyotrophic lateral sclerosis. *Ann. Clin. Transl. Neurol.* **5**, 976–981 (2018).

339. H. Taalman, C. Wallace, R. Milev, Olfactory functioning and depression: A systematic review. *Front. Psychiatry.* **8**, 1–11 (2017).

340. N. Degirmenci, B. Veyseller, H. Hanagasi, B. Bilgic, D. Gurbuz, A. Toprak, O. Ozturan, Olfactory function and olfactory bulb volume in Wilson's disease. *Eur. Arch. Oto-Rhino-Laryngology.* **276**, 139–142 (2019).

341. G. U. Kim, M. J. Kim, S. H. Ra, J. Lee, S. Bae, J. Jung, S. H. Kim, Clinical characteristics of asymptomatic and symptomatic patients with mild COVID-19. *Clin. Microbiol. Infect.* **26**, 948.e1-948.e3 (2020). doi:10.1016/j.cmi.2020.04.040.

342. N. Chen, M. Zhou, X. Dong, J. Qu, F. Gong, Y. Han, Y. Qiu, J. Wang, Y. Liu, Y. Wei, J. Xia, T. Yu, X. Zhang, L. Zhang, Epidemiological and clinical characteristics of 99 cases of 2019 novel coronavirus pneumonia in Wuhan, China: a descriptive study. *Lancet.* **395**, 507–513 (2020).

343. M. Day, Covid-19: four fifths of cases are asymptomatic, China figures indicate. *BMJ.* **369**, m1375 (2020).

344. C. Chen, M. Chen, C. Cheng, Y. Chi, Z. Hu, Y. Liu, S. Huang, Y. Lv, C. Liang, D. Jiao, Y. Yi, X. Zhang, W. Sun, H. Wei, A special symptom of olfactory dysfunction in coronavirus disease 2019: report of three cases. *J. Neurovirol.* **26**, 456–458 (2020).

345. R. C. Gerkin, K. Ohla, M. G. Veldhuizen, P. V Joseph, C. E. Kelly, A. J. Bakke, K. E. Steele, M. C. Farruggia, R. Pellegrino, M. Y. Pepino, C. Bouysset, G. M. Soler, V. Pereda-Loth, M. Dibattista, K. W. Cooper, I. Croijmans, A. Di Pizio, M. H. Ozdener, A. W. Fjaeldstad, C. Lin, M. A. Sandell, P. B. Singh, V. E. Brindha, S. B. Olsson, L. R. Saraiva, G. Ahuja, M. K. Alwashahi, S. Bhutani, A. D'Errico, M. A. Fornazieri, J. Golebiowski, L.-D. Hwang, L. Öztürk, E. Roura, S. Spinelli, K. L. Whitcroft, F. Faraji, F. P. S. Fischmeister, T. Heinbockel, J. W. Hsieh, C. Huart, I. Konstantinidis, A. Menini, G. Morini, J. K. Olofsson, C. M. Philpott, D. Pierron, V. D. C. Shields, V. V Voznessenskaya, J. Albayay, A. Altundag, M. Bensafi, M. A. Bock, O. Calcinoni, W. Fredborg, C. Laudamiel, J. Lim, J. N. Lundström, A. Macchi, P. Meyer, S. T. Moein, E. Santamaría, D. Sengupta, P. P. Domínguez, H. Yanık, S. Boesveldt, J. H. B. de Groot, C. Dinnella, J. Freiherr, T. Laktionova, S. Mariño, E. Monteleone, A. Nunez-Parra, O. Abdulrahman, M. Ritchie, T. Thomas-Danguin, J. Walsh-Messinger, R. Al Abri, R. Alizadeh, E. Bignon, E. Cantone, M. P. Cecchini, J. Chen, M. D. Guàrdia, K. C. Hoover, N. Karni, M. Navarro, A. A. Nolden, P. P. Mazal, N. R. Rowan, A. Sarabi-Jamab, N. S. Archer, B. Chen, E. A. Di Valerio, E. L. Feeney, J. Frasnelli, M. Hannum, C. Hopkins, H. Klein, C. Mignot, C. Mucignat, Y. Ning, E. E. Ozturk, M. Peng, O. Saatci, E. A. Sell, C. H. Yan, R. Alfaro, C. Cecchetto, G. Coureaud, R. D. Herriman, J. M. Justice, P. K. Kaushik, S. Koyama, J. B. Overdevest, N. Pirastu, V. A. Ramirez, S. C. Roberts, B. C. Smith, H. Cao, H. Wang, P. Balungwe, M. Baguma, T. Hummel, J. E. Hayes, D. R. Reed, M. Y. Niv, S. D. Munger, V. Parma, Recent smell loss is the best predictor of COVID-19 among individuals with recent respiratory symptoms. *Chem. Senses, 46,* (2021), doi:10.1093/chemse/bjaa081.

346. M. Hoffmann, H. Kleine-Weber, S. Schroeder, N. Krüger, T. Herrler, S. Erichsen, T. S. Schiergens, G. Herrler, N. H. Wu, A. Nitsche, M. A. Müller, C. Drosten, S. Pöhlmann, SARS-CoV-2 Cell Entry Depends on ACE2 and TMPRSS2 and Is Blocked by a Clinically Proven Protease Inhibitor. *Cell.* **181**, 271-280.e8 (2020).

347. Y. J. Kang, J. H. Cho, M. H. Lee, Y. J. Kim, C. S. Park, The diagnostic value of detecting sudden smell loss among asymptomatic COVID-19 patients in early stage: The possible early sign of COVID-19. *Auris Nasus Larynx.* **47**, 565–573 (2020).

348. L. Spadera, P. Viola, D. Pisani, A. Scarpa, D. Malanga, G. Sorrentino, E. Madini, C. Laria,

T. Aragona, G. Leopardi, G. Maggiore, M. Ciriolo, L. Boccuto, R. Pizzolato, L. Abenavoli, C. Cassandro, M. Ralli, E. Cassandro, G. Chiarella, Sudden olfactory loss as an early marker of COVID-19: a nationwide Italian survey. *Eur. Arch. Oto-Rhino-Laryngology*. **278**, 247–255 (2020).

349. R. L. Doty, M. G. Newhouse, J. D. Azzalina, Internal consistency and short-term test-retest reliability of the university of pennsylvania smell identification test. *Chem. Senses*. **10**, 297–300 (1985).

350. S. A. Meo, A. A. Abukhalaf, A. A. Alomar, Magnetic Resonance Imaging (MRI) and neurological manifestations in SARS-CoV-2 patients. *Eur. Rev. Med. Pharmacol. Sci.* **25**, 1101–1108 (2021).

351. M. Taquet, J. R. Geddes, M. Husain, S. Luciano, P. J. Harrison, 6-month neurological and psychiatric outcomes in 236 379 survivors of COVID-19: a retrospective cohort study using electronic health records. *The Lancet Psychiatry*. **8**, 416–427 (2021).

352. R. Haddad, R. Khan, Y. K. Takahashi, K. Mori, D. Harel, N. Sobel, A metric for odorant comparison. *Nat. Methods*. **5**, 425–429 (2008).

353. J. Meinhardt, J. Radke, C. Dittmayer, J. Franz, C. Thomas, R. Mothes, M. Laue, J. Schneider, S. Brünink, S. Greuel, M. Lehmann, O. Hassan, T. Aschman, E. Schumann, R. L. Chua, C. Conrad, R. Eils, W. Stenzel, M. Windgassen, L. Rößler, H. H. Goebel, H. R. Gelderblom, H. Martin, A. Nitsche, W. J. Schulz-Schaeffer, S. Hakroush, M. S. Winkler, B. Tampe, F. Scheibe, P. Körtvélyessy, D. Reinhold, B. Siegmund, A. A. Kühl, S. Elezkurtaj, D. Horst, L. Oesterhelweg, M. Tsokos, B. Ingold-Heppner, C. Stadelmann, C. Drosten, V. M. Corman, H. Radbruch, F. L. Heppner, Olfactory transmucosal SARS-CoV-2 invasion as a port of central nervous system entry in individuals with COVID-19. *Nat. Neurosci.* **24**, 168–175 (2021).

354. L. Thabane, L. Mbuagbaw, S. Zhang, Z. Samaan, M. Marcucci, C. Ye, M. Thabane, L. Giangregorio, B. Dennis, D. Kosa, V. B. Debono, R. Dillenburg, V. Fruci, M. Bawor, J. Lee, G. Wells, C. H. Goldsmith, A tutorial on sensitivity analyses in clinical trials: The what, why, when and how. *BMC Med. Res. Methodol.* **13**, 1–12 (2013).

355. F. E. Grubbs, Procedures for Detecting Outlying Observations in Samples. *Technometrics*. **11**, 1–21 (1969).

356. C. Menni, C. H. Sudre, C. J. Steves, S. Ourselin, T. D. Spector, Quantifying additional COVID-19 symptoms will save lives. *Lancet*. **395**, e107–e108 (2020).

357. Y. Gao, T. Li, M. Han, X. Li, D. Wu, Y. Xu, Y. Zhu, Y. Liu, X. Wang, L. Wang, Diagnostic utility of clinical laboratory data determinations for patients with the severe COVID-19. *J. Med. Virol.* **92**, 791–796 (2020).

358. S. H. Bagheri, A. Asghari, M. Farhadi, A. R. Shamshiri, A. Kabir, S. K. Kamrava, M. Jalessi, A. Mohebbi, R. Alizadeh, A. A. Honarmand, B. Ghalehbaghi, A. Salimi, F. D. Firouzabadi, Coincidence of COVID-19 epidemic and olfactory dysfunction outbreak in Iran. *Med. J. Islam. Repub. Iran*. **34**, 1–17 (2020).

359. L. A. Vaira, G. Salzano, G. Deiana, G. De Riu, Anosmia and Ageusia: Common Findings in COVID-19 Patients. *Laryngoscope*. **130**, 1787 (2020).

360. J. Netland, D. K. Meyerholz, S. Moore, M. Cassell, S. Perlman, Severe Acute Respiratory Syndrome Coronavirus Infection Causes Neuronal Death in the Absence of Encephalitis in Mice Transgenic for Human ACE2. *J. Virol.* **82**, 7264–7275 (2008).

361. K. Li, C. Wohlford-Lenane, S. Perlman, J. Zhao, A. K. Jewell, L. R. Reznikov, K. N. Gibson-Corley, D. K. Meyerholz, P. B. McCray, Middle east respiratory syndrome coronavirus causes multiple organ damage and lethal disease in mice transgenic for human dipeptidyl peptidase 4. *J. Infect. Dis.* **212**, 712–722 (2015).

362. M. Desforges, A. Le Coupanec, É. Brison, M. Meessen-Pinard, P. J. Talbot, Neuroinvasive and neurotropic human respiratory coronaviruses: Potential neurovirulent agents in humans. *Adv. Exp. Med. Biol.* **807**, 75–96 (2014).

363. K. Bilinska, P. Jakubowska, C. S. Von Bartheld, R. Butowt, Expression of the SARS-CoV-2 Entry Proteins, ACE2 and TMPRSS2, in Cells of the Olfactory Epithelium: Identification of Cell Types and Trends with Age. *ACS Chem. Neurosci.* **11**, 1555–1562 (2020).

364. C. G. Hahn, L. Y. Han, N. E. Rawson, N. Mirza, K. Borgmann-Winter, R. H. Lenox, S. E. Arnolb, In vivo and in vitro neurogenesis in human olfactory epithelium. *J. Comp. Neurol.* **483**, 154–163 (2005).

365. L. A. Vaira, G. Salzano, M. Petrocelli, G. Deiana, F. A. Salzano, G. De Riu, Validation of a self-administered olfactory and gustatory test for the remotely evaluation of COVID-19 patients in home quarantine. *Head Neck*. **42**, 1570–1576 (2020).

366. L. A. Vaira, G. Deiana, A. G. Fois, P. Pirina, G. Madeddu, A. De Vito, S. Babudieri, M. Petrocelli, A. Serra, F. Bussu, E. Ligas, G. Salzano, G. De Riu, Objective evaluation of anosmia and ageusia in COVID-19 patients: Single-center experience on 72 cases. *Head Neck*. **42**, 1252–1258 (2020).

367. D. Bagnasco, G. Passalacqua, F. Braido, E. Tagliabue, F. Cosini, M. Filauro, A. Ioppi, A. Carobbio, D. Mocellin, A. M. Riccio, F. R. Canevari, Quick Olfactory Sniffin' Sticks Test (Q-Sticks) for the detection of smell disorders in COVID-19 patients. *World Allergy Organ. J.* **14**, 1–8 (2021).